

INAUGURAL-DISSERTATION

zur
Erlangung der Doktorwürde
der
Naturwissenschaftlich-Mathematischen
Gesamtfakultät
der
Ruprecht-Karls-Universität Heidelberg

vorgelegt von

Diplom-Chemikerin
Elke Faßhauer

aus Hamburg

Tag der mündlichen Prüfung:
27. Juni 2014

**Investigation of Relativistic Effects
in Electronic Decay Processes
in Small and Large Noble Gas Clusters
by *Ab Initio* and New Simulation Approaches**

Gutachter:

PD Dr. rer. nat. Markus Pernpointner

Prof. Dr. rer. nat. Andreas Dreuw

*Ein Freund ist ein Mensch, der die Melodie deines Herzens kennt und sie dir vorsingt,
wenn du sie vergessen hast.*

(nach Albert Einstein)

Den Sängern

Kurzfassung

Der Interatomic/ Intermolecular Coulombic Decay (ICD) sowie der Electron Transfer Mediated Decay (ETMD) sind elektronische Zerfallsprozesse, die in einer Vielzahl von Systemen vorkommen, von kleinen, zweiatomigen Edelgasclustern bis hin zu biologischen Systemen. Sofern schwere Atome an diesen Prozessen beteiligt sind, können relativistische Effekte nicht von der Betrachtung ausgeschlossen werden. Ihr Einfluss ist allerdings bislang nicht eingehend untersucht worden.

In dieser Abhandlung werden sowohl der Einfluss der Spin-Bahn-Kopplung als auch skalarrelativistischer Effekte auf die Öffnungen bzw. Schließungen der Zerfallskanäle und die Zerfallsbreiten der jeweiligen Kanäle untersucht. Hierzu wurden asymptotische Formeln für die Zerfallsbreiten des ICD und ETMD hergeleitet, welche eine Abschätzung der Zerfallsbreiten auf Grundlage experimenteller Daten der Einzelkomponenten erlauben. Eine genauere Beschreibung der Zerfallsbreiten erforderte die Übertragung der nicht-relativistischen FanoADC-Stieltjes Methode auf die relativistische Behandlung und ihrer Implementierung im relativistischen, quantenchemischen Programmpaket Dirac. Hiermit wurden kleine Edelgassysteme studiert.

Die experimentellen Untersuchungen dieser Zerfallsprozesse werden vorwiegend an Edelgasclustern bestehend aus 100 – 2000 Atomen durchgeführt, die mit quantenchemischen *ab initio* Methoden aufgrund ihrer Größe nicht mehr behandelt werden können. Um eine Vergleichbarkeit herzustellen, wurde der Einfluss der Clusterumgebung auf die Zerfallsprozesse untersucht und auf dieser Grundlage eine Methode zur Simulation von Sekundärelektronenspektren entwickelt. Sie verwendet wahlweise die hergeleiteten, asymptotischen Formeln oder die in Abhängigkeit von der Geometrie berechneten Zerfallsbreiten. Mit Hilfe dieser im Programm HARDRoC automatisierten Herangehensweise wurden die beiden konkurrierenden Zerfallskanäle, ICD und ETMD, in ArXe Clustern untersucht. Darüberhinaus bildet sie die Grundlage für eine neue Methode zur Strukturaufklärung heteroatomarer Edelgascluster, welche am Beispiel von NeAr Clustern erläutert wird.

Abstract

The Interatomic/ Intermolecular Coulombic Decay (ICD) as well as the Electron Transfer Mediated Decay (ETMD) are electronic decay processes, which occur in a multitude of systems ranging from noble gas dimers to biological systems. If heavy atoms are involved in these processes, relativistic effects cannot be neglected. However, their influence has so far not been investigated thoroughly.

In this thesis, the influence of the spin-orbit coupling as well as scalar-relativistic effects on openings and closings of decay channels as well as on the corresponding decay widths are studied. For this purpose, asymptotic expressions for the decay widths of both ICD and ETMD are derived. They allow for analytic studies of basic properties and estimations of the decay widths based on properties of the constituting atoms or molecules of the total system. A more precise description of the decay widths required the transfer of the non-relativistically known FanoADC-Stieltjes method to the relativistic regime and its implementation into the relativistic quantum chemical program package Dirac. Using this method, small noble gas systems are investigated.

Experimentally, these decay processes are usually studied in noble gas clusters consisting of 100 – 2000 atoms. These clusters are too large to be treated with *ab initio* methods. In order to allow for a comparison of theoretical and experimental results, the influence of the cluster environment on the secondary electron spectra are investigated. These findings are used for the development of a method for the decay width estimation of clusters based on the asymptotic expressions or calculated decay widths for a multitude of geometries. This method was implemented as the program HARDRoC and is used for the investigation of the two competing processes ICD and ETMD in ArXe clusters. Additionally, it is the foundation of a new structure determination method of heteronuclear noble gas clusters, which is exemplarily explained for NeAr clusters.

Contents

1. Introduction	1
I. Theory	5
2. Autoionization Processes of Ionized Species	7
2.1. Auger Process	7
2.2. Interatomic Coulombic Decay	8
2.3. Electron Transfer Mediated Decay Processes	9
2.4. Resonant ICD (RICD)	10
3. Relativistic Quantum Chemistry	13
3.1. Special Relativity	13
3.2. Lorentz Transformation	13
3.3. Space-Time	14
3.4. Relativistic Mechanics	14
3.5. Relativistic Electrodynamics	15
3.6. Relativistic Quantum Mechanics	15
3.6.1. Klein-Gordon Equation for a Freely Moving Particle	16
3.6.2. Dirac Equation	16
3.7. Many-Particle Systems in Relativistic Quantum Chemistry	21
3.7.1. Dirac-Coulomb Hartree-Fock	22
3.7.2. Construction of a Basis for the Relativistic Treatment	24
3.8. Correlation Methods	25
3.9. Relativistic Effects and Spin-Orbit Coupling in Many-Electron Systems	26
3.9.1. Spin-Orbit Coupling	26
3.9.2. Scalar-Relativistic Effects	26
4. Resonances	29
4.1. General Remarks	29
4.2. Projection Method for the Evaluation of the \mathcal{T} Matrix	31
5. Decay Widths of ICD-like Processes in the Asymptotic Limit	37
5.1. Interatomic Coulombic Decay	41

5.2. Electron Transfer Mediated Decay	43
6. Clusters	47
6.1. Noble Gas Clusters	48
6.2. Creation of Noble Gas Clusters	51
6.2.1. Creation of Heteronuclear Noble Gas Clusters	53
6.3. Experimental Analysis Tools	53
II. Methodology	59
7. Continuum Properties from \mathcal{L}^2 Functions	61
7.1. Bound and Continuum States	61
7.2. Gaussian Quadrature	62
7.3. Expressing the Continuum Properties in Terms of Gaussian Quadrature	63
7.3.1. Moment Problem	65
7.3.2. Finding the Gaussian Quadrature Abscissae and Weights from Modified Moments	66
7.3.3. Stieltjes Imaging	69
7.3.4. Quality and Stability of the Results	71
8. Algebraic Diagrammatic Construction (ADC)	73
8.1. FanoADC	75
8.1.1. Partitioning by Population	76
8.1.2. Partitioning by Energy	77
8.1.3. Partial Decay Widths	77
8.2. How to Obtain Reliable Results	78
8.2.1. Choice of Basis Set and Active Space	78
8.2.2. Quality Check Using the Decay Width Profile	80
III. Results	85
9. Auger Decay of Noble Gas Atoms	87
9.1. Neon	87
9.1.1. Computational Details	88
9.1.2. Decay Widths	88
9.2. Xenon	89
9.2.1. Computational Details	89
9.2.2. Open Channels	89
9.2.3. Auger Decay from the Xe4d Region	91

9.2.4. Auger Decay from the Xe4p Region	92
9.3. Summary	98
10. Geometric Influence on ICD and ETMD3 Illustrated Using Pairs and Triples of Atoms	99
10.1. Influence of the Geometry on ICD processes	100
10.1.1. Geometry Dependence of the ICD Channel Openings and Closings	100
10.1.2. Geometry Dependence of the ICD Decay Widths	101
10.2. Influence of the Geometry on ETMD3 processes	102
10.2.1. Geometry Dependence of the ETMD3 Channel Openings and Closings	102
10.2.2. Geometry Dependence of the ETMD3 Decay Rates	103
10.3. Influence of the Coordinate System Choice	107
11. Dependence of Interatomic Coulombic Decay (ICD) Decay Widths on the Quantum Numbers	109
11.1. Total Angular Momentum	109
11.1.1. One Initial State and Several Final States	111
11.1.2. Several Initial States and One Final State	112
11.2. Projection of the Total Angular Momentum	112
12. ICD Decay Widths of ArXe Obtained by the Relativistic FanoADC	115
12.1. Computational Details	115
12.2. Results	115
12.3. Possible Improvements	118
13. Heteroatomic Noble Gas Clusters	121
13.1. ArXe-Clusters	123
13.1.1. One Argon Atom on a Xenon Surface	123
13.1.2. Cluster Structures	128
13.2. Structure Determination of NeAr Clusters	135
13.2.1. Experimental Results	135
13.2.2. Computational Details	137
13.2.3. Hypothetical, idealized structures of the NeAr clusters	138
13.2.4. Interpretation of the graphs	141
13.2.5. Assignment of the different measurements to cluster structures	143
13.2.6. Conclusions	146
14. Summary and Outlook	147
A. Properties of Noble Gas Atoms	151

B. NeAr Cluster Structure Agreement Plots	153
C. Programs and Scripts	159
C.1. HARDRoC — Hunting Asymptotic Relativistic Decay Rates of Clusters .	159
C.2. Relativistic FanoADC	161
C.3. ICOCLUS	162
C.3.1. Construction of the Core Icosahedral Cluster	162
C.3.2. Complete Shells	163
C.3.3. Incomplete Shells	164
C.3.4. Triangular Surfaces Covered by Layers of Atoms	164
C.3.5. Caps	165
C.3.6. Randomly Arranged Atoms Around Complete Shells	166
C.4. FCCCLUS	167

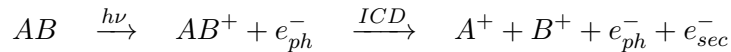
List of Acronyms

ADC Algebraic Diagrammatic Construction	3
AES Auger Electron Spectroscopy	53
CES Correlated Excited State	73
CI Configuration Interaction	35
CK Coster-Kronig	7
DIP Double Ionization Potential	87
ETI Excitation Transfer Ionization	11
ETMD Electron Transfer Mediated Decay	9
fcc face-centered-cubic	50
FWHM Full Width Half Maximum	31
HARDRoC Hunting Asymptotic Relativistic Decay Rates of Clusters	3
hcp hexagonal-closest-packing	51
ICD Interatomic Coulombic Decay	iii
ISR Intermediate State Representation	61
KBJ Kaufmann-Baumeister-Jungen	80
MCDF Multi-Configurational Dirac-Fock	91
NEXAFS Near Edge X-ray Absorption Fine Structure	53

PES Photo-Electron Spectroscopy	53
QED Quantum Electrodynamics	18
RAS Resonant Auger Electron Spectroscopy.....	53
RICD Resonant Interatomic Coulombic Decay.....	10
SCF Self-Consistent Field.....	23
SCK Super-Coster-Kronig.....	7
SIP Single Ionization Potential.....	87
UPS Ultra-Violet Photo-Electron Spectroscopy.....	53
XAS X-ray Absorption Spectroscopy	53
XES X-ray Emission Spectroscopy	53
XPS X-ray Photo-Electron Spectroscopy	53

1. Introduction

Electronic vacancies in the sub-outer-valence of an atom or molecule created by radiation or radioactive decay are excited system. These can decay via photon emission, coupling to vibrational degrees of freedom or via electronic decay processes like the Auger decay [1, 2] or the manifold of Interatomic / Intermolecular Coulombic Decay (ICD) processes. The latter was theoretically predicted in 1997 by Cederbaum and involves neighbouring atoms and molecules in the decay. It can most generally described by:



Here, a system AB is ionized in the inner-valence of atom or molecule A and the corresponding photo-electron e_{ph}^- is emitted. The ionized system AB^+ can then electronically rearrange and as a consequence the system is split into two positively charged components A^+ , B^+ and a secondary electron e_{sec}^- , also called ICD electron, which is emitted. This kind of processes occurs in a multitude of systems like noble gas clusters and hydrogen-bonded systems. Furthermore, it has been found to explain the electron detachment essential in repair of DNA lesions in the photolyases enzymes [3]. It is also discussed as source for low kinetic energy electrons in the body after an initiation by a radioactive decay in the medical treatment of cancer [4, 5, 6, 7, 8]. These low kinetic energy electrons cause double strand breaks of DNA more efficiently than electrons of higher energies. None of the competing processes has until now been proven to create these slow electrons and to explain the locally observed damage.

This process can occur if two criteria, the energy and the coupling criterion, are fulfilled. To fulfill the energy criterion it is required that the energy of the doubly ionized final state excluding the secondary electron is lower than the energy of the singly ionized initial state. If this is not the case, the channel is closed and the corresponding fragments of the channel are not observed after the decay. To fulfill the coupling criterion it is required that the process is efficient enough to compete with other decay processes like the Auger decay and the radiative decay. Hence, a typical study of ICD-like processes consists of two parts:

- determination of the kinetic energy of the secondary electron and as a consequence, which channels are open
- calculation of the decay width $\Gamma = \frac{\hbar}{\tau}$, which is proportional to the decay rate $\frac{1}{\tau}$ and anti-proportional to the lifetime τ

Throughout the last two decades, such processes have been studied intensively in experiment and in theory using non-relativistic quantum chemistry (see the review in Ref. [9] and references herein). However, if heavy elements are involved in these decay processes, relativistic effects are expected to play an important role. Therefore, the aim of this thesis is to investigate how spin-orbit coupling and scalar-relativistic effects influence both, the energies of the involved initial and final states as well as the decay widths of the processes. It will be shown that the spin-orbit coupling leads to a larger number of decay channels compared to the non-relativistic description. These channels open at different geometries of the system under investigation and can therefore lead to channel openings at geometries at which the channel in the corresponding non-relativistic description would be closed.

Scalar-relativistic effects shift the energies of the initial and final states. These shifts are most pronounced in the core region and hence might only play a minor role for decay processes in the valence. Furthermore, the quantity of interest is the energy difference between the initial and final states. If the energy shift occurs in the same direction, the effect on the measured kinetic energy of the secondary electron is rather small.

For the calculation of initial and final state energies as well as decay widths using relativistic methods, it has to be noted that the type of wavefunctions is inherently different than from the non-relativistic case. They are characterized by the total angular momentum J and its projection M_J rather than the angular momentum quantum numbers L, M_L and spin quantum numbers S, M_S . The different spatial structure compared to the non-relativistic wavefunction allows for decays, which are non-relativistically forbidden by symmetry. E.g., the transition between a $d_{3/2}$ and an $s_{1/2}$ state is allowed in the relativistic description, while it breaks the Laporte rule in the non-relativistic framework.

The difficulty in the description of the decay width is caused by the necessity to include both the bound states as well as the freely moving secondary electron, which have to fulfill different boundary conditions. Non-relativistically, it has been studied using asymptotic approximations [10] and various quantum chemical methods based on \mathcal{L}^2 functions. The asymptotic expressions for the decay width of the ICD and a competing ICD-like process, the ETMD3 (Electron Transfer Mediated Decay) with three involved units, are derived in this thesis. The basic influence of spin-orbit coupling on the decay widths of the ICD and ETMD3 is studied for various geometries and initial and final state configurations. The quantum chemical methods, which have been used for the non-relativistic description of the decay widths are the Wigner-Weisskopf theory [11], CAP-CI (Complex Absorbing Potential based on a Configuration Interaction wavefunction) [12, 13] and the FanoADC-Stieltjes method [14]. While the CAP-CI method is the most precise of the three methods above, it is at the same not size-consistent and requires a huge basis set. Therefore, it is not suited for the investigation of larger systems. In contrast to this, the Wigner-Weisskopf theory is based on the lowest non-vanishing order of perturbation theory

and therefore computationally affordable even for large systems. However, the price for the lower computational costs are less accurate results. A compromise between accuracy and computational cost is the FanoADC-Stieltjes approach, which is based on the Algebraic Diagrammatic Construction (ADC) and therefore likewise includes higher perturbational orders *and* is size-consistent. For these reasons, the FanoADC-Stieltjes method was implemented in the relativistic quantum chemical program package Dirac [15]. First results obtained with this method are found in this thesis.

For the experimental validation of the ICD-like processes, most often noble gas clusters of 100–2000 atoms are studied, because noble gases can easily be introduced into the apparatus and cleaning after the experiment is not necessary. In order to compare the theoretically obtained results with the experimental measurements of the kinetic energy of the secondary electron, it has to be noted that the cluster environment also affects the secondary electron spectrum. The ionized constituents of both the initial and the final states are stabilized by the cluster environment. However, the closer the vacancy is to the nucleus, the weaker is the interaction with the environment. Therefore, the stabilization of the ionized atoms in the final state is more pronounced than for the initially ionized atom and as a consequence, the kinetic energy spectrum of the secondary electron is shifted towards higher energies. Hence, additional channel openings can be observed. Furthermore, the larger number of decay partners increases the decay rate and for statistic reasons the decay rate for a specific initially ionized atom in a heteronuclear cluster strongly depends on its position in the cluster.

In order to model the secondary electron spectra of clusters, a method was developed based on the decomposition of cluster structures into manifolds of decaying pairs and triples. For these pairs and triples, the kinetic energies of the secondary electrons and the corresponding decay widths are evaluated based on either the asymptotic expressions for the decay widths or quantum chemical calculations for dimers and trimers. For the automatic evaluation of a large number of cluster structures the program Hunting Asymptotic Relativistic Decay Rates of Clusters (HARDRoC) [16] was developed.

The thesis consists of three main parts: First, basic theory involved in this thesis is discussed in part I. In part II, the *ab initio* methods developed and used are introduced and finally in part III, the obtained results are presented. An additional description of the programs developed in this thesis are to be found in the Appendix C.

In the theory part, the large variety of autoionization processes, especially the ICD-like processes, is presented in chapter 2. Then, an introduction into relativistic quantum chemistry in chapter 3 and resonances in chapter 4, which are needed for the calculation of the decay widths, is given. From the latter, asymptotic approximations of the decay width for the ICD and ETMD3 are derived in the relativistic framework in chapter 5. Finally, noble gas clusters and their experimental creation and measurement are presented in chapter 6.

In the methodology part, the description of continuum properties with \mathcal{L}^2 functions, the

ADC and especially the FanoADC-Stieltjes approach are presented in chapters 7 and 8. In the results part, the systems are studied with increasing number of constituents. First, in chapter 9, Auger processes of noble gas atoms are studied as the smallest systems undergoing electronic decay processes for testing purposes of the relativistic FanoADC-Stieltjes implementation. Hereby, basic influences of the relativistic effects on the autoionization processes are already investigated. Then, channel openings and decay widths for different geometries of pairs and triples are studied including relativistic effects in chapter 10. Afterwards, the relative asymptotic decay width behaviour of different decay channels, which are split due to spin-orbit coupling are investigated in chapter 11. Based on the relativistic FanoADC-Stieltjes approach validated for the Auger process, the decay widths of the ArXe dimer are investigated using the relativistic FanoADC-Stieltjes approach in chapter 12. Finally, in chapter 13, secondary electron spectra of heteronuclear ArXe and NeAr clusters are studied based on the results of the preceding chapters. In the ArXe clusters, relativistic effects, basic effects of the cluster environment and different cluster structures are investigated. For the NeAr clusters, a new procedure to determine structural information of mixed noble gas clusters with competing ICD processes is presented.

All this shows that a relativistic treatment for heavy processes involving heavy atoms and consideration of neighbour arrangements for the explanation of noble gas clusters are inherently important.

Part I.

Theory

2. Autoionization Processes of Ionized Species

Vacancies in the core or inner-valence region of atoms and molecules can decay via photon emission, via several autoionization processes or, in case of molecules, via coupling to the nuclear motion. All these processes compete and hence the fastest are observed. In the autoionization processes the vacancy is filled by an electron from an outer shell and the excess energy is simultaneously transferred to a second electron, which as a consequence is emitted. Hence the final state is composed of a doubly ionized system and an electron in the continuum. Each final state is characterized by its electronic configuration or more technical by the quantum numbers of the vacancies and is called a channel. Autoionization processes can occur when two criteria are fulfilled, the energy and the coupling criterion. The energy criterion requires the conservation of energy and hence the doubly ionized system in the final state has to be of lower energy than the singly ionized initial state. In this case the corresponding decay channel is open. If a final state configuration is energetically inaccessible, the channel is closed. The second criterion is called the coupling criterion, which requires the process to be efficient enough to compete with other decay processes.

The different autoionization processes can be classified by the initial vacancy, by where the vacancy filling electron originates and by where the secondary electron is emitted from.

2.1. Auger Process

The Auger process, independently discovered by Lise Meitner [1] and Pierre Auger [2], is the longest known of the presented autoionization processes. Here the initial ionization mostly resides in the core region of an atom. The vacancy is then filled by another electron from an orbital of higher energy of the same atom. The energy is simultaneously transferred to yet another electron of the same atom and emitted as shown in Figure 2.1. The final state is characterized by a doubly charged system.

Special cases of the Auger process are the Coster-Kronig (CK) and the Super-Coster-Kronig (SCK) decays. In a CK decay, the vacancy filling electron originates from a higher subshell of the same shell characterized by the principal quantum number n . In a SCK decay the emitted electron also stems from the same shell [17].

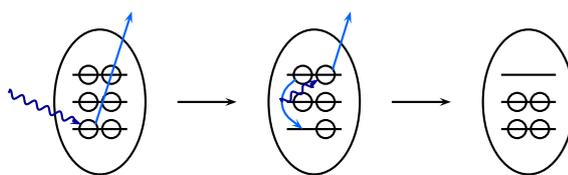


Figure 2.1.: Schematic illustration of the Auger process. The initial vacancy is filled by an electron of an energetically higher orbital and the excess energy is transferred to another electron of the same atom, which is emitted.

Since both the vacancy filling electron and the emitted electron originate from the same atom as the initial vacancy, neither energy nor electrons need to be transferred through space, this process is ultrafast with lifetimes in the attosecond regime [18].

In order to fulfill the energy criterion, the initial ionization energy has to be high in order to exceed the final state energy. This is why the process is rarely observed after ionization from the inner-valence region and therefore, it is possible to observe other autoionization processes in the latter systems.

2.2. Interatomic Coulombic Decay

The Interatomic/ Intermolecular Coulombic Decay (ICD) was predicted theoretically in 1997 by L. S. Cederbaum [19] and later verified experimentally by Marburger et al. [20]. Here the initial vacancy is filled by an electron of the same atom and simultaneously, the atom interacts with the surroundings by transferring the excess energy to another atom, which finally gets ionized. The positive charges on the different atomic sites repel each other and therefore undergo Coulomb explosion as shown in Figure 2.2.

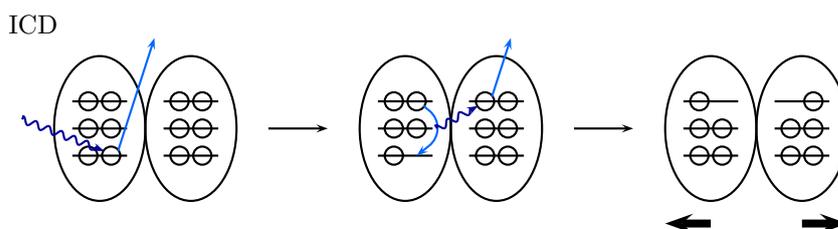


Figure 2.2.: Schematic illustration of the ICD. The initial vacancy is filled by an electron of the valence and the excess energy is transferred to an electron of a neighbouring atom, which consequently is emitted. The two positively charged units undergo Coulomb explosion.

Due to the energy transfer via a virtual photon between two subsystems the ICD has a lifetime of femto- to pico-seconds [21, 22, 23, 13, 24, 14]. The initial vacancies of observed ICD processes are normally in the inner-valence, but are not limited to these

cases. However, one might rarely observe an ICD after core ionization, because the Auger process would then be energetically allowed and outrule the slower ICD. An elaborate review including theoretical and experimental examples is to be found in reference [9].

2.3. Electron Transfer Mediated Decay Processes

In the Electron Transfer Mediated Decay (ETMD) processes the vacancy is filled by an electron from another atom or molecule. Depending on where the excess energy is transferred to and hence how many units are involved in the process, the processes are either called ETMD2 or ETMD3 as shown in Figure 2.3.

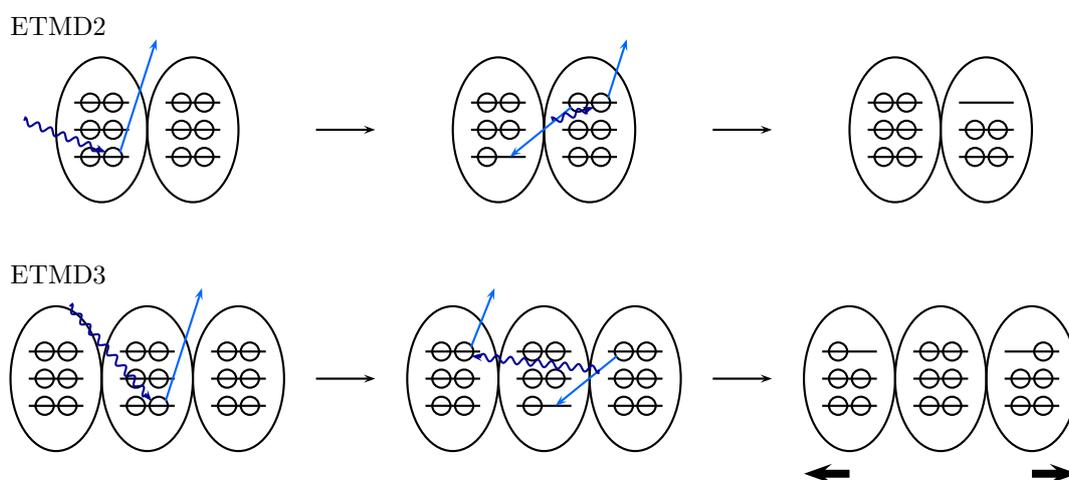


Figure 2.3.: Schematic representation of ETMD processes. In the ETMD2 the initial vacancy is filled by an electron of a neighbouring atom and the excess energy is transferred to an electron of this second atom, which consequently gets ionized. The final state is characterized by the initially ionized atom to be neutral and the neighbouring atom to be doubly ionized. In the ETMD3, the initial vacancy is filled by an electron of a neighbouring unit and simultaneously the excess energy is transferred to an electron of a third unit, which gets ionized. The final state is characterized by the initially ionized atom being neutralized and the two neighbouring atoms being singly ionized. Hence, they repel each other.

In the ETMD2 [23] the excess energy is transferred to an electron from the vacancy filling unit while in the ETMD3 the excess energy is transferred to a third unit [21]. The decay rate of the process is mostly governed by the electron transfer rate, which depends on the overlap between the electron clouds of the two units and hence decreases exponentially with the internuclear/ intermolecular distance. Therefore, the decay rate of the process is normally about two to three orders of magnitude slower than of a competing ICD process and can hence only be observed in cases where either the ICD is energetically forbidden or, in case of the ETMD3, at interfaces where the number of

potential triples of atoms is higher and therefore increases the probability for an ETMD3 process [25].

The exchange ICD process' decay rate is also governed by the electron transfer even though it is not evident from its name. As shown in Figure 2.4, the innervalent vacancy is filled by an electron from the second unit and the excess energy is then transferred back to the first, initially ionized unit. The two positively charged units then undergo Coulomb explosion.

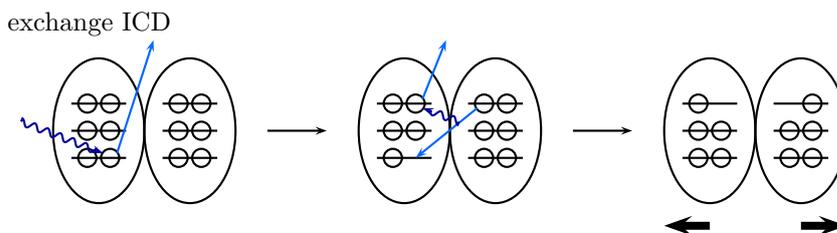


Figure 2.4.: Schematical illustration of the exchange ICD. The initial vacancy is filled by an electron of the neighbouring unit and the excess energy is transferred to another electron of the initially ionized unit, which is emitted. The two positively charged units of the final state undergo Coulomb explosion.

Because the final state of the exchange ICD is the same as in the ICD the energy criterion is the same as for the ICD and the final products are the same. Only the decay rate is in the range of an ETMD process and hence the process is much slower than an ICD process. Therefore it is not possible to experimentally observe and identify this process independently [23].

2.4. Resonant ICD (RICD)

Starting not from an ionized but from an electronically excited state, further autoionization processes can be observed as shown in Figure 2.5. These electronic decay processes have been known for the Auger process and been called resonant Auger effect (see panel a)).

Analogously ICD-like processes can be initiated by an excitation, which also have been observed experimentally [26, 27, 28]. Depending on which role the excited electron plays in the reaction, the process is either called participator Resonant Interatomic Coulombic Decay (RICD) or spectator RICD. In a participator RICD the excited electron fills the created vacancy itself. Simultaneously the excess energy is transferred to a neighbouring unit, which subsequently gets ionized (see Figure 2.5 panel b). The final state is characterized by the initially excited unit to be in its ground state and the neighbouring atom being ionized. In a spectator RICD (see Figure 2.5 panel c) the vacancy is filled by another, non-excited electron of the same unit. The excess energy is simultaneously

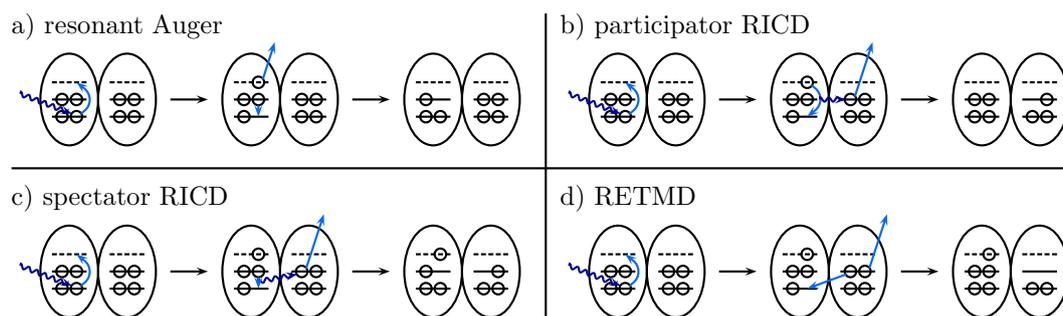


Figure 2.5.: Schematic illustration of resonant autoionization processes. For details see the main text.

transferred to a neighbouring unit, which is then ionized. Throughout the process the excited electron stays in its virtual orbital.

Recently, a special case of a participator RICD, where the excited electron does not stem from the inner valence but from the outer valence has been described and has been named Excitation Transfer Ionization (ETI) [29].

As in the case of an ionized initial state also the corresponding ETMD processes called RETMD (see Figure 2.5 panel d) are possible.

3. Relativistic Quantum Chemistry

3.1. Special Relativity

The theory of relativity describes observations of physical properties depending on the movement of the inertial system with respect to the observer. First proposed by Albert Einstein in 1905 [30], it postulates the equality of laws of physics in uniformly moving inertial systems. One of the motivations for its development was the possibility to unify classical mechanics with electrodynamics.

The special relativity is based on two postulates:

1. Principle of relativity: All physical laws are the same in all systems uniformly moving relative to each other.
2. The speed of light in vacuum is constant and independent of the location and movement of the light source.

Their consistent application led to a new understanding of space and time and awareness that energy and mass are equivalent [31].

3.2. Lorentz Transformation

In non-relativistic physics the transformation of coordinates between two inertial systems moving relative to each other can be calculated from the Galilei transformation. However, this allows for relative velocities larger than the speed of light, which contradicts the second postulate of relativity. Therefore, for a relativistic description it has to be replaced by the Lorentz transformation between the coordinates of the two inertial systems Σ and Σ' . As an example consider an object in the inertial system Σ' moving in x direction with respect to the inertial system of an observer Σ . Without loss of generality Σ can be supposed to be resting. Let the two inertial systems to coincide at time $t = 0$. Under these conditions, the spacial coordinates transform as equation (3.1) and equation (3.2). Without a relative movement in a certain direction, the corresponding coordinates $y = y'$ and $z = z'$ do not change.

$$\begin{aligned}x' &= \gamma(x - \beta ct) \\ ct' &= \gamma(ct - \beta x)\end{aligned}\tag{3.1}$$

$$\begin{aligned}x &= \gamma(x' + \beta ct') \\ ct &= \gamma(ct' + \beta x)\end{aligned}\tag{3.2}$$

In this transformation two new variables are introduced: the ratio between the relative speed of the inertial systems and the speed of light $\beta = \frac{v}{c}$ and the Lorentz factor $\gamma = \frac{1}{\sqrt{1-\beta^2}}$.

For small relative speeds, or alternatively $c \rightarrow \infty$, the Lorentz transformation equals the Galilei transformation.

The Lorentz transformation motivates an equal treatment of time and spacial coordinates. Therefore the contravariant 4-position vector x^μ is introduced

$$x^\mu = \begin{pmatrix} ct \\ x \\ y \\ z \end{pmatrix}\tag{3.3}$$

Since all fundamental laws of physics need to hold in all inertial systems, they need to be invariant under Lorentz transformation. Hence, they need to be reformulated with respect to the new set of coordinates according to the principles of relativity [32].

3.3. Space-Time

From the latter section it is obvious that distances and times are not invariant to a Lorentz transformation. Therefore they can not be treated separately. But, motivated by the evolution of a spherical wave, one corresponding invariant property can be found, which is the square of the space-time s

$$s^2 = x^\mu x_\mu = (ct)^2 - x^2 = (ct')^2 - x'^2\tag{3.4}$$

where x_μ is the covariant form of the 4-vector x^μ mediated by the metric $g = \text{diag}(1, -1, -1, -1)$ and Einstein's summation convention is applied. The space-time vectors x together with the metric g span the so-called Minkowski space.

3.4. Relativistic Mechanics

Starting from the four dimensional space-time the relativistic velocity vector $u^\mu = \frac{d}{d\tau}x^\mu$ and the corresponding momentum $p = mu$ can be derived. Furthermore it can be shown that the mass of an object also depends on the velocity of the moving particle with respect to the observer,

$$m = \gamma m_0 \quad (3.5)$$

where, m_0 is the mass of the particle at rest. Considering the acceleration of the particle leads to the famous relation between energy and mass $E = mc^2$, which is the sum over the rest mass energy and the kinetic energy of the particle.

Utilizing the relativistic 4-momentum the following relation for the energy can be obtained as

$$E = \sqrt{p^2 c^2 + m_0^2 c^4} \quad (3.6)$$

Because of the Lorentz invariance of $p^2 - \frac{E^2}{c^2} = -m_0^2 c^2$ the definition of the momentum vector can be defined as

$$p = \begin{pmatrix} \frac{iE}{c} \\ p_x \\ p_y \\ p_z \end{pmatrix} \quad (3.7)$$

In the following, only rest masses are considered and hence the rest masses will be denoted as m .

3.5. Relativistic Electrodynamics

The Maxwell equations describing the interactions of magnetic and electric fields and charged particles are Lorentz covariant. Therefore, their shape is conserved under Lorentz transformation and the modifications to the non-relativistic formulation are limited to the introduction of a four-component vector potential

$$A = \begin{pmatrix} \frac{\phi}{c} \\ \mathbf{A} \end{pmatrix}, \quad (3.8)$$

where \mathbf{A} is a three dimensional vector potential and ϕ is a scalar potential.

3.6. Relativistic Quantum Mechanics

Motivated by the knowledge of relativistic phenomena in classical mechanics the quantum mechanics were reformulated accordingly. This led to the Dirac equation, which is the equation of motion of a particle with a spin $\frac{1}{2}$ including relativistic effects. We will first discuss basic properties of the relativistic effects on a freely moving particle and afterwards use these basics for the description of the hydrogen atom and later for the more complex many particle systems.

3.6.1. Klein-Gordon Equation for a Freely Moving Particle

By utilizing the correspondence principle and substituting the classical variables by their quantum analogs one obtains for the square of the relativistic energy

$$E^2\Psi = \left(i\hbar\frac{\partial}{\partial t}\right)^2\Psi = (m^2c^4 - \hat{\mathbf{p}}^2c^2)\Psi \quad (3.9)$$

This expression is known as the Klein-Gordon equation and describes the movement of a spinless particle [33]. Even though equation (3.9) is Lorentz covariant it needs some further investigation. First, its solutions enable negative energies, which at that time had no proper interpretation and second, the corresponding time-dependent probability density $\Psi^*(\vec{r}, t)\Psi(\vec{r}, t)$ is not positive definite, which contradicts the probabilistic picture of quantum mechanics.

Despite these weaknesses the Klein-Gordon equation was the basis for the derivation of the Dirac equation.

3.6.2. Dirac Equation

The derivation of the Dirac equation aimed at the description of the moving electron also considering relativistic effects and to include all intrinsic properties such as spin. It was later found to hold for fermions with a spin of $\frac{1}{2}$ in general. Special relativity requires a treatment of time and spacial coordinates on an equal footing. Since the non-relativistic Schrödinger equation contains the first derivative with respect to time and the second derivative with respect to the spacial coordinates, the Schrödinger is obviously not Lorentz invariant and hence, does not include relativistic effects.

Dirac Equation for a Freely Moving Particle

1928 Dirac established his famous equation which incorporates first order derivatives of both time and spacial coordinates [34]

$$i\hbar\frac{\partial}{\partial t}\Psi = c(\alpha \cdot \hat{\mathbf{p}} + \beta mc)\Psi \quad (3.10)$$

Here, $\hat{\mathbf{p}}$ denotes the three dimensional momentum operator and the variables α and β have to be determined appropriately considering the relations based on the comparison of the Dirac equation to the Klein-Gordon equation

$$[\alpha_i, \alpha_j]_+ = \alpha_i\alpha_j + \alpha_j\alpha_i = 2\delta_{ij} \quad (3.11)$$

$$\alpha_i\beta + \beta\alpha_i = 0 \quad (3.12)$$

$$\beta^2 = 1 \quad (3.13)$$

Since numbers do not commute, the variables α_i are obviously matrices. They have eigenvalues of either $+1$ or -1 , their traces have to be 0 and their dimension has to be even. These requirements are fulfilled by the three Pauli matrices. However, in order to describe four parameters, a set of at least four matrices is required. Therefore a dimension of at least four is mandatory. In case of 4×4 matrices more than one set fulfills the requirements. The one conventionally used is constructed from the Pauli matrices and reads

$$\alpha_x = \begin{pmatrix} 0 & 0 & 0 & 1 \\ 0 & 0 & 1 & 0 \\ 0 & 1 & 0 & 0 \\ 1 & 0 & 0 & 0 \end{pmatrix} \quad \alpha_y = \begin{pmatrix} 0 & 0 & 0 & -i \\ 0 & 0 & i & 0 \\ 0 & -i & 0 & 0 \\ i & 0 & 0 & 0 \end{pmatrix} \quad \alpha_z = \begin{pmatrix} 0 & 0 & 1 & 0 \\ 0 & 0 & 0 & -1 \\ 1 & 0 & 0 & 0 \\ 0 & -1 & 0 & 0 \end{pmatrix} \quad (3.14)$$

$$\beta = \begin{pmatrix} 1 & 0 & 0 & 0 \\ 0 & 1 & 0 & 0 \\ 0 & 0 & -1 & 0 \\ 0 & 0 & 0 & -1 \end{pmatrix} \quad (3.15)$$

Due to the matrix dimension of the operators, the wave function Ψ has to have the same dimension and hence is represented by a four dimensional vector

$$\Psi = \begin{pmatrix} \Psi_1 \\ \Psi_2 \\ \Psi_3 \\ \Psi_4 \end{pmatrix} \quad (3.16)$$

A convenient way of writing the Dirac equation (3.10) using α and β is the two-component form

$$\begin{pmatrix} -E + mc^2 & c(\boldsymbol{\sigma} \cdot \hat{\mathbf{p}}) \\ c(\boldsymbol{\sigma} \cdot \hat{\mathbf{p}}) & -E - mc^2 \end{pmatrix} \begin{pmatrix} \Psi^L \\ \Psi^S \end{pmatrix} = 0 \quad (3.17)$$

Here, E is the energy of the freely moving particle and $\boldsymbol{\sigma}$ is the row vector containing the Pauli matrices. In this formulation the wavefunction is partitioned into the so-called large and small components depicted by the superscripts L and S of the wavefunctions Ψ , respectively.

The latter eigenvalue equation (3.17) can be written as two coupled differential equations

$$\begin{aligned} (-E + mc^2)\Psi^L + c(\boldsymbol{\sigma} \cdot \hat{\mathbf{p}})\Psi^S &= 0 \\ c(\boldsymbol{\sigma} \cdot \hat{\mathbf{p}})\Psi^L + (-E - mc^2)\Psi^S &= 0 \end{aligned} \quad (3.18)$$

From equations (3.17) the non-relativistic limit can be calculated as well as a relation

between the large and the small component of the wavefunction can be obtained.

$$\Psi^S = \frac{c(\boldsymbol{\sigma} \cdot \hat{\mathbf{p}})}{E + mc^2} \Psi^L \quad (3.19)$$

Inserting equation (3.19) into the first equation in (3.17) yields

$$(-E + mc^2)\Psi^L + \frac{c^2(\boldsymbol{\sigma} \cdot \hat{\mathbf{p}})^2}{E + mc^2} \Psi^L = 0 \quad (3.20)$$

In general, the energies can be shifted to any meaningful value, which then serves as a new reference energy. For a comparison with the non-relativistic result, it is convenient to shift the energies such that the kinetic energy of the particle coincides with the positive energy as in the non-relativistic description. Hence, the energies are shifted by mc^2 . The non-relativistic limit is then achieved by taking the limit $c \rightarrow \infty$

$$E'\Psi^L = \frac{c^2(\boldsymbol{\sigma} \cdot \hat{\mathbf{p}})^2}{E' + 2mc^2} \Psi^L \quad \text{and} \quad (3.21)$$

$$\lim_{c \rightarrow \infty} E'\Psi^L = \frac{(\boldsymbol{\sigma} \cdot \hat{\mathbf{p}})^2}{2m} \quad \text{with} \quad (\boldsymbol{\sigma} \cdot \hat{\mathbf{p}})^2 = \hat{\mathbf{p}}^2 \quad (3.22)$$

Obviously, equation (3.22) is equivalent to the non-relativistic eigenvalue problem with the large component of the wavefunction as eigenfunction. The two components can be identified with the two possible spin states $\alpha = \begin{pmatrix} 1 \\ 0 \end{pmatrix}$ and $\beta = \begin{pmatrix} 0 \\ 1 \end{pmatrix}$.

The solution of the Dirac equation leads to both positive and negative energy eigenvalues E_+ and E_- , which are the same as in the Klein-Gordon equation

$$E_{\pm} = \pm \sqrt{m^2c^4 + p^2c^2} \quad (3.23)$$

This means that two continua of eigenvalues exist with an energy gap of $2mc^2$ as shown in Figure 3.1. Particles at rest always have the energy mc^2 and hence positive energies. Such particles should normally deexcite to a state of lower energy and emit the excess energy as a photon. In order to take care of this unphysical behaviour Dirac postulated that all states of negative energies are occupied and hence inaccessible. An excitation of an electron from the negative energy region into the positive energy region would then correspond to a pair creation process yielding an electron and a hole. This hole needs to have the same mass and the opposite charge of the electron and was called positron. It was experimentally found and hence the theory was verified in 1933 [35]. However, it has to be noted that even though the Dirac equation allows for the description of such a pair creation process and motivated further theoretical investigation, the more rigorous description for all kinds of interactions between particles and electromagnetic fields is described by Quantum Electrodynamics (QED). The latter will also be important for

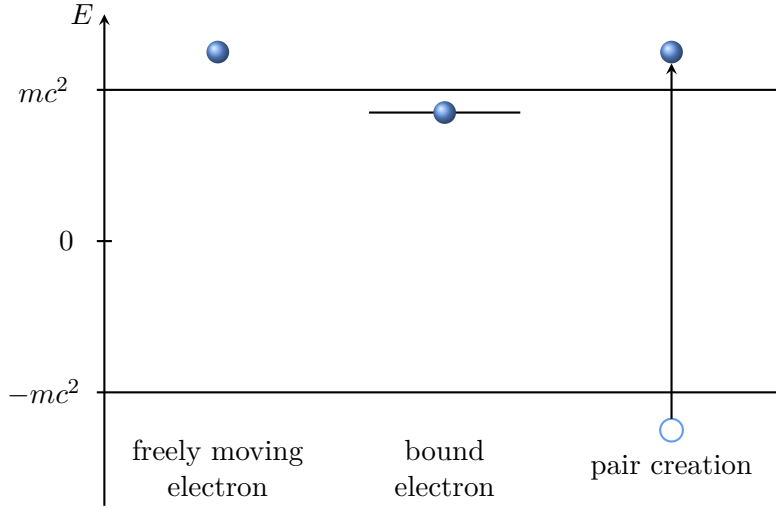


Figure 3.1.: Illustration of electronic properties of the Dirac equation solutions.

the description of interaction between electrons in many particle systems.

Solution of the Dirac Equation for the Hydrogen Atom

The hydrogen atom is the most simple system of quantum chemistry. Its solutions are the foundation for the description of any more complex system. In the hydrogen atom the electron is no longer moving freely but within the Coulomb field of the proton. The proton is assumed to be fixed in space and hence the potential in which the electron moves can be described by the scalar potential $\phi = \frac{eZ}{r}$ only. The other components of the four dimensional potential A are zero. Therefore the electronic part of the time-independent Dirac equation for one electron in the field of a positive charge reads

$$\left(e\phi + c(\boldsymbol{\alpha} \cdot \hat{\mathbf{p}}) + \beta mc^2 \right) \Psi = E\Psi. \quad (3.24)$$

In non-relativistic quantum chemistry the solutions can be separated into a radial $R(r)$ and an angular part $Y(\theta, \phi)$.

$$\Psi^{NR}(r, \theta, \phi) = \frac{1}{r} R_{nl}(r) Y_l^{ml}(\theta, \phi) \quad (3.25)$$

Here the angular part can be described by the spherical harmonics $Y_l^{ml}(\theta, \phi)$. Analogously the relativistic wave functions can be separated, which leads to

$$\Psi(r, \theta, \phi, \tau) = \frac{1}{r} \begin{pmatrix} P_{n\kappa}(r) & \xi_{\kappa,m}(\theta, \phi) \\ iQ_{n\kappa}(r) & \xi_{-\kappa,m}(\theta, \phi) \end{pmatrix} \quad (3.26)$$

Here, $P_{n\kappa}(r)$ and $Q_{n\kappa}(r)$ are the radial solutions of the large and small component of

the 4-spinor, respectively. $\xi_{\kappa,m}(\theta, \phi)$ and $\xi_{-\kappa,m}(\theta, \phi)$ are two component spinors describing the angular distribution. As in the non-relativistic approach, the radial solutions depend on the principal quantum number n . The radial solutions of the large and small components each have nodes at certain distances. However, these nodes normally do not coincide and therefore the radial density of the total radial solution does not show nodes as in the non-relativistic case.

Non-relativistically, the solutions of the angular wave function depend on the angular and magnetic quantum numbers l and m_l . However, the Dirac equation additionally to relativistic effects incorporates spin and hence also spin-orbit coupling. Therefore l and m_l are not good quantum numbers, but rather the total angular momentum $j = l \pm s$. For the characterization of the angular solutions it is convenient to introduce another quantum number $\kappa = \mp(j + \frac{1}{2})$, which is connected to the eigenvalue of the operator $\mathbf{k} = \boldsymbol{\sigma} \cdot \mathbf{l} + \hbar \mathbf{1}_2$

$$\mathbf{k} \xi_{\pm\kappa,m} = \pm\hbar(j + \frac{1}{2}) \xi_{\pm\kappa,m} = \hbar\kappa_{\pm} \xi_{\pm\kappa,m} \quad (3.27)$$

The resulting angular wavefunction of a particle with a spin of $\frac{1}{2}$ reads

$$\begin{aligned} \xi_{\kappa,m} &= \frac{1}{\sqrt{2l+1}} \begin{pmatrix} \sqrt{l+m_l+1} Y_l^{m_l} \\ \sqrt{l-m_l} Y_l^{m_l+1} \end{pmatrix} & \text{for } \kappa < 0 \\ \xi_{\kappa,m} &= \frac{1}{\sqrt{2l+1}} \begin{pmatrix} -\sqrt{l-m_l} Y_l^{m_l} \\ \sqrt{l+m_l+1} Y_l^{m_l+1} \end{pmatrix} & \text{for } \kappa > 0 \end{aligned} \quad (3.28)$$

In Table 3.1 the non-ambiguous assignment of quantum numbers and atomic spinors is illustrated.

	$s_{\frac{1}{2}}$	$p_{\frac{1}{2}}$	$p_{\frac{3}{2}}$	$d_{\frac{3}{2}}$	$d_{\frac{5}{2}}$	$f_{\frac{5}{2}}$	$f_{\frac{7}{2}}$
l	0	1	1	2	2	3	3
j	$\frac{1}{2}$	$\frac{1}{2}$	$\frac{3}{2}$	$\frac{3}{2}$	$\frac{5}{2}$	$\frac{5}{2}$	$\frac{7}{2}$
κ	-1	1	-2	2	-3	3	-4

Table 3.1.: Assignment of the quantum numbers to two-component spinors [36].

The shape of the absolute square angular solutions differs from their non-relativistic counterparts. It no longer depends on l but on the total angular momentum j and its projection m_j as illustrated in Figure 3.2. The $s_{\frac{1}{2}}$ orbital has spherical symmetry as in the non-relativistic case, but the $p_{\frac{1}{2}}$ orbital shows spherical symmetry as well. In case of the $p_{\frac{3}{2}}$ orbital with $m_j = \pm\frac{1}{2}$ the shape is similar to a non-relativistic p_z -orbital.

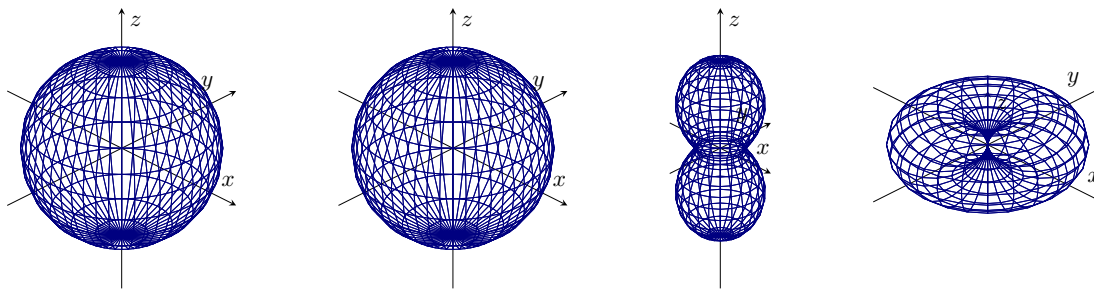


Figure 3.2.: Density plots of the angular solutions of the Dirac equation of the hydrogen atom $\xi_{\kappa,m}$. From left to right: $s_{\frac{1}{2}}$, $p_{\frac{1}{2}}$, $p_{\frac{3}{2},\frac{1}{2}}$, $p_{\frac{3}{2},\frac{3}{2}}$.

However, it does not have a node at the origin. The $p_{\frac{3}{2}}$ orbital with $m_j = \pm\frac{3}{2}$ has the same shape as the non-relativistic $p_{\pm 1}$ orbitals, from which the p_x and p_y orbital can be constructed. In contrast to the $m_j = \pm\frac{1}{2}$ case, the $p_{\frac{3}{2},\frac{3}{2}}$ orbital does have a node at the origin.

From the above considerations an expression for the energy of bound states can be determined

$$E = mc^2 \left[1 + \frac{1}{c^2} \left(\frac{\frac{Ze^2}{\hbar c}}{n - |\kappa| + \sqrt{\kappa^2 - \frac{Ze^2}{\hbar c}}} \right)^2 \right]^{\frac{1}{2}} \quad (3.29)$$

The smaller $|\kappa|$ and n are, the more is the corresponding one-particle state energetically stabilized. This energetic stabilization is accompanied by a contraction of the radial density. Hence, the $1s$ orbital exhibits the largest energy shift and largest contraction. From equation (3.29) it can also be seen that for a given azimuthal quantum number l the splitting into states of quantum numbers j is achieved such that the state with the lower total angular momentum has the lower energy.

3.7. Many-Particle Systems in Relativistic Quantum Chemistry

Until now only the interaction of one electron with a static potential has been discussed. However, in chemistry most systems contain several electrons, whose interactions also have to be taken into account. In non-relativistic quantum chemistry it is assumed that the Born-Oppenheimer approximation, which leads to a separation of electronic and nuclear solutions is reasonable and the electronic solutions can be obtained with the nuclear positions as fixed parameters. Here, a Hamiltonian of an N electron system is applied, which consists of a one-particle and a two-particle part. The one-particle operator $\hat{h}(i)$ describes the kinetic energy of a single electron and its interaction with the static Coulomb field of the nuclei and the two-particle part \hat{g}_{ij} describes the interactions of the electrons amongst each other, which in the non-relativistic case is the Coulomb

operator $\frac{1}{r_{ij}}$.

$$\mathcal{H} = \sum_{i=1}^N \hat{h}(i) + \sum_{i<j} \hat{g}_{ij} \quad (3.30)$$

From the solutions of the hydrogen atom the behaviour of an electron in a constant Coulomb field is known. Inserting it into the latter equation yields the relativistic Hamiltonian

$$\mathcal{H}_D = \sum_{i=1}^N (-e\phi(r_i) + c(\hat{\boldsymbol{\alpha}}^i \cdot \hat{\mathbf{p}}^i) + \beta mc^2) + \sum_{i<j} \hat{g}_{ij} \quad (3.31)$$

The electron-electron interaction term \hat{g}_{ij} can only be derived from QED, where the interaction of two moving particles is investigated. The result is expanded in series of $\frac{1}{c}$ and truncated after the second order term. This yields the Coulomb-Breit term \hat{g}_{ij}^{CB} , which contains the unretarded Coulomb interaction $\hat{g}_{ij}^C = \frac{1}{r_{ij}}$ describing the interaction of particles and the Breit term \hat{g}_{ij}^B describing the current-current interaction.

$$\begin{aligned} \hat{g}_{ij}^{CB} &= \hat{g}_{ij}^C + \hat{g}_{ij}^B \\ &= \frac{1}{r_{ij}} - \frac{1}{2r_{ij}} \left(\boldsymbol{\alpha}_i \cdot \boldsymbol{\alpha}_j + \frac{(\boldsymbol{\alpha}_i \cdot \mathbf{r}_{ij})(\boldsymbol{\alpha}_j \cdot \mathbf{r}_{ij})}{r_{ij}^2} \right) \end{aligned} \quad (3.32)$$

The latter can be divided into the Gaunt term $\hat{g}_{ij}^G = -\frac{1}{r_{ij}} \boldsymbol{\alpha}_i \cdot \boldsymbol{\alpha}_j$ describing the interaction with magnetic fields and a term purely containing retardation effects. Since the Gaunt term provides the largest contribution in the Breit term and the implementation of the full Breit term is difficult, very often only the Gaunt term is considered in numerical calculations. However, the Breit term is damped by a factor of $\frac{1}{c^2}$ hidden in the $\boldsymbol{\alpha}$ operators. Therefore, it is normally applied for high precision calculations only and the Dirac-Coulomb operator \mathcal{H}_{DC} is applied instead.

$$\mathcal{H}_{DC} = \sum_{i=1}^N (-e\phi(r_i)\mathbb{1} + c\hat{\boldsymbol{\alpha}}^i \cdot \hat{\mathbf{p}}^i + \beta mc^2) + \sum_{i>j}^N \frac{1}{r_{ij}} \quad (3.33)$$

Since the Gaunt interaction has been shown to affect the ionization energies of TIH by no more than 0.06 eV [37] and the errors of decay width calculations are by far larger than the effect of the Gaunt interaction, the Dirac-Coulomb Hamiltonian is used throughout this thesis. Even though this Hamiltonian is not Lorentz invariant the description is good enough to cover all relevant effects.

3.7.1. Dirac-Coulomb Hartree-Fock

Starting from the Dirac-Coulomb operator of equation (3.33) it is assumed that the wavefunction can be written as a anti-symmetrized product of one particle functions ϕ_i

called a Slater determinant as in the non-relativistic quantum chemistry.

$$\Psi = \mathcal{A} \left(\prod_{i=1}^N \phi_i(r_i) \right) \quad (3.34)$$

$$= \frac{1}{\sqrt{n!}} \begin{vmatrix} \phi_1(r_1) & \phi_2(r_1) & \cdots & \phi_N(r_1) \\ \phi_1(r_2) & \phi_2(r_2) & \cdots & \phi_N(r_2) \\ \vdots & \vdots & \ddots & \vdots \\ \phi_1(r_N) & \phi_2(r_N) & \cdots & \phi_N(r_N) \end{vmatrix} \quad (3.35)$$

From this ansatz follows the energy as a functional:

$$E = \langle \Psi | \mathcal{H}_{DC} | \Psi \rangle \quad (3.36)$$

$$= \sum_{i=1}^N \langle \phi_i | \hat{h}_D(i) | \phi_i \rangle + \frac{1}{2} \sum_{i,j}^N \left(\langle \phi_i \phi_j | \frac{1}{r_{ij}} | \phi_i \phi_j \rangle - \langle \phi_i \phi_j | \frac{1}{r_{ij}} | \phi_j \phi_i \rangle \right) \quad (3.37)$$

From the latter expression the Dirac-Hartree-Fock equation is derived, which describes the motion of an electron in the averaged field of the other electrons $v^{DHF}(i)$.

$$\mathbf{f}_i |\phi_i\rangle = \left(\mathbf{h}_D(i) + v^{DHF}(i) \right) |\phi_i\rangle \quad (3.38)$$

$$= \left(\mathbf{h}_D(i) + \sum_{l=1}^N (\mathbf{J}_l - \mathbf{K}_l) \right) |\phi_i\rangle \quad (3.39)$$

$$= \varepsilon_i |\phi_i\rangle \quad (3.40)$$

Here, the operators \mathbf{J}_l and \mathbf{K}_l both depend on the one-particle functions and denote the Coulomb and the exchange term, respectively. Starting from an educated guess of the one-particle functions, the Fock operator \mathbf{F} is constructed and applied to yield another set of one-particle functions. This iterative procedure is carried out until the system is converged or *self-consistent*, which is why the method is called a Self-Consistent Field (SCF) method [38].

In non-relativistic quantum mechanics the variational principle ensures the lowest energy solution to be closest to the true energy and hence the wavefunction to be optimized. In relativistic quantum mechanics negative energy solutions are possible but unphysical. The variational principle would therefore lead to negative energy states. In order to prevent this so-called *variational collapse*, the basis is subject to certain restrictions, which will be discussed later in section 3.7.2.

For the actual energy calculations the one-particle functions $\{\phi_i\}$ are constructed as a linear combination of atomic functions. The latter are expanded in a finite set of basis functions $\{\varphi_\mu\}$ for the large and small component. The resulting molecular one-particle function then reads

$$\phi_i = \sum_{\mu}^{N^L} c_{\mu\alpha}^{iL} \varphi_{\mu\alpha}^L + \sum_{\mu}^{N^L} c_{\mu\beta}^{iL} \varphi_{\mu\beta}^L + \sum_{\mu}^{N^S} c_{\mu\alpha}^{iS} \varphi_{\mu\alpha}^S + \sum_{\mu}^{N^S} c_{\mu\beta}^{iS} \varphi_{\mu\beta}^S. \quad (3.41)$$

Here, N^L and N^S are the numbers of basis functions of the large and small component, respectively. This means that the energy depends on the expansion coefficients $c_{\mu s}^{iX}$, where $X = L, S$ denotes the component of the spinor and s denotes the spin state. The resulting relativistic Roothan-Hall equations in matrix notation read as

$$\mathcal{F}\mathcal{C} = \mathcal{S}\mathcal{C}\mathcal{E} \quad (3.42)$$

The Fock matrix \mathcal{F} and the overlap matrix \mathcal{S} hereby consist of the matrix elements:

$$\begin{aligned} F_{\mu\nu}^{XY,sp} &= \langle \varphi_{\mu s}^X | \mathbf{f}_i | \varphi_{\nu p}^Y \rangle \\ S_{\mu\nu}^{XY,sp} &= \langle \varphi_{\mu s}^X | \varphi_{\nu p}^Y \rangle \end{aligned} \quad (3.43)$$

3.7.2. Construction of a Basis for the Relativistic Treatment

As already discussed, the four components of a spinor are expanded into a finite set of one-particle basis functions. Thereby the basis sets of the large and small component are treated separately.

$$\phi_i^L = \begin{pmatrix} \phi_{i\alpha}^L \\ \phi_{i\beta}^L \\ 0 \\ 0 \end{pmatrix} \quad \phi_i^S = \begin{pmatrix} 0 \\ 0 \\ \phi_{i\alpha}^S \\ \phi_{i\beta}^S \end{pmatrix} \quad (3.44)$$

The two components are expressed as linear combinations of scalar atomic basis functions φ_{μ}^X , which are weighted by the expansion coefficients $c_{\mu s}^{iX}$.

$$\phi_{is}^L = \sum_{\mu=1}^{N^L} c_{\mu s}^{iL} \varphi_{\mu}^L \quad \phi_{is}^S = \sum_{\mu=1}^{N^S} c_{\mu s}^{iL} \varphi_{\mu}^S \quad (3.45)$$

They are constructed starting from the solutions of the hydrogen atom centered at the corresponding atoms, which have the form

$$s_{\tau}^X = N_{\tau}^X r^{n-1} e^{\alpha_{\tau}^X r} Y_l^{m_l}(\theta, \varphi) \quad (3.46)$$

It is not possible to solve the associated integrals of the *slater-type functions* analytically

and therefore, they are expanded into a set of primitive Gauss functions g_τ^X yielding contracted Gauss functions. These contracted Gauss functions do not show the correct asymptotic behaviour for short and large distances ($r \rightarrow 0$, $r \rightarrow \infty$), but allow to solve the integrals analytically and thereby reducing the computational cost. In spherical coordinates they are given by

$$g_\tau^X = N_\tau^X r^l e^{-\alpha_\tau^X r^2} Y_l^{m_l}(\theta, \varphi) \quad (3.47)$$

and in cartesian coordinates by

$$g_\tau^X = N_\tau^X x^{n_x^X} y^{n_y^X} z^{n_z^X} e^{-\alpha_\tau^X r^2}. \quad (3.48)$$

Here, N_τ^X denotes the normalization factor and the sum of the spacial coordinate exponents n_i^X corresponds to the azimuthal quantum number l .

$$n_x^X + n_y^X + n_z^X = l \quad (3.49)$$

The final contraction then gives the basis functions

$$\varphi_\mu^X = \sum_\tau d_{\mu\tau}^X g_\tau^X, \quad (3.50)$$

where the factor $d_{\mu\tau}^X$ weights the different primitive Gauss functions.

In order to prevent the variational collapse, the basis sets have to fulfill the *kinetic balance* condition, which is based on the non-relativistic limit of equation (3.19). Since the energy E of the electron is much smaller than $2mc^2$, the following relation between the coefficients of the large and small component functions has to be obeyed:

$$\phi_S = \frac{1}{2mc} (\boldsymbol{\sigma} \cdot \hat{p}) \phi_L \quad (3.51)$$

Because of the appearance of the operator $\boldsymbol{\sigma} \cdot \hat{p}$ a given basis function of the large component with a distinct l value leads to the generation of two functions of the small component with $l - 1$ and $l + 1$. This means that the small component basis contains almost twice as many basis functions as the basis of the large component. Hence, the computational cost of a relativistic calculation is higher than its non-relativistic analog.

3.8. Correlation Methods

In quantum chemical calculations the electron correlation is treated by taking into account excitations of different classes from the ground state. Formally, this is achieved by pairs of creation and annihilation operators acting on the ground state. By allowing all possible combinations of such operators pair creation processes would be introduced in

the configurations. However, in quantum chemistry energies high enough to overcome the energy gap of $2mc^2$ are hardly achieved. Therefore, it is reasonable to exclude these configurations from the calculations. This practice is called *no-pair approximation*.

3.9. Relativistic Effects and Spin-Orbit Coupling in Many-Electron Systems

3.9.1. Spin-Orbit Coupling

Since spin is intrinsically included in the Dirac equation, so is the coupling of the angular and the spin momentum. This leads to only the total quantum number J and the corresponding projection M_J being good quantum numbers rather than L, M_L and S, M_S . As a consequence, the energy levels of a specific L value are split and the symmetry of some of the wavefunctions are changed (see Figure 3.2). The spin-orbit coupling constant a is proportional to Z^4 . This means that the most pronounced spin-orbit splittings are to be observed in heavy atoms, where also scalar-relativistic effects can not be neglected. In order to describe relativistic effects without spin-orbit coupling several spin-free formulations of the Dirac equation, where the results depend on the definition [39]. Extensive discussions about these Hamiltonians and their applications can be found in references [40, 41].

Observed consequences of the spin-orbit coupling are the spectral splittings, the so-called *inert electron pair*, which describes the observation that lower oxidation states are favoured in elements of higher periods compared to their lower period analogs. This *inert electron pair* does not contribute in bondings to other atoms and hence systems like e.g. TIH exhibit shorter bond lengths than would be expected non-relativistically.

3.9.2. Scalar-Relativistic Effects

The orbital energies of the hydrogen atoms have been shown to decrease due to the inclusion of relativistic effects. However, in many-electron atoms the interaction of both nucleus and several electrons have to be taken into account. From equation (3.29) describing the energy of the one-electron system, it is evident that electronic states are energetically stabilized. This effect is largest for electrons close to the nucleus inhabiting s and $p_{1/2}$ -orbitals which have a non-zero electron density at the nucleus. Hence, these orbitals experience a contraction of the radial densities. Thereby, they shield the nuclear charge such that electrons further apart feel a reduced effective nuclear charge and are therefore less attracted to the nucleus which leads to a decontracted radial electron density. As a rule of thumb, s - and p -orbitals are energetically stabilized compared to the non-relativistic result and the radial densities are contracted, while the d - and f -orbitals are energetically destabilized and the corresponding radial densities are decontracted.

Consequences are shifts of orbital energies compared to each other. An example is the colour of gold, where the band energy of the $6s$ valence band is decreased, while the band energy of the $5d$ orbitals is increased. Hence, the energy difference is decreased and an excitation is observed in the visible spectrum of light.

4. Resonances

4.1. General Remarks

A short introduction to scattering theory is essential for the understanding of resonances in quantum mechanics [42, 43, 44].

In a general scattering experiment a system A approaches another system B . In the beginning they are freely moving particles and do not interact with each other. The closer these two particles get, the stronger is their interaction. At some time t they may form a compound system, which can have a long lifetime. This meta-stable state can decay via different channels characterized by internal degrees of freedom of the fragments. If the fragments are the same system as before the scattering A and B have the same internal energies and no electronic rearrangement has occurred, the process is called an elastic scattering process. Otherwise, the process is called an inelastic scattering process. Several combinations of characterizing properties of the fragments such as quantum numbers may be possible. Each process characterized by a different of such combinations is called a channel.

The total Hamiltonian of the system reads

$$H = H_0 + V \tag{4.1}$$

where V describes the interaction of the involved systems and H_0 is the Hamiltonian of the complete system without this interaction.

The wavefunctions of both the incoming systems and the outgoing fragments inside the so-called interaction region are unknown. However, their behaviour and characteristics at infinite times before and after the scattering process can easily be described. In the stationary description of the scattering process this requires the functions to fulfill outgoing and incoming boundary conditions denoted by the superscripts "+" and "-" for the initial and final states, respectively. These wavefunctions $|E_i^{(+)}\rangle$ and $|E_f^{(-)}\rangle$ with the correct asymptotic behaviour of the initial and final states at the time $t = 0$ of the interaction are constructed from the corresponding states $|E_i^{(0)}\rangle$ and $|E_f^{(0)}\rangle$ of the system disregarding the interaction V . They are eigenfunctions of H_0 and hence are characterized by the energies $E_n^{(0)}$. Their connection to the asymptotic wavefunctions is formulated in the Lippmann-Schwinger equation

$$|E_n^{(\pm)}\rangle = |E_n^{(0)}\rangle + G_n^{(\pm)}V|E_n^{(0)}\rangle \quad (4.2)$$

where

$$G_n^{(\pm)} = \frac{1}{E_n^{(0)} - H \pm i0^+} \quad (4.3)$$

is the Green's function with 0^+ being an infinitesimal positive value.

The probability of finding the system with an initial state $|E_i^{(+)}\rangle$ in a distinct final state $|E_f^{(-)}\rangle$ after the scattering process is given by the absolute square of the corresponding matrix elements of the scattering matrix

$$w_{fi} = \left| \langle E_f^{(-)} | E_i^{(+)} \rangle \right|^2 \quad (4.4)$$

$$= |S_{fi}|^2 \quad (4.5)$$

These matrix elements are given by

$$S_{mn} = \delta_{mn} - 2\pi i \delta(E_m^{(0)} - E_n^{(0)}) \langle E_m^{(0)} | V | E_n^{(+)} \rangle \quad (4.6)$$

The Kronecker delta describes the elastic scattering process and the second part describes those scattering processes, in which electronic rearrangements are involved. This second part has poles of different kinds. For energies, where the real part is positive and the imaginary part is negative, the poles correspond to resonances ($E_{res} = E_R - i\frac{\Gamma}{2}$), which hence can be understood as the maximum response of the system to the interaction [45]. The real part corresponds to the energy at which the resonance occurs and Γ in the imaginary part is the so-called decay width, which is connected to the lifetime τ of the meta-stable state

$$\Gamma = \frac{\hbar}{\tau} \quad (4.7)$$

If the process of interest is an inelastic scattering process the above scattering matrix is reformulated using the so-called transition operator

$$T^{(n)} \equiv V \left(\mathbf{1} + G_n^{(+)}V \right) \quad (4.8)$$

Its action on $|E_n^{(0)}\rangle$ equals the action of V on the asymptotic states $|E_n^{(-)}\rangle$

$$V|E_n^{(+)}\rangle = T^{(n)}|E_n^{(0)}\rangle \quad (4.9)$$

Hence, the scattering matrix reads

$$S_{mn} = \delta_{mn} - 2\pi i \delta(E_m^{(0)} - E_n^{(0)}) \langle E_m^{(0)} | T^{(n)} | E_n^{(0)} \rangle \quad (4.10)$$

The corresponding \mathcal{T} matrix contains all information about the inelastic scattering process and is going to be used in order to find an expression for the calculation of the decay width. It has poles at the resonance energies and its absolute square has the shape of a Lorentzian with a Full Width Half Maximum (FWHM) of $2\Gamma = \Gamma$.

4.2. Projection Method for the Evaluation of the \mathcal{T} Matrix

One of the approaches to address the treatment of multi-state systems is the partitioning of the Hilbert space into initial and final state subspaces and using the appropriate eigenfunctions of these subspaces for the calculation of the decay widths. Several theories had been used for the description of different nuclear reactions before they were first unified by Feshbach [46, 47, 48]. Somewhat later, Fano extended this ansatz to describe excitation spectra, which are inverse processes to Feshbach's nuclear reactions.[49]

In the following, Feshbach's formulation using projection operators is applied for the case of a meta-stable decaying state, where the initial state is bound-like and the final states are continuum states. Starting from the Schrodinger equation of the total system under investigation

$$H\Psi = E\Psi \quad (4.11)$$

the projection operators P and Q are defined. P projects the final states or the so-called open channels out of the total wavefunction Ψ and is defined with respect to eigenstates of the system without interaction. Hence, the initial and final state subspaces are orthogonal ($PQ = 0$). Q is analogously defined with respect to the rest of the system as $Q = 1 - P$. Therefore after insertion into eq. (4.11)

$$H(P + Q)\Psi = E\Psi \quad (4.12)$$

$$(E - H_{PP})P\Psi = H_{PQ}Q\Psi \quad (4.13)$$

$$(E - H_{QQ})Q\Psi = H_{QP}P\Psi \quad (4.14)$$

can easily be derived with

$$\begin{aligned} H_{PP} &\equiv PHP & H_{PQ} &\equiv PHQ \\ H_{QP} &\equiv QHP & H_{QQ} &\equiv QHQ. \end{aligned}$$

From equation (4.14) a straightforward solution for the system excluding the selected final states can be found.

$$Q\Psi = \frac{1}{E - H_{QQ}} H_{QP} P\Psi \quad (4.15)$$

The latter expression holds in case of all open channels being included in the final state description. In case of selectively chosen open channels, which do not resemble the total space of open channels, E is to be substituted by $E^{(-)} = E - i\eta$.

After insertion of eq. (4.15) into eq. (4.13) one arrives at

$$\mathcal{H} P\Psi = E P\Psi \quad (4.16)$$

with \mathcal{H} being the effective Hamiltonian of the final states.

$$\mathcal{H} = H_{PP} + H_{PQ} \frac{1}{E - H_{QQ}} H_{QP} \quad (4.17)$$

In order to solve these expressions we define $\{\Phi_n\}$ to be the solutions of the Hamiltonian excluding the final state solutions (or the closed channels solutions in case of all open channels being defined as final states). These initial state functions are assumed to be bound and to fulfill the Schrödinger equation

$$(\varepsilon_n - H_{QQ}) |\Phi_n\rangle = 0 \quad (4.18)$$

It has to be noted that these functions and energies are solutions to a stationary problem and therefore, expressing the meta-stable, but long-lived state in terms of these functions is an approximation. However, for systems with long lifetimes, this approximation is reasonable.

Together with a set of continuum wavefunctions $\{\Phi(\alpha, E)\}$, they are defined to fulfill the following orthogonality relations

$$\langle \Phi_n | \Phi_n \rangle = 1 \quad \langle \Phi_n | \Phi(\alpha, E) \rangle = 0 \quad (4.19)$$

$$\langle \Phi(\alpha, E) | \Phi(\alpha', E') \rangle = \delta(\alpha - \alpha') \delta(E - E') \quad (4.20)$$

and thereby to form an orthonormal basis. These continuum wavefunctions are characterized by their energy E and their quantum numbers, which at this stage are both contained in the index α .

$$1 = \sum_n |\Phi_n\rangle \langle \Phi_n| + \int d\alpha \int dE |\Phi(\alpha, E)\rangle \langle \Phi(\alpha, E)| \quad (4.21)$$

Expanding eq. (4.16) into this complete set yields an effective final state Hamiltonian

$$\mathcal{H} = H_{PP} + \sum_n H_{PQ} \frac{|\Phi_n\rangle\langle\Phi_n|}{E - \varepsilon_n} H_{QP} + \int d\alpha \int d\varepsilon H_{PQ} \frac{|\Phi(\alpha, \varepsilon)\rangle\langle\Phi(\alpha, \varepsilon)|}{E - \varepsilon} H_{QP} \quad (4.22)$$

which is useful to split into two parts: One describing the interaction \mathcal{V} with the initial state Φ_s with its energy ε_s being in resonance with the continuum and the rest \mathcal{H}'

$$\mathcal{H} = \mathcal{H}' + H_{PQ} \frac{|\Phi_s\rangle\langle\Phi_s|}{E - \varepsilon_s} H_{QP} = \mathcal{H}' + \mathcal{V} \quad (4.23)$$

with

$$\mathcal{H}' = H_{PP} + \sum_{n \neq s} H_{PQ} \frac{|\Phi_n\rangle\langle\Phi_n|}{E - \varepsilon_n} H_{QP} + \int d\alpha \int d\varepsilon H_{PQ} \frac{|\Phi(\alpha, \varepsilon)\rangle\langle\Phi(\alpha, \varepsilon)|}{E - \varepsilon} H_{QP} \quad (4.24)$$

This reformulation leads to the following version of eq. (4.16)

$$(E - \mathcal{H}') P\Psi = H_{PQ} \frac{|\Phi_s\rangle\langle\Phi_s|}{E - \varepsilon_s} H_{QP} P\Psi \quad (4.25)$$

$P\Psi$ has to be described in terms of the final states in the asymptotic region, which means that the wavefunction has to satisfy the appropriate boundary conditions of the escaping particle. Therefore, the eigenfunctions of \mathcal{H}' have to fulfill incoming boundary conditions, which is labelled by the superscript $(-)$

$$(E - \mathcal{H}') |\psi_f^{(-)}\rangle = 0 \quad (4.26)$$

This relation can then be utilized to find a solution for $|P\Psi\rangle$ using the Lippmann-Schwinger equation (4.2):

$$|P\Psi\rangle = |\psi_f^{(-)}\rangle + \frac{1}{E^{(-)} - \mathcal{H}'} \frac{H_{PQ} |\Phi_s\rangle\langle\Phi_s| H_{QP} |P\Psi\rangle}{E - \varepsilon_s} \quad (4.27)$$

In order to solve this expression for $|P\Psi\rangle$, eq. (4.27) is multiplied from the left with $\langle\Phi_s|H_{QP}|$ to give:

$$\langle\Phi_s|H_{QP}|P\Psi\rangle = \langle\Phi_s|H_{QP}|\psi_f^{(-)}\rangle - \frac{1}{E^{(-)} - \mathcal{H}'} \frac{\langle\Phi_s|H_{QP}H_{PQ}|\Phi_s\rangle\langle\Phi_s|H_{QP}|P\Psi\rangle}{E - \varepsilon_s} \quad (4.28)$$

Defining the quantity

$$W_{QQ} = H_{QP} \frac{1}{E^{(-)} - \mathcal{H}'} H_{PQ} \quad (4.29)$$

and solving eq. (4.28) for

$$\langle \Phi_s | H_{QP} | P\Psi \rangle = \frac{\langle \Phi_s | H_{QP} | \Psi_f^{(-)} \rangle (E - \varepsilon_s)}{E - \varepsilon_s + \langle \Phi_s | W_{QQ} | \Phi_s \rangle} \quad (4.30)$$

yields the final state description

$$|P\Psi\rangle = |\psi_f^{(-)}\rangle - \frac{1}{E^{(-)} - \mathcal{H}'} \frac{H_{PQ} |\Phi_s\rangle \langle \Phi_s | H_{QP} | \psi_f^{(-)} \rangle}{E - \varepsilon_s + \langle \Phi_s | W_{QQ} | \Phi_s \rangle}. \quad (4.31)$$

The complex conjugate of the above mentioned matrix of transition amplitudes \mathcal{T} is therefore given by

$$\mathcal{T}_{if}^* = \langle \psi_i^{(+)} | \mathcal{V} | P\Psi \rangle \quad (4.32)$$

$$= \mathcal{T}_{if}^{(P)*} + \frac{\langle \psi_i^{(+)} | H_{PQ} | \Phi_s \rangle \langle \Phi_s | H_{QP} | \Psi_f^{(-)} \rangle}{E - \varepsilon_s + \langle \Phi_s | W_{QQ} | \Phi_s \rangle} \quad (4.33)$$

where $|\psi_i^{(+)}\rangle$ in case of a full-collision process describes the solution of the Schrödinger with outgoing boundary conditions

$$(E - \mathcal{H}') |\psi_i^{(+)}\rangle = 0 \quad (4.34)$$

Here, $\mathcal{T}_{if}^{(P)*}$ describes the non-resonant transitions between the initial and final states. Therefore, close to the resonance, this part is expected to be small compared to the second part, which describes the transition from the initial into the final states mediated by the interaction between them.

From the transition amplitudes information about the resonance energy can be obtained from its poles. Therefore, $\langle \Phi_s | W_{QQ} | \Phi_s \rangle$ needs to be examined further. We split it into its real and imaginary part by introducing a delta function using $\lim_{\varepsilon \rightarrow 0^+} \frac{1}{x \pm i\varepsilon} = \mathcal{P} \frac{1}{x} \mp i\pi\delta(x)$, where \mathcal{P} is the principal part and $\delta(x)$ denotes the Dirac delta function. [50]

$$\langle \Phi_s | W_{QQ} | \Phi_s \rangle = \langle \Phi_s | H_{QP} \frac{1}{E^{(-)} - \mathcal{H}'} H_{PQ} | \Phi_s \rangle \quad (4.35)$$

$$= \langle \Phi_s | H_{QP} \frac{\mathcal{P}}{E - \mathcal{H}'} H_{PQ} | \Phi_s \rangle - i\pi \langle \Phi_s | H_{QP} \delta(E - \mathcal{H}') H_{PQ} | \Phi_s \rangle \quad (4.36)$$

$$= \Delta_s(E) - i \frac{\Gamma_s(E)}{2} \quad (4.37)$$

It consists of a real part, which can be related to an energetic shift of the resonance energy caused by the interaction, and an imaginary part, which is related to decay width Γ . Inserting the latter expression into the transition matrix yields

$$\mathcal{T}_{if}^* = \mathcal{T}_{if}^{(P)*} + \frac{\langle \psi_i^{(+)} | H_{PQ} | \Phi_s \rangle \langle \Phi_s | H_{QP} | \Psi_f^{(-)} \rangle}{E - \varepsilon_s + \Delta_s - i\frac{\Gamma}{2}} \quad (4.38)$$

From the imaginary part of $\langle \Phi_s | W_{QQ} | \Phi_s \rangle$ the decay width can easily be deduced. Inserting a complete set of eigenfunctions with incoming boundary conditions as defined in eq. (4.26) the decay width can be described as a sum over the different open channel solutions for a given resonant initial state:

$$\Gamma_s = 2\pi \langle \Phi_s | H_{QP} \delta(E - \mathcal{H}') H_{PQ} | \Phi_s \rangle \quad (4.39)$$

$$= 2\pi \sum_r \left| \langle \Phi_s | H_{QP} | \psi_r^{(-)} \rangle \right|^2 \quad (4.40)$$

$$= 2\pi \sum_r \Gamma_{sr}(E) \quad (4.41)$$

Here it has to be remembered that E is the energy of a final state, which means that only such functions give a contribution, which have the same energy as those.

This formulation is sufficient for all cases, which are going to be discussed in this thesis. However, Åberg *et al.* have proposed a slightly different ansatz with a different partitioning, where configurations can contribute both to the description of the initial and final state subspace. The expression for the decay width Γ is very similar to the above approach in equation (4.39), with more complex conditions in the delta function [51]. This approach is not valid for exact eigenfunctions, but may be useful in case of mappings to \mathcal{L}^2 functions as e.g., Configuration Interaction (CI) used by Fano [49]. The resulting expression reads

$$\Gamma_s = 2\pi \left| \langle \Phi_s | H - E | \psi_r^{(-)} \rangle \right|^2 \quad (4.42)$$

and is called *Fano's Golden Rule*. In the following, the latter will be the starting point but a partitioning into orthogonal initial and final states is always chosen, which means that equation (4.40) applies.

5. Decay Widths of ICD-like Processes in the Asymptotic Limit

Excited electronic states decaying in ICD or ETMD processes are an example of resonance states. In the Fano-Feshbach theory of resonances they are depicted as bound states embedded into and interacting with the continuum [49, 46, 47]. Formally, the eigenstates of the Hamiltonian in the vicinity of a resonance can be represented as a linear superposition of the square integrable “decaying state” $|\Phi\rangle$ and the continuum states $|\chi_{\beta,\varepsilon}\rangle$ satisfying ingoing boundary conditions where ε is the energy of the outgoing electron and β enumerates open decay channels. These states obey the following normalization conditions

$$\langle\Phi|\Phi\rangle = 1, \quad \langle\chi_{\alpha,\varepsilon}|\chi_{\beta,\varepsilon'}\rangle = \delta_{\alpha\beta}\delta(\varepsilon - \varepsilon'), \quad (5.1)$$

and one usually assumes that the continuum states prediagonalize the Hamiltonian \hat{H}

$$\langle\chi_{\alpha,\varepsilon}|\hat{H}|\chi_{\beta,\varepsilon'}\rangle = \varepsilon\delta_{\alpha\beta}\delta(\varepsilon - \varepsilon'). \quad (5.2)$$

We further assume the decaying and continuum states to be orthogonal

$$\langle\Phi|\chi_{\beta,\varepsilon}\rangle = 0. \quad (5.3)$$

The partial decay width Γ_β in the lowest order of perturbation theory is given by [51]

$$\Gamma_\beta(E_\Phi) = 2\pi \left| \langle\chi_{\beta,\varepsilon}|\hat{H} - E_\Phi|\Phi\rangle \right|^2, \quad (5.4)$$

where $E_\Phi = \langle\Phi|\hat{H}|\Phi\rangle$ is the resonance energy and the energy of the final state is $\varepsilon = E_\Phi$. The total decay width Γ is obtained as the sum over all partial widths $\Gamma = \sum_\beta \Gamma_\beta$.

The expression in Eq.(5.4) represents a suitable starting point for the *ab initio* computation of radiationless decay widths [51, 52]. However, in the case of interatomic decay

Parts of this chapter have already been published in

E. Fasshauer, M. Pernpointner, and K. Gokhberg

Interatomic decay of inner-valence ionized states in ArXe clusters: Relativistic approach

J. Chem. Phys. **138**, 014305 (2013)

Copyright 2013, American Institute of Physics.

processes such as ICD or ETMD3, simple analytic expressions can be derived for the case of large interatomic distances between the monomers. For ICD such an expression was derived previously in the non-relativistic limit and was shown to be accurate for the interatomic distances where the orbital overlap between the monomers is negligible [24, 10]. This formula is valid in the non-relativistic regime and becomes inadequate for systems exhibiting pronounced relativistic effects. Therefore, we derive in the following analogous expressions for the case when \hat{H} is the many-electron Dirac-Coulomb Hamiltonian \hat{H}_{DC} according to

$$\hat{H}_{DC} = \sum_{i=1}^N \left(c\vec{\alpha}_i \cdot \vec{p}_i + \beta_i m_e c^2 + \hat{V}_{\text{ext}}(i) \mathbf{1}_4 \right) + \sum_{i<j}^N \frac{1}{r_{ij}}. \quad (5.5)$$

Hereby $\vec{\alpha}_i$ and β_i are the usual 4×4 Dirac matrices for particle i in the standard notation. In the electron-electron interaction term magnetic (Gaunt) contributions to the Coulomb term and retardation effects are neglected. As can be seen in Eq.(5.2) already in the non-relativistic case continuum functions not normalizable in an L^2 sense appear in the positive energy range together with discrete, normalizable bound states. As an additional difficulty coming along with the use of \hat{H}_{DC} one has to mention that, strictly speaking, there are no normalizable many-electron eigenfunctions of \hat{H}_{DC} [53, 54, 55, 56] requiring the extra condition that the negative energy eigenstates be not accessible. We therefore work with a DC Hamiltonian that is projected onto the space of the positive energy states allowing for a construction of a normalizable many-electron basis describing bound states together with continuum states lying in the positive energy range. For actual implementations, the operators are generally used in their second-quantized form. As a consequence of the projection of \hat{H}_{DC} , the corresponding creation and annihilation operators act in the positive energy space exclusively (no pair formalism, see e.g. [57]) and refer to occupied and virtual one-particle states from which the many-particle wave functions are built.

Now we turn our attention to the system under investigation. Let \mathbf{S}_1 and \mathbf{S}_2 denote two subsystems participating in the interatomic or intermolecular decay which are located at a distance R from each other. We assume that the initial inner-valence vacancy resides on \mathbf{S}_1 . In the decay, an outer-valence electron of \mathbf{S}_1 fills the inner-valence vacancy, while an outer-valence electron of \mathbf{S}_2 is being ionized in the process. The chosen general partitioning is suitable for the description of ICD and ETMD3 processes. In the latter case the two monomers participating in the charge transfer are combined to one subsystem and the third monomer which is ionized forms the second subsystem.

The $(N - 1)$ -electron Hamiltonian \hat{H}_{DC} can be written as

$$\hat{H}_{DC} = \hat{H}_{S_1} + \hat{H}_{S_2} + \hat{H}_{S_1, S_2}, \quad (5.6)$$

where $\hat{H}_{S_k} = \sum_{i \in S_k}^{N_{S_k}} \hat{h}_{DC}(i) + \sum_{i>j; i,j \in S_k}^{N_{S_k}} \frac{1}{r_{ij}}$ denotes the Hamilton operator of the electrons residing on subsystem \mathbf{S}_k ($k = 1, 2$) consisting of the corresponding one-electron part and the Coulomb interaction between electrons localized within the subsystem \mathbf{S}_k and $\hat{H}_{S_1, S_2} = \hat{V}_{S_1, S_2} = \sum_{i \in S_1, j \in S_2}^N \frac{1}{r_{ij}}$ describes the Coulomb interaction between electrons located on different subsystems. At large distances between the monomers the decaying and continuum states can be approximated by the product forms

$$\begin{aligned} |\Phi\rangle &= |\phi_{iv}^{(S_1)}\rangle |\phi_0^{(S_2)}\rangle \\ |\chi_{\beta, \varepsilon}\rangle &= |\phi_{ov_1}^{(S_1)}\rangle |\chi_{ov_2, \varepsilon}^{(S_2)}\rangle. \end{aligned} \quad (5.7)$$

Here $|\phi_{iv}^{(S_1)}\rangle$ and $|\phi_{ov_1}^{(S_1)}\rangle$ are orthogonal eigenstates of the Hamilton operator \hat{H}_{S_1} of subsystem \mathbf{S}_1 describing the inner-valence (iv) and outer-valence (ov_1) ionized states of \mathbf{S}_1 . The states $|\phi_0^{(S_2)}\rangle$ and $|\chi_{ov_2, \varepsilon}^{(S_2)}\rangle$ are the ground state of \mathbf{S}_2 and a scattering state $|\chi_{ov_2, \varepsilon}^{(S_2)}\rangle$ corresponding to the outer-valence vacancy (ov_2) of \mathbf{S}_2 and a free electron of energy ε . The bound and the continuum state of \mathbf{S}_2 in Eq. (5.7) are, therefore, orthogonal by construction.

Inserting the Dirac-Coulomb Hamiltonian Eq. (5.6) and the wavefunctions in Eq. (5.7) into the expression for the decay rate in Eq. (5.4) and using the orthogonality relations, we arrive at the following expression for the partial decay width

$$\Gamma_{\beta} = 2\pi \left| \langle \chi_{\beta, \varepsilon} | \hat{V}_{S_1, S_2} | \Phi \rangle \right|^2, \quad (5.8)$$

where β denotes the combination of electrons involved in the corresponding pathways.

This expression was first obtained by Wentzel [58, 59] for the Auger decay widths. Its applicability is limited to processes where the coupling of the discrete and continuum states is weak and which can be treated as two-step processes, which means, that the electronic decay is independent of the primary ionization process. Both requirements are fulfilled for the ICD and ETMD processes discussed in this paper.

In order to arrive at working expressions we expand the Coulomb interaction \hat{V}_{S_1, S_2} in powers of $\frac{1}{R}$ obtaining the asymptotic expansion [11]:

$$\frac{1}{|\mathbf{x}_1 - \mathbf{x}_2|} = \frac{1}{R} - \frac{\hat{\mathbf{u}}_R \cdot (\mathbf{r}_1 - \mathbf{r}_2)}{R^2} + \frac{3(\hat{\mathbf{u}}_R \cdot (\mathbf{r}_1 - \mathbf{r}_2))^2 - (\mathbf{r}_1 - \mathbf{r}_2)^2}{2R^3} + \mathcal{O}\left(\frac{1}{R^4}\right) \quad (5.9)$$

where $R = |\mathbf{R}| = |\mathbf{R}_1 - \mathbf{R}_2|$ is the distance between the COMs (see Fig.5.1) and $\hat{\mathbf{u}}_R = \mathbf{R}/|\mathbf{R}|$ is the unit vector along \mathbf{R} . Each of the subsystems has its own coordinate system residing in the respective center of mass. Such an expansion converges uniformly if $|\mathbf{r}_i| < R/2$, corresponding to the absence of overlap of electron densities localized on

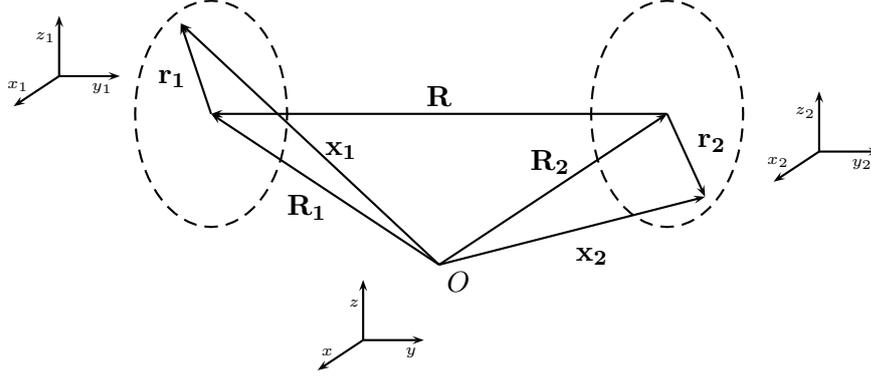


Figure 5.1.: The total system is split into subsystems \mathbf{S}_1 and \mathbf{S}_2 . The \mathbf{R}_i ($i = 1, 2$) point to the corresponding centers of mass (COMs) with respect to an arbitrary origin O . The \mathbf{x}_i as well as the \mathbf{r}_i describe the electron coordinates once with respect to O and once with respect to the COMs. Reprint with permission from Ref. [25]. Copyright 2013, AIP Publishing LLC.

different subsystems [60]. We truncate the series in Eq. (5.9) after the third term and focus on dipole transitions alone. Inserting it into Eq.(5.8) yields

$$\begin{aligned} \langle \chi_{\beta,\varepsilon} | \hat{V}_{S_1,S_2} | \Phi \rangle &= -\frac{3}{R^3} \left\langle \phi_{ov_1}^{(S_1)} \left| \sum_i \mathbf{r}_1^{(i)} \cdot \hat{\mathbf{u}}_R \right| \phi_{iv}^{(S_1)} \right\rangle \cdot \left\langle \phi_0^{(S_2)} \left| \sum_j \mathbf{r}_2^{(j)} \cdot \hat{\mathbf{u}}_R \right| \chi_{ov_2,\varepsilon}^{(S_2)} \right\rangle \\ &+ \frac{1}{R^3} \left\langle \phi_{ov_1}^{(S_1)} \left| \sum_i \mathbf{r}_1^{(i)} \right| \phi_{iv}^{(S_1)} \right\rangle \cdot \left\langle \phi_0^{(S_2)} \left| \sum_j \mathbf{r}_2^{(j)} \right| \chi_{ov_2,\varepsilon}^{(S_2)} \right\rangle \end{aligned} \quad (5.10)$$

where we made use of the fact that the matrix elements over the first two terms in the expansion (5.9) vanish due to orthogonality of the decaying and final continuum states. For rewriting Eq.(5.10) in spherical coordinates it is convenient to orient \mathbf{R} along the z_2 axis leading to

$$\langle \chi_{\beta,\varepsilon} | \hat{V}_{S_1,S_2} | \Phi \rangle = \frac{1}{R^3} \sum_{m=0,\pm 1} B_m \langle \phi_{ov_1}^{(S_1)} | D_{1m} | \phi_{iv}^{(S_1)} \rangle \langle \phi_0^{(S_2)} | D_{2m} | \chi_{ov_2,\varepsilon}^{(S_2)} \rangle, \quad (5.11)$$

where $B_0 = -2$, $B_{\pm 1} = 1$ and $D_{im} = \sum_i r_{im}$ ($i = 1, 2$) are the dipole operators acting on the electron coordinates of the subsystems \mathbf{S}_1 and \mathbf{S}_2 , respectively (see [61] for further details). The general expression for the decay width Γ_β referring to the decay process then reads

$$\Gamma_\beta = \frac{2\pi}{R^6} \sum_{m=0,\pm 1} B_m^2 \left| \langle \phi_{ov_1}^{(S_1)} | D_{1m} | \phi_{iv}^{(S_1)} \rangle \right|^2 \left| \langle \phi_0^{(S_2)} | D_{2m} | \chi_{ov_2,\varepsilon}^{(S_2)} \rangle \right|^2 \quad (5.12)$$

and serves as the starting equation for the special cases of ICD and ETMD3 as discussed

in the following subsections.

5.1. Interatomic Coulombic Decay

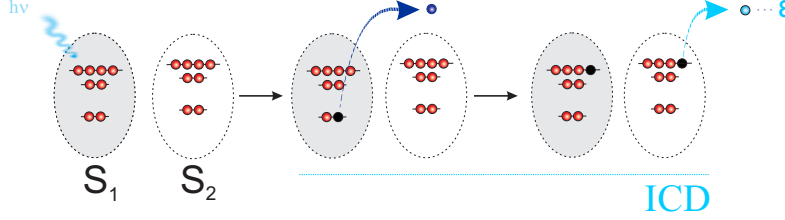


Figure 5.2.: ICD process in subsystems \mathbf{S}_1 and \mathbf{S}_2 . After creating an inner valence vacancy in \mathbf{S}_1 the hole is filled by an outer-valence electron of \mathbf{S}_1 . The excess energy is transferred to \mathbf{S}_2 and is used to remove an outer-valence electron (ICD electron). Reprint with permission from Ref. [25]. Copyright 2013, AIP Publishing LLC.

In the ICD process the inner valence vacancy is filled with an electron of the same atom or molecule. The excess energy is transferred to the second subunit and is used to ionize it (see Fig. 5.2). In rare gas clusters the corresponding subunits are atoms leading to the partition \mathbf{S}_1 as atom A and \mathbf{S}_2 as atom B . In atoms, the total angular momentum quantum number J and its projection M are good quantum numbers. As an ansatz for the initial and final state wave functions under the assumption of no interaction, the product of individual atomic configuration state functions is taken:

$$|\Phi\rangle = |E_A J_A M_A\rangle |E_B J_B M_B\rangle \quad \text{and} \quad |\chi_{\beta,\varepsilon}\rangle = |E'_A J'_A M'_A\rangle |E'_B J'_B M'_B\rangle. \quad (5.13)$$

In this expression the initial and final states are characterized by the energies of the atoms E_A , E_B and E'_A , E'_B , the corresponding total angular momenta of the atoms are denoted as J_A , J_B and J'_A , J'_B and their projections on the z -axis as M_A , M_B and M'_A , M'_B , respectively. At the beginning of the process atom B is assumed to be in its closed shell ground state $|\Phi_0^{(B)}\rangle$ with $J_B = M_B = 0$. Inserting Eqs. (5.13) into (5.12) we obtain

$$\Gamma_\beta = \frac{2\pi}{R^6} \sum_m B_m^2 \left| \langle E'_A J'_A M'_A | \hat{D}_m^{(A)} | E J_A M_A \rangle \right|^2 \times \left| \langle \Phi_0^{(B)} | \hat{D}_m^{(B)} | E'_B J'_B M'_B \rangle^* \right|^2 \delta(E - E') \quad (5.14)$$

At large distances the energies of the decaying and final state can be assumed to be the sum of the energies of the two subsystems A and B : $E = E_A + E_B$, $E' = E'_A + E'_B$. The resonance condition $E = E'$ can therefore be expressed through the energy matching of virtual photons emitted in the transition on atom A , $\omega_A = E_A - E'_A$, and absorbed by atom B , $\omega_B = E'_B - E_B$, i.e. $\omega_A = \omega_B = \omega_{vp}$. We can use the conservation of the

projection of the angular momentum on the z -axis $M_A = M'_A + M'_B$ to further simplify the expression in Eq. (5.14). By setting $m = -M'_B$ and using the Wigner-Eckart theorem [62] we arrive at

$$\Gamma_\beta = \frac{2\pi}{R^6} \sum_{M'_A} B_{M'_A-M_A}^2 \left| \begin{pmatrix} J'_A & 1 & J_A \\ -M'_A & M'_A - M_A & M_A \end{pmatrix} \langle E'_A J'_A || \hat{D}^{(A)} || E J_A \rangle \right|^2 \times \frac{1}{3} \left| \langle \Phi_0^{(B)} || \hat{D}^{(B)} || E'_B J'_B \rangle \right|^2, \quad (5.15)$$

where each decay channel β is characterized by E'_A , J'_A , E'_B and J'_B .

To find numerical values of Γ_β , the necessary dipole transition moments of the isolated atoms in Eq. (5.15) can either be computed directly or obtained from experimentally accessible quantities. At first we use the fact that the square of the reduced matrix element of atom A , the so-called line strength, is proportional to the state-to-state transition probability W_{J_A, J'_A} , which is in turn the inverse of the radiative lifetime τ of the initial state [63]:

$$\left| \langle E'_A J'_A || \hat{D}^{(A)} || E J_A \rangle \right|^2 = (2J_A + 1) \frac{3c^3}{4\omega_{vp}^3} W_{J_A, J'_A}. \quad (5.16)$$

Second, the square of the reduced matrix element of atom B is related to its partial photoionization cross section $\sigma^{(B)}(\omega_{vp})$ which depends on the energy atom B is exposed to [63]:

$$\left| \langle \Phi_0^{(B)} || \hat{D}^{(B)} || E'_B J'_B \rangle \right|^2 = \frac{3c \sigma^{(B)}(\omega_{vp})}{4\pi^2 \omega_{vp}}. \quad (5.17)$$

After insertion of Eq.(5.16) and (5.17) into (5.15) we arrive at a working expression for the partial decay width according to

$$\Gamma_\beta = \frac{2\pi}{R^6} \sum_{M'_A} B_{M'_A-M_A}^2 \left| \begin{pmatrix} J'_A & 1 & J_A \\ -M'_A & M'_A - M_A & M_A \end{pmatrix} \right|^2 (2J_A + 1) \frac{3c^4 \sigma^{(B)}(\omega_{vp})}{16\pi^2 \omega_{vp}^4 \tau_A}. \quad (5.18)$$

As could be expected from the non-relativistic formula, the relativistic expression also shows an R^{-6} -behaviour for the energy transfer corresponding to the interaction of two dipoles. Setting atomic parameters to their non-relativistic values and summing over all partial decay widths $\Gamma = \sum_{\beta} \Gamma_\beta$ produces the known non-relativistic result for the total decay width [24, 10].

One of our major goals is the inclusion of relativistic effects in the computation of the decay widths which is achieved by using J/M_J adapted initial and final state wave

functions. As a result, we observe more energetically distinguishable decay pathways leading to a different energy distribution of the emitted ICD electrons compared to the non-relativistic description. Moreover, if ICD takes place close to its threshold, the number of open channels might differ in the two cases resulting in different total ICD rates.

5.2. Electron Transfer Mediated Decay

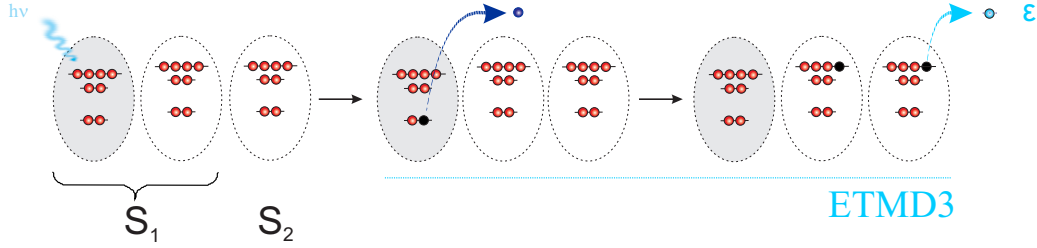


Figure 5.3.: ETMD3 process in subsystems \mathbf{S}_1 and \mathbf{S}_2 where the two atoms A and B participate in the electron transfer and are combined to \mathbf{S}_1 . After inner valence ionization of A, the vacancy is filled by an electron from B in \mathbf{S}_1 . The energy is transferred to C (\mathbf{S}_2) which is ionized and hereby emits the ETMD electron. Reprint with permission from Ref. [25]. Copyright 2013, AIP Publishing LLC.

In the ETMD3 process (see Fig. 5.3) three atoms are involved which we denote by A, B and C. The two subsystems in this case are AB (\mathbf{S}_1) and C (\mathbf{S}_2). The initial inner valence hole is assumed to be located on atom A. The electron is transferred from atom B to atom A, while the excess energy is transferred from \mathbf{S}_1 to atom C and used to ionize it. For a convenient geometric description of the triatomic system undergoing the ETMD3 process we use Jacobi coordinates as shown in Fig.5.4. All properties of the AB comprising subsystem \mathbf{S}_1 are described in its local $(\tilde{x}_1, \tilde{y}_1, \tilde{z}_1)$ coordinate system which is later backtransformed.

Analog to eq. (5.11) we arrive at

$$\begin{aligned} \langle \chi_{\beta, \varepsilon} | \hat{V}_{S_1, S_2} | \Phi \rangle &= \frac{1}{R^3} \sum_{ov_1, ov_2, \varepsilon} \left[\langle \phi_{ov_1}^{(S_1)} | \begin{pmatrix} -\frac{1}{\sqrt{2}}(\tilde{x}_1 \cos \alpha - \tilde{z}_1 \sin \alpha + i\tilde{y}_1) \\ \frac{1}{\sqrt{2}}(\tilde{x}_1 \cos \alpha - \tilde{z}_1 \sin \alpha - i\tilde{y}_1) \\ -2(\tilde{x}_1 \sin \alpha + \tilde{z}_1 \cos \alpha) \end{pmatrix} | \phi_{iv}^{(S_1)} \rangle \right. \\ &\quad \left. \cdot \langle \phi_0^{(S_2)} | \begin{pmatrix} r_{2+} \\ r_{2-} \\ r_0 \end{pmatrix} | \chi_{ov_2, \varepsilon}^{(S_2)} \rangle \right]. \end{aligned} \quad (5.19)$$

We define the initial state of ETMD as $|\Phi\rangle = |E_{AB} M_{AB}\rangle |\Phi_0^{(C)}\rangle$ and the final state

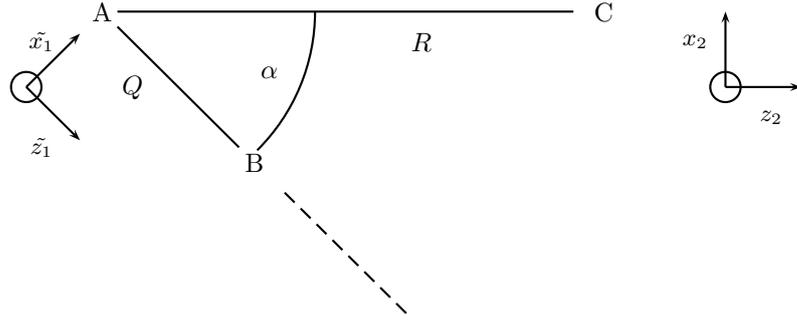


Figure 5.4.: Jacobi coordinates used for the geometric description of the trimer. Q is the distance between A and B , R the distance from the center of mass of AB to C and α the angle between the lines represented by Q and R .

as $|\chi_{\beta,\varepsilon}\rangle = |E'_{AB} M'_{AB}\rangle |E'_C J'_C M'_C\rangle$, where E_{AB} and E'_{AB} , E'_C are the energies of the corresponding initial and final states of the subsystems. Since the subsystem AB is of linear symmetry the total angular momentum J_{AB} is no longer a good quantum number but the projections M_{AB} , M'_{AB} still are and serve for the characterization of AB . J'_C is the total angular momentum of C in its final state and $|\Phi_0^{(C)}\rangle$ is the closed shell ground state of atom C in its initial state. Using Eq. (5.12) and expressing the electron dipole moment \vec{D}_1 of \mathbf{S}_1 in the coordinates $(\tilde{x}_1, \tilde{y}_1, \tilde{z}_1)$ we arrive at an intermediate equation for Γ_β as

$$\begin{aligned} \Gamma_\beta = & \frac{2\pi}{R^6} \sum_{M'_{AB}} \left[2 \left(\left| \langle M'_{AB} | \tilde{D}_x | M_{AB} \rangle \right|^2 (1 + \cos^2 \alpha) + \left| \langle M'_{AB} | \tilde{D}_z | M_{AB} \rangle \right|^2 \sin^2 \alpha \right) \right. \\ & \left. + 4 \left(\left| \langle M'_{AB} | \tilde{D}_x | M_{AB} \rangle \right|^2 \sin^2 \alpha + \left| \langle M'_{AB} | \tilde{D}_z | M_{AB} \rangle \right|^2 \cos^2 \alpha \right) \right] \\ & \times \frac{1}{3} \left| \langle \Phi_0^{(C)} | \hat{D}^{(C)} | J'_C \rangle \right|^2, \end{aligned} \quad (5.20)$$

where each decay channel β is characterized by its own E'_{AB} , E'_C and J'_C . The reduced matrix elements of atom C can again be expressed in terms of its ionization cross section

$$\left| \langle \Phi_0^{(C)} | \hat{D}^{(C)} | E'_C J'_C \rangle \right|^2 = \frac{3c \sigma^{(C)}(\omega_{vp})}{4\pi^2 \omega_{vp}} \quad (5.21)$$

and the transition dipole moments of AB can be conveniently computed using quantum chemical program packages. Finally we arrive at the following working equation for the

decay width according to

$$\begin{aligned}
\Gamma_\beta = & \frac{2\pi}{R^6} \sum_{M'_{AB}} \left[2 \left(\left| \langle M'_{AB} | \tilde{D}_x | M_{AB} \rangle \right|^2 (1 + \cos^2 \alpha) + \left| \langle M'_{AB} | \tilde{D}_z | M_{AB} \rangle \right|^2 \sin^2 \alpha \right) \right. \\
& \left. + 4 \left(\left| \langle M'_{AB} | \tilde{D}_x | M_{AB} \rangle \right|^2 \sin^2 \alpha + \left| \langle M'_{AB} | \tilde{D}_z | M_{AB} \rangle \right|^2 \cos^2 \alpha \right) \right] \\
& \times \frac{c\sigma^{(C)}(\omega_{vp})}{4\pi^2\omega_{vp}} \delta(\omega_{AB} - \omega_C). \tag{5.22}
\end{aligned}$$

The corresponding non-relativistic expression for the ETMD decay width is obtained by using L and S instead of the total angular momentum J for each electronic state together with the non-relativistic virtual photon energy and the corresponding photoionization cross section. Analogously to the ICD we observe the R^{-6} behaviour of the energy transfer. Additionally, an $e^{-\alpha Q}$ dependence is hidden in the transition dipole moments due to the charge transfer occurring in the ETMD process.

6. Clusters

Clusters are aggregations of atoms or molecules connected via non-covalent bonds such as van der Waals interaction, hydrogen bonds or metallic bonding. They are interesting because their properties lie in between the properties of atoms and molecules on the one hand and macroscopic solid state matter on the other hand.

Therefore the investigation of clusters touches the basic question, from what point on a cluster turns into a macroscopic solid. Very often this question is answered by the number of involved atoms or molecules defining a cluster to consist of 2–50000 constituents [64]. However, already cluster can exhibit properties of macroscopic solid state matter (see e.g. [65]). For example they do have an ordered structure, which for the same compound may differ between small and large clusters. In small clusters a comparatively large number of constituents is not completely surrounded by other constituents. These so-called surface atoms or molecules therefore have a large impact on the minimum energy structure. With increasing cluster size, their relative number decreases and consequently the bulk atoms and molecules, which are completely surrounded by other constituents, gain more and more impact on the minimum energy structure. This structure is in most cases not the same as for the smaller clusters, but is instead space filling and the same structure as observed for the macroscopic solid state matter [66, 67].

Defining a solid state by the constituting atoms or molecules to have fixed positions with respect to their neighbours, both macroscopic solid matter and clusters can be solid. It has to be noted, that also in this definition of the solid state, the constituents are able to move, but only as coupled vibrations of the total system. Compounds of solid states are able to melt and sublime. Microscopically, melting can be defined as atoms or molecules changing from having a fixed position within the ensemble to a random position with respect to their neighbours, but still being part of the overall ensemble. This means that internuclear distance patterns characterizing the structure are no longer observable and instead a broad distance distribution is to be examined. Analogously, sublimation can be defined as atoms or molecules moving far enough away from the rest of the cluster to not being captured again. With these definitions both melting and sublimation is possible for very small clusters of at least three constituents, even though one would in this case rather speak of rapid vibrations or bond breaking. The initiation of a melting or a sublimation process is governed by external conditions such as temperature and pressure. These initiation conditions differ between small clusters and macroscopic matter. Small clusters need less energy for the initiation of a melting

or sublimation process. With increasing cluster size, those external initiation conditions approach the characteristic melting and sublimation temperatures and pressures of the macroscopic solid matter [68, 69].

Furthermore, properties based on an electronic band structure like electric conductivity and group orientation of spins like magnetism appear with increasing cluster size. Interestingly, not only the size, but also the structure of the cluster is essential for their observance [70].

Research on clusters very often uses noble gas clusters as workhorses for the investigation of basic properties. In general, atoms are preferred for the investigation of clusters because they have spherical symmetry and hence different orientations of the constituents in the cluster are impossible and hence need not be investigated. Noble gas atoms only interact via van der Waals forces and hence the electronic states are very localized, which means that an electron can to a good approximation be assigned to the electron cloud of a specific atom. Therefore, the solutions of the atomic Schrödinger or Dirac equation are reasonably good starting points for the description of atoms within the clusters. Noble gases as such are theoretically easy to describe because of their electronic closed shell structure. It leads to a very well defined ground state which allows to neglect difficulties arising from multi-reference states during a calculation.

Experimentally, rare gas clusters can be prepared easily by expanding the noble gas through a cooled nozzle into vacuum. Furthermore, they are thermally stable, and cleaning of the apparatus after the experiment is not necessary, while cleaning after an experiment with e.g. metals is tedious and time-consuming.

6.1. Noble Gas Clusters

The noble clusters are held together by the London dispersion force stemming from the interaction of induced dipole moments in the polarizable noble gas atoms, which is a special case of the van der Waals forces and inhibits an attractive R^{-6} behaviour. The interaction potential between two atoms is therefore reasonably well described by the so called Lennard-Jones potential

$$V_{LJ}(R) = 4\varepsilon \left(\left(\frac{\sigma}{R} \right)^{12} - \left(\frac{\sigma}{R} \right)^6 \right) \quad (6.1)$$

where R denotes the internuclear distance, and ε is the depth of the potential. Due to different conventions of the formulation of the Lennard-Jones potential $\sigma = \frac{R_{min}}{\sqrt[6]{2}}$ with R_{min} being the distance of the potential minimum.

Its repulsive part takes care of the description of the Pauli repulsion due to overlapping orbitals at short distances. The R^{-12} dependency is theoretically not justified but convenient for an analytic description. For some noble gas dimers the Lennard-Jones

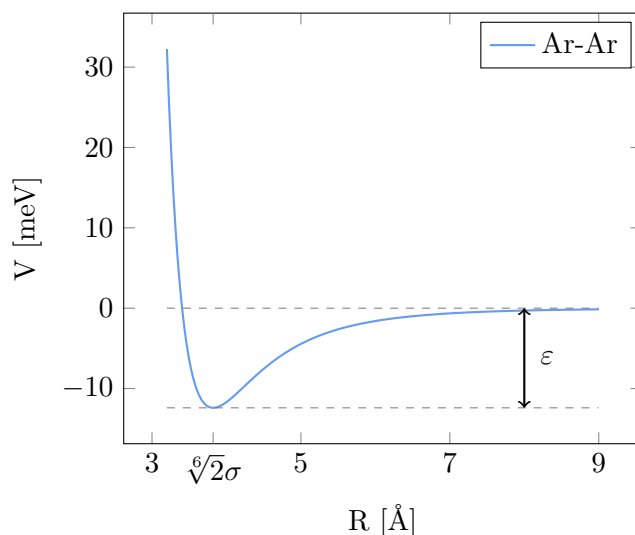


Figure 6.1.: Lennard-Jones potential of the argon dimer illustrating the Lennard-Jones parameters σ and ϵ .

parameters are given in Table 6.1 and the potentials are shown in Figure 6.1.

Table 6.1.: Lennard-Jones parameters for noble gas dimers used in this thesis [71, 72].

Atom type	σ [Å]	ϵ [meV]
Ar-Ar	3.40	12.4
Ar-Xe	3.72	14.4
Xe-Xe	3.96	23.1

The Lennard-Jones potentials describe the interaction between two atoms. Another characteristic entity is the van der Waals radius obtained from the interatomic distances in crystals. The values for the noble gases are displayed in Table 6.2.

To a first approximation homonuclear noble gas clusters are spheres because in order to minimize the energy of the cluster the interaction between the constituting atoms needs to be maximized. Atoms at the surface of a cluster have less interaction partners than atoms in the bulk, which are completely surrounded by neighbours as illustrated in Figure 6.2 showing a cut through a cuboctahedral cluster. Here it can also be seen that even in each shell, the atoms inhabit different positions with different numbers of nearest neighbours. An atom inhabits either a vertex position or an edge position as shown in Figure 6.2 or a position in a plane. An atom in the plane has more nearest neighbours than an atom in the edge, which again has more nearest neighbours of the same shell as a vertex atom. Overall, the three dimensional structure with the smallest surface to volume ratio or, in terms of atoms, surface to bulk ratio $\frac{S}{B}$, which therefore

Table 6.2.: Van der Waals radii of the noble gas atoms [73].

	R_{vdW} [Å]
Ne	1.54
Ar	1.88
Kr	2.02
Xe	2.16

allows a maximization of neighbours and hence of the binding energy, is the sphere.

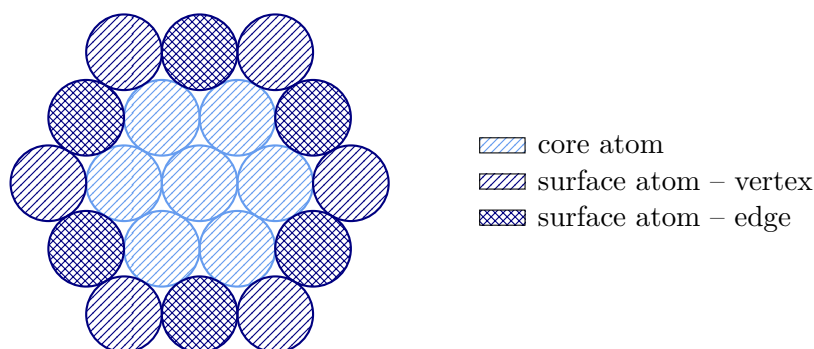


Figure 6.2.: Cut through a cuboctahedral cluster illustrating the different kinds of atoms within a cluster. The bright blue colored atoms are bulk atoms whereas the dark blue atoms belong to the surface. Within a shell atoms can either be vertices (striped), belong to an edge (crosshatched) or lie within a layer (not depicted in this two dimensional sketch).

At a closer look the structure is not a perfect sphere because of the shape of the atoms. Both theoretical calculations and mass spectrometry of rare gas mixtures show that for small clusters, the icosahedral structure, where icosahedral shells are nested into each other, is energetically beneficial [74, 75, 64, 66].

The number of atoms of such an icosahedral structure can be calculated via

$$n_{atoms} = \frac{10}{3}c^3 - 5c^2 + \frac{11}{3}c - 1, \quad (6.2)$$

where c denotes the number of shells, where the central atom is also counted as a shell [66]. Using this definition, c is identical to the number of atoms in the edge of the outermost shell.

In contrast to this, larger clusters and the solid show a cuboctahedral pattern, which infinitely extended leads to a face-centered-cubic (fcc) structure. In the fcc structure every atom is symmetrically surrounded by 12 atoms in the same distance, while in icosahedral structures, the atomic distance between atoms of different shells are smaller than the interatomic distance within a shell. A large number of surface atoms compared to the total number of atoms in the cluster will therefore have a higher binding energy in

an icosahedral structure than in an fcc structure and will therefore induce an icosahedral structure. The larger the clusters are, the smaller is their surface to bulk ratio $\frac{S}{B}$ as illustrated in Figure 6.3 for ideal icosahedral clusters. Therefore, the relative contribution of the surface atoms to the overall binding energy decreases with increasing cluster size and hence a minimum energy is to be achieved from maximizing the interactions of the bulk atoms. Closest packing structures such as fcc and hexagonal-closest-packing (hcp) fulfill this criterion of maximized interactions and are hence minimum energy structures of larger clusters. From a certain cluster size on the preferred structure therefore changes from icosahedral to cuboctahedral. This size is not exactly known and a topic of ongoing research. It is well accepted, that the transition is supposed to lie somewhere between 800–3000 atoms [67, 76], which corresponds to $c = 7 - 11$.

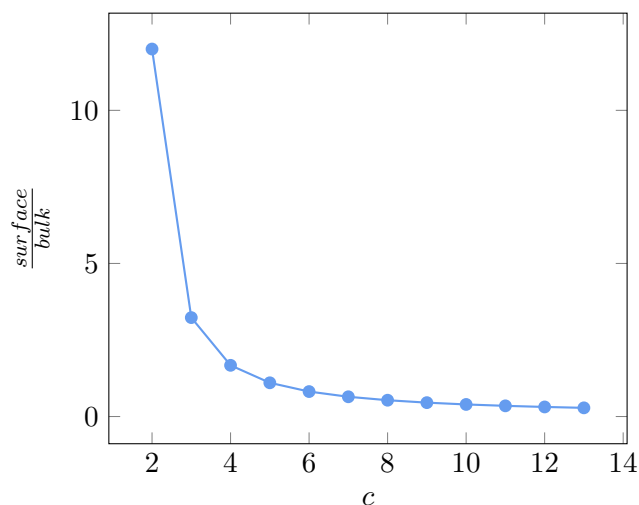


Figure 6.3.: Surface to bulk ratio for icosahedral structures with c complete shells illustrating the decreasing impact of the surface atoms.

The structure of heteronuclear clusters is expected to be similar to the homonuclear rare gas cluster with a core consisting of the more polarizable atom type somehow surrounded by atoms of the other atom type, which will be discussed in the next section. A new method for the investigation of the structure is found in this thesis.

6.2. Creation of Noble Gas Clusters

In order to create a stable cluster, its kinetic energy $k_B T$ needs to be lower than the sum over the cohesive energies in the cluster. Experimentally, noble gas clusters can be prepared by expanding gas through a nozzle into vacuum. If the mean free path of an atom or molecule λ is large compared to the diameter d of the nozzle, then the flow is molecular. In case of λ being much smaller than d , the atoms inside the nozzle collide

often and their individual velocities approach the group velocity of the directed beam. Consequently, the width of the lateral velocity distribution is decreased and due to energy and momentum conservation the temperature in expansion direction is decreased, which allows the formation of clusters. When all atoms have the same velocity, the atoms do not collide any longer and hence, sound would not be transferred through this medium. Therefore, such a stream of atoms or molecules is called supersonic [77].

Cluster growth starts with the creation of a dimer. Due to energy conservation a three-particle collision is required. Two particles form a dimer and the third particle removes kinetic energy. For all further additions of particles a two particle collision is sufficient. The kinetic energy of the additional atom is then used to excite vibrations within the cluster [78].

The likelihood for three-particle collisions is proportional to the pressure in the nozzle squared. By increasing the pressure, therefore the primary nucleation is supported. On the other hand the pressure inside the vacuum chamber needs to be low to avoid collisions between the clusters and residual gas. The maximum applicable pressure is therefore limited by the pumping power installed at the experimental chamber.

Whenever one speaks of rare gas clusters, one has to keep in mind that with today's experimental knowledge and apparatus, single clusters inhibiting a defined number of atoms or even structure can not be created. In every experiment a whole manifold of clusters with different sizes are formed. This manifold is characterized by the average number of atoms per cluster \bar{N} . This number is not necessarily the most abundant cluster in the mixture as can easily be seen from Figure 6.4. The width of the cluster size distribution is normally estimated to be $2\bar{N}$.

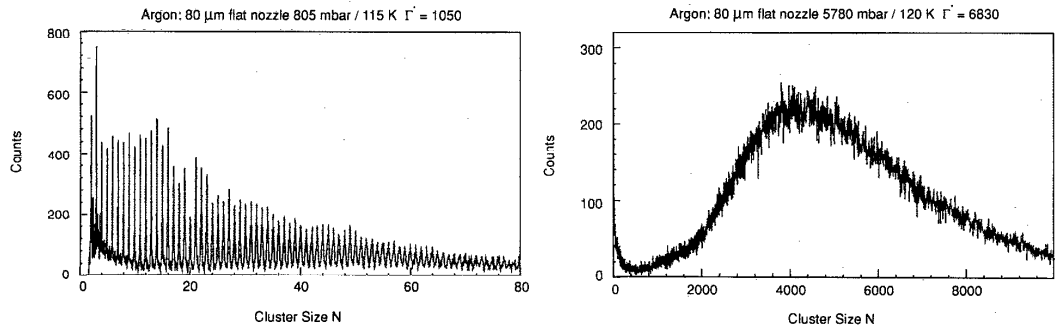


Figure 6.4.: Mass distribution of argon clusters. Reprint with permission from Ref. [79]. Copyright 1993, AIP Publishing LLC.

The mean cluster size \bar{N} can be estimated with the help of the empirical scaling parameter Γ^* of Hagena *et al.* [80, 81] for different experimental conditions.

$$\Gamma^* = \frac{p_0 d_{eq}^q}{T_0^{5/2-q/4}} K_{ch} \quad (6.3)$$

Here, p_0 and T_0 are the expansion pressure and the temperature of the nozzle and d_{eq} is the equivalent nozzle diameter for conical nozzles. K_{ch} is a constant depending on the material and can be calculated by the means of Hagenau [82]. The values for the rare gases for the experimental setup, which will be compared to in this work are $K_{ch}(Ne) = 185$, $K_{ch}(Ar) = 1646$, $K_{ch}(Kr) = 2980$ and $K_{ch}(Xe) = 5554$ [71].

From the scaling parameter the mean cluster size \bar{N} of homonuclear clusters can be estimated as

$$\bar{N} = 33 \left(\frac{\Gamma^*}{1000} \right)^{2.35}. \quad (6.4)$$

6.2.1. Creation of Heteronuclear Noble Gas Clusters

Heteronuclear noble gas clusters can be created in different ways: the *pick-up* method or co-expansion of two different gases are two examples. For the pick-up method, the jet of homonuclear clusters is directed through a volume with a high concentration of the other species. The clusters collide with the second species of which consequently atoms or molecules are attached to the surface of the parent cluster. Depending on the species and the experimental conditions, different cluster arrangements can be observed. Either, few atoms of the second species stay on the surface of the parent cluster, several atoms form a shell around the parent cluster or the second species diffuses into the bulk of the parent cluster.

In the co-expansion method two gases are mixed before the expansion and then led into the nozzle together. The species with the higher cohesive energy is more likely to start nucleation and form dimers which then grow into larger clusters.

6.3. Experimental Analysis Tools

Noble gas clusters are investigated using mass spectrometry and spectroscopy. From the mass spectrometry information about the mean number of atoms can be obtained. Within spectroscopy two ansatzes are used to gain information about clusters. In the first one, measurements of atomic properties for atoms in clusters are compared to the results of atoms. From the number of peaks, the energy shift and the relative peak intensity conclusions about the surroundings about the atoms inside the cluster are drawn. These methods are Photo-Electron Spectroscopy (PES), especially X-ray Photo-Electron Spectroscopy (XPS) and Ultra-Violet Photo-Electron Spectroscopy (UPS), Auger Electron Spectroscopy (AES), Resonant Auger Electron Spectroscopy (RAS), X-ray Emission Spectroscopy (XES), Near Edge X-ray Absorption Fine Structure (NEXAFS) and X-ray Absorption Spectroscopy (XAS). Their different working principles are illustrated in Figure 6.5.

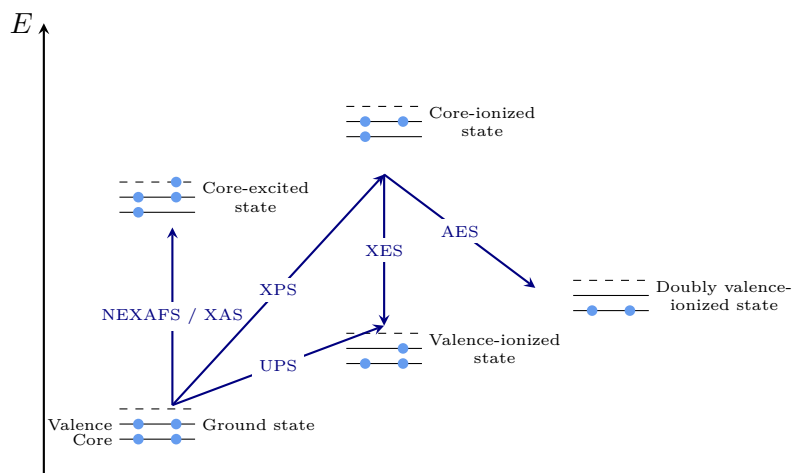


Figure 6.5.: Schematic overview over the physical mechanisms of different spectroscopic methods [64].

XAS, also known as NEXAFS probes the absorption of light from the ground state to a core excited state. With PES, ionization energies can be determined. More accurately UPS gives information about the ionization potentials of valence orbitals and XPS of core orbitals. AES measures the kinetic energy of the emitted Auger electron resulting in a doubly (mostly valence) ionized final state, while XES measures the photon emitted during an relaxation from a core ionized to valence ionized state.

Using those techniques, atoms in the bulk can be differentiated from atoms in the surface and even different positions in the outermost shell could be resolved. The obtained surface-to-bulk ratios can then also be used for an estimation of the mean cluster size [64, 83, 84].

The second ansatz, which is developed in this thesis, uses electron-electron and ion-ion coincidence spectroscopy. They exploit the interaction between neighbouring atoms directly using the ICD. Until now, these techniques have been used for the investigation of the ICD and ICD-like processes alone. But since the ICD-like processes strongly depend on the geometry, I am going to show that for systems with two competitive processes of comparable lifetime, having information about the decay widths, conclusions about the cluster structure can be drawn with the help of experimental electron-electron spectra.

The principle experimental setup for both coincidence measurements is very similar. As shown in Figure 6.6, the clusters are created using supersonic expansion into the expansion chamber. The jet is then directed through a conical skimmer into the reaction chamber. Here, the jet is crossed with synchrotron radiation. One pulse has of course many photons. However, only 1 in about 10000 pulses creates a vacancy. This created vacancy can then decay via ICD. In this case, a second electron is emitted and the two positively charged subsystems undergo Coulomb explosion within a timescale of fs to

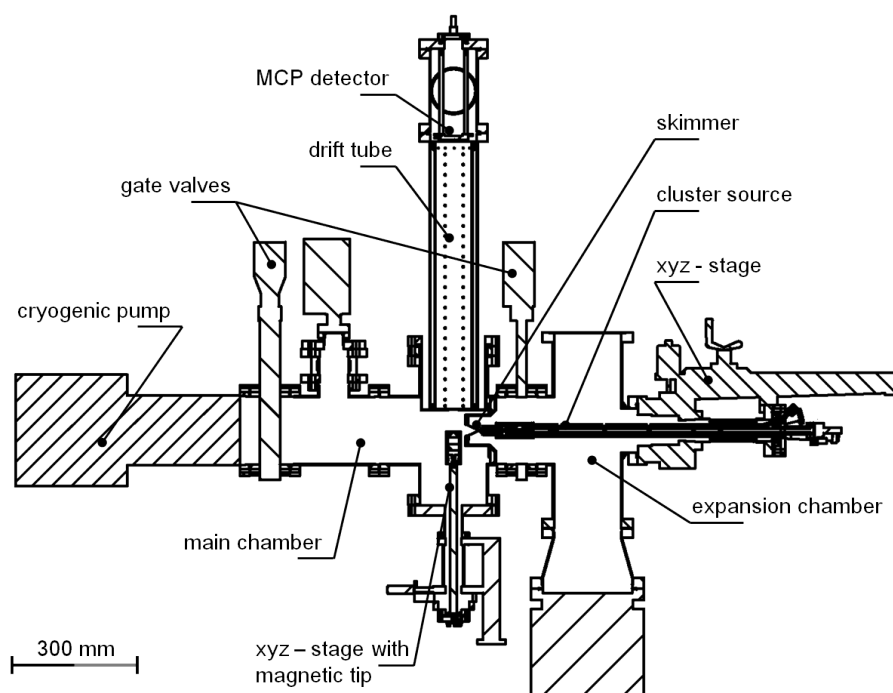


Figure 6.6.: Schematic view of the experimental setup of an electron-electron coincidence measurement. The synchrotron radiation axis is perpendicular to the plane of the diagram. Reprinted with permission from [71].

ps. In this time scale, the ionized cluster is still inside the reaction sphere. Initiated by the synchrotron photon, four charged particles are created, two electrons and two ions. Being charged, these particles can easily be withdrawn from the reaction chamber to detectors using a so-called magnetic bottle for both positively and negatively charged particles. In experiments normally only either electrons or ions are investigated at a time.

A coincidence of two particles is experimentally defined by two events measured in a specific time range after one synchrotron pulse. For the electron-electron coincidence, the coincidence time range is 1600 ns [85]. Coincidences are very often displayed in a so-called coincidence map, where the kinetic energy of one electron is plotted against the kinetic energy of the other electron. Two electrons measured in coincidence can stem from several physical processes. In the coincidence map these processes are distinguishable from the form of the signal.

Figure 6.7 illustrates such a coincidence map. There, the signal a) is a spot at defined energies e_1 and e_2 . It corresponds to a process, where the electrons both stem from orbitals of a well defined, small energy range and the final state energy is not influenced by perturbations like vibrations. This could e.g. be an Auger decay. Signal b) is a

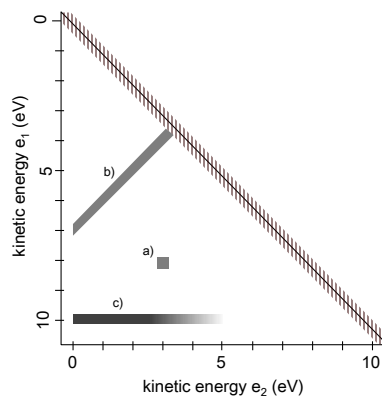


Figure 6.7.: Schematic illustration of electron-electron coincidence signatures for different physical processes. Printed with permission from [71]. See the text for details.

straight line with a constant sum of the kinetic electron energies. For example electron-electron scattering shows such a behaviour. Signal c) is a smeared out line, where one electron energy is constant and the kinetic energy of the second electron underlies a distribution. An ICD process would exhibit such a signal. Here the ionization energy for the creation of the initial state is quite well defined, whereas the energy of the final states shows a broad distribution due to vibrations and, as is to be shown in this thesis, due to several decay channels with different final state energies as well as a decay involving atoms at different distances inside larger clusters.

To visualize the coincident data and especially the ICD feature one can extract and plot only those electrons which are detected in coincidence with electrons from the initially excited, autoionizing state. The histogrammized counts of these electrons over their kinetic energy is then the coincidence spectrum. An example of a coincident electron spectrum is shown in Figure 6.8. Two distinct features can be seen which are detected in coincidence with a Ne2s electron. They correspond to the two competing processes of NeNe-ICD and NeAr-ICD, which will be discussed in detail in chapter 13.2.

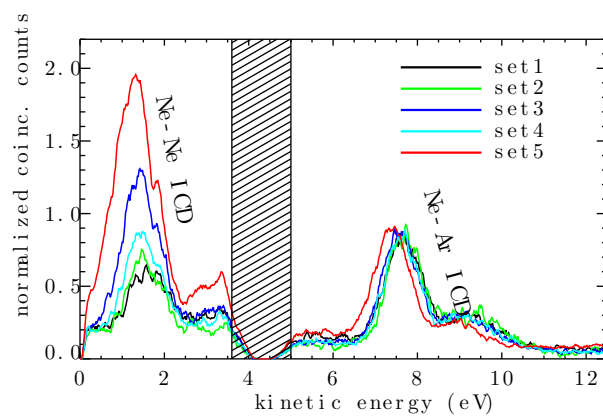


Figure 6.8.: Electron-electron coincidence spectra for NeAr clusters showing both NeNe-ICD and NeAr-ICD signals [86].

Part II.

Methodology

7. Obtaining Continuum Properties from \mathcal{L}^2 -Functions

7.1. Bound and Continuum States

Before the decay of a metastable state is described one has to remember that both bound and continuum states are involved in such a process. Bound states are localized and in quantum mechanics represented by square integrable functions of the \mathcal{L}^2 Hilbert space. Their boundary conditions lead to a quantized energy spectrum and the functions of the bound states are normalized to represent the N -particle wavefunction. Unperturbed bound states are eigenstates of H_0 only and can therefore conveniently be described using the time-independent Schrödinger equation. In contrast to the bound states the continuum states are very delocalized, are not square-integrable and are hence not accessible for a probabilistic interpretation. Their energy spectrum is continuous and the functions are normalized to their respective energy.

In decay processes where bound and continuum states interact, it is necessary to find a way to properly represent bound states in an energy normalization or continuum states in an \mathcal{L}^2 normalization. Since most quantum chemical program packages are based on \mathcal{L}^2 functions, it is most convenient to go for the latter approach. Especially for properties like decay widths or ionization cross sections, one possibility is to interpret the evaluation of an expectation value including the continuum in either the initial or the final state as Gaussian quadrature and compare them to analogous expressions for the expectation value in a discrete set of eigenstates. The given equivalence allows to use the machinery of Gaussian quadrature combined with an imaging procedure, both known in the literature, for the determination of the required entity [87].

After an explanation of Gaussian quadrature it is going to be shown that the discrete spectrum of a Hamiltonian in \mathcal{L}^2 representation contains information of the continuum using Gaussian quadrature based on the discussion of [87]. Then, it is going to be shown how the decay width can be obtained from a discrete pseudo-spectrum by using Stieltjes imaging [88, 89]. Finally we are going to introduce the FanoADC approach for the representation of states in the \mathcal{L}^2 Intermediate State Representation (ISR) basis.

7.2. Gaussian Quadrature

The gaussian quadrature is a numerical method for integration. The function to be integrated $g(x) = \rho(x)f(x)$ is approximated to be a product of a positive definite weight function $\rho(x)$ and a continuous and bounded function $f(x)$ [90]. The evaluation of the integral is then obtained as

$$\int_a^b \rho(x)f(x)dx \approx \sum_{i=1}^n \omega_i f(x_i). \quad (7.1)$$

Here the weights ω_i and the abscissae x_i are to be determined analytically, if possible, or otherwise in an optimal way. This leads the abscissae to be unequally spaced unlike in the basic integration schemes such as the trapezoidal rule.

The function $f(x)$ can be expressed as a polynomial. For certain weight functions and boundaries of integration, these polynomials can be determined analytically. It can furthermore be shown that the roots (zeros) of the highest order polynomial describing the function $f(x)$ give the optimal abscissae x_i . These polynomials Q_n are normalized with respect to the weight function as

$$\int_a^b \rho(x)Q_n(x)Q_m(x) = N_n\delta_{nm}, \quad (7.2)$$

where N_n denotes the normalization factor.

In the special case of the weight function $\omega(x) = \frac{1}{\sqrt{1-x^2}}$ and the interval $[-1, +1]$ the solution to the polynomials are the so-called Chebyshev polynomials, with the analytical abscissae and weights

$$x_{i,n} = \cos\left(\frac{2i-1}{2n}\pi\right) \quad \omega_{i,n} = \frac{\pi}{n} \quad (7.3)$$

This means that the integration of an arbitrary function $h(x)$ within the interval $[-1, 1]$ can be integrated as

$$\int_{-1}^1 h(x)dx = \int_{-1}^1 \omega(x)\sqrt{1-x^2}h(x)dx \approx \frac{\pi}{n} \sum_{i_1}^n h(x_{i_1})\sqrt{1-x_{i_1}^2} \quad (7.4)$$

By appropriately transforming the variables, the limits of integration can be chosen differently.

An example for such an integration is shown in Figure 7.1 for $h(x) = x^3 + 1$. The dark blue curve shows $h(x)$, the points are the calculated h_i at the abscissae x_i and the light blue hatched areas are the approximations to the integral for the certain areas. Obviously, the finer the grid for the integration, the more precise is the approximation

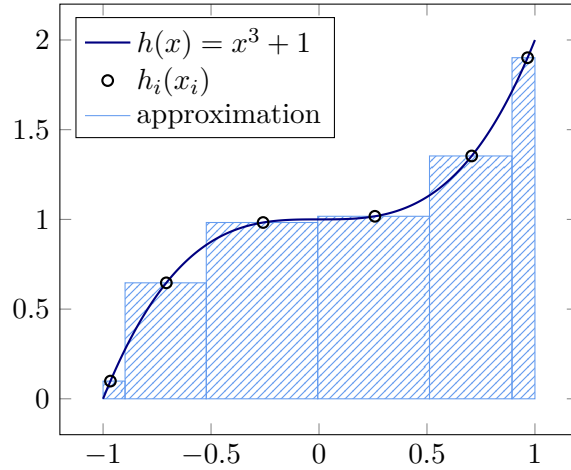


Figure 7.1.: Integration by Gauss-Chebyshev quadrature of the function $h(x) = x^3 + 1$ (dark blue) with $n = 6$. The integral (light blue) is obtained by summation over all product of optimal abscissae and weights $x_i h(x_i)$ (circles).

to the analytical integral.

The above discussion holds for a known weight function. For an unknown weight function, the integral can be obtained by solving the so-called moment problem [87].

7.3. Expressing the Continuum Properties in Terms of Gaussian Quadrature

Now the question arises how Gaussian quadrature can help to calculate decay widths. The Hamiltonian can be expressed in terms of a complete set of eigenfunctions

$$H = \sum_i |\phi_i\rangle E_i \langle \phi_i| + \int_0^\infty dE |\phi(E)\rangle E \langle \phi(E)|, \tag{7.5}$$

where the manifold of ϕ_i denote the bound state eigenfunctions being orthonormal in the sense of the probabilistic picture $\langle \phi_j | \phi_i \rangle = \delta_{ij}$. The continuum functions $\phi(E)$ also form an orthonormal set of basis functions but are normalized with respect to their energy.

$$\langle \phi(E) | \phi(E') \rangle = \delta(E - E') \tag{7.6}$$

In a calculation using a finite \mathcal{L}^2 basis, the diagonalization of the Hamiltonian yields an approximative set of eigenfunctions χ_i with corresponding eigenvalues \tilde{E}_i such that

$$\tilde{H} |\chi_i\rangle = \tilde{E}_i |\chi_i\rangle \quad \langle \chi_j | \chi_i \rangle = \delta_{ij}. \tag{7.7}$$

The approximative Hamiltonian can be rewritten in terms of these \mathcal{L}^2 functions

$$\tilde{H} = \sum_{E_i < 0} |\chi_i\rangle \tilde{E}_i \langle \chi_i| + \sum_{E_j > 0} |\chi_j\rangle \tilde{E}_j \langle \chi_j|, \quad (7.8)$$

where the first part with eigenvalues smaller than 0 corresponds to the bound states and the second part with energies higher than 0 corresponds to the continuum. In this representation the continuum is not described explicitly, but in a discretized representation.

The eigenfunctions and eigenvalues of the positive energy solutions have no physical meaning. Still, they inhibit a useful mathematical meaning if the continuum part is interpreted in terms of a numerical quadrature. For this purpose the continuum part of the energy expectation value $\langle \Psi | H | \Psi \rangle$ of the full Hamiltonian in (7.5) is evaluated using Gaussian quadrature

$$\int_0^\infty dE \langle \Psi | \phi(E) \rangle E \langle \phi(E) | \Psi \rangle \simeq \sum_j \omega_j \langle \Psi | \phi(E_j) \rangle E_j \langle \phi(E_j) | \Psi \rangle, \quad (7.9)$$

where ω_j are the quadrature weights. Compared to this the continuum part of the energy expectation value of the discretized Hamiltonian $\langle \Psi | \tilde{H} | \Psi \rangle$ reads

$$\int_0^\infty dE \langle \Psi | \phi(E) \rangle E \langle \phi(E) | \Psi \rangle \simeq \sum_{E_j} \langle \Psi | \chi \rangle \tilde{E}_j \langle \chi | \Psi \rangle. \quad (7.10)$$

In both cases, the integral is approximated by a sum and in some special cases, where the analytic continuum functions are known, it can be shown from the results that a one-to-one correspondence between each \mathcal{L}^2 eigenfunction of the positive energy part and the continuum function evaluated at the energy \tilde{E}_j exists. The so-called equivalent quadrature weight ω_j^{Eq} connects the discrete and the continuum function over a limited region of coordinate space for the given energy and can be interpreted as a renormalization [87].

$$|\chi_j\rangle = \sqrt{\omega_j^{Eq}} |\phi(\tilde{E}_j)\rangle \quad (7.11)$$

In the following, it is assumed that this equivalence between \mathcal{L}^2 and continuum functions with the integral interpreted as Gaussian quadrature is valid for all systems under investigation.

Assumed for a moment the appropriate equivalent quadrature weights to be known, the decay width could be calculated from a discretized representation substituting the continuous basis $\sum_r |\psi_r^{(-)}\rangle \langle \psi_r^{(-)}|$ of equation (4.39) by the discrete basis $\sum_r |\chi_r\rangle \langle \chi_r|$.

$$\Gamma = \frac{1}{\omega_j^{E_q}} |\langle \Phi_s | H - E | \chi_j \rangle|^2 \delta(E - E_j) \quad (7.12)$$

Since in most cases, the weight function is unknown, the weight function is going to be calculated by solving the moment problem. The following gedankenexperiment will show this possibility. Consider the matrix element $\langle \Phi_s | H H^k H | \Phi_s \rangle$ is well defined. Evaluating this matrix element for the Hamiltonian in the representation including continuous functions as given in equation (7.5) yields

$$\langle \Phi_s | H H^k H | \Phi_s \rangle = \sum_i \langle \Phi_s | H | \phi_i \rangle E_i^k \langle \phi_i | H | \Phi_s \rangle + \int_0^\infty dE \langle \Phi_s | H | \phi(E) \rangle E^k \langle \phi(E) | H | \Phi_s \rangle \quad (7.13)$$

Substituting H^k by \tilde{H}^k of equation (7.8) gives

$$\langle \Phi_s | H \tilde{H}^k H | \Phi_s \rangle = \sum_i \langle \Phi_s | H | \phi_i \rangle \tilde{E}_i^k \langle \phi_i | H | \Phi_s \rangle + \sum_j \langle \Phi_s | H | \chi_j \rangle \tilde{E}_j^k \langle \chi_j | H | \Phi_s \rangle \quad (7.14)$$

The two second terms approximately equal each other and additionally they are the moments of the decay width, exact in equation (7.13) and approximately in equation (7.14).

From the latter the moments are accessible as

$$\Gamma^k = 2\pi \sum_i E_i^k |\langle \Phi_s | H - E | \chi_i \rangle|^2 \delta(E - E_i) \quad (7.15)$$

where orthogonality of Φ_s and χ_i is assumed. Otherwise the operators in the equations would just need to be adjusted to $(H - E)$ in the formulation of Fano or H_{PQ} and H_{QP} for Feshbach's formulation.

7.3.1. Moment Problem

The moments $S(k)$ of a real and continuous function $f(\omega)$ are defined as [91]

$$S(k) = \int_a^b \omega^k f(\omega) d\omega \quad k = 0, 1, \dots \quad (7.16)$$

In the case of $f(\omega)$ being a probability density function or a weight function in the nomenclature of Gaussian quadrature, it is connected to the probability distribution function $F(\omega)$ via

$$F(\omega) = \int f(\omega) d\omega. \quad (7.17)$$

Note that the standard assignment of variables in Gaussian quadrature and the formulation of the moment problem is confusing. The equivalent weight function and probability density is in Gaussian quadrature denoted by $\omega(x)$, while in moment theory it is written as $f(\omega)$. We are going to stick to the conventions of both fields.

The probability density function $f(\omega)$ is completely determined by the manifold of moments. Therefore, when all moments are known, the probability density function (weight function) can be calculated from the moments. In the present case $f(\omega)$ is the decay width $\Gamma(E)$, but the theory is also applicable and previously used for the description of cross sections. Its pseudo-spectrum has the same mathematical properties as the pseudo-spectrum of the decay width. Therefore, the knowledge obtained in the description of cross sections can be adopted to the description for the decay widths.

In practice, all moments are never available unless they can be calculated analytically. Therefore, one has to approximately solve the reduced moment problem since the density function is not completely defined. In this case the $2r$ moments are

$$S(k) = \int_a^b \omega^k f(\omega) d\omega \quad k = 0, 1, \dots, 2r - 1 \quad (7.18)$$

In principle the moment problem can be solved by requiring the abscissae and weights to reproduce a minimum number of moments. Unfortunately, this determination is ill-conditioned and, therefore one expresses the moments by orthogonal polynomials of some known weight function. Then the transformation to the polynomials is still ill-conditioned, but the abscissae and weights can be obtained by a well-conditioned problem [92]. The latter approach of so-called modified moments has proved to be useful in the case of properties such as the ionization cross section and decay width.

7.3.2. Finding the Gaussian Quadrature Abscissae and Weights from Modified Moments

The procedure for the calculation of cross sections combining moment theory and Gaussian quadrature has been investigated thoroughly. In this section the argumentation of Müller-Plathe [91] is followed, from which the `stieltjes` routine has been written by Averbukh and which is used in combination with the FanoADC implemented in Dirac. The routine covers the construction of the polynomials, the calculation of abscissae and weights as well as the Stieltjes Imaging. These topics are normally discussed together in the literature [93, 89, 88].

For the ionization cross sections it has been shown that the moments with $k > 2$ diverge and hence are useless for the evaluation of the probability density function $f(\omega)$. Therefore the inverse moments $S(-k)$ are investigated instead:

$$S(-k) = \int_a^b \left(\frac{1}{\omega}\right)^k f(\omega) d\omega \quad (7.19)$$

For each *order of Stieltjes* r , a set of Chebyshev polynomials $Q_n(1/\omega) = \sum_{i=0}^n Q_n^i \left(\frac{1}{\omega}\right)^i$, of order $0 - r$ can be assigned, using $2r - 1$ moments for their construction. They are orthogonal with respect to the weight function to be determined $f(\omega)$:

$$\int_a^b Q_n(1/\omega) Q_m(1/\omega) f(\omega) d\omega = N_n \delta_{nm} \quad (7.20)$$

Chebyshev polynomials in general can be constructed from the recurrence formula

$$Q_n(1/\omega) = \frac{1}{\omega - a_n} Q_{n-1}(1/\omega) - b_{n-1} Q_{n-2}(1/\omega), \quad (7.21)$$

so that all polynomials can be constructed if Q_0 and Q_1 are known. From these recursion relations, expressions for the recurrence coefficients a_n and b_n can be obtained:

$$a_n = \frac{1}{b_0 b_1 \cdots b_{n-1}} \int (1/\omega)^n Q_{n-1}(1/\omega) f(\omega) d\omega - \sum_{l=1}^{n-1} a_l \quad (7.22)$$

$$b_{n-1} = \frac{1}{b_0 b_1 \cdots b_{n-2}} \int (1/\omega)^{n-1} Q_{n-1}(1/\omega) f(\omega) d\omega \quad (7.23)$$

By expansion of the integral in equations 7.22 and 7.23 into a sum over moments obtained from the pseudo-spectra, approximate expressions can be obtained for the recurrence coefficients depending on the energies $\bar{\omega}_i$ (the inverse abscissae), and couplings or the weights \bar{f}_i of the pseudo-spectrum.

$$a_n = \frac{1}{b_0 b_1 \cdots b_{n-1}} \sum_{i=1}^N (1/\bar{\omega}_i)^n Q_{n-1}(1/\bar{\omega}_i) \bar{f}_i - \sum_{l=1}^{n-1} a_l \quad (7.24)$$

$$b_{n-1} = \frac{1}{b_0 b_1 \cdots b_{n-2}} \sum_{i=1}^N (1/\bar{\omega}_i)^{n-1} Q_{n-1}(1/\bar{\omega}_i) \bar{f}_i \quad (7.25)$$

Hence, the recurrence relation now reads

$$Q_n(1/\bar{\omega}_i) = \frac{1}{\bar{\omega}_i - a_n} Q_{n-1}(1/\bar{\omega}_i) - b_{n-1} Q_{n-2}(1/\bar{\omega}_i) \quad (7.26)$$

with

$$Q_0(1/\bar{\omega}_i) = 1 \quad Q_1(1/\bar{\omega}_i) = (1/\bar{\omega}_i) - a_1 \quad (7.27)$$

as starting points of the determination of the polynomials.

In order to determine the distribution function $F(\omega)$ from the modified moments, the abscissae and weights have to be calculated. Again, the abscissae (ω_i) are the roots of the highest order polynomial for each order of Stieltjes r

$$Q_r(1/\omega_i) = 0 \quad i = 1, 2, \dots, r. \quad (7.28)$$

The connection between the weights and the polynomials is given by

$$af_i = \left[\sum_{m=0}^{n-1} \frac{Q_m^2(1/\omega_i)}{N_m} \right]^{-1}. \quad (7.29)$$

In order to obtain the roots of the highest order polynomial, in principle any program for root detection can be used. However, the problem can be reformulated in terms of general polynomials $R_n(1/\omega)$ connected to the obtained Chebyshev polynomials as

$$Q_n(1/\omega) = (-1)^n \sqrt{N_n} R_n(1/\omega) \quad (7.30)$$

with the respective recurrence formulas

$$(1/\omega)R_{n-1}(1/\omega) = -\sqrt{b_n}R_n(1/\omega) + a_n R_{n-1}(1/\omega) - \sqrt{b_{n-1}}R_{n-2}(1/\omega) \quad (7.31)$$

and

$$(1/\omega)R_0(1/\omega) = -\sqrt{b_1}R_1(1/\omega) + a_1 R_0(1/\omega). \quad (7.32)$$

Now, the roots can be determined from the following equation disregarding the last vector as solution of the eigenvalue problem.

$$\begin{aligned}
 & \begin{pmatrix} a_1 & -\sqrt{b_1} & & & & & \\ -\sqrt{b_1} & a_2 & -\sqrt{b_2} & & & & \\ & -\sqrt{b_2} & a_3 & -\sqrt{b_3} & & & \\ & & \ddots & \ddots & \ddots & & \\ & & & -\sqrt{b_{n-2}} & a_{n-1} & -\sqrt{b_{n-1}} & \\ & & & & -\sqrt{b_{n-1}} & a_n & \end{pmatrix} \begin{pmatrix} R_0(1/\omega) \\ R_1(1/\omega) \\ R_2(1/\omega) \\ \vdots \\ R_{n-2}(1/\omega) \\ R_{n-1}(1/\omega) \end{pmatrix} \\
 & = (1/\omega) \begin{pmatrix} R_0(1/\omega) \\ R_1(1/\omega) \\ R_2(1/\omega) \\ \vdots \\ R_{n-2}(1/\omega) \\ R_{n-1}(1/\omega) \end{pmatrix} - \begin{pmatrix} 0 \\ 0 \\ 0 \\ \vdots \\ 0 \\ -\sqrt{b_n}R_n(1/\omega) \end{pmatrix} \tag{7.33}
 \end{aligned}$$

Therefore the solution is simplified to diagonalization of the coefficients matrix. Its eigenvalues are the roots of the polynomial and hence the desired abscissae. The eigenfunctions \mathbf{u}_i are normalized to 1. For the determination of the weights f_i from the eigenvectors the following relation

$$1 = f_i \sum_{m=0}^{n-1} R_m^2(1/\omega_i) = \mathbf{u}_i \cdot \mathbf{u}_i \tag{7.34}$$

of equation (7.29) has to be employed to give

$$f_i = N_0 u_{0i}^2 \tag{7.35}$$

Hence, the negative moments are approximated by the abscissae $(1/\omega_i)$ and weights f_i as

$$S(-k) \approx \sum_{i=1}^n (1/\omega_i)^k f_i \quad k = 0, 1, \dots, 2r - 1 \tag{7.36}$$

7.3.3. Stieltjes Imaging

Having obtained the abscissae and weights, the probability distribution function $F(\omega)$ can be approximated. For this purpose, the so-called Stieltjes imaging is employed, where

$$F^{(n)}(\omega) = \begin{cases} 0 & \omega < \omega_1 \\ \sum_{j=1}^i f_j & \omega_i < \omega < \omega_{i+1} \\ \sum_{j=1}^n f_j = S(0) & \omega_n < \omega \end{cases} \quad (7.37)$$

The procedure is illustrated in Figure 7.2 for a sixth order Stieltjes imaging using a pseudo-spectrum for the NeAr ICD in a Stieltjes histogram.

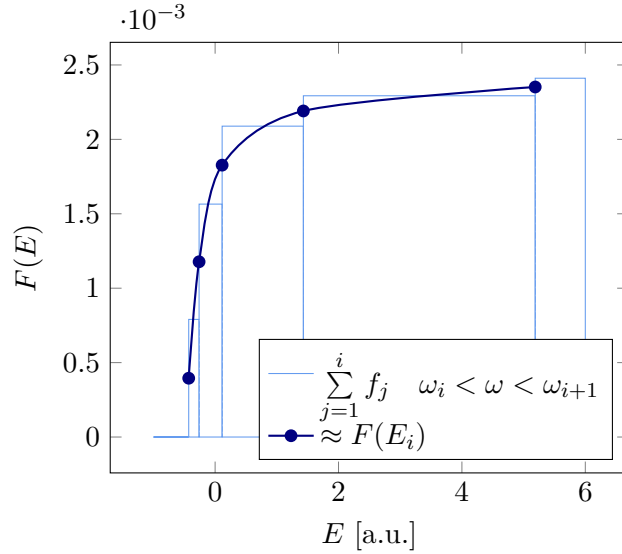


Figure 7.2.: Stieltjes histogram of a sixth order integration from a NeAr ICD pseudo-spectrum (light blue). At the abscissae ω_i , the histogram provides lower and upper bounds for the actual values. The mean of these two bounds (dark blue) is normally a good approximation of the distribution function $F(E)$ at this point.

This procedure is based on the so-called Chebyshev inequalities

$$F^{(n)}(\omega_i - 0) \leq F^{(n+1)}(\omega_i - 0) \leq F(\omega_i) \leq F^{(n+1)}(\omega_i + 0) \leq F^{(n)}(\omega_i + 0). \quad (7.38)$$

This means that the distribution functions obtained from the Chebyshev polynomials approaching the abscissae ω_i from below and from above give lower and upper bounds to the actual value of the distribution function at this particular point $F(\omega_i)$. In fact, the mean of these two values usually is a very good approximation to the exact value:

$$F^{(n)}(\omega_i) = \frac{1}{2} [F^{(n)}(\omega_i - 0) + F^{(n)}(\omega_i + 0)] \quad (7.39)$$

Since the integral was evaluated, which was the equaling quantity for both the Gaussian quadrature ansatz in equation (7.5) and the discrete spectrum in equation (7.8), the

distribution function obtained from the discrete pseudo-spectrum is normalized correctly. This distribution function is then numerically differentiated via

$$f^{(n)}(\omega) = \begin{cases} \frac{1}{2} \frac{f_1}{\omega_1} & \omega < \omega_1 \\ \frac{1}{2} \frac{f_{i+1} + f_i}{\omega_{i+1} - \omega_i} & \omega_i < \omega < \omega_{i+1} \\ 0 & \omega_n < \omega \end{cases} \quad (7.40)$$

to give $r - 1$ non-zero points of the desired density function $f(\omega)$, which are subsequently interpolated. In the routine of Averbukh, a monotonicity-preserving piecewise cubic Hermite spline interpolation is used for this purpose. Afterwards, the interpolated density function is evaluated for the energy of interest, which is the resonance energy E_r in case of the autoionization processes.

7.3.4. Quality and Stability of the Results

The abscissae of the polynomials constructed from different orders of moments alternate as is schematically shown in Figure 7.3, where each colour of points corresponds to one order. Therefore, in an ideal world, where all these points exactly lie on the desired density function, the combination of all abscissae and weights for the interpolation is beneficial.

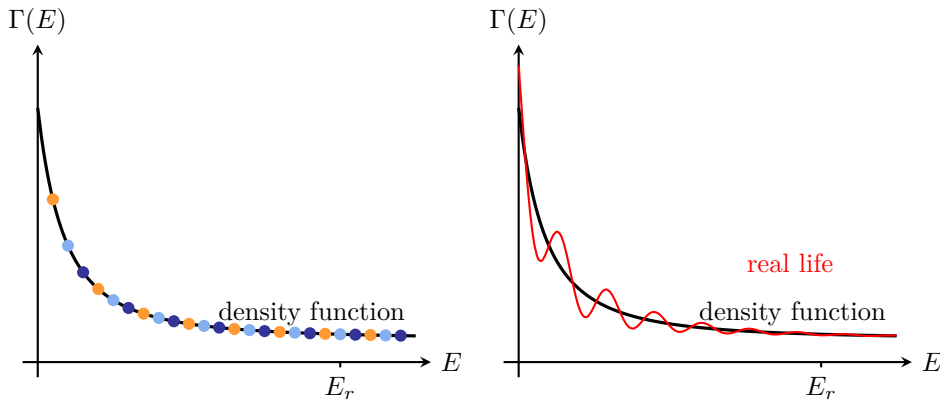


Figure 7.3.: Schematic illustration of the interpolation after the Stieltjes calculations to yield the density function $\Gamma(E)$, which is to be evaluated at the resonance energy E_r . Suppose the black curve to be the exact result. Then (left panel), for each order of Stieltjes calculation the points lie on this curve, where points from different orders (different colours of the points) intersect each other. The interpolation gives the exact result. In reality (right panel) the interpolations (even of one order of Stieltjes) are likely to show oscillations due to non-orthogonalities of Chebyshev polynomials in the higher orders and inaccurate descriptions due to a large gap between the lower and upper bounds for low orders.

As can be seen from the Chebyshev inequalities in equation 7.38, the higher the highest power of the polynomials and hence the larger the degrees of freedom, the closer the

lower and upper bounds get to the exact result.

Unfortunately, the moment problem is ill-conditioned and by introducing the polynomials, the moment problem as such get well-conditioned but instead the construction of the polynomials from the pseudo-spectrum is ill-conditioned. As can be seen from the Chebyshev inequalities, one would like to go to as high orders as possible in order to get more accurate results. But in the construction of the recurrence coefficients 7.24, two very large numbers are subtracted from each other. This is known to be numerically unstable. And the higher the order of the moment, the bigger are these numbers and hence the introduced error. Therefore the number of moments to be successfully employed for the approximation of the density function is limited by the quality of the orthogonality of the corresponding set of constructed polynomials. In the final density function non-orthogonalities as well as errors from inaccurate descriptions of lower orders can be detected by the presence of oscillations as shown in Figure 7.3 in the right panel. In the case of the density function being well behaved in the area of the resonance energy E_r , the description might still be feasible. In case of strong oscillations, the validity of the results is highly questionable. The interpolation can be smoothed by taking only stable orders of stieltjes into account or, in other words, by reducing the threshold of allowed non-orthogonality.

Another error is introduced by treating effects such as channel openings, which are characterized by discontinuities, with Gaussian quadrature which is valid for smooth density functions only.

8. Algebraic Diagrammatic Construction (ADC)

The Algebraic Diagrammatic Construction is a Green's function approach, which is a method for the calculation of ionization energies and electron affinities. Its advantage is the ability to determine the desired ionization energies without explicit calculation of the initial and final states, but instead obtaining their energy differences directly. Moreover, this approach is size-consistent and is hence suitable for the description of larger systems. [94]

Originally, the Green's function was formulated in the Dyson ansatz and determined using perturbation theory. This way both the ionization and the electron affinity part had to be included in the description. In the non-Dyson scheme those two are separable and hence, the dimension of the problem is reduced when one is interested in either the $N + 1$ (electron affinity) or the $N - 1$ (ionization energy) part [95].

$$G_{pq}(\omega) = G_{pq}^+(\omega) + G_{pq}^-(\omega) \quad (8.1)$$

The ionization part $\mathbf{G}^-(\omega)$ is a function of the energy ω and is transposed to give $\tilde{G}_{pq}^-(\omega) = G_{qp}^-(\omega)$. From this, the compact and orthogonal matrix form can be deduced

$$\tilde{\mathbf{G}}^-(\omega) = \mathbf{x}^\dagger (\omega \mathbf{1} - \mathbf{\Omega})^{-1} \mathbf{x} \quad (8.2)$$

where \mathbf{x} are the spectroscopic amplitudes and $\mathbf{\Omega}$ is the diagonal matrix of energy eigenvalues. This diagonal representation was reformulated using Goldstone diagrams into the non-diagonal expression

$$\tilde{\mathbf{G}}(\omega) = \mathbf{f}^\dagger (\omega \mathbf{1} - \mathbf{M})^{-1} \mathbf{f} \quad (8.3)$$

where \mathbf{M} denotes the ADC matrix and \mathbf{f} denotes the effective transition moments. Later it was found that this transformation could alternatively be derived by inserting a set of so-called *intermediate states* [96]. These are formally constructed from Correlated Excited State (CES), which are constructed using the same kind of excitation operators as in an CI expansion. In contrast to the CI approach, the CES are constructed from these operators acting on the exact and therefore correlated groundstate rather than the Hartree Fock ground state. These CES are then grouped into excitation classes and these classes are orthogonalized with respect to each other. Afterwards, the states within

each class are orthogonalized [94].

Equation (8.3) can be solved by considering the eigenvalue problem

$$\mathbf{M}\mathbf{Y} = \mathbf{Y}\mathbf{\Omega} \quad \text{with} \quad \mathbf{Y}^\dagger\mathbf{Y} = \mathbf{1} \quad (8.4)$$

The spectroscopic amplitudes \mathbf{x} can then be obtained from the effective transition moments \mathbf{f} as

$$\mathbf{x} = \mathbf{Y}^\dagger\mathbf{f} \quad (8.5)$$

To this point, the approach is exact. For the actual construction of the ADC matrix \mathbf{M} and the effective transitions moments \mathbf{f} , \mathbf{M} and \mathbf{f} are expanded into different orders of perturbations based on the Møller-Plesset partitioned Hamiltonian.

$$\mathbf{M} = \mathbf{M}^{(0)} + \mathbf{M}^{(1)} + \mathbf{M}^{(2)} + \dots \quad (8.6)$$

$$\mathbf{f} = \mathbf{f}^{(0)} + \mathbf{f}^{(1)} + \mathbf{f}^{(2)} + \dots \quad (8.7)$$

From this, different orders of perturbation theory of the Hamiltonian can be constructed successively. Hereby, the truncation after the n -th order leads to ADC(n). The contributions to the different classes for different orders of ADC are shown in Figure 8.1 [97].

	1h	2h1p
1h	0,1,2,2,3	-, -,1,1,2
2h1p	-, -,1,1,2	-, -,0,1,1

Figure 8.1.: Schematic illustration of an ADC(n) matrix for different orders of perturbation for $n = 0, 1, 2, 2x, 3$. In the illustration, the respective highest order contribution is shown for the different blocks. Hence, ADC(2x) is an extended ADC(2) including first order contributions to the satellite block.

The matrix elements of ADC(2x) are explicitly given by

- $1h/1h$ ($1h$ block):

$$M_{kk'}^{(0)} = \varepsilon_k \delta_{kk'} \quad (8.8)$$

$$M_{kk'}^{(1)} = 0 \quad (8.9)$$

$$M_{kk'}^{(2)} = -\frac{1}{2} \sum_{abl} V_{ab[kl]} V_{k'l[ab]} \frac{\varepsilon_a + \varepsilon_b - \varepsilon_l - \frac{1}{2}\varepsilon_k - \frac{1}{2}\varepsilon_{k'}}{(\varepsilon_a + \varepsilon_b - \varepsilon_k - \varepsilon_l)(\varepsilon_a + \varepsilon_b - \varepsilon_{k'} - \varepsilon_l)} \quad (8.10)$$

- $1h/2h1p$ (coupling block):

$$M_{j,akl}^{(1)} = V_{kl[aj]} \quad (8.11)$$

- $2h1p/2h1p$ (satellite block):

$$M_{akl,a'k'l'}^{(0)} = (-\varepsilon_a + \varepsilon_k + \varepsilon_l) \delta_{aa'} \delta_{kk'} \delta_{ll'} \quad (8.12)$$

$$M_{akl,a'k'l'}^{(1)} = -\delta_{aa'} V_{k'l'[kl]} + \delta_{kk'} V_{al'[a'l]} + \delta_{ll'} V_{ak'[a'k]} - (k \leftrightarrow l) \quad (8.13)$$

Here, ε_r denotes the r -th Hartree Fock orbital energy. The occupied states are labelled by i, j, k, \dots and the unoccupied states are labelled by a, b, c, \dots . The two-electron integrals for any combination of occupied and unoccupied orbitals labelled by p, q, r, s read as

$$V_{pqrs} = \langle \varphi_p(1) \varphi_q(2) | V(1, 2) | \varphi_r(1) \varphi_s(2) \rangle \quad (8.14)$$

and $V_{pq[rs]} = V_{pqrs} - V_{pqsr}$.

8.1. FanoADC

In the FanoADC, the discrete ADC Hamiltonian is used for the construction of the pseudo-spectrum of the decay width Γ . Due to multiple possible final states, the procedure of Feshbach using projection operators for the partitioning of the Hamiltonian into an initial and a final state subspace is employed. The processes of interest have a singly ionized initial state and a doubly ionized final state with an additional electron in the continuum. Therefore, the final state configurations are chosen from the class of $2h1p$ states, where the $2h$ part is assumed to describe the doubly ionized final state and the particle resembles the continuum electron. The initial state can be described as a $1h$ state.

For the partitioning, two different methods are known in the literature: the selection by $2h$ contributions, which correspond to final states of the process, or by energy [14]. The first is easy to implement while the second automatically enables the correct calculation of decay widths in systems with lower than spherical symmetry, when the final state vacancies are distributed over two symmetry equivalent atoms.

8.1.1. Partitioning by Population

In the partitioning, all $2h1p$ configurations characterized by a $2h$ part corresponding to one of the final state configurations are chosen to be part of the final state subspace. All $1h$ configurations and those $2h1p$ configurations not corresponding to a possible final state configuration are used for the description of the initial state. This leads to a resorted ADC matrix as shown in Figure 8.2, where the subspace of the initial state is denoted by \mathbf{M} , the final state subspace by \mathbf{N} , and the interaction coupling those two subsets is named \mathbf{W} .

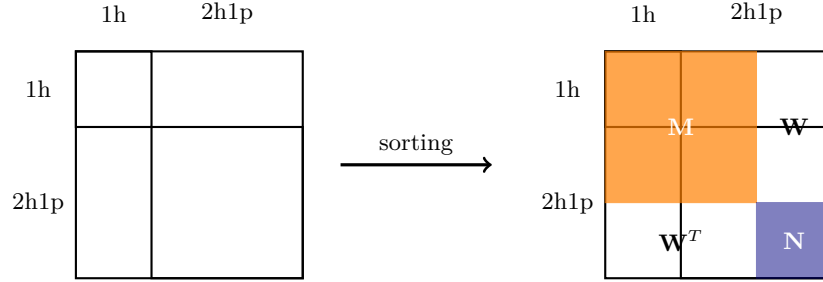


Figure 8.2.: Schematic illustration of the partitioning of the ADC matrix according to the projection operators of the initial and final states.

The separate diagonalization of the initial and final state subspaces \mathbf{M} and \mathbf{N} yields the corresponding eigenvectors and eigenvalues on the diagonal of the matrices $\mathbf{\Lambda}$ and $\mathbf{\Omega}$

$$\mathbf{\Lambda} = \mathbf{I}^T \mathbf{M} \mathbf{I} \quad (8.15)$$

$$\mathbf{\Omega} = \mathbf{F}^T \mathbf{N} \mathbf{F} \quad (8.16)$$

and the Hamiltonian is represented in the basis of their eigenstates as illustrated in Figure 8.3 with $\mathbf{V} = \mathbf{I}^T \mathbf{W} \mathbf{F}$ being the interaction part in this new basis.

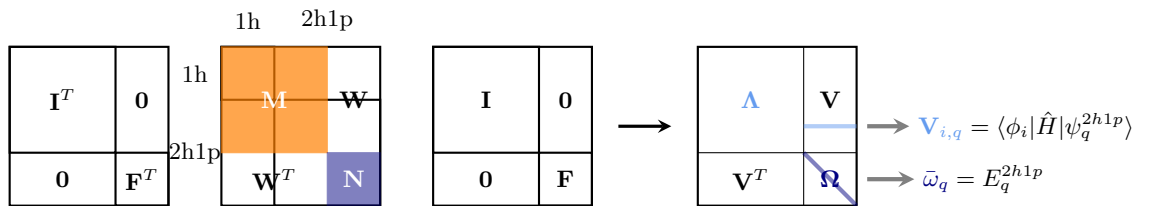


Figure 8.3.: Schematic illustration of the basis transformation of the full ADC matrix into the basis of initial and final states. The pseudo-spectrum is given by the manifold of $\bar{\omega}_q$ and $V_{i,q} = \langle \phi_i | \hat{H} | \psi_q^{2h1p} \rangle$.

The desired pseudo-spectrum which enters the Stieltjes calculation is then for a specific

initial state choice i given by the manifold of final state energies $\bar{\omega}_q$ and the corresponding interaction part in the basis of the initial and final eigenstates $V_{i,q} = \langle \phi_i | \hat{H} | \psi_q^{2h1p} \rangle$.

8.1.2. Partitioning by Energy

A partitioning by energy requires first a calculation of the double ionization spectrum with the same conditions as regarded for the later decay width calculation. From the results, the number of open channel contributions for each symmetry are determined manually. Then, the satellite block of the ADC matrix is constructed such, that for each particle the corresponding small $2h1p$ block is to be found on the diagonal. These blocks are diagonalized separately. It is assumed that the resulting order of the $2h$ configurations is the same for all particles and equals the one from the former double ionization potential calculation. These *precorrelated* final states are then partitioned with respect to energy into the initial or the final state subspace. In practice, rather the coefficients which allow for the construction of the precorrelated final states from the uncorrelated matrix elements are stored. Finally the ADC matrix is constructed using the precorrelated final states.

From this point on, the calculation is the same as in the case of the partitioning based on population.

8.1.3. Partial Decay Widths

Approximating the complete set of continuum functions by another set of complete basis functions is verified for the determination of the total decay width only. However, an *ad hoc* procedure for the determination of partial decay widths has been postulated [98], in which a subset of the determined coupling elements $V_{i,q} = \langle \phi_i | \hat{H} | \psi_q^{2h1p} \rangle$ and the corresponding $\bar{\omega}_q$ is related to a specific channel β .

$$\gamma_{i,q}^\beta = 2\pi \left| \langle \phi_i | \hat{H} | \hat{P}_\beta \psi_q^{2h1p} \rangle \right|^2 \quad (8.17)$$

Here, \hat{P}_β denotes the projection operator choosing the channel contributions. The pseudo-spectra of the channels are independently treated by the Stieltjes routine and primal partial decay widths $\tilde{\Gamma}_\beta$ are obtained. Afterwards, the primal partial decay widths are renormalized with respect to the total decay width Γ

$$\Gamma_\beta = \frac{\tilde{\Gamma}_\beta}{\sum_\beta \tilde{\Gamma}_\beta} \Gamma \quad (8.18)$$

The quality of the partial decay widths depends on the mixing between the different channels. For partitioning by population such mixing is completely neglected, whereas it is treated in the partitioning by energy in an approximative way. Therefore, the

calculated partial decay widths require a critical analysis, especially when orbitals from lower than the outer valence are included in the final state subspace.

8.2. How to Obtain Reliable Results

8.2.1. Choice of Basis Set and Active Space

A good basis set for a decay width calculation has to both, describe the initial state of the process reasonably well and to mimic the outgoing secondary electron. The first requires a correlated basis set, since the initial state is ionized in the inner- or subvalence region. The latter requires the basis set to be:

1. of high density
2. including diffuse functions
3. uncontracted

Since in the Stieltjes approach the Chebyshev polynomials are constructed from the pseudo-spectrum, the denser this pseudo-spectrum is, the better can the description of the decay width be expected to be. A Stieltjes calculation starting from a pseudo-spectrum with less than four couplings with a significant contribution in the energy range of interest can not be expected to give reasonable results.

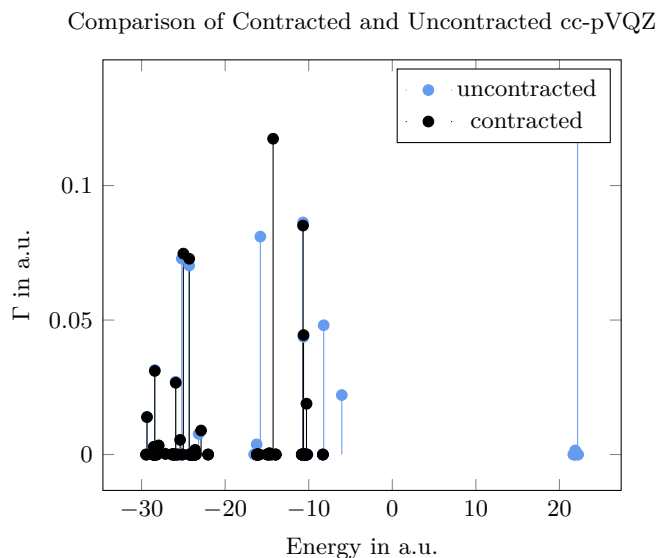


Figure 8.4.: Shifted pseudo-spectra with $E_r = 0$ for the Auger process following an ionization of the neon 1s. Comparison of contracted and uncontracted cc-pVQZ.

A contraction of the basis set reduces its flexibility and optimizes the description of the electron cloud close to the nuclei. Since in the decay width calculation one aims to mimic the delocalized outgoing electron by \mathcal{L}^2 functions, a contraction leads to a very narrow pseudo-spectrum in energy regions which are of no interest and is therefore counterproductive.

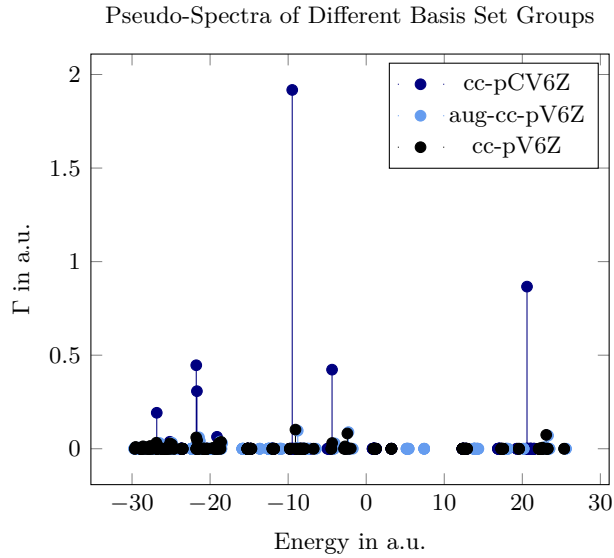


Figure 8.5.: Shifted pseudo-spectra for different basis sets with $E_r = 0$ for the Auger process following an ionization of the neon 1s. Different basis set classes.

An example is given in Figure 8.5 for a cc-pVQZ basis set for the Auger following an ionization of the Ne1s. It can easily be seen that the pseudo-spectrum of the uncontracted basis set spans a wider energy range than the corresponding pseudo-spectrum of the calculation with the contracted basis set. The pseudo-spectrum obtained using the contracted basis set would not even include the resonance energy. However, the basis set is small and the density close to the resonance energy $E_R = 0$ is sparse and hence will not give a good description of the outgoing electron.

In order to mimic the outgoing electron with \mathcal{L}^2 functions, the exponents of the basis set have to include the energy range of the expected kinetic energy of the electron. Preferably, the basis set is very dense in this energy region. An example of the pseudo-spectra obtained from calculations with three different basis sets is shown in Figure 8.5. The pseudo-spectrum of the smallest basis set cc-pV6Z is reasonably dense and the one for the aug-cc-pV6Z is comparably dense but shows points at shifted energies. However, compared to the pseudo-spectrum obtained with the cc-pCV6Z basis set including the correlations between the neon core and the neon valence orbitals the couplings are rather small. However, close to the resonance energy the pseudo-spectrum is not very dense. Additionally, and especially for processes close to threshold with slow secondary elec-

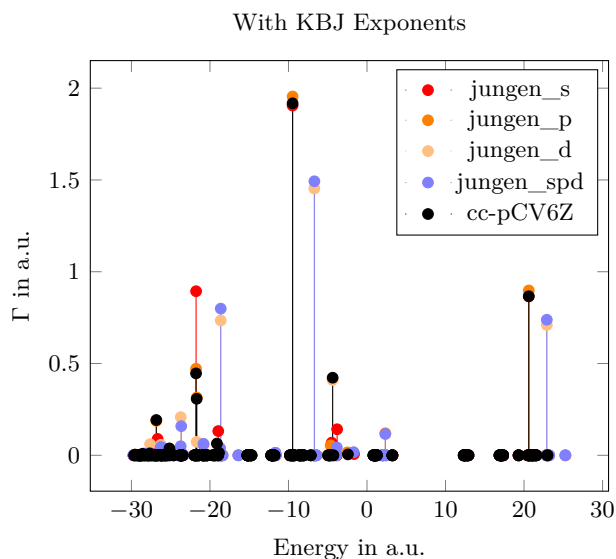


Figure 8.6.: Pseudo-spectra for the Auger process following the ionization out of the Ne1s for the aug-cc-pV6Z basis set with additional Kaufmann-Baumeister-Jungen (KBJ) basis functions of the s, p and d type.

trons, the basis set should contain many diffuse and hence delocalized functions. They allow to cover the spatial range of the interaction region and hence states with the electron being disrupted from the nuclei. For this purpose additional basis functions of the KBJ[99] type are used at the atomic positions or in case of molecules on ghost atoms positioned between the atoms. Their effect on the density of the pseudo-spectrum is illustrated in Figure 8.6. There, the contributions of the different angular momentum functions are shown. Each class adds some significant couplings to the pseudo-spectrum and hence, in combination, a reasonably dense pseudo-spectrum is created.

Additionally, the active space needs to include the orbitals of the initial state shell as well as a reasonably large number of positive energy solutions. These positive energy solutions describe the outgoing electron and hence the kinetic energy of the electron has to be included. Furthermore, since the Stieltjes procedure is based on an interpolation, energies higher than the kinetic energy of the outgoing electron are as well needed. From experience, the positive energy of the active space should at least cover the kinetic energy of the outgoing electron plus 10 a.u..

8.2.2. Quality Check Using the Decay Width Profile

Errors and instabilities of the FanoADC-Stieltjes calculation can be observed in the energy dependence of the calculated decay width $\Gamma(E)$. As already shown in Figure 7.3, the optimum interpolation result is a smooth, monotonically decreasing function. The

decay width for the given resonance energy $\Gamma(E_r)$ can in this case easily be evaluated. The error of the calculated decay width is estimated by the decay widths close to the resonance energy. There is no rigorous definition of how exactly to choose this energy range in the literature. In general, it is estimated by the quality of the initial state description in the initial state subspace compared to the one of the full Hamiltonian and the manual inspection of the density of points obtained from the FanoADC-Stieltjes calculation. If the obtained density function has a low curvature at the resonance energy, the error of the decay width is usually very small, while for resonance energies, where the decay width has a high curvature, the error can be of the same order as the obtained decay width.

In addition to numerical instabilities introduced by the Stieltjes procedure discussed in section 7.3.4, two further characteristic patterns might be observed in a calculated decay width: channel openings and interactions of the initial state with Rydberg states.

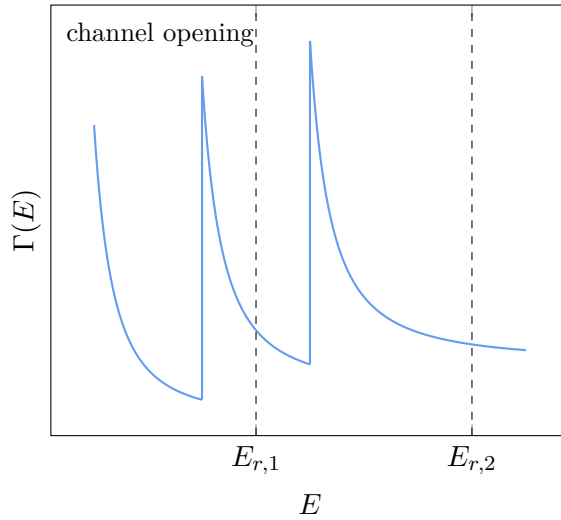


Figure 8.7.: Schematic illustration of a decay width profile with three channels. At the resonant energy $E_{r,1}$, the first two channels are open and at the resonance energy $E_{r,2}$ all three channels are open.

In case of channel openings, the decay width is decreasing at low energies, but at a certain energy another channel opens and the decay width of both are added as shown in Figure 8.7. In case of the resonance energy being higher than all the channel opening energies as for $E_{r,2}$, the selection of the final state subspace can be expected to be correct and the initial and final state description of the partitioned Hamiltonian to be reasonable.

In case of the resonance energy being lower than the highest channel opening energy, like for $E_{r,1}$, a closed channel is treated as a final state. If such a result is obtained, one should carefully check the selection of the final state configurations. However, it is still possible that the partitioning of the Hamiltonian yields such descriptions of the initial

and final states that the channel opening and closing is not reproduced in the decay width. In these cases the obtained results need to be analyzed carefully and might not be meaningful at all.

Rydberg states are bound states of the systems and hence do not contribute to the decay. However, an interaction of the initial state with those Rydberg states is possible and leads to a density function as shown in Figure 8.8.

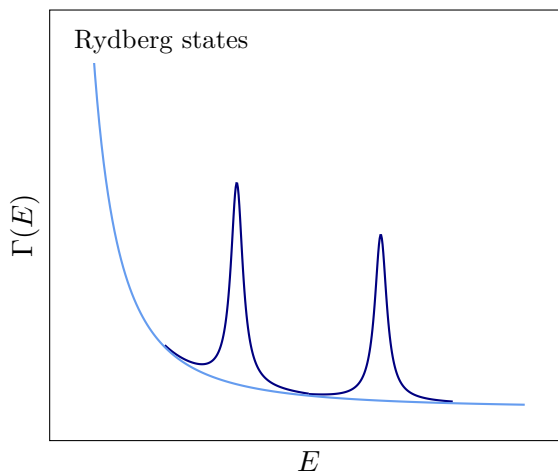


Figure 8.8.: Schematic illustration of a decay width profile with couplings of the initial state to Rydberg states.

Here, the density function is in principle a monotonically decreasing function but has additional peaks at certain energies. They can be distinguished from channel openings by observing the behaviour after the peak. In case of interactions with Rydberg states, the decay width is the same as if the interaction would not take place, while in case of a channel opening, the decay widths of the two channels are added to give a total decay width. If the resonance energy coincides with the position of a Rydberg interaction, the Rydberg interaction is not to be taken into account in the determination of the decay width.

In a real calculation, these two features are more diffuse than in the illustrations above in figures 8.7 and 8.8, because the Stieltjes procedure smoothes discontinuities as observed in the case of channel openings and sharp peaks as for the Rydberg states. In the Stieltjes procedure such density functions are more accurately described with higher orders of Stieltjes being based on higher order polynomials with more degrees of freedom. An observed phenomenon related to this is a splitting of the decay width described by either low or high orders of Stieltjes. In these cases, one has to decide based on the knowledge of all other parameters, which of these two curves might be more trustworthy.

Close to channel openings, the determination of the decay width is difficult, since the resonance energies are approximations and not exact. Therefore, the energy range spans a

wide distribution of different decay widths. Furthermore the broadened decay width being based on points obtained from the Stieltjes procedure might not cover the maximum of the peak and hence the theoretical maximum of the decay width.

Additionally, when this channel opening is the first opening channel, i.e. the resonance is close to threshold, the pseudo-spectrum might not cover the resonance energy. In this case a Stieltjes calculation would make no sense. However, it is possible to obtain points with the Stieltjes routine, which do not cover the resonance energy. This is mostly observed for low orders of Stieltjes. In these cases, the points can be interpolated to give an estimation of the decay width at higher energies, but it would have to be evaluated at lower energies from an extrapolated function.

Having obtained a reasonable pseudo-spectrum and employed the Stieltjes routine, the above discussions indicate that the decay width calculation using the FanoADC-Stieltjes method is not a black box method. Summarizing, they lead to the following procedure for the decay width evaluation:

1. Inspect the decay width profile and look for oscillations in the points of each order. All orders above the lowest order showing oscillations as illustrated in Figure 7.3 have to be neglected in the further procedure.
2. Are features connected to channel openings or couplings to Rydberg states observable in the resonance energy region? In this case, the higher order polynomials are normally better to describe the curve and hence they should be favoured for the interpolation. Otherwise the lower orders normally give reasonable approximations.
3. When two or more lines from different orders are observed without channel openings or coupling to Rydberg states in the decay width profile, the decay width can be expected to be either represented by one or the other. In this case, the lower order result should be preferred, because numerical instabilities should be less pronounced.
4. Interpolate the points obtained from the Stieltjes calculation including those orders which seem to be reasonable.

Part III.

Results

9. Auger Decay of Noble Gas Atoms

The decay widths of noble gas atoms have been thoroughly studied in the literature. Therefore, the main aim of this chapter is to prove the implementation of the FanoADC-Stieltjes in the Dirac program [15] to work reliably and reproduce some of these results. Both, the neon atom and the xenon atom are investigated. The neon atom is chosen because reference data is available obtained from a non-relativistic implementation of the same method. Then, the xenon atom is studied, due to the importance of relativistic effects in its description, which is the focus of this thesis. Finally, the results will be used to verify that the program is able to predict the decay widths of autoionization processes. In contrast to other comparable relativistic programs [100, 101], the FanoADC-Stieltjes approach does not rely on spherical symmetry and is therefore capable of describing the decay widths of ICD processes.

9.1. Neon

The $\text{Ne}1s^{-1}$ vacancy with a Single Ionization Potential (SIP) of 870 eV [102] is the initial state of the Auger decay. The Double Ionization Potential (DIP) of the final states are shown in Table 9.1. Hence, the kinetic energy of the emitted electron lies between 748 eV and 808 eV.

Table 9.1.: Experimental ionization energies of the doubly ionized final states [103].

Final states	SIP [eV]	
$2p^{-2}$	3P_0	62.52
	3P_1	62.60
	3P_2	62.64
	1D	65.73
	1S	69.44
$2s^{-1}2p^{-1}$	3P_0	87.85
	3P_1	87.92
	3P_2	87.96
	1P	98.41
$2s^{-2}$	1S	121.89

9.1.1. Computational Details

The decay width calculations were performed using the FanoADC-Stieltjes approach implemented in the program package Dirac [15]. A cc-pCV6Z basis set was employed with additional s , p and d functions (5,5,6) of the KBJ type [99]. The active space covered an energy range of $-33.0 - 56.0$ a.u., and included 376 spinors in both, the relativistic and the non-relativistic calculation.

9.1.2. Decay Widths

The calculated decay widths are outlined and compared to experimental results in Table 9.2. Hereby, the contributions to the total decay widths are given for the three groups $2p^{-2}$, $2s^{-1}2p^{-1}$ and $2s^{-2}$ as well as for the different terms explicitly, as far as numbers are available.

Table 9.2.: Auger decay widths and contributions of the different channels to the total decay width in % for an initial vacancy in the NeIs. The decay widths are given in meV.

Final states	This work		Kolorenč		Kelly		Yarzhemsky		exp.			
	rel.	nrel.	Ref.[104]	Ref.[105]	Ref.[106]	Refs. [107], [108]						
$2p^{-2}$	3P	(0.0)	0.0	0.0	0.0	–						
	1D	53.9	81.6	50.5	60.0	61.2	70.8	58.2	68.4	60.9	70.4	
	1S		(81.6)	9.5		9.6		10.2		9.5		
$2s^{-1}2p^{-1}$	3P	38.0	(1.1)	7.8	10.6	30.1	6.1	23.1	9.3	26.1	6.3	23.5
	1P		(6.8)		19.5		17.0		16.8		17.2	
$2s^{-2}$	1S	8.1	10.4	10.4	9.9	9.9	6.1	6.1	5.5	5.5	6.1	6.1
Γ		344	268		251		219		242		220 ± 30	

The results of this work were obtained using the FanoADC-Stieltjes method and the same basis set as in the work of Kolorenč *et al.* [104]. However, the latter non-relativistic description uses an energy based partitioning. Focussing on the total decay width, the non-relativistic decay width obtained in this thesis is of the same order of magnitude as both the experimental result and the other theoretical predictions, while the relativistic result overestimates the experimental decay width by 56%. However, this discrepancy is still inside the error margins of the FanoADC-Stieltjes method.

The branching ratios obtained from the partial decay widths of the present results have the correct order of magnitude in the relativistic calculation, but deviate from the values found in the literature. In the non-relativistic case the $2s^{-1}2p^{-1}$ channel's contribution is substantially underestimated. It is known from the literature [51] that taking into account the coupling of the 2s and the 2p orbitals is crucial in order to obtain reliable values for the decay width. Since this coupling is neglected in the current projection scheme, these branching ratios cannot be reproduced. The partial decay width of the

$2p^{-2} \ ^3P$ channel is forbidden by symmetry. In an Auger decay the angular momentum and the spin need to be conserved in the Russel-Saunders coupling scheme, i.e. $\Delta L = \Delta S = 0$. The initial state is characterized by $L_i = 0$, $S_i = \frac{1}{2}$ and has g symmetry. The $2p^{-2} \ ^3P$ final state without the electron is characterized by $L_f = 1$ and $S_f = 1$ and is a g state. In order to conserve the momenta, the outgoing electron would have to be characterized by $L_e = 1$ and $S_e = \frac{1}{2}$. However, this outgoing electron would have ungerade symmetry. Since the coupling operator is the gerade Coulomb operator, the corresponding matrix elements are zero. In order to investigate the correct prediction of this feature, the $\alpha\alpha$ and the $\beta\beta$ final states of the $2p^{-2}$ and $2s^{-1}2p^{-1}$ final state channel groups were treated separately as distinct channels. However, the third triplett wavefunction would have to be constructed from a linear combination, which is not possible in the current implementation of the FanoADC based on partitioning by population of $2h$ configurations. The numbers affected by this choice of channels are shown in brackets in Table 9.2. The chosen triplett final states of the $2p^{-2} \ ^3P$ yield a decay width of zero and therefore predicts this property correctly up to the accuracy, which is accessible.

9.2. Xenon

From single and double ionization spectra and Auger spectroscopy it is known that vacancies from the Xe4d and lower are energetically allowed to decay via Auger processes [109]. In the following, I will focus on two energetic initial state regions, namely the 4p and the 4d region.

9.2.1. Computational Details

All calculations in this chapter, including the decay width calculations, were performed using the Dyllal cv4z basis set [110] with additional five s, p and d and three diffuse basis functions of the KBJ type [99]. The active space was chosen to include the fourth shell completely and the positive energies to be limited by 40.0 a.u..

9.2.2. Open Channels

The different open channels are to be determined by comparison of the single and double ionization spectra shown in Figure 9.1. These spectra have been calculated using the DC-ADC(2x) method implemented in Dirac [111, 112, 15].

From the calculated single and double ionization spectra the open channels for different singly ionized initial states can be determined for doubly ionized final states as shown in Table 9.3. These results are the basis for the choice of the final state subspace in the decay width calculations.

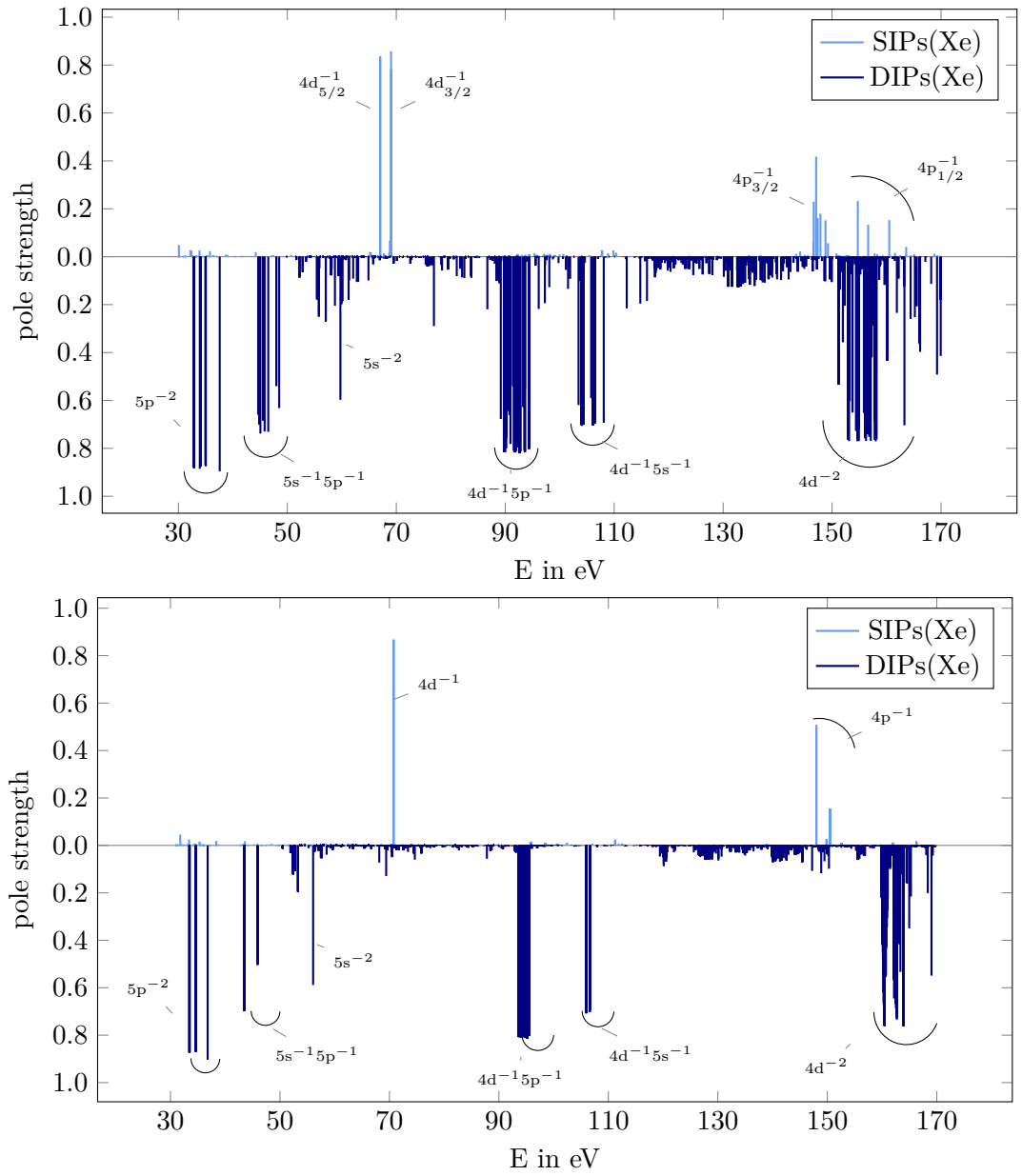


Figure 9.1.: Comparison of calculated single and double ionization spectra for the determination of open channels in of the later decay width calculation. Upper panel: relativistic description, lower panel: non-relativistic description.

Table 9.3.: Channels of the Auger processes for different singly ionized initial states and doubly ionized final states of the xenon atom. Open channels are marked by "x", while closed channels are marked by "-".

	$4d^{-2}$	$4d^{-1}5s^{-1}$	$4d^{-1}5p^{-1}$	$5s^{-2}$	$5s^{-1}5p^{-1}$	$5p^{-2}$
$4d_{5/2}^{-1}$	–	–	–	x	x	x
$4d_{3/2}^{-1}$	–	–	–	x	x	x
$4p_{3/2}^{-1}$	–	x	x	x	x	x
$4p_{1/2}^{-1}$	x	x	x	x	x	x
$4d_{nrel}^{-1}$	–	–	–	x	x	x

9.2.3. Auger Decay from the Xe4d Region

The Auger process from the Xe4d subshell has been experimentally measured to high accuracy [113] and is used as a calibration standard. The corresponding decay widths have among others been measured by Ausmees *et al.* [114, 115]. Theoretically they have been investigated by Mäntykenttä [116] using Multi-Configurational Dirac-Fock (MCDF) [117]. The experimental and theoretical findings are compared to the results of the present calculations using the relativistic FanoADC-Stieltjes method presented in Table 9.4.

From the single ionization spectrum of the full Hamiltonian, initial state energies of 67.03 eV and 69.04 eV were obtained. They deviate from the experimental values shown in Table 9.4 by about 0.5 eV and are very close to the values calculated with MCDF [117]. The spin-orbit splitting of $\Delta_{SO,calc} = 2.01$ eV is very close to the experimental value of $\Delta_{SO,exp} = 1.99$ eV. Even though the initial state energies obtained from the initial state subspace deviate from the experimental numbers, the spin-orbit splitting is well predicted to be $\Delta_{SO,part} = 2.04$ eV.

According to Table 9.3 the open channels are characterized by the two hole configurations $5s^{-2}$, $5s^{-1}5p^{-1}$ and $5p^{-1}5p^{-1}$, which in the following are utilized for the construction of the final state subspace.

In order to obtain the decay widths at the resonance energies, higher orders of Stieltjes were predominantly used for the interpolation to yield the approximate decay width function. This choice became necessary because in the partitioned Hamiltonian the $5s^{-2}$ channel opens very close to threshold and hence the resonance energy at which the decay width function is evaluated is very steep. Therefore, for a reasonable description the higher orders polynomials were needed. In such cases the error $\Delta(\Gamma) = 0.1$ eV of the evaluated decay width is rather large compared to the decay widths themselves.

The total relativistic decay widths obtained with the FanoADC-Stieltjes method agree with both the experimental results and the MCDF results within the error margins. Even

Table 9.4.: Auger decay widths of the $Xe4d_{5/2}$ and $Xe4d_{3/2}$ and the non-relativistic $4d$ initial states with the doubly ionized final states compared to experimental values [114]. All widths are given in eV. The partial widths are renormalized to the total width.

	energy [eV]	pole str.	$5s^{-2}$	$5s^{-1}5p^{-1}$	$5p^{-1}5p^{-1}$	total
$4d_{5/2,\pm 5/2}$	66.87	0.879	$2.34 \cdot 10^{-2}$	$5.40 \cdot 10^{-2}$	$8.45 \cdot 10^{-2}$	0.1619 ± 0.1
$4d_{5/2,\pm 3/2}$	66.87	0.879	$2.30 \cdot 10^{-2}$	$5.34 \cdot 10^{-2}$	$8.57 \cdot 10^{-2}$	0.1621 ± 0.1
$4d_{3/2,\pm 3/2}$	68.91	0.879	$1.73 \cdot 10^{-2}$	$3.35 \cdot 10^{-2}$	$8.15 \cdot 10^{-2}$	0.1323 ± 0.1
$4d_{3/2,\pm 1/2}$	68.91	0.879	$1.62 \cdot 10^{-2}$	$3.21 \cdot 10^{-2}$	$8.21 \cdot 10^{-2}$	0.1304 ± 0.1
$4d_{spinfree}$	67.67	0.879	$2.29 \cdot 10^{-2}$	$5.17 \cdot 10^{-2}$	$9.31 \cdot 10^{-2}$	0.1678 ± 0.1
$4d_{nrel}$	70.68	0.878	$1.15 \cdot 10^{-2}$	$1.78 \cdot 10^{-2}$	$5.72 \cdot 10^{-2}$	0.0898 ± 0.1
exp. $4d_{5/2}$	67.55 [118]					$0.110 - 0.130$ [114]
exp. $4d_{3/2}$	69.54 [118]					$0.105 - 0.116$ [114]
calc. $4d_{5/2}$	67.55[116]					0.160 [116]
calc. $4d_{3/2}$	69.54[116]					0.143 [116]

though the error margins are large, the deviation of the results from the experimental findings are less than 52 meV and hence much smaller than the error margin. Comparing the results of this thesis to the results of the MCDF calculations the deviations are much smaller. For the $4d_{5/2}$ the results are very close with a difference of 2 meV and for the $4d_{3/2}$ with a difference of 10 meV.

The results of the non-relativistic calculations are smaller than the results of the relativistic calculations by a factor of two, while the spinfree calculation yields a decay width of the same order as the relativistic calculation. This means that the higher decay width is not a consequence of spin-orbit coupling but rather of scalar-relativistic effects. Non-relativistically, the radial distance expectation value of the electron cloud distribution from the nucleus of the $5s$ and $5p$ is larger than the one for the $4d$ orbital. Due to the scalar-relativistic effects, the $5s$ and $5p$ orbitals are contracted while the $4d$ orbital is decontracted. Therefore, the overlap between those orbitals is larger as is their possible interaction. Hence, the decay width including both kinds of vacancies is increased.

As shown in Figure 9.1, some of the final state groups in reality consist of different terms which have been thoroughly analyzed by Pernpointner *et al.* [119]. From this analysis it can be seen that the terms are combinations of different $2h$ configurations. Therefore a definition of the final state by $2h$ configurations is unfortunately insufficient for a more detailed study of partial decay widths. However, the Auger process from the $Xe4d$ region with an improved method would be worth investigating, since decay widths and branching ratios have been measured in experiment [115].

9.2.4. Auger Decay from the Xe4p Region

The $Xe4p$ is expected to be split into $4p_{1/2}$ and $4p_{3/2}$ states with a spin-orbit splitting of few eV. However, in experimental single ionization spectra only one peak in the ex-

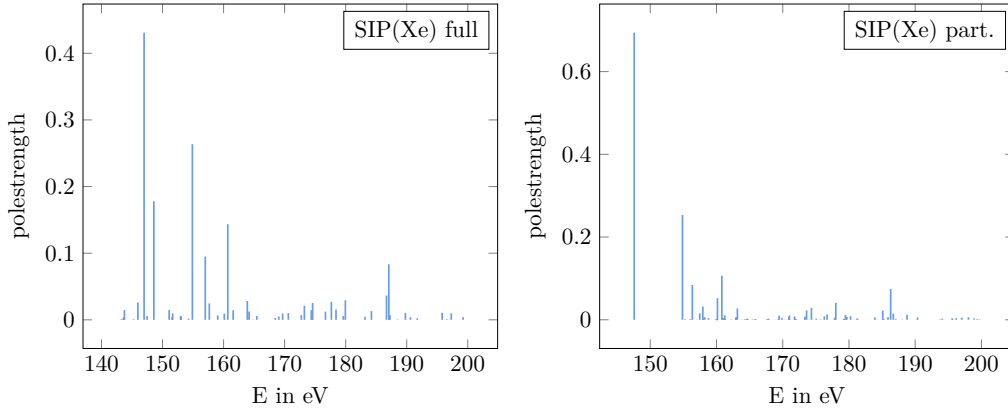


Figure 9.2.: Left panel: Single ionization spectrum of the xenon atom in the 4p region calculated with DC-ADC(2x). Right panel: Eigenvalues of the initial state subspace of the xenon atom in the 4p region calculated with DC-FanoADC(2x).

pected $4p_{3/2}$ region is observed. Where one would expect a second peak from the $4p_{1/2}$, the spectrum shows a broad structure of lower intensity. This observation has been interpreted to originate from a very fast decay process, the Super-Coster-Kronig process, where both the vacancy filling and the Auger electron stem from the same shell as the initial vacancy. In this case, this process would have a $4d^{-2}$ final state. It is assumed to be much faster than the Auger process of the $4p_{3/2}$.

The decay widths of the Auger process with a $4p_{3/2}$ initial state have been thoroughly studied [120], leading to decay widths of 0.1 eV to 0.6 eV for different satellite states using MCDF. In the same publication it is stated, that the SCK decay is expected to have decay widths of about 10–100 eV. The latter is used as explanation for the non-observation in the Auger electron spectra.

The single ionization spectrum of the energetic region of interest between 140 eV and 170 eV is shown in the left panel of Figure 9.2 for the full Hamiltonian without any partitioning into initial and final state subspaces.

Below 150 eV fewer and higher peaks stem from the ionization of the $4p_{3/2}$. The main peaks are at 146.98 eV and 148.58 eV. At energies between 150 eV and 165 eV the broader distribution mainly originating from the $4p_{1/2}$ can be seen with the largest peaks at 154.89 eV, 157.00 eV and 160.69 eV. Both clearly show a breakdown of the one-particle picture.

However, due to the underlying method of partitioning the Hamiltonian into initial and final state subspaces, the configurations shown in the left panel of Figure 9.2 are not the initial states used in the FanoADC approach. All configurations characterized by $4d^{-1}5s^{-1}$, $4d^{-1}5p^{-1}$, $5s^{-2}$, $5s^{-1}5p^{-1}$ or $5p^{-1}5p^{-1}$ form the final state subspace. Therefore, the spectrum of the initial state subspace is the source for the description of the initial state vector instead. Its spectrum is shown in the right panel of Figure 9.2.

The partitioning causes a reduction of complexity of the initial state spectrum to a main state of the $4p_{3/2}$ at 147.57 eV and a reduced distribution for the $4p_{1/2}$ with highest peaks at 156.42 eV, 158.16 eV and 160.22 eV. This causes an error of the initial state description, which is normally neglected.

From the FanoADC and a following Stieltjes calculation points along $\Gamma(E)$ are determined for each calculated order of Stieltjes. Such decay width profiles are shown in Figures 9.3, and 9.4 for the $4p_{3/2}$ and $4p_{1/2}$, respectively. Their analysis is mandatory for the evaluation of the results' quality.

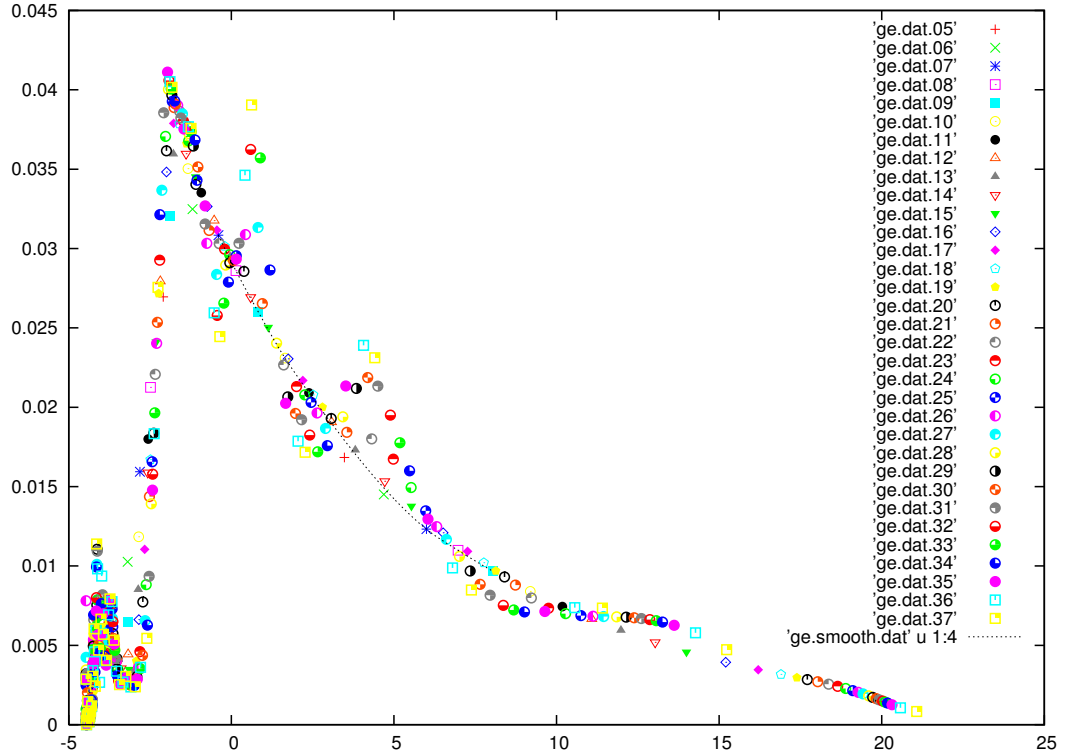


Figure 9.3.: Shifted Stieltjes profile of $\Gamma(E)$ obtained from the relativistic FanoADC calculation from a $4p_{3/2}$ initial state with both Γ and E given in atomic units. The resonance energy is $E_{res} = 0$ and the resulting points of the different orders of Stieltjes are plotted separately. The smooth curve shows two additional peaks related to interactions with Rydberg states as discussed in section 8.2.2.

In case of a $4p_{3/2}$ initial state, the decay width profile for Stieltjes orders between 5 and 37 shows a decay with a threshold at energies below $E_{ref} = 0$, which leads to a fairly smooth curve at the energy of interest. At higher energies of about 1.5 a.u. and 4.5 a.u. additional peaks are observed, which can be explained by interactions of the initial state description with Rydberg states. These do not contribute to the decay and hence a smoothing of the total curve neglecting them is necessary.

Table 9.5.: Auger decay widths of the Xe $4p_{3/2}$ initial states with different M_J values and different doubly ionized final states. All widths are given in eV.

	$4p_{3/2,\pm 3/2}$	$4p_{3/2,\pm 1/2}$
energy [eV]	147.57	147.57
pole strength	0.694	0.694
$4d^{-2}$	–	–
$4d^{-1}5s^{-1}$	$1.31 \cdot 10^{-1}$	$1.44 \cdot 10^{-1}$
$4d^{-1}5p^{-1}$	$6.36 \cdot 10^{-1}$	$6.29 \cdot 10^{-1}$
$5s^{-2}$	$6.27 \cdot 10^{-4}$	$6.29 \cdot 10^{-4}$
$5s^{-1}5p^{-1}$	$1.50 \cdot 10^{-2}$	$1.49 \cdot 10^{-2}$
$5p^{-1}5p^{-1}$	$3.21 \cdot 10^{-2}$	$2.90 \cdot 10^{-2}$
total	0.814	0.818

Table 9.6.: Total Auger decay widths of the Xe $4p_{3/2}$ obtained from experiment, MCDF and this work. All widths are given in eV.

	exp	calc ¹	calc ²	calc ³
energy [eV]	145.6	145.0	145.0	147.57
Γ [eV]	0.54	1.80	0.3116	0.814

¹ MCDF calculation excluding final ionic state configuration interaction [120].

² MCDF calculation including final ionic state configuration interaction [120].

³ This work.

The total and partial decay widths for the $4p_{3/2}$ initial state are shown in Table 9.5. The projection of the angular total angular momentum of the initial state does not influence the results, which can be deduced from the almost equal results for the $4p_{3/2,\pm 3/2}$ and $4p_{3/2,\pm 1/2}$ initial state. It can easily be seen that the Coster-Kronig processes characterized by the $4d^{-1}5s^{-1}$ and $4d^{-1}5p^{-1}$ final states dominate the decay.

The total decay widths are compared to experimental values and the results obtained using MCDF in Table 9.6. All decay widths are in the order of 1 eV. While the calculation including the final ionic state configuration interaction underestimates the experimental decay width by 0.23 eV, the calculation excluding the final ionic state configuration interaction overestimates the experimental value by 1.26 eV. The decay width obtained in this work overestimates the experimental decay width by 0.27 eV. The FanoADC-Stieltjes approach intrinsically contains configuration interaction inside the final state subspace. However, only those states characterized by certain $2h$ configurations imaging the final state configuration are taken into account. In contrast to this, in the MCDF calculation further hand-picked satellite contributions are added to the final state de-

Table 9.7.: Contributions of the different channels to the total decay width for the Auger decay of Xe4p_{3/2} in %.

	4d ⁻¹ 5s ⁻¹	4d ⁻¹ 5p ⁻¹	5s ⁻²	5s ⁻¹ 5p ⁻¹	5p ⁻²
Ref. ¹	77.7	20.7	0.5	–	1.1
Ref. ²	33.6	59.4	2.2	–	4.8
This work	16.1	78.1	0.1	1.8	3.9

¹ MCDF calculation excluding final ionic state configuration interaction [120].

² MCDF calculation including final ionic state configuration interaction [120].

³ This work.

scription. Hence, the final state description of the MCDF can be more precise than the one of the FanoADC method.

Considering the large errors of both decay width calculations and their experimental determination, the total decay widths obtained in this work are in agreement with both the experimental findings and the other calculations.

As discussed in section 8.1.3, the obtained partial decay widths might suffer from inter-channel mixing, which is mainly observed in the sub-valence region. According to this, the intensity distribution of this work differs from the ones of reference [120] as shown in Table 9.7. However, the dominance of the CK process is qualitatively observed in accordance with the other calculations.

The Xe4p_{1/2} initial state can, as already mentioned, not be described by a single 1h configuration and therefore, all states with a pole strength larger than 0.05 and a major contribution of the Xe4p_{1/2} spinor are investigated. Hereby, also the 4d⁻² configurations are sorted into the final state subspace in order to take into account a possible SCK process.

Figure 9.4 shows the decay width profile of the lowest energy state investigated, which also inhabits the largest pole strength. It is a well-behaved and smooth curve at energies above $E = 0$. As can easily be seen, the SCK decay channel opens directly in the energy region of interest at $E_{res} = 0$. Since the Stieltjes procedure is not able to produce a clear energy cut at the threshold and the initial state energies can be expected not to be completely exact due to errors introduced by the partitioning and additional errors from the ADC(2x) itself, an unambiguous conclusion, whether the SCK channel is open or not, cannot be drawn. This decision also determines the choice of which curve of the decay width profile to choose for the evaluation of the decay width. The results shown in Table 9.8 are the numbers obtained from the lower curve excluding the opening channel from the interpolation. In weighing the higher order moments more than the lower order moments, the decay width would be about twice as large as the numbers presented and hence in the order of $\Gamma_{max} \approx 2$ eV.

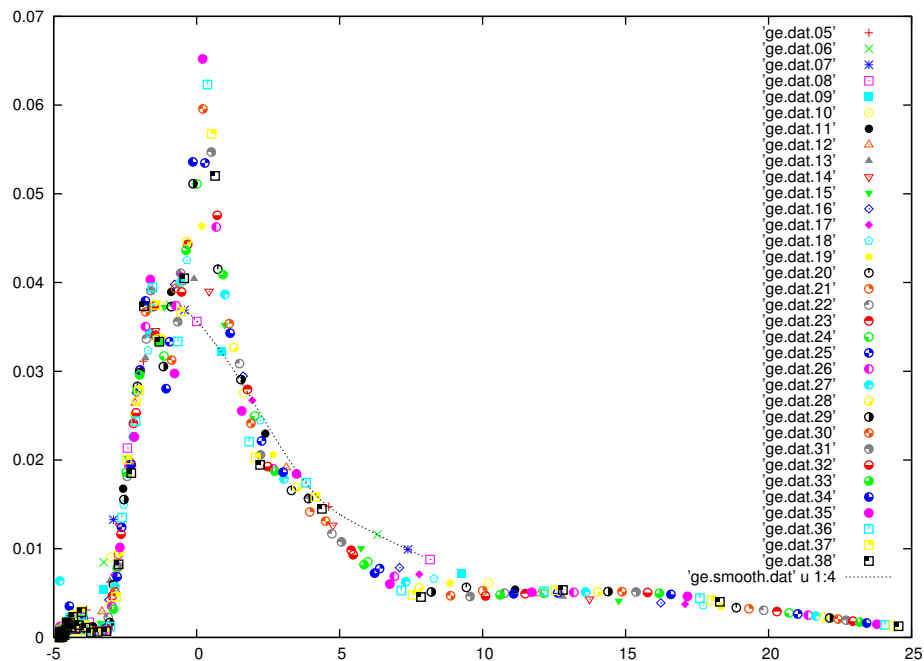


Figure 9.4.: $\Gamma(E)$ of the relativistic FanoADC calculation from a $4p_{1/2}$ initial state with both Γ and E given in atomic units.

Table 9.8.: Auger decay widths of non-negligible satellites with a major contribution of the Xe $4p_{1/2}$. All widths are given in eV.

energy [eV]	156.42	158.16	160.22	177.77	186.31
pole strength	0.332	0.093	0.123	0.058	0.068
$4d^{-2}$	$6.78 \cdot 10^{-1}$	$4.45 \cdot 10^{-1}$	$1.07 \cdot 10^{-1}$	$1.68 \cdot 10^{-1}$	$1.56 \cdot 10^{-1}$
$4d^{-1}5s^{-1}$	$1.34 \cdot 10^{-1}$	$6.93 \cdot 10^{-2}$	$8.61 \cdot 10^{-2}$	$1.12 \cdot 10^{-1}$	$3.39 \cdot 10^{-1}$
$4d^{-1}5p^{-1}$	$2.51 \cdot 10^{-1}$	$9.08 \cdot 10^{-2}$	$1.09 \cdot 10^{-1}$	$1.45 \cdot 10^{-1}$	$3.72 \cdot 10^{-1}$
$5s^{-2}$	$3.10 \cdot 10^{-4}$	$2.21 \cdot 10^{-4}$	$1.91 \cdot 10^{-4}$	$2.12 \cdot 10^{-4}$	$1.81 \cdot 10^{-4}$
$5s^{-1}5p^{-1}$	$3.84 \cdot 10^{-3}$	$1.32 \cdot 10^{-3}$	$2.16 \cdot 10^{-3}$	$1.45 \cdot 10^{-3}$	$8.13 \cdot 10^{-3}$
$5p^{-1}5p^{-1}$	$1.02 \cdot 10^{-2}$	$3.40 \cdot 10^{-3}$	$5.12 \cdot 10^{-3}$	$2.18 \cdot 10^{-3}$	$1.55 \cdot 10^{-2}$
total	1.077	0.610	0.310	0.429	0.891

Even though the FanoADC calculations imply the SCK process to have a large decay width, the calculated value is smaller than the estimated value of 10 – 100 eV [120]. The FanoADC-Stieltjes results therefore indicate that the broad feature of the single ionization spectrum in the $4p_{1/2}$ region is caused by both the breakdown of the single particle picture with additional fast decay of all corresponding satellite configurations.

9.3. Summary

From these examples I have shown that the FanoADC-Stieltjes method implemented in Dirac is able to both reproduce results of the comparable non-relativistic code of Kolorenč and results from MCDF calculations including relativistic effects in Auger processes as well as the corresponding experimental results. It is to be expected that the relativistic FanoADC-Stieltjes Code is also able to predict unknown decay widths for larger systems such as dimers and small clusters, since it is able to treat lower than spherical symmetries.

10. Geometric Influence on ICD and ETMD3 Illustrated Using Pairs and Triples of Atoms

Decomposing every system into pairs and triples of atoms is a very useful first order approximation to both the investigation of energies and decay widths of a larger system. Pairs and triples are combinations of two and three atoms, respectively. These atoms do not necessarily need to form bonds between each other or even be close, but they are characterized according to fixed internal coordinates. Each pair and triple can be described by its properties which are in first order of approximation independent of further, eventually present, atoms. In the following, this approach is going to be called model of pairs and triples.

In case of the electronic decay processes one is interested in the energies of the initial E_{in} and the final states E_{fin} of the corresponding processes in order to determine, whether a channel β is open, i.e., in accordance with energy conservation, or not. When the channel is open, the excess energy is carried away by the emitted electron E_{sec} in form of its kinetic energy. These energies can in the model of pairs and triples be approximated to be

$$E_{in}^{\beta} = SIP(X_{in}^{\beta}) \quad (10.1)$$

$$E_{fin}^{\beta} = SIP(X_{fin1}^{\beta}) + SIP(X_{fin2}^{\beta}) + \frac{1}{d} \quad (10.2)$$

$$E_{sec}^{\beta} = E_{in}^{\beta} - E_{fin}^{\beta} \quad (10.3)$$

where X_{in} denotes the initially ionized atom and X_{fin1} and X_{fin2} describe the two ionized atoms in the final state. β denotes the decay channel characterized by the quantum numbers of the ionized atoms in the pairs and triples and d denotes the interatomic distance between the atoms X_{fin1} and X_{fin2} . The initially ionized atom X_{in} can coincide with one or both of the final state atoms X_{fin1} and X_{fin2} . As explained in chapter 2, the distribution of the vacancies over the different atoms determines the kind of electronic decay process at hand. Hence, in an Auger process all three atoms would coincide, for an ICD X_{in} would coincide with one of X_{fin1} and X_{fin2} and for an ETMD3 all ionized states are located on different atoms.

In all autoionization processes considered, a second electron is emitted with the kinetic energy E_{sec} . If $E_{sec} < 0$, then the final state energy is higher than the initial state energy and the process is energetically not accessible. Hence, the corresponding channel is closed.

This ad hoc approach easily allows to correct for energetic shifts of ionization potentials as observed in larger clusters.

The decay widths of the pairs and triples can be estimated with different accuracy, but in general, the total decay width Γ of a system is the sum over the decay widths of all channels β for all possible pairs or triples i .

$$\Gamma = \sum_{i,\beta} \Gamma_{i,\beta} \quad (10.4)$$

10.1. Influence of the Geometry on ICD processes

10.1.1. Geometry Dependence of the ICD Channel Openings and Closings

In case of the ICD process, the atoms X_{in} and one of the finally ionized atoms X_{fin1} and X_{fin2} coincide. For the sake of simplicity it is now assumed that this atom is X_{fin1} . d is then the interatomic distance R of X_{fin1} and X_{fin2} .

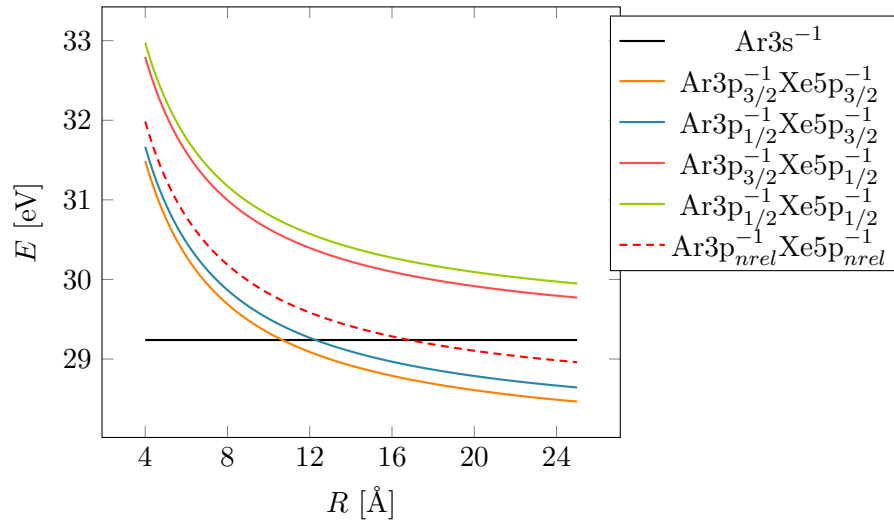


Figure 10.1.: Initial and final state energies of the ICD channels of ArXe in the model of pairs. Both the four relativistic channels and the non-relativistic estimate are shown. From the distance on, where the final state energy is lower than the initial state energy, the decay channel is open.

The ArXe dimer is chosen as an illustrative example in order to show the distance dependency of the final state energies compared to the initial state in the model of pairs

using ionization properties of the corresponding atoms given in Table A.2. In Figure 10.1 the energy of the $\text{Ar}3s^{-1}$ initial state is assumed to be constant, independent of any stabilization by the neighbour and drawn as a black line. Additionally both the curves of the four final states of the relativistic description and a hypothetical non-relativistic curve calculated by the means of equation (10.2) are shown.

For small distances up to 10 \AA , all channels are closed. As soon as the final state curves cross the energy of the initial state the respective channels open. For the four relativistic channels these channel opening distances are 10.67 \AA , 12.29 \AA and 334.1 \AA for the $\text{Ar}3p_{3/2}^{-1}\text{Xe}5p_{3/2}^{-1}$, $\text{Ar}3p_{1/2}^{-1}\text{Xe}5p_{3/2}^{-1}$ and $\text{Ar}3p_{3/2}^{-1}\text{Xe}5p_{1/2}^{-1}$ channels, respectively. The sum of the two ionization potentials of the $\text{Ar}3p_{1/2}^{-1}\text{Xe}5p_{1/2}^{-1}$ channel are already higher than the initial state energy. Therefore this channel never opens. In the non-relativistic treatment, the atomic ionization energies of the $\text{Ar}3p$ and the $\text{Xe}5p$ are estimated by the statistically weighted average of the $p_{3/2}$ and the $p_{1/2}$ ionization energies. The non-relativistic opening distance would then be 16.84 \AA .

Considering a distinct distance in an experiment as many secondary electron peaks would be observed as energetically distinguishable channels are open. The non-relativistic treatment predicts one single peak, whereas the relativistic approach takes care of the different channels due to spin-orbit coupling and therefore is able to predict the correct number of peaks for a reasonable choice of initial and final state energies.

Hence, for an ArXe dimer with an equilibrium distance of 4.04 \AA all ICD channels are closed. As can be seen in the discussion of mixed ArXe clusters, that in case of shifted curves, ICD channels might open at atomic distances, where the decay widths are non-negligible.

10.1.2. Geometry Dependence of the ICD Decay Widths

The decay widths Γ in the asymptotic description of equation (5.18) shows a pure R^{-6} behaviour. However, this does not contain any information about whether the channel is open and hence, whether such a process would be observable. Therefore, in Figure 10.2 the decay width is plotted over R with the additional condition, that the corresponding channel needs to be open at the distance of interest for both the relativistic treatment and the non-relativistic analogon.

In this double logarithmic plot, the decay width determined non-relativistically is a straight line starting from the opening distance of 16.84 \AA . In contrast to this, the relativistic treatment shows a decay at much smaller distances, as was to be expected from the smaller opening distance of the $\text{Ar}3p_{3/2}^{-1}\text{Xe}5p_{3/2}^{-1}$ channel. Already from this point it can be seen, that the non-relativistic treatment is not sufficient for systems with a large spin-orbit coupling. Between 12 \AA and 13 \AA the relativistic decay widths are approximately constant rather than decreasing with R^{-6} . In this region, the second channel, $\text{Ar}3p_{1/2}^{-1}\text{Xe}5p_{3/2}^{-1}$, opens and its contribution to the decay is added to the decay width

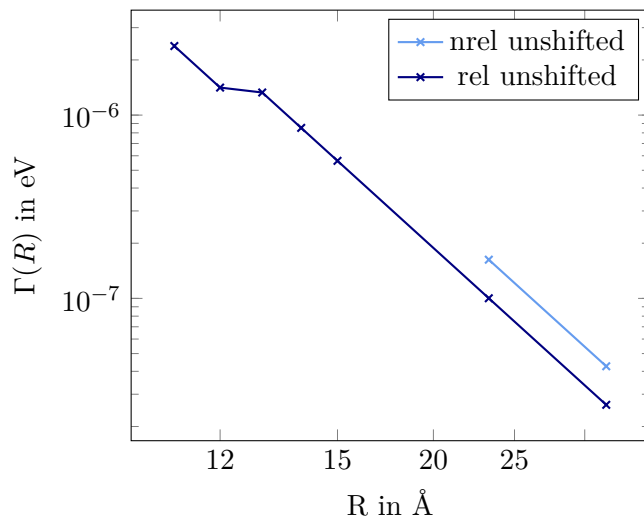


Figure 10.2.: Decay widths of the ArXe dimer in relativistic and non-relativistic treatment plotted over the interatomic distance R . The initial and final state energies were determined from unshifted experimental atomic ionization potentials. Only such channels are considered, which are open at the corresponding distances.

of the first decay channel. However, at distances where the non-relativistic channel is open, for the distances shown in this illustration, the non-relativistic decay width is higher than the total relativistic one. This observation stems from the fact, that in a first order approximation, when all channels are open in the relativistic treatment, the sum over their decay widths has to equal the non-relativistic one. In the case of the ArXe dimer and the distances shown in Figure 10.2, not all relativistic channels are open, and hence the non-relativistic treatment overestimates the decay width.

The sum over the relativistic decay widths will for these calculations never exactly give the non-relativistic result, because even though a thorough partitioning of the lifetime τ and the ionization cross section $\sigma(\omega_{vp})$ are taken care of, the cross section as well as the decay width depend on the energy of the virtual photon ω_{vp} non-linearly and this energy differs for different ionization energies of the final state of the initially ionized atom.

10.2. Influence of the Geometry on ETMD3 processes

10.2.1. Geometry Dependence of the ETMD3 Channel Openings and Closings

Atomic triples are characterized by three coordinates which for this discussion are chosen to be the Jacobi coordinates R , Q and θ as illustrated in Figure 5.4. However, the choice of appropriate coordinates is not unambiguous, since it is unknown, which way the energy

travels during its transfer between the subsystems. A more detailed discussion is to be found in section 10.3.

Energetically the geometry is crucial for the determination of open channels. Already in the first approximation of the final state energy iE_{fin} of equation (10.2) it strongly depends on the distance between the two atoms X_{fin1} and X_{fin2} ionized in the final state. This dependence is explicitly formulated as

$$E_{fin} = SIP(X_1) + SIP(X_2) + \frac{1}{\sqrt{Q^2 - 2QR \cos \theta + R^2}}. \quad (10.5)$$

When this final state energy is higher than the initial state, the particular channel is closed. For the case of the ArXe_2 this relation is illustrated in Figure 10.3 for the $\text{ArXe}5p_{1/2}^{-1}\text{Xe}5p_{1/2}^{-1}$ channel and $Q = R_{eq} = 4.04 \text{ \AA}$ using the atomic values as given in Table A.2.

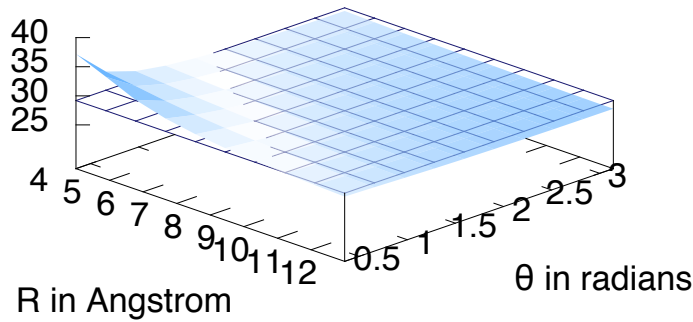


Figure 10.3.: Energy hyper surface of the doubly ionized $\text{ArXe}5p_{1/2}^{-1}\text{Xe}5p_{1/2}^{-1}$ (light blue surface) and the ionization potential of the $\text{Ar}3s^{-1}$ initial state with 29.2 eV (dark blue grid). Q is constant, whereas R and the angle θ (see Figure 10.9) are varied. This ETMD3 channel is open for structures where the final state energy is lower than the initial state energy.

At a hypothetical very small angle θ and $R \approx Q$, the channel closes. In this example those geometries are mostly unrealistic, because the two xenon atoms would be closer than in a neutral Xe dimer, but in other systems channel closings due to the geometry are to be expected.

10.2.2. Geometry Dependence of the ETMD3 Decay Rates

The decay rate also crucially depends on the geometry of the triple. From eq. (5.22) the R dependency is easily interpreted as being $\Gamma \propto R^{-6}$ corresponding to the energy transfer mainly being caused by a dipole-dipole interaction. The dependency of Q is

implicitly included in the transition dipole moments. These depend on the overlap between the two atoms of the electron transfer, which decreases exponentially with Q . The angular part of equation (5.22) can be reformulated using the equivalence of transitions in \tilde{x} and \tilde{y} direction to yield

$$\Gamma_i \propto 2 \left(|\langle \tilde{D}_z \rangle|^2 (1 + \cos^2 \alpha) + |\langle \tilde{D}_x \rangle|^2 (2 + \sin^2 \alpha) \right) \quad (10.6)$$

The decay widths corresponding to electron transfers from orbitals oriented along (\tilde{z}) and perpendicular to the internuclear axis (\tilde{x}) are illustrated separately in Figure 10.4, supposing $|\langle \tilde{D}_z \rangle|^2 = |\langle \tilde{D}_x \rangle|^2 = 1$. Obviously, the two different transition types add up to give the full angular dependence of a given trimer. It has to be kept in mind that in reality $|\langle \tilde{D}_z \rangle|^2$ is about an order of magnitude larger than $|\langle \tilde{D}_x \rangle|^2$.

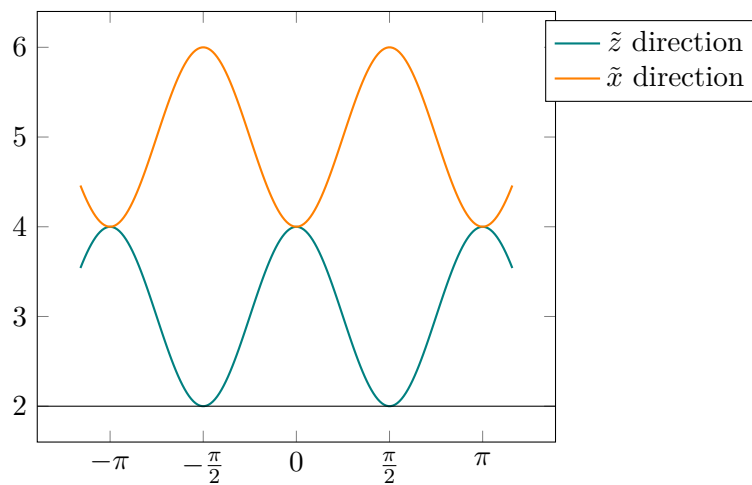


Figure 10.4.: Angle dependence of the ETMD3 decay widths for electron transfers along the internuclear axis \tilde{z} of subsystem S_1 and perpendicular to the internuclear axis \tilde{x} .

For a more realistic picture consider the distances R and Q as defined in Figure 5.4 to be constant and the ratio between the transition dipole moments in the \tilde{z} and the \tilde{x} direction $q = \frac{|\langle \tilde{D}_x \rangle|^2}{|\langle \tilde{D}_z \rangle|^2}$ to be fixed to some number. In this case the decay width for each M'_{AB} has the angular dependence

$$\Gamma_i \propto \left(2q |\langle \tilde{D}_z \rangle|^2 + (4 + 2q) |\langle \tilde{D}_z \rangle|^2 \cos^2 \alpha + (2 + 4q) |\langle \tilde{D}_z \rangle|^2 \sin^2 \alpha \right) \quad (10.7)$$

$$\propto 4q + 2 + 2 \cos^2 \alpha + 2q \sin^2 \alpha. \quad (10.8)$$

It is an oscillating function with maxima at even multiples of $\frac{\pi}{2}$ and minima at uneven multiples at $\frac{\pi}{2}$ as shown in Figure 10.5.

In a real system, an energy transfer between two dipoles is most efficient, if they are

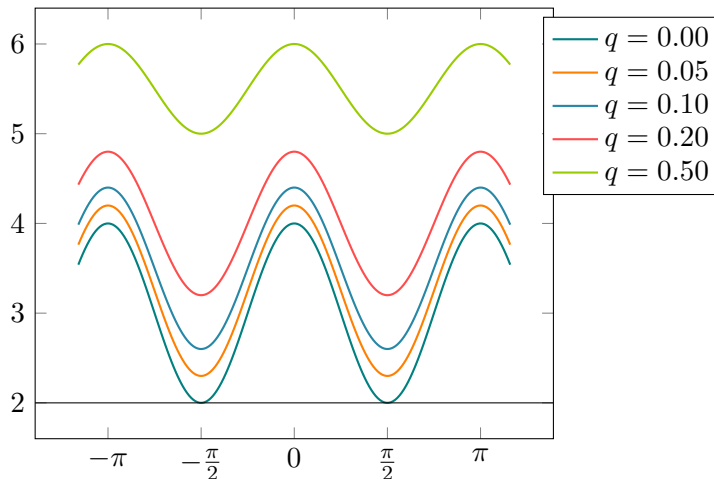


Figure 10.5.: Angular dependence of the ETMD3 decay width for electron transfers both along and perpendicular to the internuclear axis of subsystem S_1 . Different values of $q = \frac{|\langle \tilde{D}_x \rangle|^2}{|\langle \tilde{D}_z \rangle|^2}$.

aligned in one direction. Within a dimer the most efficient electron transfer results in a dipole aligned along the bonding axis and hence $q < 1$. A typical value of q would be $\frac{1}{10}$. In the case of q approaching 0, the angular part of the decay width approaches a shifted $2 \cos^2 \alpha$ with maxima at even multiples of $\frac{\pi}{2}$ and minima at uneven multiples of $\frac{\pi}{2}$ with values between 4 and 2. Therefore, for typical numbers of q the energy transfer to an atom on the same axis ($\alpha = 0, \pi$), corresponding to a linear arrangement, is preferred.

The previous discussions are based on the decay of one specific atom being the electron donor and another atom being the electron emitter. In reality both atoms can be donor as well as emitter while the energy of the resulting final state stays the same. For both bond lengths between the two atoms ionized in the final state and initially ionized atom being the same, both contribute the same amount to the total decay rate. With one of the atoms ionized in the final state being further apart, its probability in donating the vacancy filling electron decreases exponentially and can hence be neglected.

Combining both the view on the energetic accessibility of the decay channels and the decay widths results in the pictures in Figure 10.6. Here the geometry dependence of the decay width for the case of the four ArXe₂ channels is shown summing the decay widths of the two possible geometric combinations of the triple. The numbers were obtained by HARDRoC using the asymptotic formula (5.22) with redefined R and θ . Here $Q = 4.04 \text{ \AA}$ is chosen constant to the internuclear distance of the neutral ArXe dimer while R and θ are varied. The plots display the channel closing for very small Xe-Xe distances and the R^{-6} behaviour as well as the expected angle dependence explicitly shown in Figure 10.5. Implicitly the exponential decrease of the decay width is shown

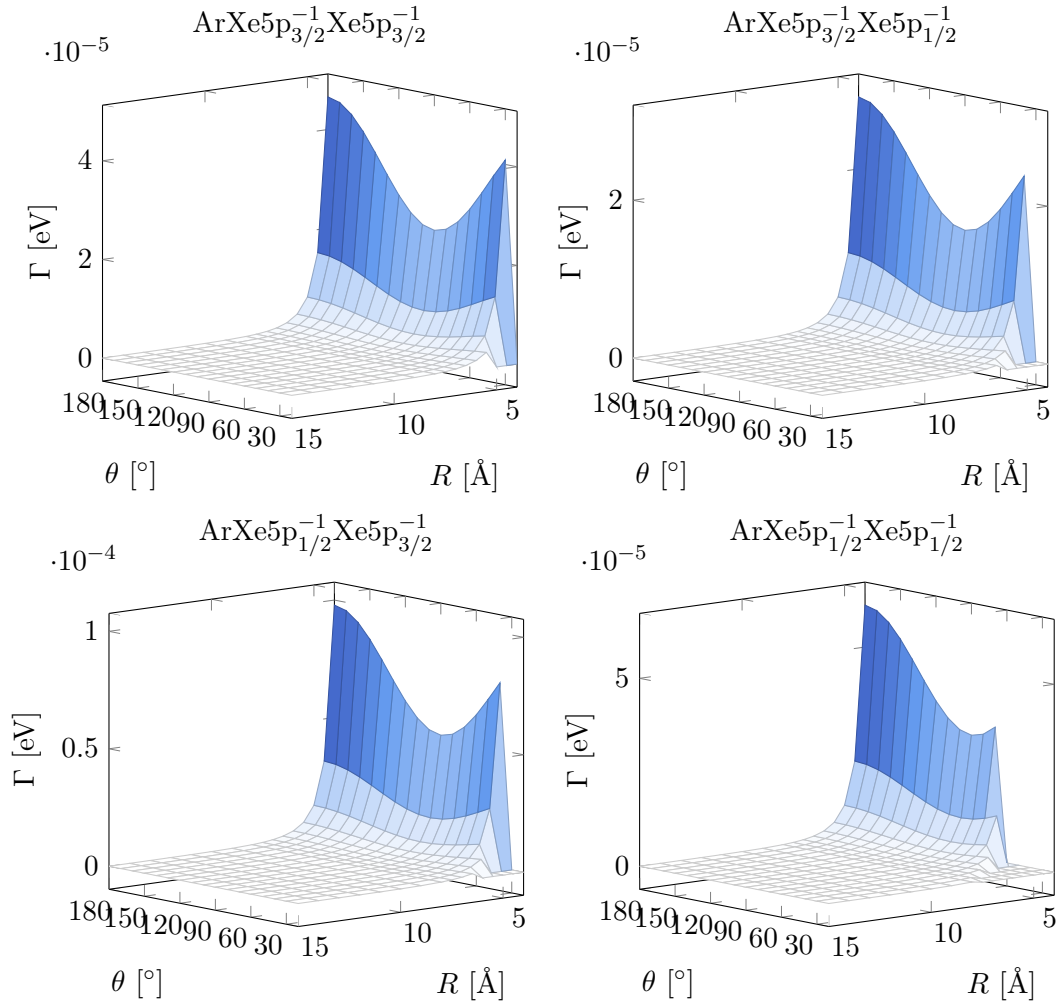


Figure 10.6.: ETMD3 decay widths Γ hyper surfaces for an ArXe_2 trimer. The four electronic decay channels are shown separately.

by one of the two triple combinations in the trimer showing a contribution only at small internuclear distances.

The decay widths of the four different decay channels shown in Figure 10.6 can be summed up to yield the total decay width of the ArXe_2 trimer as illustrated in Figure 10.7.

Also here the R^{-6} dependence is observed but the dependency of the angle θ shows spikes. These changes are due to the channel closing. For a large angle θ all channels are open. Imagine a linear trimer, which now starts bending. The closer the two xenon atoms get, the more the two positive charges in the final state repel each other. At one point the atoms are so close, that the $\text{ArXe}5p_{1/2}^{-1}\text{Xe}5p_{1/2}^{-1}$ channel being highest in energy

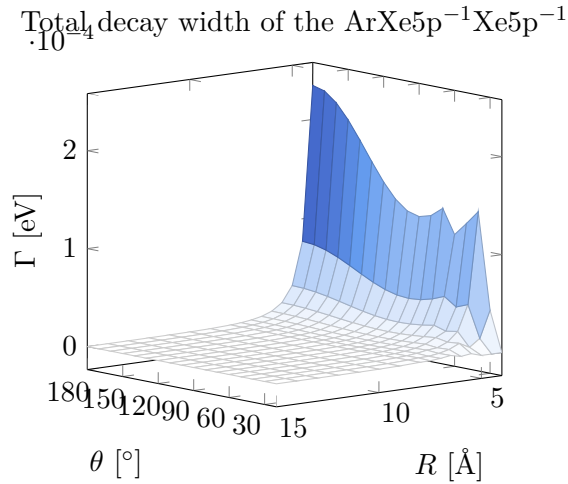


Figure 10.7.: Sum over the decay widths of all four channels, illustrated separately in Figure 10.6. The opening of channels at different angles θ and internuclear distances R are to be seen at the spikes.

is no longer energetically accessible. Bending further, first the $\text{ArXe5p}_{3/2}^{-1}\text{Xe5p}_{1/2}^{-1}$ and the $\text{ArXe5p}_{1/2}^{-1}\text{Xe5p}_{1/2}^{-1}$ channels, being equal in energy, close. In the illustrated angle range the $\text{ArXe5p}_{3/2}^{-1}\text{Xe5p}_{3/2}^{-1}$ channel does not close.

10.3. Influence of the Coordinate System Choice

In Figure 5.4 a coordinate system was chosen to describe the triatomic system ABC . The distance Q between the two atoms involved in the electron transfer is reasonably defined. However, where the center of the oscillating dipole moment of subsystem S_1 is located, can not unambiguously be defined. Most probable it is somewhere between the atoms A and B . The coordinates were chosen as illustrated in the left panel of Figure 10.8 with the distance R of the energy transfer anchored at the initially ionized atom A . This choice is convenient for the calculation of the decay widths of large system, since for triples consisting of atoms at larger distances the possibility of the anchorage to coincide with atom C is avoided. Another possible choice would be some point between the atoms A and B as illustrated in the right panel of Figure 10.8.

For the following discussion we will therefore refer to two sets of coordinates of maximum deviation with origins residing in atoms A and B with subscripts A and B .

We assume that we have two constant distances R_A and R_B where either of these distances is larger than or equal to Q . In this case the maximum and minimum of the ratio between the two corresponding decay rates $\frac{\Gamma_A}{\Gamma_B}$ will occur in the case of $\alpha = 0, \pi$ and $R_B = \frac{1}{2}R_A = Q$ and $R_B = 2R_A = 2Q$, respectively.

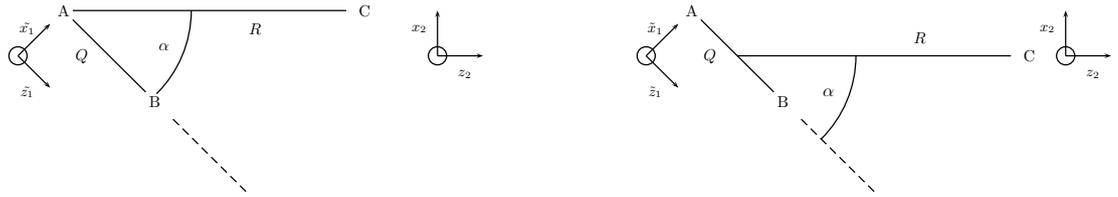


Figure 10.8.: Two different set of Jacobi coordinates for the description of a triple ABC (compare Figure 5.4). In the left Figure the distance of the energy transfer originates at the initially ionized atom A , while in the right panel the energy transfer distance is defined with respect to some point between atoms A and B . The right choice might be physically more precise, even though it is unknown, how to choose the anchorage point. The left set of coordinates is preferable in the modelling of cluster structures. The graphic in the right panel was reprinted with permission from Ref. [25]. Copyright 2013, AIP Publishing LLC.

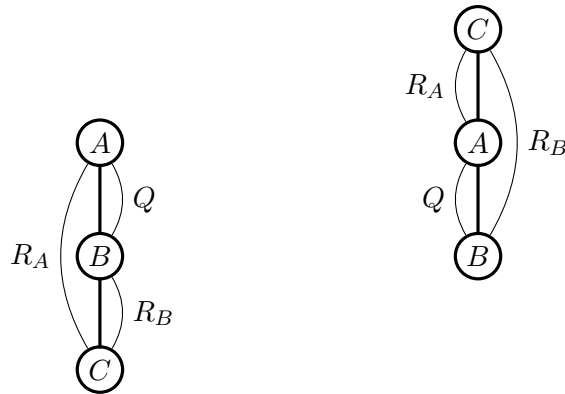


Figure 10.9.: Illustration of two geometry parameter sets, which lead to the largest possible deviation of the ETMD decay width.

$$\text{minimum: } \frac{\Gamma_A}{\Gamma_B} = \frac{1}{64} = \frac{1}{2^6} \quad , \quad \text{maximum: } \frac{\Gamma_A}{\Gamma_B} = \frac{64}{1} \quad (10.9)$$

From this we conclude, that the absolute numbers of calculated ETMD decay widths are obviously error-prone. In the worst case the uncertainty is given by factors $\frac{1}{64}$ or $\frac{64}{1}$. In reality these worst cases will rarely be observed, since it on the one hand is very unlikely to find two atoms at exactly the same place and on the other hand ETMD preferably occurs at interfaces, which leads to preferred angles higher than 0 and below π . Additionally the larger the difference between Q and R is, the smaller this effect is going to be.

11. Dependence of ICD Decay Widths on the Quantum Numbers

In the working equation of the asymptotic ICD decay widths in the jj -coupling picture (5.18)

$$\Gamma_\beta = \frac{2\pi}{R^6} \sum_{M'_A} B_{M'_A - M_A}^2 \left| \begin{pmatrix} J'_A & 1 & J_A \\ -M'_A & M'_A - M_A & M_A \end{pmatrix} \right|^2 (2J_A + 1) \frac{3c^4 \sigma^{(B)}(\omega_{vp})}{16\pi^2 \omega_{vp}^4 \tau_A}. \quad (11.1)$$

the total angular momenta of the initial and final states enter explicitly. Therefore, the question arises, how the ratio between the decay widths behaves both for the total angular momenta as well as their projections within the same total angular momentum. In the LS-coupling scheme only one L-state is possible, which is why an investigation of the behaviour of ratios is senseless in this case. However, the ratios of the different projections of this angular momentum can be obtained and have been shown to be [10]

$$\frac{\Gamma_0}{\Gamma_{\pm 1}} = 4. \quad (11.2)$$

The orbital with $L = 1$ and $M_L = 0$ corresponds to a p-orbital aligned along the internuclear axis, whereas for $M_{\pm 1}$ the orbitals are aligned perpendicular to the internuclear axis. In the picture of a classical oscillating dipole it is to be expected to have a much more efficient induction of another dipole in direction of the oscillation. The ratio of the decay widths therefore corresponds to the expectations.

In a relativistic treatment including the jj -coupling scheme, where the wavefunction is a four component spinor with the elements being linear combinations of LS-coupling functions, and different density functions the behaviour is not evident a priori.

11.1. Total Angular Momentum

First we are going to assume a process from a non-degenerate initial state with $J = \frac{1}{2}$ into different p-type final state configurations in the initially ionized atom for an ICD process. Afterwards we are going to assume different initial states of p-type orbitals with an s-type character in the final state of the initially ionized atom. However the classification is more accurate in terms of the order of ionization energies of the split

states. In the discussion we assume $SIP_{3/2} < SIP_{1/2}$, which is not necessarily true for all atoms. E.g., the order of the ionization potentials of the calcium 3p orbitals are switched.

In equation (5.18) most of the entities are independent of the total angular momenta and therefore the ratio between the decay widths reduces to

$$\frac{\Gamma_{1/2}}{\Gamma_{3/2}} = \frac{P_{1/2}}{P_{3/2}} \frac{\sigma^B(\omega_{vp1/2})}{\omega_{vp1/2}^4 \tau_{1/2}} \frac{\omega_{vp3/2}^4 \tau_{3/2}}{\sigma^B(\omega_{vp3/2})} \frac{2J_{A1/2} + 1}{2J_{A3/2} + 1} \quad (11.3)$$

$$\approx \frac{P_{1/2}}{P_{3/2}} \frac{\omega_{vp3/2}^5}{\omega_{vp1/2}^5} \frac{\tau_{3/2}}{\tau_{1/2}} \frac{2J_{A1/2} + 1}{2J_{A3/2} + 1} \quad (11.4)$$

$$= \frac{P_{1/2}}{P_{3/2}} \frac{\omega_{vp3/2}^5}{\omega_{vp1/2}^5} \frac{2J_{A1/2} + 1}{2J_{A3/2} + 1} \chi \quad (11.5)$$

where the sum of the products of the absolute square of Wigner's 3j-symbol and $B_{M'_A - M_A}$ are grouped to the variable P . The ionization cross section is proportional to the inverse of the energy of the virtual photon $\sigma\omega \propto \frac{1}{\omega}$ and the ratio between the lifetimes of the two different total angular momenta $\chi = \frac{\tau_{3/2}}{\tau_{1/2}}$ is experimentally accessible for atoms. Hence, the ratio of the decay widths does not depend on properties of the atom B explicitly.

$M_A \backslash M'_A$	$\frac{3}{2}$	$\frac{1}{2}$	$-\frac{1}{2}$	$-\frac{3}{2}$
$\frac{1}{2}$	$\frac{1}{2}$ (1)	$-\sqrt{\frac{1}{6}}$ (0)	$\sqrt{\frac{1}{12}}$ (-1)	–
$-\frac{1}{2}$	–	$-\sqrt{\frac{1}{12}}$ (1)	$\sqrt{\frac{1}{6}}$ (0)	$-\frac{1}{2}$ (-1)

Table 11.1.: Evaluation of Wigner's 3j-symbols for $J = \frac{3}{2}$ in the argon-xenon dimer. The numbers in brackets denote the difference of the projections of the angular momenta $M'_A - M_A$.

$M_A \backslash M'_A$	$\frac{1}{2}$	$-\frac{1}{2}$
$\frac{1}{2}$	$\sqrt{\frac{1}{6}}$ (0)	$-\sqrt{\frac{1}{3}}$ (-1)
$-\frac{1}{2}$	$-\sqrt{\frac{1}{3}}$ (1)	$\sqrt{\frac{1}{6}}$ (0)

Table 11.2.: Evaluation of Wigner 3j-symbols for $J = \frac{1}{2}$ in the argon-xenon dimer. The numbers in brackets denote the difference of the projections of the total angular momenta $M'_A - M_A$.

11.1.1. One Initial State and Several Final States

For one given initial state the total angular momentum is defined and hence $J_{A3/2} = J_{A1/2}$. The energies of the virtual photon transferred between the units of the ICD differ for the two final state configurations of the initially ionized atom as

$$\omega_{vp1/2} = SIP_{in} - SIP_{fin1/2} \quad (11.6)$$

$$\omega_{vp3/2} = SIP_{in} - SIP_{fin3/2} \quad (11.7)$$

In case of the SIP of the $J = \frac{3}{2}$ state being lower than the SIP of the $J = \frac{1}{2}$ state, the difference in energy of the two virtual photons is given by the positive spin-orbit coupling constant a .

$$\omega_{vp3/2} = \omega_{vp1/2} + SIP_{fin1/2} - SIP_{fin3/2} \quad (11.8)$$

$$\omega_{vp3/2} = \omega_{vp1/2} + a \quad (11.9)$$

$P_{1/2}$ and $P_{3/2}$ are evaluated using the expressions for the 3j-symbols given in Tables 11.1 and 11.2 and $B_0 = -2$, $B_{\pm 1} = 1$ to give 1 in both cases. From these considerations it follows that the ratio between the decay widths of $J'_A = \frac{3}{2}$ and $J'_A = \frac{1}{2}$ is given by

$$\frac{\Gamma_{1/2}}{\Gamma_{3/2}} = \frac{\omega_{vp3/2}^5}{\omega_{vp1/2}^5} \frac{2J_{A1/2} + 1}{2J_{A3/2} + 1} \frac{1}{\chi} \quad (11.10)$$

$$= \frac{(\omega_{vp1/2} + a)^5}{\omega_{vp1/2}^5} \frac{1}{\chi} \quad (11.11)$$

In the non-relativistic limit the spin-orbit coupling constant a is zero and hence the ratio is given by the ratio of the two different lifetimes. Without relativistic effects this ratio χ is determined purely by the degeneracy of the states and therefore $\chi_{nrel} = 2$. In the relativistic case $a > 0$ and a splitting additional to the degeneracy of the final states configurations is to be observed. Furthermore χ varies with the strength of the spin-orbit coupling. For increasing spin-orbit coupling constant χ increases. In the neighbourhood of other atoms, neither the asymptotic expression is valid nor is the spin-orbit coupling constant a a real constant [121]. Therefore, the following results are only valid for large distances.

11.1.2. Several Initial States and One Final State

Normally, the starting point for such gedankenexperiments is a given initial state. However, decay widths from different initial states with the same final state can also be compared. It has to be kept in mind, that the sum of the resulting decay widths would not resemble a total decay width.

Consider the initially ionized atom to be an alkaline earth metal atom being ionized from the p-level. In this case the initial state can both be $J_A = \frac{3}{2}$ and $J_A = \frac{1}{2}$. The final state configuration being a vacancy in the 4s shell is defined by $J'_A = \frac{1}{2}$. Hence, in this section the decay widths of two different initial states with the same final state are compared. The virtual photon energies would then be defined as

$$\omega_{vp1/2} = SIP_{in1/2} - SIP_{fin} \quad (11.12)$$

$$\omega_{vp3/2} = SIP_{in3/2} - SIP_{fin} \quad (11.13)$$

$$\omega_{vp3/2} = \omega_{vp1/2} + SIP_{fin3/2} - SIP_{fin1/2} \quad (11.14)$$

$$\omega_{vp3/2} = \omega_{vp1/2} - a \quad (11.15)$$

Notice, that in this case the sign in front of the spin-orbit coupling constant a is different from the one for one specific initial state. The last of the above equations only hold in the case of $SIP_{fin1/2} > SIP_{fin3/2}$.

Considering the degeneracies of the states $\frac{2J_{A1/2}+1}{2J_{A3/2}+1} = \frac{1}{2}$. The evaluation of $\frac{P_{1/2}}{P_{3/2}}$ is possible for all kinds of initial states with a specific value for the projection M_A , but the focus of this section lies on the influence of the total angular momentum without the consideration of their projections, here the channels are defined with respect to M'_A instead of M_A . In this case $\frac{P_{1/2}}{P_{3/2}} = 1$. Hence the ratio of the decay widths can be evaluated to be

$$\frac{\Gamma_{1/2}}{\Gamma_{3/2}} = \frac{P_{1/2}}{P_{3/2}} \frac{\omega_{vp3/2}^5}{\omega_{vp1/2}^5} \frac{2J_{A1/2} + 1}{2J_{A3/2} + 1} \frac{1}{\chi} \quad (11.16)$$

$$= \frac{1}{2} \frac{(\omega_{vp1/2} - a)^5}{\omega_{vp1/2}^5} \frac{1}{\chi} \quad (11.17)$$

11.2. Projection of the Total Angular Momentum

Again consider the ICD from a defined initial state with $J_A = \frac{1}{2}$ and $M_A = \frac{1}{2}$. Within the final state specification of $J'_A = \frac{3}{2}$, several projections $M'_A = +\frac{3}{2}, +\frac{1}{2}, -\frac{1}{2}$ are possible. In the asymptotic picture, these three states are obviously degenerate and are described by the same total angular momentum. In the following, they are assumed to have the

same radiative lifetime.

Hence, in equation (11.4) the only difference relies on P , which has to be remembered to be a sum over the different possible projections and orientation factors B . Evaluating the ratios for the different final state projections yields

$$\frac{\Gamma_{+1/2}}{\Gamma_{+3/2}} = \frac{P_{+1/2}}{P_{+3/2}} = \frac{8}{3} \quad (11.18)$$

$$\frac{\Gamma_{+1/2}}{\Gamma_{-1/2}} = \frac{P_{+1/2}}{P_{-1/2}} = 8. \quad (11.19)$$

In the non-relativistic investigation, the higher efficiency of the ICD process from a z -orbital ($M_L = 0$) was explained by the spacial orientation of the oscillating dipole along the internuclear axis. However, in the relativistic investigation above, the spacial orientation can not alone be responsible for the efficiency, because the relativistic probability density of both $M'_A = +\frac{1}{2}$ and $M'_A = -\frac{1}{2}$ are aligned along the internuclear axis. Still, the decay width into a final state characterized by $M'_A = \frac{1}{2}$ is eight times as fast as the decay into the final state with $M'_A = -\frac{1}{2}$. The above considerations therefore imply that in addition to the spacial orientation of the dipole, the phase of the final state wavefunction is important as well.

An analogous treatment for the final state $J'_A = \frac{1}{2}$ with $M'_A = +\frac{1}{2}, -\frac{1}{2}$ leads to

$$\frac{\Gamma_{+1/2}}{\Gamma_{-1/2}} = \frac{P_{+1/2}}{P_{-1/2}} = 2. \quad (11.20)$$

Also in this case a difference is to be observed, even though both the initial and final states' probability densities are spherical symmetric.

12. ICD Decay Widths of ArXe Obtained by the Relativistic FanoADC

12.1. Computational Details

Both, the relativistic and the non-relativistic decay width calculations were performed using the FanoADC(2x) and Stieltjes routines implemented in Dirac [15]. The relativistic results were obtained using the Dirac-Coulomb Hamiltonian with an approximate treatment of the two-electron integrals over the small components (LVCORR) in four-component calculations.

Both the relativistic and the non-relativistic calculations were performed with the cv4z basis set of Dyall [110] and additional KBJ [99] basis functions centered on the geometric mean between the argon and the xenon atom. For this purpose five s , p and d basis functions each were used. The active space included the valence shell of the argon and the xenon atom and the virtual orbitals were included up to 15.0 a.u.. This lead to 420 and 330 active spinors in the relativistic and non-relativistic case, respectively.

In all cases the channels are either closed or very close to threshold. Therefore, the pseudo-spectrum contains only very few points for energies lower than the resonance energy. Therefore, the moments of the lower orders of Stieltjes might not cover the resonance energy. The calculated decay width is then obtained from extrapolation of the interpolated curves for higher energies. In the subsets of the pseudo-spectrum for the calculation of the partial decay widths even less or no points are given at all, therefore the partial decay widths might be less reliable.

12.2. Results

In Figure 12.1, the total decay widths obtained from the FanoADC calculations and the asymptotic approximations are shown.

The *ab initio* results of the relativistic and the non-relativistic calculations are very close and differ by no more than a factor of 2. However, which decay width is higher is not to be determined, because the curves cross each other. Since the factor of 2 is the approximate error of the calculations, these findings are within the errors bars and no statement about whether relativistic effects influence the total decay width can be concluded in this case. They both approximately show an R^{-6} behaviour at distances

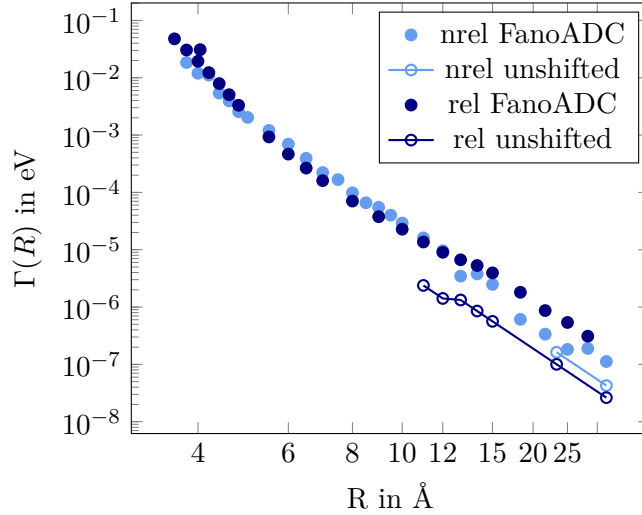


Figure 12.1.: Distance dependence of the decay widths of the heteronuclear ArXe dimer obtained from both relativistic and non-relativistic calculations using the asymptotic approximation and the FanoADC approach.

larger than $\approx 2R_{eq}$. Also for smaller distances the decay widths only differ significantly at distances below 5 \AA .

In comparison to the decay widths obtained from the asymptotic approximation the *ab initio* decay widths are higher by a factor of about 6. This behaviour is to be expected, since the asymptotic approximation does not take any overlap effects into account. Additionally, it relies on the truncation of a series over R and hence higher order terms are neglected as well. However, the asymptotic approximation does serve as a lower bound to the decay width.

Another feature is the channel opening and closing. The FanoADC-Stieltjes approach relies on an incomplete pseudo-spectrum from which points of the decay width are constructed and later interpolated and thereby the curves are smoothed. This smoothing prohibits the possibility to determine whether a channel is open or closed close to threshold. Additionally, even though the resonance energy calculated from the initial state subspace should not differ too strongly from the initial state's single ionization potential, small errors might be introduced by the partitioning of the Hamiltonian. Additionally, the ADC(2x) method as such is not exact and might contribute to the error. All these factors necessitate an interpretation of the scientist. Possibilities to treat the channel opening and closing are to calculate the channel opening distances with the ad hoc approach of equations (10.1 – 10.3) or to determine the channel opening distance by a set of single and double ionization calculations.

The total decay width of the relativistic FanoADC calculation can be divided into partial decay widths of the following channels already presented in section 10.1: $\text{Ar}3p_{3/2}^{-1}\text{Xe}5p_{3/2}^{-1}$,

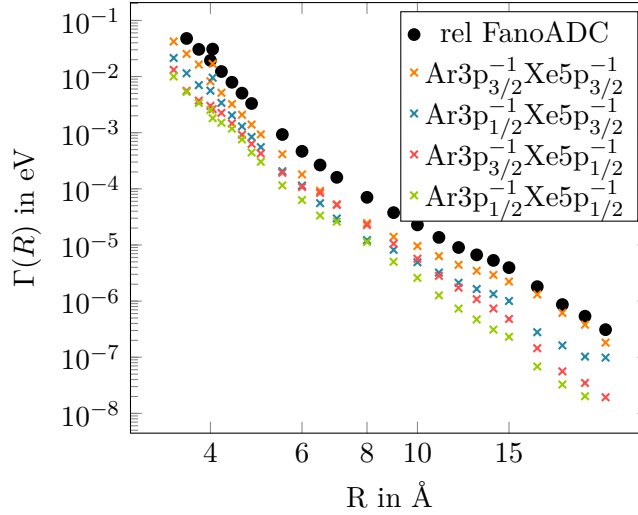


Figure 12.2.: Renormalized partial decay widths calculated with the relativistic FanoADC of the ArXe dimer compared to each other and the total decay width.

$\text{Ar}3p_{1/2}^{-1}\text{Xe}5p_{3/2}^{-1}$, $\text{Ar}3p_{3/2}^{-1}\text{Xe}5p_{1/2}^{-1}$ and $\text{Ar}3p_{1/2}^{-1}\text{Xe}5p_{1/2}^{-1}$. The sum of the partial decay widths should equal the total decay width and from the calculations only small deviations of up to 10% were observed. If this is not the case, the partial decay widths are meaningless. The calculated decay widths are renormalized to the total decay width and illustrated in Figure 12.2.

The actual decay width in ascending order are given by the channels above. These findings can be explained by two factors already discussed in the preceding section about the dependence of the decay with on the quantum numbers of the initial and final states. The ratios of the channels between different decay widths mainly depend on the ratio of the two different ionization cross sections $\sigma_{3/2}$ and $\sigma_{1/2}$ and the ratio between the radiative lifetimes $\chi = \frac{\tau_{1/2}}{\tau_{3/2}}$.

The ratio $\frac{\sigma_{3/2}}{\sigma_{1/2}} = 1.6$ can be measured experimentally [122] and for large distances the ratio of the partial decay widths should behave accordingly. The ratios of the decay widths obtained from the FanoADC-Stieltjes calculations are compared to the this experimental ratio in Figure 12.3.

The agreement of the decay width ratios to the ratios of the ionization cross sections are reasonable for distances between 5 and 10 Å. At shorter distances the ratio is much higher than expected. But especially at small distances overlap effects and higher order terms of the expansion over R might play a non-negligible role. At larger distances the decay width ratios should converge to the asymptotic limit. However, they obviously do not and hence I conclude that these partial decay widths and perhaps also the total decay width calculations with the chosen technical parameters and the current implementation are not reliable. This behaviour is observed for FanoADC-Stieltjes calculations [123, 124]

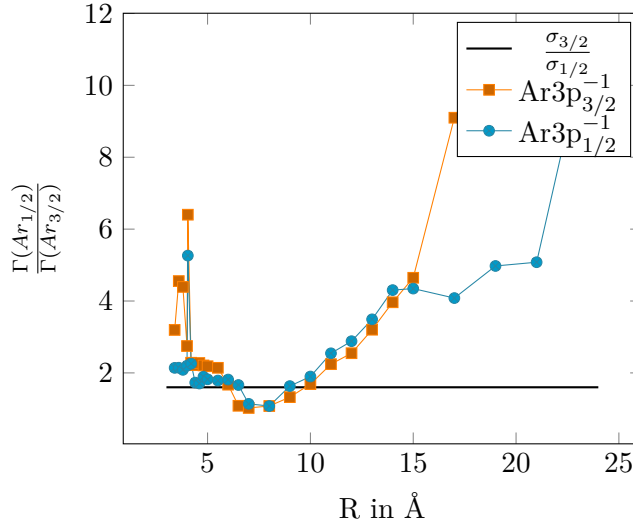


Figure 12.3.: Partial decay width ratios for decay channels of the same final state on the initially ionized atom compared to the experimentally observed ratio between the ionization cross sections of the xenon atom. The latter value provides the asymptotic limit.

in most systems.

Equation (11.11) provides the asymptotic limit for the ratios of the decay widths with different quantum numbers at the initially ionized atom. Approximated from the atomic ionization energies of argon and the experimentally determined value of $\chi = 2.05$ [125] the asymptotic ratio of these partial decay widths is given by $\frac{\Gamma_{1/2}}{\Gamma_{3/2}} = 0.52$. This number is compared to the results from the FanoADC calculation in Figure 12.4.

As for the ratio between the ionization cross sections the ratios of the partial decay widths for medium interatomic distances between 5 \AA and 15 \AA seem to be reasonably well described. At shorter distances the ratio is higher than expected from the asymptotic limit. At larger distances the description should be expected to be better, but it is worse for the $\text{Xe}5p_{3/2}^{-1}$ case.

Therefore, the partial decay width calculations in the range between distances up to 10 \AA can be assumed to be trustworthy, while the partial decay widths for larger distances would need a more elaborate treatment.

12.3. Possible Improvements

The currently implemented projectors for the partial decay widths have already previously been shown not to be trustworthy in all cases. Therefore, a more elaborate definition of the channel projection operators might improve the results. Additionally, a larger basis set might improve the results. A further augmentation would increase the basis set size in the energy regions of the emitted electron and further ghost atoms

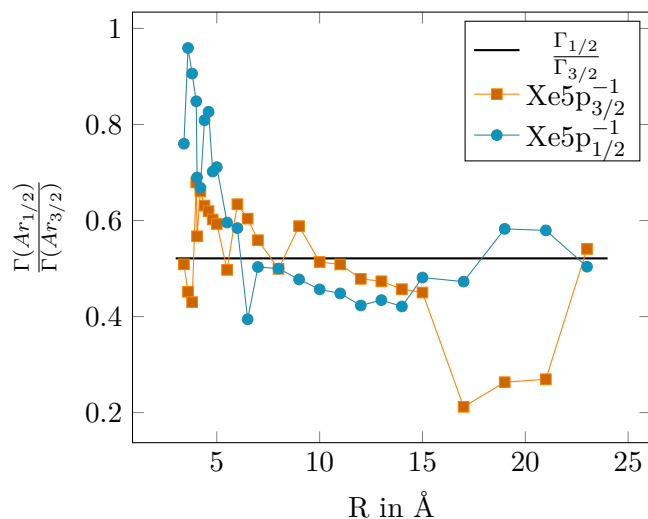


Figure 12.4.: Partial decay width ratios compared to the asymptotic limit provided by equation (11.11).

located between the argon and the xenon atom might prevent the unexpected behaviour at distances larger than 10 \AA , if the drawback of the current setup is the loss of overlap between the basis functions. However, at the current state of implementation the computational limit is reached and larger basis sets can not be investigated with the computer clusters of the group.

13. Competing Processes in Heteroatomic Noble Gas Clusters

The modelling of secondary electron spectra originating from ICD and ETMD3 processes are carried out using the program HARDRoC [16]. It is based on the model of pairs and triples explained in chapter 10 and is applied to a given cluster structure. The decay widths obtained are proportional to the probability of the underlying decay. The experimental spectra are obtained from a multitude of distinct measurements. Hence, for a reasonable large number of measurements, a distribution with the same statistical behaviour as for the decay width calculation in the model of pairs and triples is achieved. Therefore, the experimental spectra can be directly compared with the theoretically obtained spectra.

The energies of the secondary electrons are calculated using equation 10.3. The single ionization energies can be obtained in two different ways. They can be estimated by the atomic ionization energies in Table A.2 corrected by energetic shifts given in Table A.3 in order to take the effect of the cluster environment into account. Alternatively, their source can be the single ionization spectra measured at the same time and the same conditions as the electron-electron coincidence experiment. The latter approach is to be preferred, since the energy shifts of Table A.3 are obtained from analysis of homonuclear cluster's ionization spectra and hence the values only give a first approximation to the real energetic shift in heteronuclear cluster. Since both, the ICD and primarily the ETMD3 occur at interfaces, it is crucial for a good modelling to describe the ionization energies of these atoms as accurate as possible.

The decay widths Γ can either be obtained from the asymptotic expressions in equations (5.18) and (5.22) using the atomic properties given in Table A.2 or from a fit to decay widths obtained from FanoADC-Stieltjes calculations.

In the following sections, two different heteronuclear clusters are investigated illustrating different effects on the secondary electron spectra. In the case of ArXe clusters, the focus is set on the investigation of how spin-orbit coupling affects the secondary electron spectra. Furthermore, I will investigate the influence of the cluster size and number of argon shells around the xenon core and the effects of the basic structure of the cluster and discuss the difference between the spectra obtained from clusters having an icosahedral and fcc structure. In the case of NeAr clusters I will focus on the bidirectional dependence of the ICD spectra of the competing NeNe-ICD and NeAr-ICD processes

and different arrangements of neon atoms around the argon core.

13.1. ArXe-Clusters

In heteronuclear ArXe clusters, ICD and ETMD3 are energetically accessible after creation of an Ar3s vacancy. The final states of these processes are characterized by $\text{Ar}3p^{-1}\text{Xe}5p^{-1}$ and $\text{Xe}5p^{-1}\text{Xe}5p^{-1}$, respectively. As discussed in section 10.1, all ICD channels are closed for distances shorter than 10 Å. From this perspective, the slower ETMD3, which is energetically accessible at equilibrium geometries of the ArXe_2 trimer, should be observable in experiment [126].

In the following, first the basic cluster and spin-orbit coupling effects are investigated using easiest model structures. Afterwards, cluster structures are studied in comparison to experimental data.

13.1.1. One Argon Atom on a Xenon Surface

In order to model the decay processes in clusters, a cutout of a cluster is modelled by layers of xenon atoms in an fcc structure. On these layers, one argon atom is placed in either a fcc or an hcp position, as shown in Figure 13.1. The atomic distances are assumed to equal the sum of the corresponding van der Waals radii given in Table 6.2. The results of this section were published in [25].

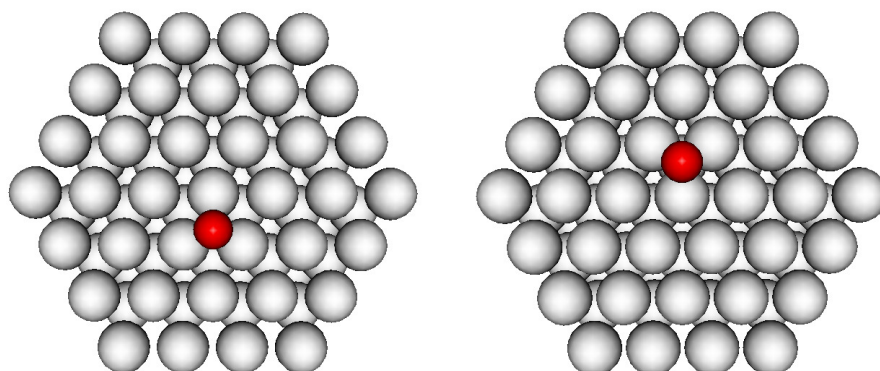


Figure 13.1.: Model structures of ArXe clusters.

Left panel: Argon atom placed in an fcc position on xenon atom layers in fcc structure.

Right panel: Argon atom placed in an hcp position on xenon atom layers in hcp structure.

Since ionized atoms in clusters are stabilized by the cluster environment, the atomic ionization energies in Table A.1 as such are no good approximation to the ionization

Parts of this section have already been published in

E. Fasshauer, M. Pernpointner, and K. Gokhberg

Interatomic decay of inner-valence ionized states in ArXe clusters: Relativistic approach

J. Chem. Phys. **138**, 014305 (2013)

Copyright 2013, American Institute of Physics.

energies of atoms in clusters. In order to take care of this stabilization effect, the ionization energies are corrected by experimentally observed shifts between atomic and cluster ionization energies of homonuclear clusters given in Table A.3 in the Appendix. These shifts do not account for higher or lower charge stabilization by neighbouring atoms of other elements. The potential curves of initial and final states estimated from these shifted ionization energies are shown in Figure 13.2.

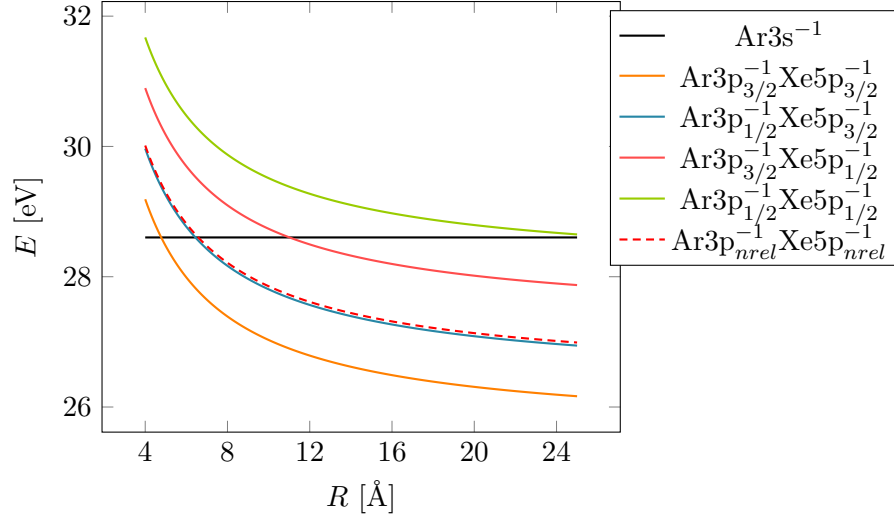


Figure 13.2.: Initial and final state energies of the ICD channels of ArXe in the model of pairs calculated from shifted atomic ionization energies. Both, the four relativistic channels and the non-relativistic estimate are shown. From the distance on, where the final state energy is lower than the initial state energy, the decay channel is open.

Compared to the results obtained using unshifted ionization energies of section 10.1 the channel opening distances are shorter. In detail, they are 4.78 Å, 6.44 Å, 11.02 Å and 27.19 Å for the $\text{Ar}3p_{3/2}^{-1}\text{Xe}5p_{3/2}^{-1}$, $\text{Ar}3p_{1/2}^{-1}\text{Xe}5p_{3/2}^{-1}$, $\text{Ar}3p_{3/2}^{-1}\text{Xe}5p_{1/2}^{-1}$ and $\text{Ar}3p_{1/2}^{-1}\text{Xe}5p_{1/2}^{-1}$ channel, respectively. The channel opening distance of the non-relativistic estimate is 6.58 Å. This means that all ICD channels are still closed at the equilibrium distance of the ArXe dimer being 4.04 Å. But inside a cluster, also larger distances are realized. Already for the next-nearest neighbours the $\text{Ar}3p_{3/2}^{-1}\text{Xe}5p_{3/2}^{-1}$ channel is open. Hence, the ICD process can not be neglected in the further discussion.

The potential curves of the initial and final states of the ETMD3 process are shown in Figure 13.3, where d denotes the distance between the two xenon atoms.

In the applied model, the final state energies of the $\text{Xe}5p_{1/2}^{-1}\text{Xe}5p_{3/2}^{-1}$ and the $\text{Xe}5p_{3/2}^{-1}\text{Xe}5p_{1/2}^{-1}$ are degenerate, but the channels differ by the quantum numbers of the electron donating and electron emitting atom. Hence, the decay widths are not necessarily equal and need to be treated separately. For all distances larger than the equilibrium distance of 4.32 Å all ETMD3 channels are open. Therefore, the decay can occur with nearest neighbours,

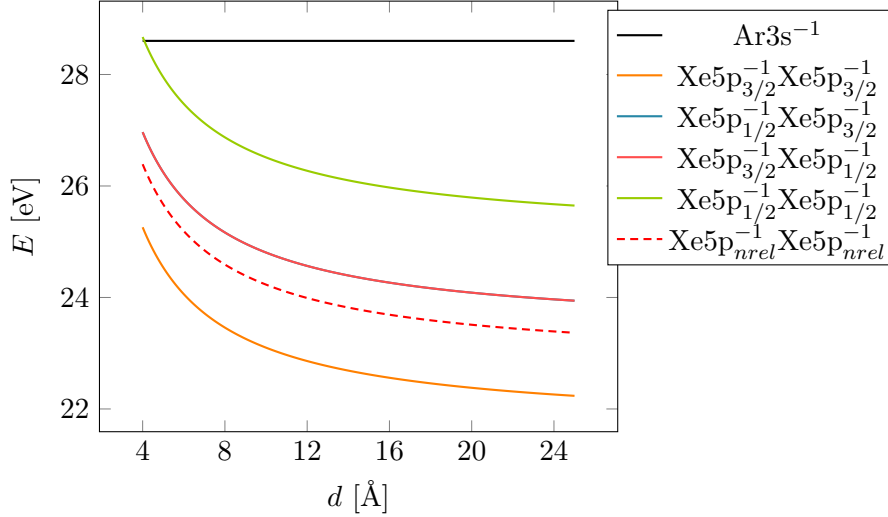


Figure 13.3.: Initial and final state energies of the ETMD3 channels in the model of triples calculated from shifted atomic ionization energies.

which enables the highest possible decay width.

Considering only the channel opening distances, it is not clear, whether one of the two competing processes is much faster and would hence dominate an experimental spectrum. Another aspect of clusters is the multitude of possible decay partners. For the ICD, the number of decay partners, considering nearest neighbours only, equals the number of xenon atoms N_{Xe} , while for the ETMD3 process the number of triples for each argon atom is given by $N_{Xe}(N_{Xe} - 1)$. This means that the ETMD3 is statistically favoured above the ICD in clusters with xenon cores consisting of more than one xenon atom.

The decay widths of the ICD and ETMD3 processes for the model structures were calculated using the model of pairs and triples introduced in chapter 10. Here, the model structures were decomposed into all possible pairs and triples. For each pair and triple with an energy transfer distance R smaller than 11 \AA , the decay width was evaluated using the asymptotic approximations of equations (5.18) and (5.22) and the experimentally obtained atomic properties shown in Tables A.1, A.2 and A.3, and absolute ionization cross sections from reference [127]. For the energy transfer distance R of the ETMD3 process the reference point was chosen to be the center of mass of subsystem S_1 . Then, the decay widths of both model structures were combined and normalized to one initially ionized argon atom.

The resulting secondary electron spectra of the ICD and ETMD3 processes are shown in Figure 13.4 for the relativistic and the non-relativistic estimates. It has to be kept in mind that the non-relativistic results intrinsically incorporates scalar-relativistic effects in the values obtained experimentally.

In the relativistic treatment (upper panel), the ETMD causes three main peaks at

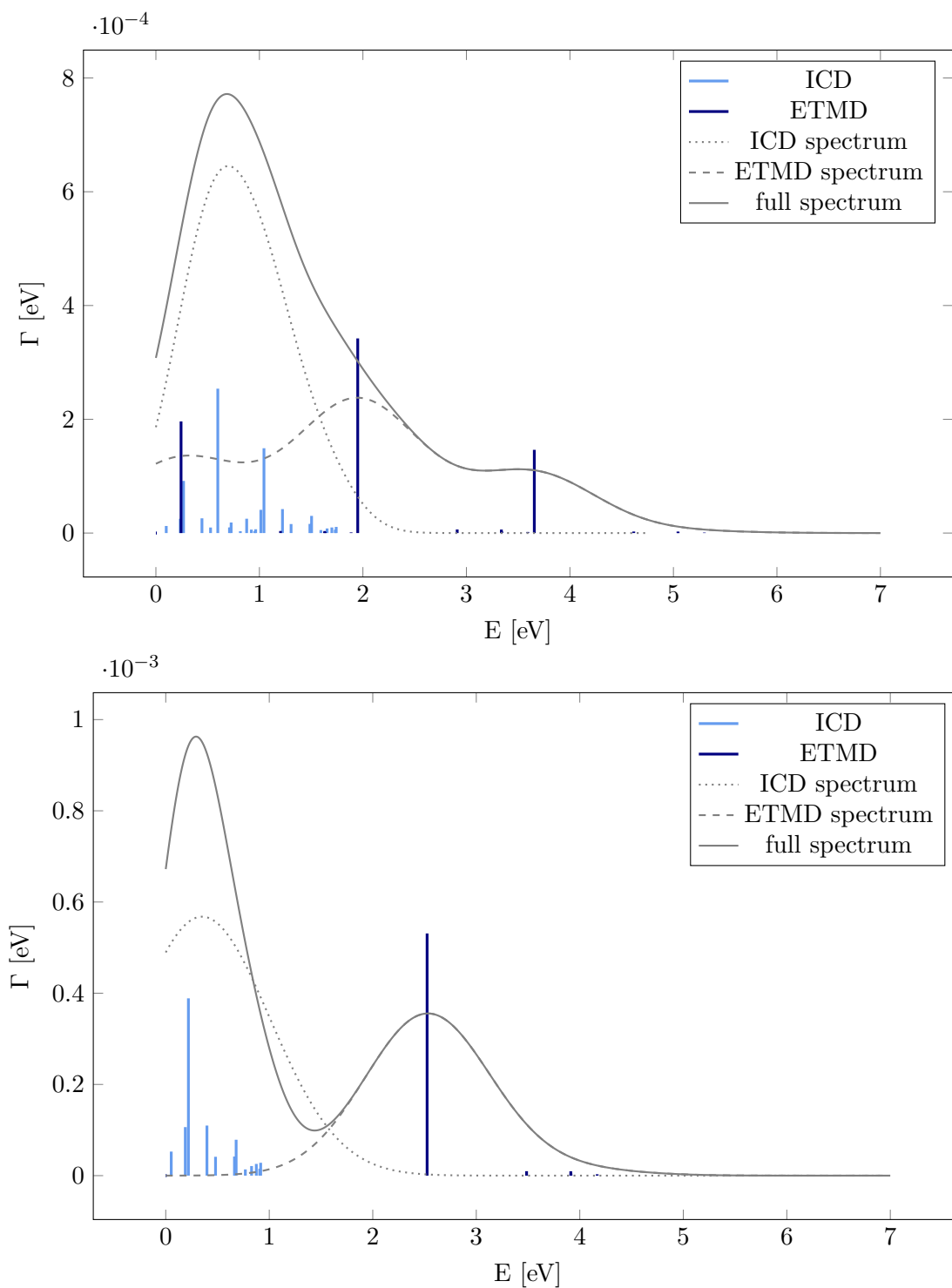


Figure 13.4.: ICD and ETMD3 secondary electron spectra for the model structures of Figure 13.1. To guide the eye of the reader, the spectra were folded with Gaussians of 300 meV and 600 meV for the ICD and ETMD, respectively.

Upper panel: Relativistic spectrum. Lower panel: Non-relativistic spectrum.

Table 13.1.: Decay widths of the ICD and ETMD processes of the model structures.

	Γ [eV]		τ [ps]	
	rel.	nrel.	rel.	nrel.
ICD	$8.3 \cdot 10^{-4}$	$9.2 \cdot 10^{-4}$	0.79	0.71
ETMD	$7.2 \cdot 10^{-4}$	$5.6 \cdot 10^{-4}$	0.92	1.18
total	$15.5 \cdot 10^{-4}$	$14.8 \cdot 10^{-4}$	0.43	0.44

0.243 eV, 1.950 eV and 3.656 eV corresponding to decay processes involving nearest neighbours. The peak at 3.343 eV originates from the $\text{Xe}5p_{3/2}^{-1}\text{Xe}5p_{3/2}^{-1}$ channel, whereas the peak at 1.637 eV originates from the sum of the energetically degenerate $\text{Xe}5p_{1/2}^{-1}\text{Xe}5p_{3/2}^{-1}$ and $\text{Xe}5p_{3/2}^{-1}\text{Xe}5p_{1/2}^{-1}$ channels. The $\text{Xe}5p_{1/2}^{-1}\text{Xe}5p_{1/2}^{-1}$ channel evokes the peak at 0.243 eV. The ICD process causes a multitude of smaller peaks at kinetic energies of the emitted electron below 1.8 eV. These originate from the $\text{Ar}3p_{3/2}^{-1}\text{Xe}5p_{3/2}^{-1}$ and the $\text{Ar}3p_{1/2}^{-1}\text{Xe}5p_{3/2}^{-1}$ channels of pairs characterized by different distances. The folded spectrum shows a large peak close to zero with two shoulders caused by the ETMD3 process.

In the non-relativistic treatment (lower panel), the secondary electron spectrum shows only one main ETMD peak at 2.525 eV corresponding to the $\text{Xe}5p^{-1}\text{Xe}5p^{-1}$ channel. At energies <1.0 eV the ICD peaks are shown. These correspond to the $\text{Ar}3p-1\text{Xe}5p^{-1}$ channel only and hence stem from pairs of different distances. The combined, folded spectrum shows two distinct peaks for the ICD and ETMD3 process.

In order to guide the eye of the reader, the spectra were folded with Gaussians of 300 meV and 600 meV for the ICD and ETMD3, respectively. The broadening of the ICD peak due to dynamics was estimated from the potential curve of the ArXe dimer. For the ETMD3, the dynamics are by far more complex and since no reasonable calculation was at hand, the broadening was estimated to be twice the width of the ICD process.

The total calculated decay widths are shown in Table 13.1. From these numbers, the spin-orbit coupled results are not equal to the results obtained in the non-relativistic estimate, but similar to them. This can be explained by the multitude of channels, which open at different distances and therefore, the basis of pairs and triples included in the open channel calculations, differ from each other. In both cases, the relativistic and the non-relativistic treatment, the decay width of the ICD is slightly larger than the one of the ETMD3 process. Since all lifetimes are three orders of magnitude smaller than the radiative lifetime of the Ar3s vacancy of 4.684 ns, these processes outrule the radiative decay. Because of the comparable decay widths of ICD and ETMD3, both processes should be experimentally observable.

Conclusions

The above discussion embarked on the investigation and calculation of electron emission spectra of mixed ArXe clusters produced in electronic decay reactions following ionization of inner-valence electrons of Ar. Together with a suitable cluster model and including energy shifts due to the environment as well as statistical effects, individual and total electron emission spectra were generated. Due to the presence of xenon, spin-orbit coupling was shown to play a major role for an adequate description of energies, ICD and ETMD thresholds and total lifetimes of the individual processes and can not be neglected. The relativistic calculations of the ICD spectrum show that the ICD electrons are expected to have kinetic energies below 2 eV. The corresponding ETMD peak is centered at 2 eV and shows a pronounced overlap with the ICD feature. These results are in stark contrast to the non-relativistic total spectrum exhibiting two well separated structures. In the relativistic formulation, the ratio of the ETMD to ICD intensity is determined to be 0.87 underlying the importance of both decay processes in ArXe clusters. If several Ar layers surround the core of xenon atoms, this ratio is expected to decrease. This is due to the fact that ICD, an energy-transfer process, can happen anywhere in the bulk, while ETMD involves electron transfer and, therefore, proceeds exclusively at the argon-xenon interface. It should be noted that experimental peak positions and intensities can be slightly different due to a number of approximations inherent in the model such as the choice of initial and final state energies, a fixed geometry and the exclusion of dynamic processes.

13.1.2. Cluster Structures

In the following section, decay widths for complete shell cluster structures of fcc and icosahedral structure are investigated. The structures were obtained using the scripts `icocclus` and `fccclus` described in the Appendix C.3 and C.4.

Dependence on Cluster Size and Number of Argon Layers

Consider a xenon cluster described by a complete icosahedral or dodecahedral structure with one additional layer of argon. With increasing cluster size, the *surface-to-bulk* ratio decreases. Both the ICD and ETMD are interface effects and hence the decay widths per ionized argon atom can be expected to increase and finally to converge to some value. However, for an ETMD the electron donor atom needs to be in proximal vicinity in order to have a significant decay width. Therefore, the decay widths of the ICD and ETMD are expected to increase differently with increasing cluster size.

Additionally, for a fixed xenon core size, different numbers of surrounding complete shells of argon atoms are possible. Since the ETMD is a pure interface effect, its decay width per initially ionized atom can be expected to decrease with an increasing number of

Table 13.2.: ICD and ETMD decay widths in eV for ArXe icosahedral clusters with increasing core cluster size and 1 – 4 layers of argon. In the last part the percentage of ETMD compared to the total decay is given.

	c_{core}	1 layer	2 layers	3 layers	4 layers
ICD	2	$1.880 \cdot 10^{-4}$	$1.336 \cdot 10^{-4}$	$7.211 \cdot 10^{-5}$	$4.220 \cdot 10^{-5}$
	3	$3.207 \cdot 10^{-4}$	$2.219 \cdot 10^{-4}$	$1.299 \cdot 10^{-4}$	$8.117 \cdot 10^{-5}$
	4	$4.004 \cdot 10^{-4}$	$2.812 \cdot 10^{-4}$	$1.733 \cdot 10^{-4}$	$1.132 \cdot 10^{-4}$
	5	$4.522 \cdot 10^{-4}$	$3.230 \cdot 10^{-4}$	$2.060 \cdot 10^{-4}$	$1.388 \cdot 10^{-4}$
	6	$4.879 \cdot 10^{-4}$	$3.536 \cdot 10^{-4}$	$2.311 \cdot 10^{-4}$	$1.592 \cdot 10^{-4}$
ETMD3	2	$1.187 \cdot 10^{-4}$	$3.722 \cdot 10^{-5}$	$1.685 \cdot 10^{-5}$	$9.101 \cdot 10^{-6}$
	3	$1.969 \cdot 10^{-4}$	$7.133 \cdot 10^{-5}$	$3.581 \cdot 10^{-5}$	$2.087 \cdot 10^{-5}$
	4	$2.429 \cdot 10^{-4}$	$9.507 \cdot 10^{-5}$	$5.072 \cdot 10^{-5}$	$3.104 \cdot 10^{-5}$
	5	$2.726 \cdot 10^{-4}$	$1.119 \cdot 10^{-4}$	$6.210 \cdot 10^{-5}$	$3.929 \cdot 10^{-5}$
	6	$2.931 \cdot 10^{-4}$	$1.242 \cdot 10^{-4}$	$7.092 \cdot 10^{-5}$	$4.597 \cdot 10^{-5}$
% ETMD3	2	38.71	21.79	18.94	17.74
	3	38.05	24.32	21.60	20.45
	4	37.76	25.27	22.64	21.52
	5	37.61	25.72	23.16	22.07
	6	37.53	26.00	23.48	22.41

argon shells. The same behaviour is expected for the ICD process. However, since the process can also occur with next-nearest neighbours as decay partners, the decrease of the decay width is expected to be less pronounced.

These two hypotheses are tested in this chapter for xenon core sizes with $c = 2 - 6$ and 1 – 4/3 additional layers of argon atoms around it, for both icosahedral and dodecahedral clusters. The calculations were performed using the program HARDRoC [16] and the same atomic data as used in the preceding section given in Tables A.1, A.2 and A.3. Here, in contrast to the previous model structures, the argon atom is chosen as the reference point for the energy transfer distance R of the ETMD3.

The results are shown in Tables 13.2 and 13.3 for the icosahedral and dodecahedral clusters, respectively. From this data the expected trend of increasing decay width with increasing cluster size for both ICD and ETMD processes and icosahedral and dodecahedral structures are proven. The same holds for the decrease of the decay width per argon atom and the contribution of the ETMD process to the total decay with increasing number of surrounding argon layers. However, the contribution of the ETMD to the total decay with increasing xenon core size is on first sight unexpected. For one layer of argon atoms the ETMD contribution decreases with increasing cluster size, while it increases for more argon layers. Here, two contrarian effects play a role. On the one hand, the number of xenon atoms in the interface shell increases compared to the number

Table 13.3.: ICD and ETMD decay widths in eV for ArXe dodecahedral clusters with increasing core cluster size and 1 – 3 layers of argon. In the last part the percentage of ETMD compared to the total decay is given.

	c_{core}	1 layer	2 layers	3 layers
ICD	2	$1.856 \cdot 10^{-4}$	$1.437 \cdot 10^{-4}$	$7.877 \cdot 10^{-5}$
	3	$3.327 \cdot 10^{-4}$	$2.418 \cdot 10^{-4}$	$1.434 \cdot 10^{-4}$
	4	$4.227 \cdot 10^{-4}$	$3.099 \cdot 10^{-4}$	$1.933 \cdot 10^{-4}$
	5	$4.815 \cdot 10^{-4}$	$3.579 \cdot 10^{-4}$	$2.309 \cdot 10^{-4}$
	6	$5.226 \cdot 10^{-4}$	$3.931 \cdot 10^{-4}$	$2.597 \cdot 10^{-4}$
ETMD	2	$1.727 \cdot 10^{-4}$	$5.416 \cdot 10^{-5}$	$2.452 \cdot 10^{-5}$
	3	$2.738 \cdot 10^{-4}$	$9.920 \cdot 10^{-5}$	$4.979 \cdot 10^{-5}$
	4	$3.318 \cdot 10^{-4}$	$1.299 \cdot 10^{-4}$	$6.928 \cdot 10^{-5}$
	5	$3.687 \cdot 10^{-4}$	$1.514 \cdot 10^{-4}$	$8.403 \cdot 10^{-5}$
	6	$3.941 \cdot 10^{-4}$	$1.671 \cdot 10^{-4}$	$9.539 \cdot 10^{-5}$
% ETMD	2	48.20	27.37	23.74
	3	45.14	29.09	25.77
	4	43.98	29.53	26.39
	5	43.37	29.72	26.68
	6	42.99	29.83	26.86

of argon atoms in the interface layer. This statistically prefers the ETMD over the ICD. On the other hand, for small xenon cores not all ICD channels are open for most of the pairs. With increasing cluster size for some atom pairs additional channels will be open compared to the smaller clusters. This favours the ICD over the ETMD, where all channels are open for each possible triple. The latter effect is most pronounced for small clusters as well as for argon atoms in the interface region and therefore, it dominates the trend for one layer of argon atoms, whereas for more argon layers the statistical effects benefit the ETMD over the ICD.

Analyzing the absolute decay width values for the icosahedral and dodecahedral cluster structures it can be seen that the ICD decay widths are comparable for both skeletal structures. Further, the ETMD decay widths of the dodecahedral structures are larger than of the icosahedral structures. Hence, also the ETMD contribution to the total decay width is higher for the dodecahedral structures. This feature can be explained by the different surfaces of the icosahedral and dodecahedral (fcc) clusters. Both clusters have triangular surfaces. However, the dodecahedral cluster has less triangular surfaces than the icosahedral cluster and some square surfaces instead. In the latter, the interatomic distances of argon and xenon atoms differ slightly from the interatomic distances for argon atoms positioned on triangular surfaces. Additionally, the number of nearest neighbours and hence of triples significantly contributing to the decay width

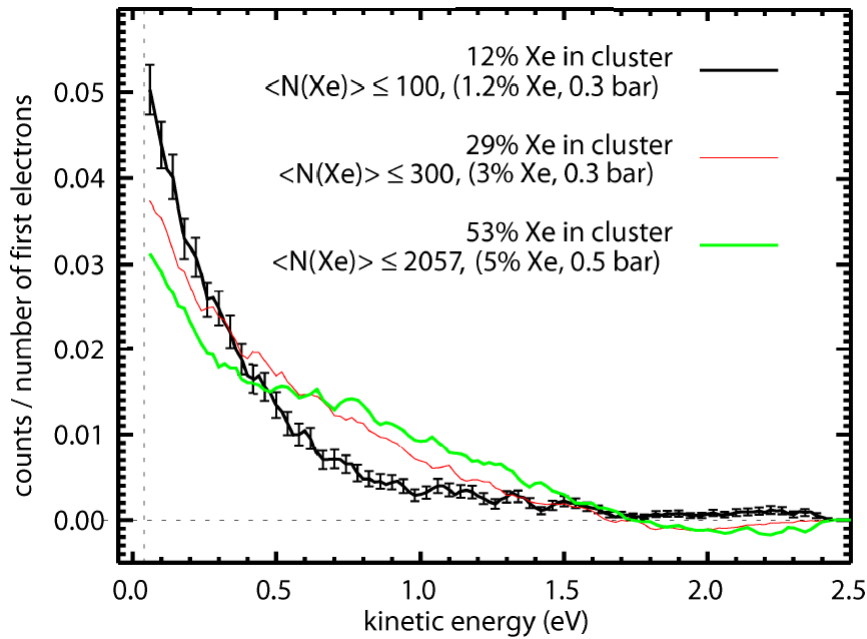


Figure 13.5.: Experimental secondary electron spectra of different ArXe cluster ensembles.

Table 13.4.: Experimental ionization energies inside the ArXe clusters [85]. These ionization energies are the average values of broad distributions.

	SIP [eV]	FWHM [eV]
Xe5p _{3/2}	11.5	1.20
Xe5p _{1/2}	13.0	0.40
Ar3p	15.3	0.60
Ar3s	28.7	0.35

is higher than on the triangular surfaces. Therefore, the ETMD decay widths are larger in dodecahedral clusters than in icosahedral clusters.

Modelling Experimental Spectra

The secondary electron spectra of three ArXe cluster ensembles were measured by Förstel and Hergenbahn in 2012 (see Figure 13.5). They studied mean xenon core sizes were ≤ 100 , ≤ 300 and ≤ 2057 atoms. The number of additional argon layers is unknown. At the same experimental conditions the single ionization spectra were measured. Therefore, the results given in Table 13.4 are going to be used for the modelling of the secondary electron spectra. It has to be noted, that these numbers are average values of very broad distributions.

In the following the two larger cluster ensembles are going to be modelled by cluster

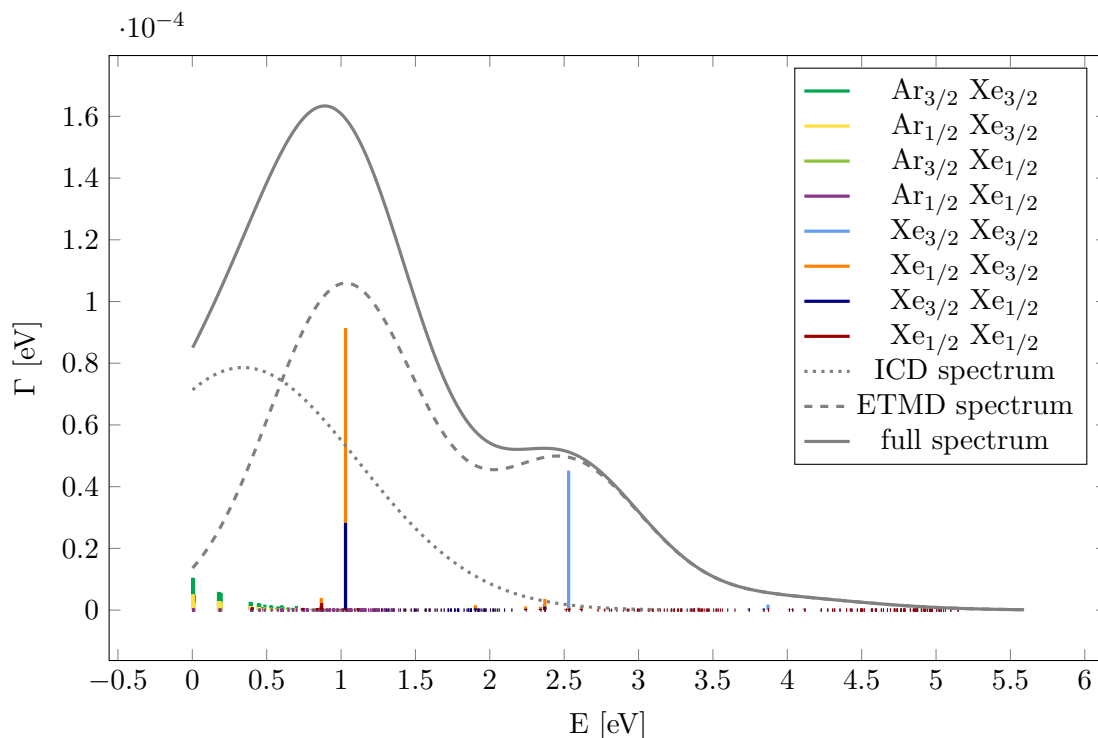


Figure 13.6.: Calculated secondary electron spectrum of the icosahedral 309 xenon core cluster with one additional layer of argon atoms. Due to usage of experimental ionization energies of mixed clusters the peaks are shifted to lower energies compared to the spectra in Figure 13.4.

structures characterized by a 309 and 923 xenon core atoms surrounded by one additional layer of argon atoms. The latter was chosen, because the calculations evaluating the ETMD decay width were computationally too expensive for a xenon core of 2057 atoms in the current implementation. The cluster with a 309 xenon atoms core can be expected to have an icosahedral structure, while the larger cluster might be of dodecahedral shape. Therefore, in the latter case, both the fcc and the icosahedral structure are investigated. The calculated spectrum of the 309 atom icosahedral model cluster is shown in Figure 13.6. The spectra of the different channels are plotted independently and the peak heights are not added.

Compared to the spectra of the principle models in Figure 13.4, the peak positions are shifted to lower kinetic energies of the emitted electron by ≈ 1 eV. This at the same time leads to channel closings, especially for the ICD. Therefore, the spectrum is dominated by the ETMD process.

The secondary electron spectra for the large cluster with a xenon core consisting of 923 atoms are shown in Figure 13.7. In the upper panel, the spectrum of the icosahedral cluster is illustrated. As shown in the previous section, the increased number of bulk

atoms leads to ICD channel openings. Therefore, the ICD peak is here more pronounced than compared to the smaller cluster.

The spectrum of the dodecahedral cluster shape of fcc structure is shown in the lower panel of Figure 13.7. As already qualitatively discussed in the preceding section, also next-nearest neighbours can significantly contribute to the total ETMD decay width. This property is not observed in the easiest model structures, because those model structures are only capable of modelling the behaviour of an argon atom on a triangular and not a square surface.

Overall, the ICD dominates the secondary electron spectrum. However, this is caused by the ICD peaks being centered at around 0.5 eV, while the ETMD peaks are spread over a large energy range. Additionally, with three involved atoms in the ETMD3 and hence more degrees of freedom, dynamic effects are expected to have a larger impact on the ETMD spectra than in the ICD spectra, which leads to an additional broadening estimated in the folding of the spectra.

Since the ionization energies used for the modelling are mean values, they might not represent the involved atoms correctly. The argon atoms with the largest contributions to the ICD and ETMD decays are the atoms at the interface region. However, it is not evident that the core is surrounded by one argon layer only. Vacancies in the interface argon atoms might due to their interaction with the neighbouring xenon atoms be better stabilized than the average argon atom in the cluster in case of several layers. Additionally, vacancies in the interface xenon atoms might be less stabilized than in the average xenon atom. Lower ionization energies of the Ar3s initial state would shift the spectrum to lower kinetic energies, while lower ionization energies of the Ar3p would shift the ICD spectrum to higher kinetic energies. Higher ionization energies of the Xe5p region would shift both the ICD and the ETMD spectra to lower kinetic energies. Hereby, the ETMD spectrum would have a larger shift. These contrary trends make it impossible to determine the accurate peak positions for the clusters without extensive ionization energy studies for different atomic positions inside the clusters. Comparison to the experimental spectrum in Figure 13.5 suggests a shift to lower kinetic energies. This might also reflect the presence of shorter interatomic distances in the cluster, which might be caused by dynamical rearrangements of the atoms due to the introduced vacancy.

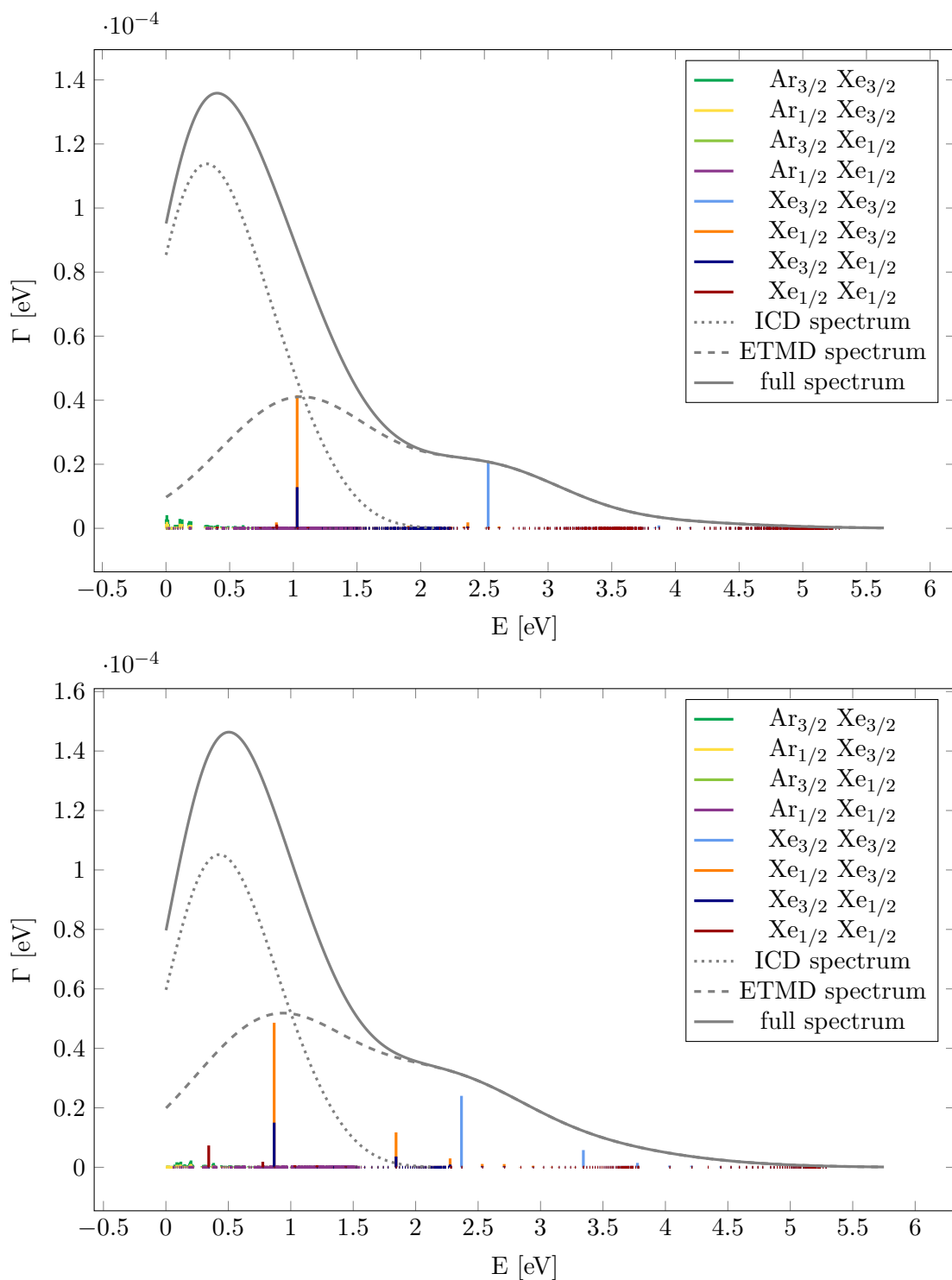


Figure 13.7.: Secondary electron spectra of ArXe clusters with a xenon core consisting of 923 atoms and one additional layer of argon atoms.

Upper panel: Icosahedral structure. Lower panel: Dodecahedral cluster with fcc structure.

13.2. Structure Determination of NeAr Clusters

In general, the structure determination of heteronuclear noble gas clusters is an unsolved problem. However, the maximization of the cohesive energy suggests a core of argon atoms surrounded by neon atoms. Electron-electron coincidence experiments proved their existence by the presence ICD electron from NeAr-ICD processes [128].

The clusters consist of neon and argon atoms. Since an inner-valence vacancy in the Ne2s can decay both via NeNe-ICD and NeAr-ICD, both competing processes are expected to be observed in an experiment. In the literature most investigations focussed on the NeAr-ICD because it, until recently, was not possible to measure the NeNe-ICD as well [86]. From these studies, large NeAr clusters established by coexpansion and consisting of an argon core with approximately 1000 atoms were determined to have a core-shell structure [128, 129] and to have a temperature of 40 – 50 K [129]. In his PhD thesis, Barth suggested the possibility to gain information about the cluster structure from the efficiency of the NeAr-ICD compared to the total decay of the Ne2s ionization. This was proposed to be possible, since the sum over the NeNe-ICD and NeAr-ICD previously had been shown to cause almost the total decay of the Ne2s vacancy [130]. The results indicated an increasing NeAr-ICD efficiency with increasing cluster size and hence a smaller surface-to-bulk ratio.

This structure determination, as is going to be shown, is indeed possible because the decay widths of the competing NeNe-ICD and NeAr-ICD processes are of the same order of magnitude and therefore both signals are observable. Additionally, as shown in the preceding section about ArXe clusters, the secondary electron spectrum crucially depends on the underlying structure.

Recently, the NeNe-ICD in NeAr clusters could be measured. Therefore, I will present the structure determination of NeAr clusters from ICD electron spectra by comparison of experimental spectra to theoretical calculations.

The chapter is structured as follows: First, the experimental results are presented and the computational details for the simulation of the ICD electron spectra are demonstrated. Afterwards, the manifold of different hypothetical cluster structures are introduced. Finally, the comparison between the experimental findings and theoretical predictions will be used for the determination of mean cluster structures.

13.2.1. Experimental Results

Recently, it was possible to measure the full secondary electron spectrum of NeAr clusters under different experimental conditions as shown in Figure 13.8 and Table 13.5.

The spectra have been normalized to the peak height of the NeAr-ICD signal. It can clearly be seen that for different experimental conditions the size of the NeNe-ICD peak varies compared to the NeAr-ICD peak as explicitly listed in Table 13.6. This can be

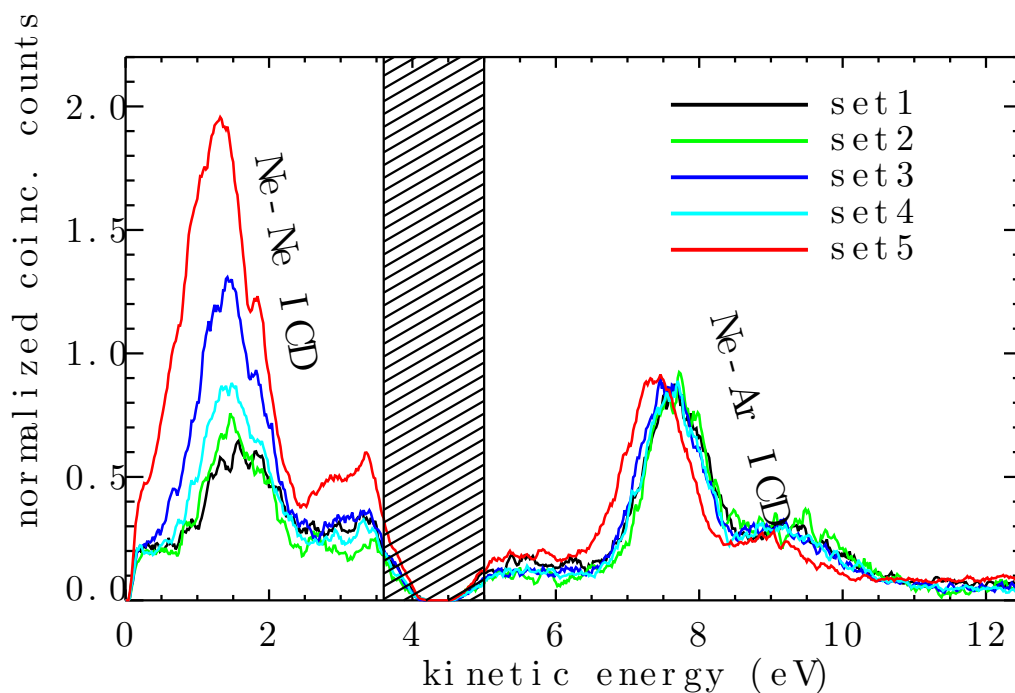


Figure 13.8.: Electron-electron coincidence spectra for NeAr clusters showing both NeNe-ICD and NeAr-ICD signals [86].

Table 13.5.: Assignment and expansion parameters of the five different cluster ensembles. Included are also the resulting mean cluster sizes calculated for the homogeneous species according to the formalism introduced by Hagena *et al.* [80]

designation	Ar content in initial mixture	expansion pressure	nozzle temperature	$\langle N \rangle_{Ne}$	$\langle N \rangle_{Ar}$
Set 1	1.7 %	0.26 bar	63 K	5	520
Set 2	7.4 %	0.40 bar	60 K	17	1850
Set 3	1.7 %	0.25 bar	57 K	7	810
Set 4	7.4 %	0.24 bar	58 K	6	670
Set 5	1.0 %	0.16 bar	54 K	3	380

explained both by different cluster sizes and by different cluster structures as I am going to show in this thesis. Both the main NeNe-ICD and the NeAr-ICD peak have a shoulder at higher energies. For NeAr dimers such a structure has been proposed to potentially stem from vibrations. However, such bound vibrational states above the ground state do not exist in neon dimers. I am going to show that this peak structure can be related

to ICD processes with next-nearest neighbours. Still, excitations to higher vibrational states might contribute to the peak structure as well.

Table 13.6.: Experimental results. Percentaged values are contributions to the respective total values. The cluster band onsets are given at half the peak height of the respective feature.

designation	Ar content in final cluster	onset Ar3p cluster band	onset Ne2p cluster band	Ne-Ar ICD contribution
Set 1	$47 \pm 10\%$	14.7 ± 0.1 eV	20.93 ± 0.08 eV	$63 \pm 7\%$
Set 2	$35 \pm 5\%$	14.6 ± 0.1 eV	20.86 ± 0.08 eV	$61 \pm 10\%$
Set 3	$21 \pm 4\%$	14.8 ± 0.1 eV	20.86 ± 0.08 eV	$38 \pm 5\%$
Set 4	$20 \pm 4\%$	14.8 ± 0.1 eV	20.86 ± 0.08 eV	$53 \pm 6\%$
Set 5	$8 \pm 2\%$	15.0 ± 0.1 eV	20.89 ± 0.08 eV	$28 \pm 3\%$

13.2.2. Computational Details

The energies of the secondary electron were calculated using the experimentally obtained ionization energies given in Table 13.7.

Table 13.7.: Experimental values used for the estimation of the decay widths [86].

indicator	value
SIP(Ne2s)	47.75 eV
SIP(Ne2p)	21.10 eV
SIP(Ar3p) _{c<3}	15.40 eV
SIP(Ar3p) _{c≥3}	15.20 eV

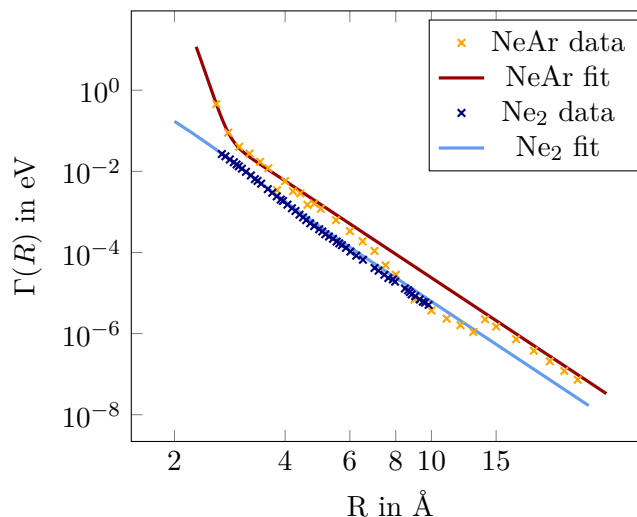
The distance dependence of the NeAr dimer was non-relativistically calculated with the Fano-Stieltjes procedure implemented in Dirac [15, 131] with an aug-cc-pV6Z basis set on both atoms. Additional basis functions of five *s*, *p* and *d* functions each of the KBJ type [99] were introduced on a ghost atom in the geometric center of the dimer.

Since inversion symmetry is until now not treated correctly, decay width data from the literature is used for the neon dimer [132], which was obtained with the same method and a comparable basis set as for the NeAr calculation. The resulting decay widths are shown in Figure 13.9 and the corresponding lifetimes are in Table 13.8 compared to other values from the literature.

The NeAr-ICD has a higher decay width than the NeNe-ICD, but since the actual value of the decay width strongly depends on the method and basis set used for its description, larger discrepancies are normal. For the decay width estimation of the NeAr clusters the values of the first column were chosen, because they were both calculated using the FanoADC-Stieltjes approach with comparable basis set size.

Table 13.8.: Decay widths of the NeNe-ICD and NeAr-ICD obtained using different theoretical methods and from experiment.

	Theory used		Theory Comp.		Experiment	
NeNe	60.4 fs	[132]	92 fs	[133]	150 ± 50 fs	[134]
NeAr	44.2 fs	This work	36 fs	[135]	–	

**Figure 13.9.:** Decay widths of the NeNe-ICD and NeAr-ICD processes fitted to curves for the decay width estimation of the NeAr clusters.

For each structure defined in the following section the NeNe-ICD and NeAr-ICD spectra were calculated using the program HARDRoC [16].

13.2.3. Hypothetical, idealized structures of the NeAr clusters

It is known that small noble gas clusters preferably form icosahedral structures, while with increasing cluster size a fcc structure becomes more favorable. This transition occurs at cluster sizes in the range from 750 to 3500 atoms [66, 136, 67]. For the simulations it is assumed that the clusters of all five experimental cluster sets have icosahedral structure. For all sets but set 2 the expansion conditions should result in clusters with mean sizes below 750 (see Table 13.5). Still, the mean size of the clusters of set 2 is well below 3500.

The actual cluster formation process is understood as follows. First, a three particle collision has to take place to form argon dimers. Subsequently, single atoms are added to the dimer due to collisions. At a later stage these clusters can also collide to form larger clusters. This process, called coagulation, becomes the dominant process for the formation of very large clusters. The experiment of Lundwall et al. [128] was interpreted

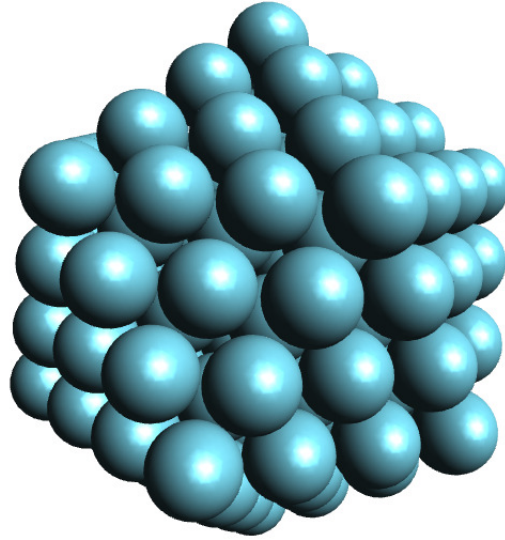


Figure 13.10.: An icosahedral argon cluster with an edge consisting of $c = 4$ atoms, containing 147 atoms, distributed over four shells. 55 atoms belong to the core, 12 are at the vertices, 60 in the edges and 20 inside the surfaces.

to show clusters consisting of an argon core with distinct, complete neon shells around it, which is plausible, since according to the sum of van der Waals energies, this should be the most stable kind of clusters. Therefore this structure is chosen as a starting point for the considerations about the average structure of the clusters.

In all structures considered throughout this thesis, the core is build as an icosahedral structure of argon atoms as shown in Figure 13.10. In this example, it has an edge length of $c = 4$ atoms and consists of $n_{Ar} = 147$ atoms, which can be calculated as [66]

$$n_{atoms} = \frac{10}{3}c^3 - 5c^2 + \frac{11}{3}c - 1. \quad (13.1)$$

For the construction of the structure the minimum distance between two argon atoms is assumed to be twice the van der Waals radius of argon $r_{Ar} = 1.88 \text{ \AA}$ [73]. In order to abide by this minimum distance in the case of two atoms in a surface position in different shells, the distance of two atoms in the edges is slightly increased.

As is going to be seen in the discussion, the outcome of the experiment cannot completely be explained by an argon core surrounded by complete neon shells. This leads to considerations of other structures with an argon core somehow surrounded by neon atoms. These are divided into three types, so that, in total, four different classes of cluster structures are studied as shown in Figure 13.11:

1. complete shells
2. incomplete shells around complete shells

3. caps

4. randomly arranged neon atoms around complete shells

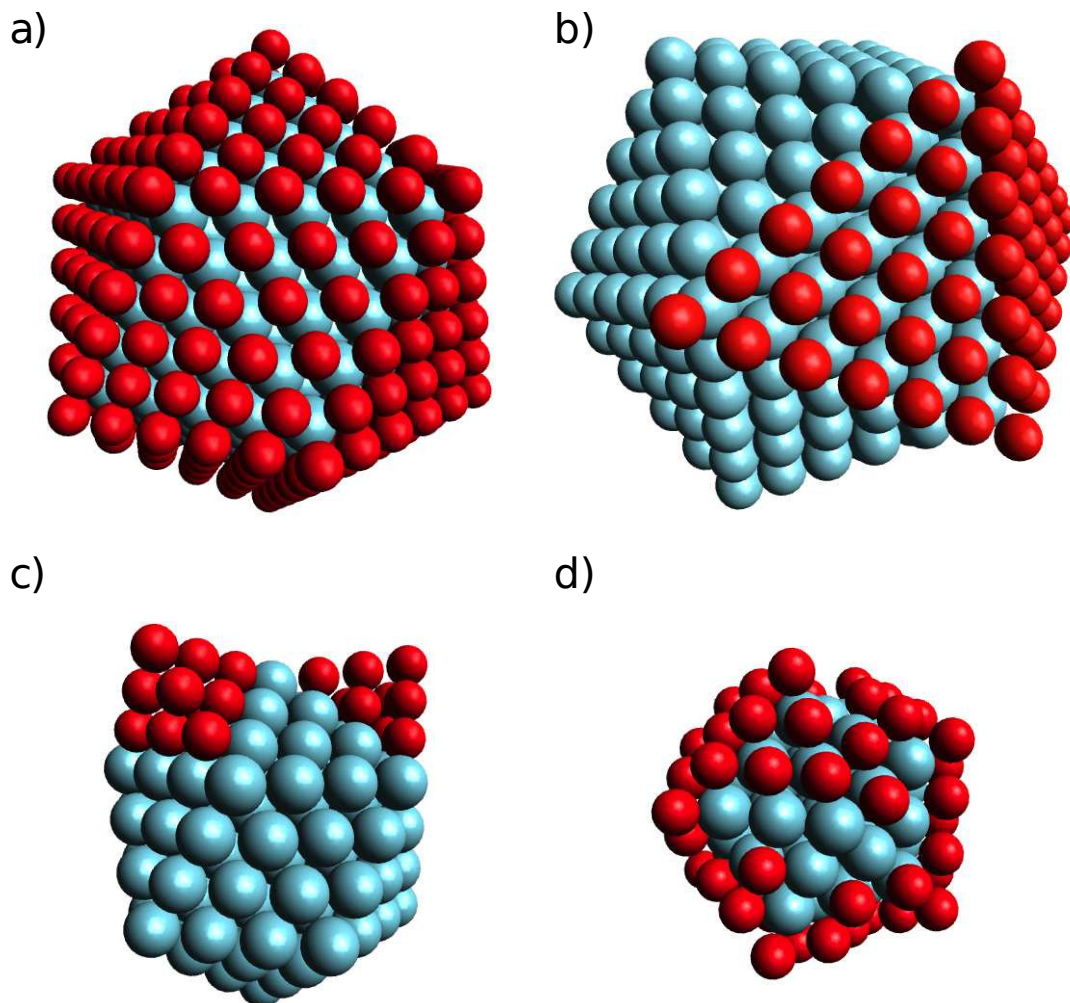


Figure 13.11.: Structure classes considered in our calculations.

a) complete shells, in this example $c = 5$ atoms with one layer neon atoms,

b) incomplete shells, in this example $c = 6$ atoms with two covered trinangular surfaces of neon,

c) caps, in this example $c = 4$ atoms with two caps,

d) randomly arranged neon atoms around a full shell cluster, here $c = 3$ atoms directly covered by neon atoms with an argon content of 47%.

In the case of an argon cluster with one or more complete shells of neon atoms around it, first the core structure is created and afterwards the outer shells are constructed around it, such that the minimum distance between a neon atom in the surface and an argon atom in the shell beneath is the sum over the van der Waals radii, where $r_{Ne} = 1.54 \text{ \AA}$ [73] (see Figure 13.11 panel a).

Not all experimentally determined argon contents in the mixed clusters fit to complete neon shells. Maintaining the idea of shells, the possibility of incomplete shells is considered. The cluster structures are created analogously to the complete shells except that not all triangular surface areas of the argon core are covered by neon atoms (for an example see Figure 13.11 panel b).

Another possibility is caps covering surface areas as shown in Figure 13.11 panel c. These structural elements do not lead to minimum energies for clusters, but they might explain a large number of neon-neon interactions compared to the number of neon-argon interactions in the experiments. The neon-neon distances within the caps are calculated in the same manner as described before for the (in-)complete shells. A whole manifold of different positionings of several caps are in principle possible, but calculations showed, that these different placements of caps did not change the ratios of NeAr- to NeNe-ICD for a constant number of caps. Since these structures cannot be distinguished by ICD spectra, the discussion is limited to structures containing different numbers of caps.

One could also think about neon atoms randomly arranged around a homonuclear or heteronuclear cluster with complete shells and randomly attached neon atoms around it as shown in Figure 13.11 panel d. It is constructed as a cluster with complete shells and afterwards adding neon atoms in random positions of the next layer until the requested n_{Ar}/n_{Ne} ratio is reached.

All these structures are idealized and highly symmetric, which reduces the computational cost. They were constructed using the set of `icoclus` scripts written for this purpose and explained in the Appendix C.3. Vibrations inside the clusters will change the interatomic distances and hence both the kinetic energies of the ICD electrons as well as the decay widths. As has been shown for NeAr [135], the ICD processes are faster than dynamical rearrangements, caused by Coulombic attraction after the initiating ionization, or vibrations. In case of the neon dimer, the ICD lifetime is of comparable size to the rearrangement time and hence influences the ICD electron spectra [137]. However, in clusters, the initially ionized atom interacts with more than one other atom, which leads to more decay partners. Hence, the decay width increases to first approximation linearly with the number of nearest neighbours. At the same time, the larger number of neighbours stabilizes the position of the initially ionized atom in space compared to the dimer. Therefore, it is assumed that the structures given above are good approximations to the decaying clusters.

13.2.4. Interpretation of the graphs

In order to have comparable numbers, for the theoretical estimations and experimental results the entities chosen for the characterization of each cluster structure and measurement are the argon content in the cluster and the amount of NeAr-ICD compared to the total ICD $\frac{\Gamma_{NeAr}}{\Gamma_{NeAr} + \Gamma_{NeNe}}$. Throughout the thesis, the same colour coding as for the

experimental spectra shown in Figure 13.8 is used, for which the numbers are listed in Table 13.6. The results are going to be plotted as in Figure 13.12 which is chosen as an example. The results for clusters of the class of an incompletely filled neon shell around an argon core with an edge size of $c = 2$ surrounded by one complete shell of neon atoms are shown. Here, the ratio of NeAr-ICD to total ICD is plotted against the argon content of the cluster. The results of the five different experimental conditions and their errors are shown by the coloured areas, where the colour corresponds to the set with the same colour as in Figure 13.8. Additionally plotted are the theoretical results for the different structures parted into first the classes of the structures and secondly by the size of the argon core. The higher the argon content is, the less of the 20 surfaces of the underlying complete shell is covered by either layer(s) or caps. The easiest way to interpret the graphs is to start from a complete shell and then covering one surface. This corresponds to the rightmost theoretical value within a group. Each step further to the left refers then to one more covered triangular surface with either caps or layers.

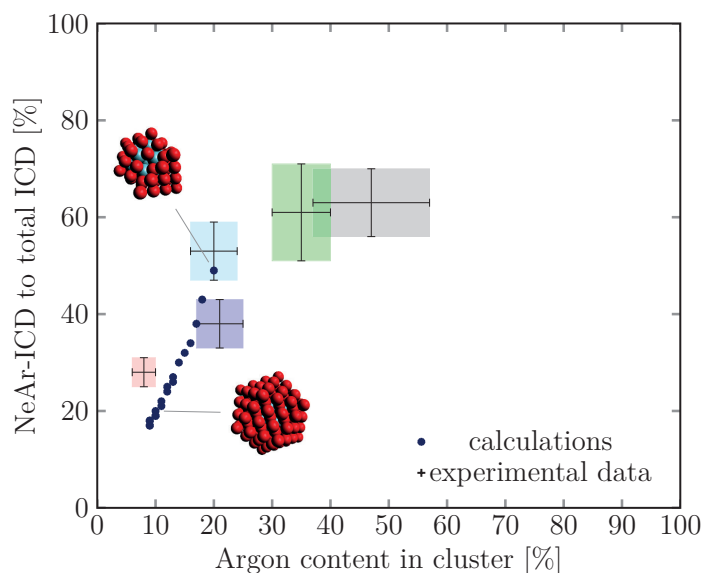


Figure 13.12.: NeAr-ICD to total ICD ratio plotted against the argon content in the cluster for both experimental results for all five sets of conditions as well as theoretical calculations for cluster structures with an incomplete outermost shell surrounding an argon core of $c = 2$ and one additional complete neon shell. For illustrative purposes, pictures of two structures are included at their respective theoretical values.

By looking for agreements of theoretical and experimental values possible structures are deduced. The agreements between experimental and theoretical results are evaluated

using the graphical distance from the experimental results

$$d = \sqrt{\Delta_{Ar}^2 + \Delta_{\Gamma}^2}, \quad (13.2)$$

where Δ_{Ar} and Δ_{Γ} denote the deviation of the argon content and the ratio of NeAr-ICD decay width and the total decay width, respectively. Only such structures are considered, where the argon content of the model structure lies within the error range of the experimental findings.

13.2.5. Assignment of the different measurements to cluster structures

For the assignments the following criteria are used:

- onsets of single ionization potentials for the determination of the size of the argon core
- positions of NeAr-ICD peak
- relative expected mean cluster sizes (see Table 13.5)
- agreement of predicted and measured ICD (see Table 13.9)

From the onsets of the single ionization potentials and the position of the NeAr-ICD peak at a lower energy it is deduced that the mean argon core of set 5 is the smallest of all measured ensembles. Since the nearest neighbours have the largest influence of such a shift these clusters can be interpreted to have an edge length of either $c = 1$ or $c = 2$. Since the estimations of mean cluster sizes based on Hagena refer to expansions of only one atom type, only the results with the same argon content should be compared. From this the core of set 2 can be expected to be bigger than the core of set 4 and the core of set 3 can be expected to be slightly larger than the core of set 1. These estimations do not have to resemble the final conclusions, since the approach is only valid for homogeneous clusters, but can give hints in the following procedure. The assignment due to geometrical distance of the predicted results from the experimental counterparts is to be found in Table 13.9. There, the best results for all sets are shown in the following way: c depicts the number of atoms in the longest edge of the argon core, which is then covered by a number of additional complete neon shells with additional covered triangular surfaces or randomly arranged atoms and d denotes the geometrical distance.

The structure assignment is going to be discussed in descending order of the set number, which more or less corresponds to a discussion with increasing size of the clusters.

The assignment is started with set 5 (red). As already mentioned, these clusters can be expected to be small and, additionally, the smallest ones measured. These expectations

Table 13.9.: The smallest geometric distances for each set of clusters and the corresponding cluster structures. Note that for set 4 only the random arrangement is listed, for which the argon content exactly equals the experimental one.

Set	c	complete Ne shells	covered surfaces	random	d
1	4	1	1	-	2.000
1	5	1	2	-	4.472
1	2	0	5	-	4.472
2	3	1	-	x	1.000
2	3	1	1	-	3.162
2	2	0	8	-	4.123
3	2	1	3	-	4.000
3	3	1	7	-	4.123
3	3	1	8	-	4.472
4	2	1	-	x	2.000
4	2	1	1	-	4.000
5	2	1	13	-	8.246
5	2	1	14	-	9.220
5	2	1	15	-	9.220

are in agreement with the results of Figure 13.12 (also to be found in the Appendix in Figure B.5), where the red square can be matched with a cluster to an argon core with $c = 2$, one complete shell of neon atoms and one almost complete shell with 13 – 20 out of 20 surfaces covered by neon atoms. None of the theoretical estimates coincide with the experimental findings. This might be explained by even smaller clusters not showing an icosahedral argon core, but a coagulation of 2–11 atoms plus some neon atoms.

Set 4 (turquoise) shows a very good agreement for a structure with $c = 2$ with one complete shell of neon atoms and some additional atoms (see Figures B.9 and B.5 or in the example above). Whether these atoms are randomly arranged around the complete shells or are to be found together cannot finally be decided. From the geometric distance, the random arrangement should be preferred.

The results of set 3 (blue) shows a good agreement with structures of $c = 2$ or $c = 3$ surrounded by one complete shell of neon atoms and additional neon atoms covering 3 or 7 – 8 triangular surfaces, respectively as shown in Figures B.5 and B.6.

With the two latter assignments it is possible to distinguish the structures of two cluster manifolds with the same argon content by utilizing the ICD spectra.

Set 2 (green) can be assigned to core sizes of $c = 2 - 3$ plus further neon atoms (see Figures B.4 and B.6). In the case of $c = 3$, one additional complete shell of neon atoms fits best to the experimental results, but as for set 4 the arrangement as such for some

few additional atoms can either be random or coagulated. In case of $c = 2$ the best fit holds for no additional complete shell of neon atoms but with 8 triangular surfaces covered, the shell is almost halfway filled. Further structures with larger core sizes as $c = 4$ are also quite probable. Considering, that both from Hagena's approach and the single ionization potential onsets of the Ar3p band, set 2 is supposed to have the largest mean structure core, the latter structures might be closer to reality than the ones of the small clusters with $c = 2, 3$.

Due to the large error bars, set 1 (black) can be assigned to a whole manifold of different structures with $c = 2 - 6$ within the error bars either with caps or, more probably, with about one complete shell of neon atoms, plus maybe additional covered surfaces or randomly surrounded by neon atoms. Since caps should be energetically less favourable than the other structures, I will suspend those structures and concentrate on the rest. From Hagena's approach I concluded that the core of the clusters of set 1 should be slightly smaller or of comparable size as the clusters from set 3. Therefore I assume the average cluster structure to consist of an argon core of $c = 2 - 4$ shells with one complete neon shell and possibly one further incomplete shell, of which I cannot give more detailed information.

One might have to consider completely different structures not investigated in this thesis. Formed, mixed clusters might collide and coagulate, yielding structures impossible to be estimated by a core-shell structure of the kinds presented in this work.

From the best agreement of the calculated NeAr-ICD to total ICD ratios listed in Table 13.9, the corresponding estimated spectra are folded with gaussians with a width of 250 meV and are plotted in Figure 13.13. From these spectra and the underlying calculations I conclude, that the shoulders of both the NeNe-ICD and the NeAr-ICD peak at 2.5–4 eV and 8–10 eV correspond to next-nearest neighbours inside the clusters, while the differences in the main peak stem from almost equal interatomic distances but different positions in the cluster such as corner, edge or surface.

The main peaks of the NeNe-ICD correspond well with the experimental observations of Figure 13.8.

The onset of the NeAr-ICD peak depends on the shielding of the argon atom and hence the cluster size. For set 5 the assignment seems to be correct, while for set 4, the experiment shows a higher energy of the ICD electron. This deviation implies that either the core of the mean cluster structure is larger than evaluated from the theoretical calculations or that the choice of $c = 3$ as the minimum core size for the for the lower ionization potential of the Ar3p was wrong. The truth, however, is not a spontaneous jump from one shell to the other, but rather a decrease with more and more atoms. If one is interested in clusters of $c \leq 2$ only, one should take care of a more detailed description of the different ionization potentials for different cluster sites.

An analysis of the peaks creating the shoulders reveals them to originate from ICD processes involving next-nearest neighbours as decay partners.

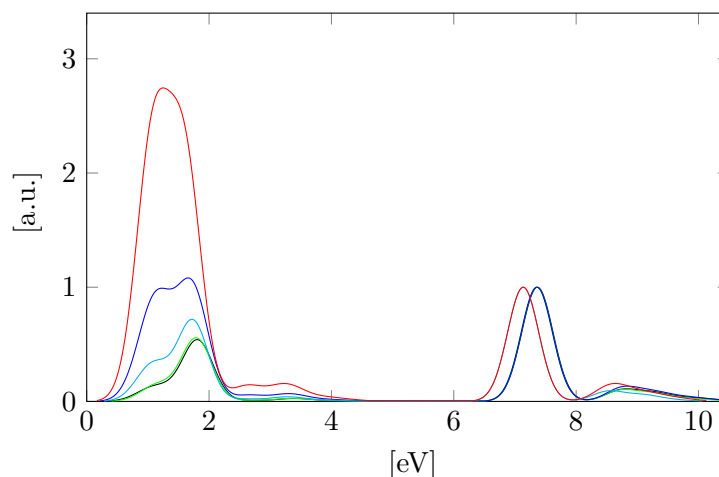


Figure 13.13.: Calculated ICD electron spectra for those structures given in Table 13.9 with the best agreement to the experimental argon content and NeAr-ICD to total ICD ratio. The intensities are given in arbitrary units and are normalized to the peak height of the NeAr-ICD peak and the spectra are folded by Gaussians with widths of 250 meV. The theoretically calculated spectra nicely match the experimental ones in Figure 13.8. Both, the NeNe-ICD peak at low energies and the NeAr-ICD peak at higher kinetic energies, show a peak structure which can be related to different distances of the atoms involved in the process within the clusters. For more details, see the text.

13.2.6. Conclusions

I have developed a method for the analysis of a mean cluster structure of noble gases utilizing the relative ICD decay widths of two competitive decay processes. This I have exploited onto five different cluster ensembles. I am able to explain the five experimental spectra by different underlying mean structures. Furthermore, the peak structure was shown to originate from ICD processes involving next-nearest neighbours. From the results I conclude, that clusters formed in a supersonic beam most likely can be described by a core-shell structure with additional layers. In some limited cases, when only few additional neon atoms around complete shells are needed to fulfill the argon content, the random arrangement seems to be possible.

14. Summary and Outlook

In this thesis, the importance of relativistic effects in autoionization processes, especially ICD-like processes, and cluster environments have been discussed. For this purpose, asymptotic expressions for the relativistic decay width of the ICD and both, relativistic and non-relativistic asymptotic expressions for the ETMD3 have been derived. Additionally, the non-relativistically well-established FanoADC-Stieltjes approach using a partitioning by population has been implemented in the relativistic program package Dirac, which allows for the description of decay width including relativistic effects. In order to simulate the experimental secondary electron spectra of noble gas clusters, the model of pairs and triples was introduced and automatized in the program HARDRoC. It enables the estimation of decay widths of large systems like clusters from data of the compounds.

In the studies of the atomic Auger process, scalar-relativistic effects were found to increase the decay width compared to the non-relativistic results due to larger orbital overlaps of the initial and final states. Especially in ETMD processes, whose decay widths are governed by the orbital overlap of the two units involved in the electron transfer, similar significant decay width influences might be observed.

Throughout all systems containing heavy elements, the spin-orbit coupling shows a pronounced effect on the secondary electron spectrum by increasing the number of possible channels and hence, the number of peaks. This feature cannot be explained using a non-relativistic methodology. If the decay channels are close to threshold, this energetic splitting can for a non-relativistically closed decay channel cause some of the corresponding decay channels in the relativistic description to be open. On the other hand, not all relativistic channels corresponding to one specific open non-relativistic channel need to be energetically accessible.

Additionally, geometry has a great impact on the opening and closing of channels in ICD-like processes. The closer the ionized atoms of the final state are, the lower is the kinetic energy of the secondary electron and at some internuclear distance the decay channel closes. For the ICD, it is a channel closing internuclear distance and for the ETMD3 considering a fixed electron transfer distance, it is a curve along the intersection of the initial and final state hypersurfaces.

In larger clusters, the additional effect of charge stabilization shifts the kinetic energy of the secondary electron. These shifts were treated by using experimentally obtained ionization energies for exactly the same experimental conditions as for the secondary

electron spectra and by shifting the atomic ionization potentials by experimentally obtained shifts in homonuclear clusters. A more predictive way would be to simulate the influence of the surrounding atoms in order to obtain ionization energies for different positions in the cluster. Furthermore, statistical effects were found to increase the decay width for both the ICD and the ETMD. Since the ICD decay width in the model of pairs, considering nearest neighbours only, scales linearly with the number of nearest neighbours N and the ETMD3 decay width in the model of triples scales like $N(N - 1)$, the ETMD3 is statistically preferred and can therefore compete with the usually faster ICD.

Based on the strong structure dependence of the secondary electron spectrum observed during the PhD, a new structure analysis method for noble gas clusters was developed. If two competing ICD-like processes are energetically accessible and can be measured independently, the comparison of the experimentally obtained cluster composition and relative peak intensities can be compared to theoretically modelled spectra for a large variety of structures. From the best agreement, the mean cluster structure can be deduced as was carried out for a set of experimentally created NeAr cluster manifolds. They were shown to have a shell structure with an argon core of different sizes surrounded by complete and incomplete shells of neon atoms.

In the future, it would be worth investigating ICD processes with electron transitions forbidden in the non-relativistic description. Additionally, for the ETMD3 the determination of a physically reasonable choice of the energy transfer distance R would be beneficial. Furthermore, the ETMD3 should be investigated using the relativistic FanoADC-Stieltjes approach studying the scalar-relativistic effects observed for the case of the Auger effect following an ionization of the Xe4d. An analytic investigation of the angular distribution of the emitted ICD electron would give further insights and could be compared to the experimental data available.

It might be worth implementing the FanoADC based on a partitioning by energy in order to obtain partial decay widths for the different terms stemming from the same 2h configuration of the final states and to improve their accuracy by including interchannel couplings. This approach would also automatically allow for the treatment of systems, where the atoms ionized in the final state can be generated by a symmetry operation of the system's point group. Furthermore, a more rigorous investigation of the couplings between the initial state and Rydberg states would be beneficial for the development of a method to exclude these couplings from the decay width calculation automatically. For decay width calculations for different interatomic distances, a rapid change is observed at distances of about 10 – 15 Å. This behaviour is known for the non-relativistic treatment for all investigated systems as well, but the reason is so far unknown. It might be caused by insufficient basis sets and additional ghost centers between the atoms of the decay partners might shift this effect to larger distances. However, the reason for this behaviour should be investigated and the results should be taken into account in later

studies.

In the Stieltjes Imaging, the pseudo-spectra are currently shifted such, that the lowest energy has some predefined, small number. This number needs to be small in order to allow for numerical stability for as high order moments as possible. However, whether there is an optimal choice of this number and if it exists, what it depends on, is currently unknown. It would be worth investigating, because an improvement of the Stieltjes imaging procedure might lead in more reliable results or decay width profiles, which are easier to interpret, which might allow for a more automatized evaluation of the results. So far, no automatic error estimation is available in the FanoADC-Stieltjes approach. However, it would be very helpful for the validation of the calculated decay widths. Further, the Stieltjes-Imaging applied to a combination of two or more pseudo-spectra of the same system calculated using different basis sets as shown in Ref. [87] would be worth investigating. In this way, the density of the pseudo-spectrum would ideally increase in the energy region of interest. Therefore, a more accurate description of the decay widths might be possible. At the same time, this approach might enable decay width calculations of larger systems, where a huge basis set cannot be applied due to lacking computational resources required in the integral transformation step, which is the bottleneck of the calculations.

For the estimation of secondary electron spectra of clusters, the investigation of cluster dynamics and their influence on the secondary electron spectra should be developed and included in HARDRoC. This knowledge about the oscillations and their displacements would at the same time allow for an error estimation of the calculated decay widths.

The investigated structures have so far been chosen by educated guesses. For a more detailed study, optimized cluster structures would be beneficial. Furthermore, it would be a challenging task to develop the possibility to treat clusters with constituents of lower than spherical symmetry, e.g., water molecules.

A. Properties of Noble Gas Atoms

Table A.1.: Atomic, experimental ionization energies. The non-relativistic ionization energies of the np were estimated by the weighted average of the experimental ionization energies of the $np_{3/2}$ and $np_{1/2}$.

	$SIP(np_{3/2})$		$SIP(np_{1/2})$		$SIP(ns_{1/2})$	
Ne	21.5645 eV	[103]	21.6613 eV	[103]	48.475 eV	[103]
Ar	15.7596 eV	[103]	15.9371 eV	[103]	29.239 eV	[103]
Xe	12.1298 eV	[103]	13.4363 eV	[103]	23.397 eV	[138]
Ne_{nrel}	21.5968 eV				48.475 eV	
Ar_{nrel}	15.8188 eV				29.239 eV	
Xe_{nrel}	12.5652 eV				23.397 eV	

Table A.2.: Lifetimes and relative ionization cross sections of noble gas atoms. The ratio of ionization cross sections for the neon atom was estimated from the degeneracies of the $p_{3/2}$ and $p_{1/2}$ states.

	$\tau(ns_{1/2})$		$\chi = \frac{\tau_{1/2}}{\tau_{3/2}}$		$\frac{\sigma_{3/2}}{\sigma_{1/2}}$	
Ne	1.429 ns	[138]	2.04	[125]	2.0	
Ar	4.684 ns	[138]	2.05	[125]	1.875	[139]
Xe	35.93 ns	[138]	8.40	[140]	1.6	[122]

Table A.3.: Shift of atomic ionization energies due to a cluster environment [141]. All values are given in eV.

	$\Delta(np_{3/2})$	$\Delta(np_{1/2})$	$\Delta(ns_{1/2})$	
			bulk	surface
Ar	-1.0	-0.4	-0.636	-0.313
Xe	-1.3	-0.9	-0.756	-0.346

B. NeAr Cluster Structure Agreement Plots

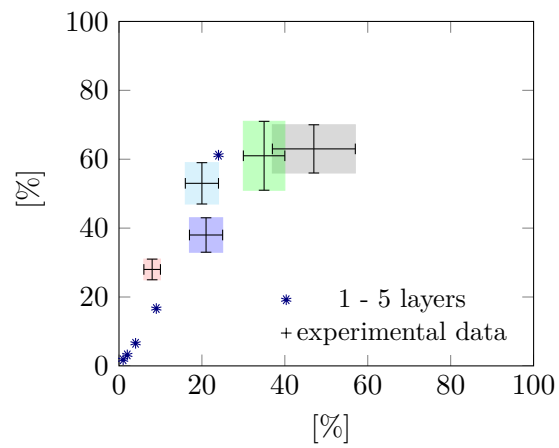


Figure B.1.: Complete neon shells with $c = 2$.

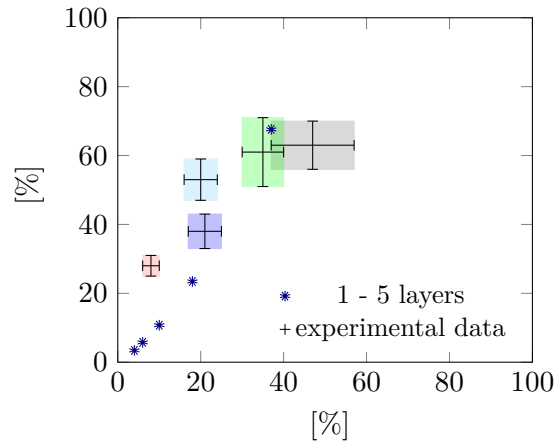


Figure B.2.: Complete neon shells with $c = 3$.

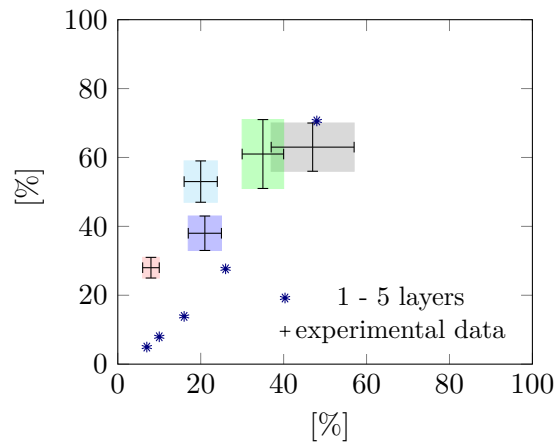


Figure B.3.: Complete neon shells with $c = 4$.

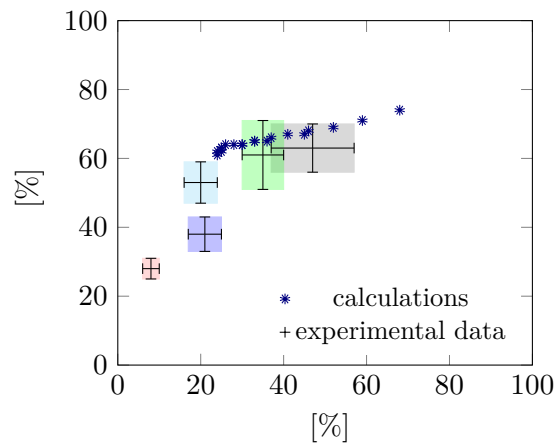


Figure B.4.: Incomplete shells with $c = 2$ and no complete neon shell.

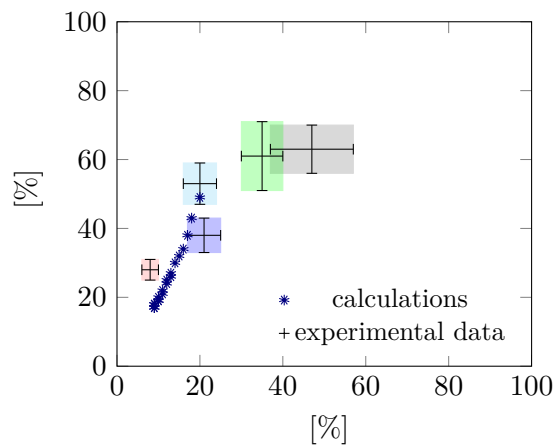


Figure B.5.: Incomplete shells with $c = 2$ and one complete neon shell.

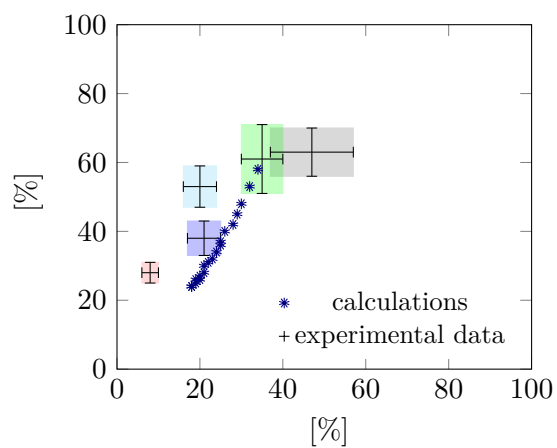


Figure B.6.: Incomplete shells with $c = 3$ and one complete neon shell.

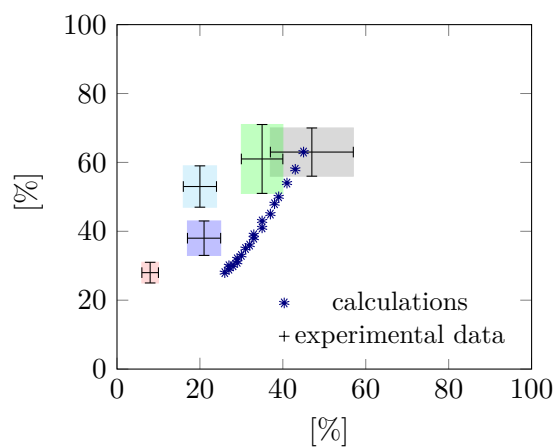


Figure B.7.: Incomplete shells with $c = 4$ and one complete neon shell.

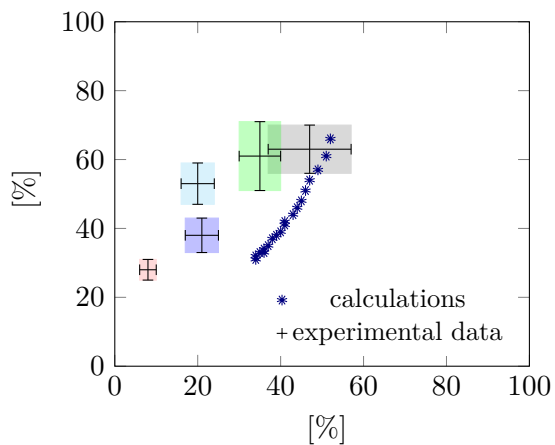


Figure B.8.: Incomplete shells with $c = 5$ and one complete neon shell.

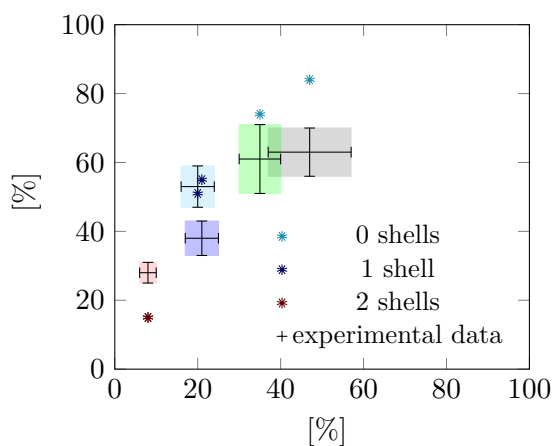


Figure B.9.: Random arrangements with $c = 2$.

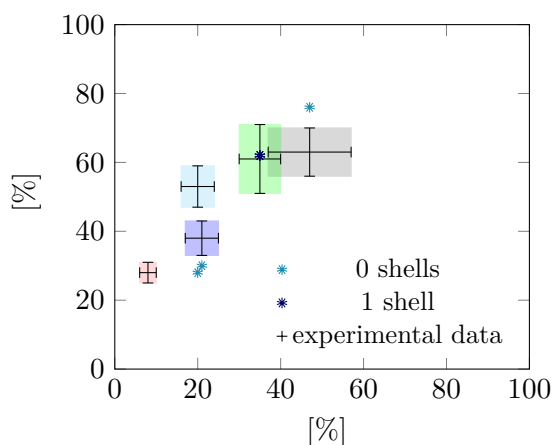


Figure B.10.: Random arrangements with $c = 3$.

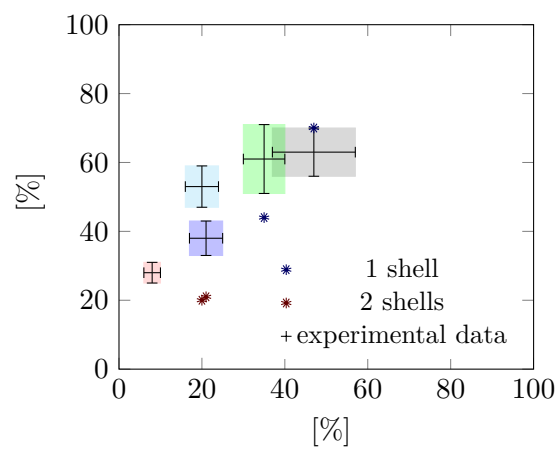


Figure B.11.: Random arrangements with $c = 4$.

C. Programs and Scripts

This chapter gives an introduction to the programs and special scripts written during the PhD, which are used in this thesis. The aim is to give insight into the structure of the programs rather than repeating the manual, if it is given elsewhere. This is the case for HARDRoC [16] and the relativistic FanoADC-Stieltjes implemented in Dirac [15].

C.1. HARDRoC — Hunting Asymptotic Relativistic Decay Rates of Clusters

The program calculates the ICD and ETMD3 decay widths of given cluster structures. Thereby, it is possible to choose between the evaluation of the asymptotic expressions of equations (5.18) and (5.22) using atomic data and the evaluation of a function obtained from fitting *ab initio* results to $\Gamma(R) = c_{pre}e^{-c_{exp}} + \frac{c_6}{R^6}$ for the ICD.

The required input information is:

- xyz-file
- desired decay process(es)
- evaluation type
- ICD based in atomic properties:
 - SIPs of the initial and final state atoms for each channel and eventual energetic shifts caused by the cluster environment
 - radiative lifetime τ of the initially ionized state
 - optionally, the ratio $\chi = \frac{\tau_{1/2}}{\tau_{3/2}}$
 - ratio of ionization cross sections
- ICD based on *ab initio* results:
 - SIPs of the initial and final state atoms for each channel and eventual energetic shifts caused by the cluster environment
 - parameters of the function fitted to the decay width c_{pre} , c_{exp} and c_6
- ETMD:

- SIPs of the initial and final state atoms for each channel and eventual energetic shifts caused by the cluster environment
- ratio of ionization cross sections

Additionally, the total ionization cross section is required. Since it is energy dependent, parameters of the function $\sigma(\omega) = a\omega^2 + b\omega + c + \frac{d}{\omega}$ were fitted to the experimental data of references [142, 127] for the noble gases and incorporated in the program. This function is evaluated when needed.

The transition dipole moments required for the ArXe ETMD3 calculation were calculated by means of the Kramers-restricted configuration interaction method [143, 144, 145] available in Dirac using dual basis sets of $(26s21p16d4f)$ and $(17s12p4d)$ for argon and xenon, respectively. The analogous non-relativistic transition dipole moments could conveniently be obtained by setting the value for the speed of light to $c = 3000$ a.u. which renders SO-coupling negligible (see e.g. [41] for more details on relativistic calculations). Since, they depend on the internuclear distance, they were fitted to a function and the corresponding parameters were incorporated in the program and are evaluated for the different distances.

The algorithm proceeds in the following way:

1. decompose the cluster structure into pairs or triples depending on the required decay process
2. create statistics of equivalent pair or triple geometries
3. for each decay channel and for each non-equivalent geometry determine energetic accessibility of the decay channel
4. evaluate the corresponding decay width in case of energetic accessibility
5. normalize the decay width to one initially ionized atom and multiply it by the occurrence of the pair or triple geometry of the cluster
6. for each channel write the geometry parameters, secondary electron energies and the decay widths to an output file
7. for each channel sum over the obtained decay widths
8. sum the decay widths of the different channels to give the total decay width of all channels

The computationally most expensive step in the above procedure is the sorting procedure in order to obtain a shorter array consisting of the non-equivalent geometries and the corresponding weights. It scales like $\frac{N(N_{neq}-1)}{2}$ with N being the total number of

pairs or triples and N_{neq} being the number of non-equivalent pairs or triples of the cluster. In the worst case $N = N_{neq}$. For the ICD, $N = N_{in} \cdot N_{fin}$, where N_{in} denotes the number of atoms of the atomtype, which is initially ionized and N_{fin} denotes the number of potential decay partners. For the ETMD3, $N = N_{in} \cdot N_{fin1} \cdot N_{fin2}$, where $N_{fin1,2}$ denote the number of atoms of the atom type of electron donor and electron emitter. For clusters consisting of several hundreds or thousands of atoms, these numbers are huge, especially for the ETMD. Since the transition dipole moments in equation (5.22) decrease exponentially with the internuclear distance, triples with large Q have a negligible contribution to the total decay width. Therefore, an additional parameter for the maximum allowed electron transfer distance Q can be introduced, which reduces the number of triples before the sorting dramatically for large clusters.

Despite its computational cost, this sorting step is highly regarded for all following steps. Since mostly, highly symmetric structures are investigated, the length of the array and hence the number of operations can be decreased up to a factor of about 50. Also the written output is shortened by the same factor and has an improved readability.

The manual is to be found in reference [16].

C.2. Relativistic FanoADC

The FanoADC code used in this thesis is implemented in Dirac [15] and based on the symmetry handling and calculation of matrix elements of the relativistic ADC and Lanczos code of Pernpointner [111, 146].

In this FanoADC code the partitioning by population is applied. Hence, the three subspace matrices of the initial states, the interaction and the final states can be obtained from resorting the available matrix elements. The selection of the final state subspace is based on manually chosen $2h$ configurations. Since the ADC matrix can have dimensions of $10^5 \times 10^5$, they are not kept in memory but stored to disk. A resorting from reading in these matrix elements would be inefficient and therefore, the matrices are build correctly sorted. The heart of the sorting is an array, in which the positions within a $2h1p$ vector are stored, which correspond to final state configurations of different channels called `finalpos`.

Due to the hermiticity of the ADC matrix, it is sufficient to store the lower triangle and the diagonal, which are build separately. First, the $1h/1h$ block is constructed as in the `reladc` code, since all configurations contribute to the initial state subspace.

As in the `reladc` code, the matrix is build columnwise. In the coupling block, this leads to an easy sorting by leaving out all those matrix elements, for which the row index corresponds to a final state position within a column. At the end of the column, the skipped matrix elements are added to the interaction part.

In the satellite block, both row and column indices can correspond to a final state position. Still, the FanoADC matrices are constructed using the column indices of

the `reladc` code. For those columns corresponding to the initial state subspace, the sorting is obtained as in the coupling block explained above. However, those matrix elements, which stem from a column, which corresponds to a final state configuration, those matrix elements, which mediate the interaction with the initial state subspace need to be correctly sorted into the interaction matrix. Thereby, the final state subspace matrix elements are left out. For the interaction matrix elements, the indices are first shifted correctly and then switched and the matrix elements are complex conjugated, due to the hermiticity of the ADC matrix.

The final state subspace of the satellite block is constructed calling those matrix elements, corresponding to the final state positions stored in `finalpos`.

After the construction of the three matrices, the final state matrix is diagonalized by full diagonalization. Then, the initial state matrix is diagonalized using the Lanczos routine. After the first Lanczos run, a set of short eigenvectors with an overlap higher than a given threshold with the initial state spinor and those with the same energies is chosen for the calculation of long eigenvectors. After calculation of these long eigenvectors, they are merged into linearly independent vectors. From each of these long eigenvectors the interaction is calculated using the interaction matrix and the final state vectors.

The pseudo-spectrum which afterwards enters the Stieltjes calculation is obtained from the final state eigenenergies and the corresponding interaction matrix elements.

The manual can be found as part of the Dirac manual from the release of 2014 on [15].

C.3. `icoclus`

`icoclus` is a selection of python scripts creating xyz-coordinate files for idealized heteronuclear clusters with a basic icosahedral structure. All structures contain an icosahedral core of one atom type surrounded by atoms of the second atom type in different ways. Hereby, it has to be mentioned that these cluster structures are not energetically optimized but build using the scientific guess that the interatomic distances of each pair of atoms in the clusters can be described as the sum of the van der Waals radii.

The newest version is currently available in a git repository in the local network of the Theoretical Chemistry group at the University of Heidelberg and can be cloned via

```
git clone /home/elke/pub/icoclus
```

In each script, the first line might need to be adjusted to hold the path to the favourite installation of python on the current machine.

C.3.1. Construction of the Core Icosahedral Cluster

The vertex coordinates of a regular icosahedron are given by [147]

$$\begin{aligned}
 & \left(0, \pm \frac{a}{2}, \pm \frac{a}{2} \varphi \right) \\
 & \left(\pm \frac{a}{2}, \pm \frac{a}{2} \varphi, 0 \right) \\
 & \left(\pm \frac{a}{2} \varphi, 0, \pm \frac{a}{2} \right)
 \end{aligned} \tag{C.1}$$

where a describes both the distance from the center to each vertex and the length of an edge and $\varphi = \frac{1}{2}(1 + \sqrt{5})$.

Icosahedral clusters are build of different shells, each of them characterized by the number of atoms per edge c . Starting from a central atom, a shell with $c = 2$ is added, afterwards one with $c = 3$ and so on, until the desired cluster size is achieved. a is determined by the appropriate sum over v. d. Waals radii.

Here, one needs to consider that in these packed icosahedral shells the distance between the closest atoms within one shell is larger than the closest distance of two atoms of neighbouring shells. In order to achieve the overall minimum distance between two atoms to be the sum of their van der Waals radii, the vertex distance a is scaled such, that the distance between two atoms in neighbouring surfaces is given by the sum of the v. d. Waals radii.

$$a' = a \frac{2}{\sqrt{1 + \varphi^2}} \tag{C.2}$$

In each shell first the vertex atoms are created and then, corresponding to the size of the shell, atoms in the edges and in the end the atoms lying in the triangular surfaces.

C.3.2. Complete Shells

Around the icosahedral core cluster more complete shells consisting of the second atom type are constructed. Hereby the distance between the central atom and the vertices is calculated as the sum over the contributing v. d. Waals radii. and scaled as in the case of the core vertices.

Manual of `icoclus.py`

In the header of the script `icoclus.py` the following controlling variables are defined.

```

1 #####Input Variables #####
2   atcore = 'Ar' # atomtype of the core atoms
3   atouter = 'Ne' # atomtype of the outer shells
4
5   rcore = 1.88 # radius of core atoms
6   router = 1.54 # radius of outer shell atoms

```

```

7
8   n_core = 1      # number of atoms in the longest edge
9   #n_outer = raw_input('How many layers of atoms do you want to have? ')
10  #n_outer = int(n_outer)
11  n_outer = 1     # number of additional shells

```

These are to be adjusted according to the desired structure. Afterwards the script is run from the terminal. The two commented lines are convenient if several cluster structures of the same type but with different numbers of second atom type shells. In this case the two commented lines need to be uncommented and the last line to be commented out.

C.3.3. Incomplete Shells

It is also possible to generate incomplete shells around a core and eventually complete shells of the second atom type.

Manual of `incompl_shells.py`

In the header of `incompl_shells.py` the following section with the input variables is to be found.

```

1 #####Input Variables #####
2   atcore = 'Ar' # atomtype of the core atoms
3   atouter = 'Ne' # atomtype of the outer shells
4
5   rcore = 1.88 # radius of core atoms
6   router = 1.54 # radius of outer shell atoms
7
8   n_core = 1    # number of atoms for the longest edge
9   n_sec = 2     # number of complete layers of the second atom type
10  n_outer = 1   # do not change
11
12  #no_surfaces = 3 + 1
13  no_surfaces = raw_input('How many surfaces do you want to be covered? ')
14  no_surfaces = int(no_surfaces)

```

Here, `n_outer` declares the number of shells being partially filled. Changing it results in a different cluster class. A nicer way to accomplish structures of this other class is to use the script `area_ico.py`.

It is important to notice, that the script is going to fail, if the number of covered triangular surfaces is 0. In the case of no additional incomplete shells covered being the desired structure, one should consider using `icoclus.py`.

C.3.4. Triangular Surfaces Covered by Layers of Atoms

One might consider triangular surfaces covered by several layers of atoms of the second atom type, hereby creating subsets of complete shells as shown in Figure 13.11.

Manual of area_ico.py

In the header of `area_ico.py` the following control section is found with the variables to be adjusted.

```
1 #####Input Variables #####
2   atcore = 'Ar' # atomtype of the core atoms
3   atouter = 'Ne' # atomtype of the outer shells
4
5   rcore = 1.88 # radius of core atoms
6   router = 1.54 # radius of outer shell atoms
7
8   n_core = 3 #number of atoms for the longest edge
9   n_outer = raw_input('How many layers of atoms do you want to have? ')
10  n_outer = int(n_outer)
11  #n_outer = 1 # number of layers on top of the selected surfaces
12
13  no_surfaces = 5 + 1 # number of triangular surfaces covered
```

C.3.5. Caps

One might think of a structure as shown in Figure 13.11, where the surfaces of the core cluster are covered with caps.

In contrast to the incomplete shells, here, one might consider both different numbers of caps as well as multiple arrangements of the caps on the surfaces. Within the script the 20 surfaces are numbered and hence a manifold of combination of structures for a given number of caps is possible. Since the calculation of all different combinations is tedious it is beneficial to be able to know which of these combinations are symmetry equivalent. This information can be obtained with the help of the script `stat_caps.py`. For a given number of caps it prints one surface number combination for each group of symmetry equivalent structures and the number of possible realizations of it. Afterwards the structures can be constructed with `scatter_cap_ico.py`.

Manual of stat_caps.py

```
1 #####Input Variables #####
2   atcore = 'Ar' # atomtype of the core atoms
3   atouter = 'Ne' # atomtype of the outer shells
4
5   rcore = 1.88 # radius of core atoms
6   router = 1.54 # radius of outer shell atoms
7
8   n_core = 2 #number of atoms for the longest edge
9   n_outer = n_core - 1 # do not change
10
11  n_caps = 2 # number of caps
```

The only number to be adjusted is `n_caps`, all other variables do not influence the result.

Manual of `scatter_cap_ico.py`

```

1 #####Input Variables #####
2   atcore = 'Ar' # atomtype of the core atoms
3   atouter = 'Ne' # atomtype of the outer shells
4
5   rcore = 1.88 # radius of core atoms
6   router = 1.54 # radius of outer shell atoms
7
8   n_core = 4 #number of atoms for the longest edge
9   #n_core = raw_input('How many core layers do you want to have? ')
10  #n_core = int(n_core)
11  n_outer = n_core - 1 # do not change
12
13  caps = [1,5]
14  n_caps = len(caps)

```

`caps` is a python list and here, the combination of surface numbers obtained from `stat_caps.py` is to be entered.

C.3.6. Randomly Arranged Atoms Around Complete Shells

For a given ratio between the number of core and the number of surrounding atoms one can create structures with a fixed icosahedral cluster of closed shells and atoms of the second type randomly arranged in the next shell until the desired ratio is obtained. In the script `random_ico.py` the structures are not created by adding atoms randomly to the outermost shell but by constructing the shell, shuffling the order of atoms in this shell using python's random functionality based on the Mersenne Twister method [148, 149] and then deleting as many atoms as necessary to achieve the desired ratio.

Manual of `random_ico.py`

```

1 #####Input Variables #####
2   atcore = 'Ar' # atomtype of the core atoms
3   atouter = 'O' # atomtype of the outer shells
4
5   rcore = 1.88 # radius of core atoms
6   router = 1.54 # radius of outer shell atoms
7
8   n_core = 5 # number of atoms for the longest edge
9   n_sec = 0 # number of complete shells of second atom type
10  ratio = 3.8868 # nc_atoms/no_atoms
11
12  n_outer = 1 # do not change

```

C.4. fccclus

Clusters with an fcc structure have a dodecahedral shape. It consists of a central atom surrounded by shells of other atoms. All distances between atoms and their nearest neighbours both within one shell and atoms of different shells are equal.

They can be constructed starting from a central atom, which is surrounded by 12 atoms. Of these 12 atoms, six are positioned in a regular hexagon around the central atom. Additional three are positioned in a triangle above the plane defined by the hexagon and three below. Thereby, the triangles are rotated by 30° with respect to the hexagon and 60° with respect to each other.

Hence, the positions of the corners of every shell are with $i = 0, 1, \dots, 6$ and $j = 0, 1, 2$ given by

$$\begin{pmatrix} a \cos\left(\frac{\pi}{3}i\right) \\ a \sin\left(\frac{\pi}{3}i\right) \\ 0 \end{pmatrix} \quad \begin{pmatrix} -\frac{a}{\sqrt{3}} \sin\left(\frac{2\pi}{3}j\right) \\ \frac{a}{\sqrt{3}} \cos\left(\frac{2\pi}{3}j\right) \\ \sqrt{\frac{2}{3}}a \end{pmatrix} \quad \begin{pmatrix} \frac{a}{\sqrt{3}} \sin\left(\frac{2\pi}{3}j\right) \\ -\frac{a}{\sqrt{3}} \cos\left(\frac{2\pi}{3}j\right) \\ -\sqrt{\frac{2}{3}}a \end{pmatrix} \quad (\text{C.3})$$

for the hexagon, the three atoms above and the three atoms below the plane. Here, a denotes the length of an edge, and at the same time from the central atom to the vertex, defined by the sum of van der Waals radii.

From the positions of these vertices, the atomic positions of atoms in the edges and together with the latter, the coordinates of atoms in the triangular and square planes are constructed.

For heteronuclear clusters a is determined by the sum over the van der Waals radii in seen from the central atom to the vertex to be constructed.

List of Figures

2.1. Schematic illustration of the Auger process. The initial vacancy is filled by an electron of an energetically higher orbital and the excess energy is transferred to another electron of the same atom, which is emitted.	8
2.2. Schematic illustration of the ICD. The initial vacancy is filled by an electron of the valence and the excess energy is transferred to an electron of a neighbouring atom, which consequently is emitted. The two positively charged units undergo Coulomb explosion.	8
2.3. Schematic representation of ETMD processes. In the ETMD2 the initial vacancy is filled by an electron of a neighbouring atom and the excess energy is transferred to an electron of this second atom, which consequently gets ionized. The final state is characterized by the initially ionized atom to be neutral and the neighbouring atom to be doubly ionized. In the ETMD3, the initial vacancy is filled by an electron of a neighbouring unit and simultaneously the excess energy is transferred to an electron of a third unit, which gets ionized. The final state is characterized by the initially ionized atom being neutralized and the two neighbouring atoms being singly ionized. Hence, they repel each other.	9
2.4. Schematical illustration of the exchange ICD. The initial vacancy is filled by an electron of the neighbouring unit and the excess energy is transferred to another electron of the initially ionized unit, which is emitted. The two positively charged units of the final state undergo Coulomb explosion.	10
2.5. Schematic illustration of resonant autoionization processes. For details see the main text.	11
3.1. Illustration of electronic properties of the Dirac equation solutions.	19
3.2. Density plots of the angular solutions of the Dirac equation of the hydrogen atom $\xi_{\kappa,m}$. From left to right: $s_{\frac{1}{2}}, p_{\frac{1}{2}}, p_{\frac{3}{2},\frac{1}{2}}, p_{\frac{3}{2},\frac{3}{2}}$	21
5.1. The total system is split into subsystems \mathbf{S}_1 and \mathbf{S}_2 . The \mathbf{R}_i ($i = 1, 2$) point to the corresponding centers of mass (COMs) with respect to an arbitrary origin O . The \mathbf{x}_i as well as the \mathbf{r}_i describe the electron coordinates once with respect to O and once with respect to the COMs. Reprint with permission from Ref. [25]. Copyright 2013, AIP Publishing LLC.	40

5.2.	ICD process in subsystems \mathbf{S}_1 and \mathbf{S}_2 . After creating an inner valence vacancy in \mathbf{S}_1 the hole is filled by an outer-valance electron of \mathbf{S}_1 . The excess energy is transferred to \mathbf{S}_2 and is used to remove an outer-valence electron (ICD electron). Reprint with permission from Ref. [25]. Copyright 2013, AIP Publishing LLC.	41
5.3.	ETMD3 process in subsystems \mathbf{S}_1 and \mathbf{S}_2 where the two atoms A and B participate in the electron transfer and are combined to \mathbf{S}_1 . After inner valence ionization of A, the vacancy is filled by an electron from B in \mathbf{S}_1 . The energy is transferred to C (\mathbf{S}_2) which is ionized and hereby emits the ETMD electron. Reprint with permission from Ref. [25]. Copyright 2013, AIP Publishing LLC.	43
5.4.	Jacobi coordinates used for the geometric description of the trimer. Q is the distance between A and B, R the distance from the center of mass of AB to C and α the angle between the lines represented by Q and R	44
6.1.	Lennard-Jones potential of the argon dimer illustrating the Lennard-Jones parameters σ and ε	49
6.2.	Cut through a cuboctahedral cluster illustrating the different kinds of atoms within a cluster. The bright blue colored atoms are bulk atoms whereas the dark blue atoms belong to the surface. Within a shell atoms can either be vertices (striped), belong to an edge (crosshatched) or lie within a layer (not depicted in this two dimensional sketch).	50
6.3.	Surface to bulk ratio for icosahedral structures with c complete shells illustrating the decreasing impact of the surface atoms.	51
6.4.	Mass distribution of argon clusters. Reprint with permission from Ref. [79]. Copyright 1993, AIP Publishing LLC.	52
6.5.	Schematic overview over the physical mechanisms of different spectroscopic methods [64].	54
6.6.	Schematic view of the experimental setup of a electron-electron coincidence measurement. The synchrotron radiation axis is perpendicular to the plane of the diagram. Reprinted with permission from [71].	55
6.7.	Schematic illustration of electron-electron coincidence signatures for different physical processes. Printed with permission from [71]. See the text for details.	56
6.8.	Electron-electron coincidence spectra for NeAr clusters showing both NeNe-ICD and NeAr-ICD signals [86].	57
7.1.	Integration by Gauss-Chebyshev quadrature of the function $h(x) = x^3 + 1$ (dark blue) with $n = 6$. The integral (light blue) is obtained by summation over all product of optimal abscissae and weights $x_i h(x_i)$ (circles).	63

- 7.2. Stieltjes histogram of a sixth order integration from a NeAr ICD pseudo-spectrum (light blue). At the abscissae ω_i , the histogram provides lower and upper bounds for the actual values. The mean of these two bounds (dark blue) is normally a good approximation of the distribution function $F(E)$ at this point. 70
- 7.3. Schematic illustration of the interpolation after the stieltjes calculations to yield the density function $\Gamma(E)$, which is to be evaluated at the resonance energy E_r . Suppose the black curve to be the exact result. Then (left panel), for each order of Stieltjes calculation the points lie on this curve, where points from different orders (different colours of the points) intersect each other. The interpolation gives the exact result. In reality (right panel) the interpolations (even of one order of Stieltjes) are likely to show oscillations due to non-orthogonalities of Chebyshev polynomials in the higher orders and inaccurate descriptions due to a large gap between the lower and upper bounds for low orders. 71
- 8.1. Schematic illustration of an $\text{ADC}(n)$ matrix for different orders of perturbation for $n = 0, 1, 2, 2x, 3$. In the illustration, the respective highest order contribution is shown for the different blocks. Hence, $\text{ADC}(2x)$ is an extended $\text{ADC}(2)$ including first order contributions to the satellite block. 74
- 8.2. Schematic illustration of the partitioning of the ADC matrix according to the projection operators of the initial and final states. 76
- 8.3. Schematic illustration of the basis transformation of the full ADC matrix into the basis of initial and final states. The pseudo-spectrum is given by the manifold of $\bar{\omega}_q$ and $V_{i,q} = \langle \phi_i | \hat{H} | \psi_q^{2h1p} \rangle$ 76
- 8.4. Shifted pseudo-spectra with $E_r = 0$ for the Auger process following an ionization of the neon 1s. Comparison of contracted and uncontracted cc-pVQZ. 78
- 8.5. Shifted pseudo-spectra for different basis sets with $E_r = 0$ for the Auger process following an ionization of the neon 1s. Different basis set classes. 79
- 8.6. Pseudo-spectra for the Auger process following the ionization out of the Ne1s for the aug-cc-pV6Z basis set with additional KBJ basis functions of the s, p and d type. 80
- 8.7. Schematic illustration of a decay width profile with three channels. At the resonant energy $E_{r,1}$, the first two channels are open and at the resonance energy $E_{r,2}$ all three channels are open. 81
- 8.8. Schematic illustration of a decay width profile with couplings of the initial state to Rydberg states. 82

9.1. Comparison of calculated single and double ionization spectra for the determination of open channels in of the later decay width calculation. Upper panel: relativistic description, lower panel: non-relativistic description.	90
9.2. Left panel: Single ionization spectrum of the xenon atom in the 4p region calculated with DC-ADC(2x). Right panel: Eigenvalues of the initial state subspace of the xenon atom in the 4p region calculated with DC-FanoADC(2x).	93
9.3. Shifted Stieltjes profile of $\Gamma(E)$ obtained from the relativistic FanoADC calculation from a $4p_{3/2}$ initial state with both Γ and E given in atomic units. The resonance energy is $E_{res} = 0$ and the resulting points of the different orders of Stieltjes are plotted separately. The smooth curve shows two additional peaks related to interactions with Rydberg states as discussed in section 8.2.2.	94
9.4. $\Gamma(E)$ of the relativistic FanoADC calculation from a $4p_{1/2}$ initial state with both Γ and E given in atomic units.	97
10.1. Initial and final state energies of the ICD channels of ArXe in the model of pairs. Both the four relativistic channels and the non-relativistic estimate are shown. From the distance on, where the final state energy is lower than the initial state energy, the decay channel is open.	100
10.2. Decay widths of the ArXe dimer in relativistic and non-relativistic treatment plotted over the interatomic distance R . The initial and final state energies were determined from unshifted experimental atomic ionization potentials. Only such channels are considered, which are open at the corresponding distances.	102
10.3. Energy hyper surface of the doubly ionized $\text{ArXe}5p_{1/2}^{-1}\text{Xe}5p_{1/2}^{-1}$ (light blue surface) and the ionization potential of the $\text{Ar}3s^{-1}$ initial state with 29.2 eV (dark blue grid). Q is constant, whereas R and the angle θ (see Figure 10.9) are varied. This ETMD3 channel is open for structures where the final state energy is lower than the initial state energy.	103
10.4. Angle dependence of the ETMD3 decay widths for electron transfers along the internuclear axis \tilde{z} of subsystem S_1 and perpendicular to the internuclear axis \tilde{x}	104
10.5. Angular dependence of the ETMD3 decay width for electron transfers both along and perpendicular to the internuclear axis of subsystem S_1 . Different values of $q = \frac{ \langle \tilde{D}_x \rangle ^2}{ \langle \tilde{D}_z \rangle ^2}$	105
10.6. ETMD3 decay widths Γ hyper surfaces for an ArXe_2 trimer. The four electronic decay channels are shown separately.	106

-
- 10.7. Sum over the decay widths of all four channels, illustrated separately in Figure 10.6. The opening of channels at different angles θ and internuclear distances R are to be seen at the spikes. 107
- 10.8. Two different set of Jacobi coordinates for the description of a triple ABC (compare Figure 5.4). In the left Figure the distance of the energy transfer originates at the initially ionized atom A , while in the right panel the energy transfer distance is defined with respect to some point between atoms A and B . The right choice might be physically more precise, even though it is unknown, how to choose the anchorage point. The left set of coordinates is preferable in the modelling of cluster structures. The graphic in the right panel was reprinted with permission from Ref. [25]. Copyright 2013, AIP Publishing LLC. 108
- 10.9. Illustration of two geometry parameter sets, which lead to the largest possible deviation of the ETMD decay width. 108
- 12.1. Distance dependence of the decay widths of the heteronuclear ArXe dimer obtained from both relativistic and non-relativistic calculations using the asymptotic approximation and the FanoADC approach. 116
- 12.2. Renormalized partial decay widths calculated with the relativistic FanoADC of the ArXe dimer compared to each other and the total decay width. . . 117
- 12.3. Partial decay width ratios for decay channels of the same final state on the initially ionized atom compared to the experimentally observed ratio between the ionization cross sections of the xenon atom. The latter value provides the asymptotic limit. 118
- 12.4. Partial decay width ratios compared to the asymptotic limit provided by equation (11.11). 119
- 13.1. Model structures of ArXe clusters. Left panel: Argon atom placed in an fcc position on xenon atom layers in fcc structure. Right panel: Argon atom placed in an hcp position on xenon atom layers in hcp structure. . . 123
- 13.2. Initial and final state energies of the ICD channels of ArXe in the model of pairs calculated from shifted atomic ionization energies. Both, the four relativistic channels and the non-relativistic estimate are shown. From the distance on, where the final state energy is lower than the initial state energy, the decay channel is open. 124
- 13.3. Initial and final state energies of the ETMD3 channels in the model of triples calculated from shifted atomic ionization energies. 125

- 13.4. ICD and ETMD3 secondary electron spectra for the model structures of Figure 13.1. To guide the eye of the reader, the spectra were folded with Gaussians of 300 meV and 600 meV for the ICD and ETMD, respectively. Upper panel: Relativistic spectrum. Lower panel: Non-relativistic spectrum. 126
- 13.5. Experimental secondary electron spectra of different ArXe cluster ensembles. 131
- 13.6. Calculated secondary electron spectrum of the icosahedral 309 xenon core cluster with one additional layer of argon atoms. Due to usage of experimental ionization energies of mixed clusters the peaks are shifted to lower energies compared to the spectra in Figure 13.4. 132
- 13.7. Secondary electron spectra of ArXe clusters with a xenon core consisting of 923 atoms and one additional layer of argon atoms. Upper panel: Icosahedral structure. Lower panel: Dodecahedral cluster with fcc structure. 134
- 13.8. Electron-electron coincidence spectra for NeAr clusters showing both NeNe-ICD and NeAr-ICD signals [86]. 136
- 13.9. Decay widths of the NeNe-ICD and NeAr-ICD processes fitted to curves for the decay width estimation of the NeAr clusters. 138
- 13.10 An icosahedral argon cluster with an edge consisting of $c = 4$ atoms, containing 147 atoms, distributed over four shells. 55 atoms belong to the core, 12 are at the vertices, 60 in the edges and 20 inside the surfaces. . . 139
- 13.11 Structure classes considered in our calculations. a) complete shells, in this example $c = 5$ atoms with one layer neon atoms, b) incomplete shells, in this example $c = 6$ atoms with two covered trinangular surfaces of neon, c) caps, in this example $c = 4$ atoms with two caps, d) randomly arranged neon atoms around a full shell cluster, here $c = 3$ atoms directly covered by neon atoms with an argon content of 47%. 140
- 13.12 NeAr-ICD to total ICD ratio plotted against the argon content in the cluster for both experimental results for all five sets of conditions as well as theoretical calculations for cluster structures with an incomplete outermost shell surrounding an argon core of $c = 2$ and one additional complete neon shell. For illustrative purposes, pictures of two structures are included at their respective theoretical values. 142

13.13	Calculated ICD electron spectra for those structures given in Table 13.9 with the best agreement to the experimental argon content and NeAr-ICD to total ICD ratio. The intensities are given in arbitrary units and are normalized to the peak height of the NeAr-ICD peak and the spectra are folded by Gaussians with widths of 250 meV. The theoretically calculated spectra nicely match the experimental ones in Figure 13.8. Both, the NeNe-ICD peak at low energies and the NeAr-ICD peak at higher kinetic energies, show a peak structure which can be related to different distances of the atoms involved in the process within the clusters. For more details, see the text.	146
B.1.	Complete neon shells with $c = 2$	153
B.2.	Complete neon shells with $c = 3$	154
B.3.	Complete neon shells with $c = 4$	154
B.4.	Incomplete shells with $c = 2$ and no complete neon shell.	154
B.5.	Incomplete shells with $c = 2$ and one complete neon shell.	155
B.6.	Incomplete shells with $c = 3$ and one complete neon shell.	155
B.7.	Incomplete shells with $c = 4$ and one complete neon shell.	155
B.8.	Incomplete shells with $c = 5$ and one complete neon shell.	156
B.9.	Random arrangements with $c = 2$	156
B.10.	Random arrangements with $c = 3$	156
B.11.	Random arrangements with $c = 4$	157

List of Tables

3.1. Assignment of the quantum numbers to two-component spinors [36]. . . .	20
6.1. Lennard-Jones parameters for noble gas dimers used in this thesis [71, 72].	49
6.2. Van der Waals radii of the noble gas atoms [73].	50
9.1. Experimental ionization energies of the doubly ionized final states [103]. .	87
9.2. Auger decay widths and contributions of the different channels to the total decay width in % for an initial vacancy in the Ne1s. The decay widths are given in meV.	88
9.3. Channels of the Auger processes for different singly ionized initial states and doubly ionized final states of the xenon atom. Open channels are marked by "x", while closed channels are marked by "-".	91
9.4. Auger decay widths of the Xe4d _{5/2} and Xe4d _{3/2} and the non-relativistic 4d initial states with the doubly ionized final states compared to experimental values [114]. All widths are given in eV. The partial widths are renormalized to the total width.	92
9.5. Auger decay widths of the Xe4p _{3/2} initial states with different M_J values and different doubly ionized final states. All widths are given in eV. . . .	95
9.6. Total Auger decay widths of the Xe4p _{3/2} obtained from experiment, MCDF and this work. All widths are given in eV.	95
9.7. Contributions of the different channels to the total decay width for the Auger decay of Xe4p _{3/2} in %.	96
9.8. Auger decay widths of non-negligible satellites with a major contribution of the Xe 4p _{1/2} . All widths are given in eV.	97
11.1. Evaluation of Wigner's $3j$ -symbols for $J = \frac{3}{2}$ in the argon-xenon dimer. The numbers in brackets denote the difference of the projections of the angular momenta $M'_A - M_A$	110
11.2. Evaluation of Wigner $3j$ -symbols for $J = \frac{1}{2}$ in the argon-xenon dimer. The numbers in brackets denote the difference of the projections of the total angular momenta $M'_A - M_A$	110
13.1. Decay widths of the ICD and ETMD processes of the model structures. .	127

13.2. ICD and ETMD decay widths in eV for ArXe icosahedral clusters with increasing core cluster size and 1 – 4 layers of argon. In the last part the percentage of ETMD compared to the total decay is given.	129
13.3. ICD and ETMD decay widths in eV for ArXe dodecahedral clusters with increasing core cluster size and 1 – 3 layers of argon. In the last part the percentage of ETMD compared to the total decay is given.	130
13.4. Experimental ionization energies inside the ArXe clusters [85]. These ionization energies are the average values of broad distributions.	131
13.5. Assignment and expansion parameters of the five different cluster ensembles. Included are also the resulting mean cluster sizes calculated for the homogeneous species according to the formalism introduced by Hagena <i>et al.</i> [80].	136
13.6. Experimental results. Percentaged values are contributions to the respective total values. The cluster band onsets are given at half the peak height of the respective feature.	137
13.7. Experimental values used for the estimation of the decay widths [86].	137
13.8. Decay widths of the NeNe-ICD and NeAr-ICD obtained using different theoretical methods and from experiment.	138
13.9. The smallest geometric distances for each set of clusters and the corresponding cluster structures. Note that for set 4 only the random arrangement is listed, for which the argon content exactly equals the experimental one.	144
A.1. Atomic, experimental ionization energies. The non-relativistic ionization energies of the np were estimated by the weighted average of the experimental ionization energies of the $np_{3/2}$ and $np_{1/2}$	151
A.2. Lifetimes and relative ionization cross sections of noble gas atoms. The ratio of ionization cross sections for the neon atom was estimated from the degeneracies of the $p_{3/2}$ and $p_{1/2}$ states.	151
A.3. Shift of atomic ionization energies due to a cluster environment [141]. All values are given in eV.	151

Bibliography

- [1] L. MEITNER, *Z. Phys.* **9**, 131 (1922).
- [2] P. AUGER, *C.R.A.S.* **177**, 169 (1923).
- [3] P. H. P. HARBACH, M. SCHNEIDER, S. FARAJI, and A. DREUW, *J. Phys. Chem. Lett.* **4**, 943 (2013).
- [4] H.-K. KIM, J. TITZE, M. SCHÖFFLER, F. TRINTER, M. WAITZ, J. VOIGTSBERGER, H. SANN, M. MECKEL, C. STUCK, U. LENZ, M. ODENWELLER, N. NEUMANN, S. SCHÖSSLER, K. ULLMANN-PFLEGER, B. ULRICH, R. COSTA FRAGA, N. PETRIDIS, D. METZ, A. JUNG, R. GRISENTI, A. CZASCH, O. JAGUTZKI, L. SCHMIDT, T. JAHNKE, H. SCHMIDT-BÖCKING, and R. DÖRNER, *Proc. Nat. Acad. Sci.* **108**, 11821 (2011).
- [5] U. HERGENHAHN, *J. Rad. Biol.* **88**, 871 (2012).
- [6] B. BOUDAÏFFA, P. CLOUTIER, D. HUNTING, M. A. HUELS, and L. SANCHE, *Science* **287**, 1658 (2000).
- [7] X. PAN, P. CLOUTIER, D. HUNTING, and L. SANCHE, *Phys. Rev. Lett.* **90**, 208102 (2003).
- [8] F. MARTIN, P. D. BURROW, Z. CAI, P. CLOUTIER, D. HUNTING, and L. SANCHE, *Phys. Rev. Lett.* **93**, 068101 (2004).
- [9] U. HERGENHAHN, *J. Electron Spectrosc. Relat. Phenom.* **184**, 78 (2011).
- [10] K. GOKHBERG, S. KOPELKE, N. V. KRYZHEVOI, P. KOLORENČ, and L. S. CEDERBAUM, *Phys. Rev. A* **81**, 013417 (2010).
- [11] R. SANTRA and L. S. CEDERBAUM, *Phys. Reports* **368**, 1 (2002).
- [12] J. J. SAKURAI, *Modern Quantum Mechanics*, Addison-Wesley, rev. edition, 1994.
- [13] R. SANTRA, J. ZOBLEY, and L. S. CEDERBAUM, *Phys. Rev. B* **64**, 245104 (2001).
- [14] V. AVERBUKH and L. S. CEDERBAUM, *J. Chem. Phys.* **123**, 204107 (2005).

- [15] DIRAC, a relativistic ab initio electronic structure program, Release DIRAC13 (2013), written by L. Visscher, H. J. Aa. Jensen, R. Bast, and T. Saue, with contributions from V. Bakken, K. G. Dyall, S. Dubillard, U. Ekström, E. Eliav, T. Enevoldsen, E. Faßhauer, T. Fleig, O. Fossgaard, A. S. P. Gomes, T. Helgaker, J. K. Lærdahl, Y. S. Lee, J. Henriksson, M. Iliaš, Ch. R. Jacob, S. Knecht, S. Komorovský, O. Kullie, C. V. Larsen, H. S. Nataraj, P. Norman, G. Olejniczak, J. Olsen, Y. C. Park, J. K. Pedersen, M. Pernpointner, K. Ruud, P. Sałek, B. Schimmelpfennig, J. Sikkema, A. J. Thorvaldsen, J. Thyssen, J. van Stralen, S. Villaume, O. Visser, T. Winther, and S. Yamamoto (see <http://www.diracprogram.org>).
- [16] HARDRoC, Hunting Asymptotic Relativistic Decay Rates of Clusters (2013), written by E. Fasshauer (see <http://www.pci.uni-heidelberg.de/tc/usr/elke/hardroc/html/main.html>).
- [17] D. COSTER and R. D. L. KRONIG, *Physica* **2**, 13 (1935).
- [18] M. OHNO and G. A. VAN RIESEN, *J. Elec. Spec. Rel. Phen.* **128**, 1 (2003).
- [19] L. S. CEDERBAUM, J. ZOBLEY, and F. TARANTELLI, *Phys. Rev. Lett.* **79**, 4778 (1997).
- [20] S. MARBURGER, O. KUGELER, U. HERGENHAHN, and T. MÖLLER, *Phys. Rev. Lett.* **90**, 203401 (2003).
- [21] J. ZOBLEY, L. S. CEDERBAUM, and F. TARANTELLI, *J. Chem. Phys.* **108**, 9737 (1998).
- [22] R. SANTRA, J. ZOBLEY, L. S. CEDERBAUM, and F. TARANTELLI, *J. Electron Spectrosc. Relat. Phenom.* **114–116**, 41 (2001).
- [23] J. ZOBLEY, R. SANTRA, and L. S. CEDERBAUM, *J. Chem. Phys.* **115**, 5076 (2001).
- [24] V. AVERBUKH, I. B. MÜLLER, and L. S. CEDERBAUM, *Phys. Rev. Lett.* **93**, 263002 (2004).
- [25] E. FASSHAUER, M. PERNPOINTNER, and K. GOKHBERG, *J. Chem. Phys.* **138**, 014305 (2013).
- [26] S. BARTH, S. JOSHI, S. MARBURGER, V. ULRICH, A. LINDBLAD, G. ÖHRWALL, O. BJÖRNEHOLM, and U. HERGENHAHN, *J. Chem. Phys.* **122**, 241102 (2005).
- [27] K. GOKHBERG, V. AVERBUKH, and L. S. CEDERBAUM, *J. Chem. Phys.* **124**, 144315 (2006).

- [28] S. KOPELKE, K. GOKHBERG, L. S. CEDERBAUM, and V. AVERBUKH, *J. Chem. Phys.* **130**, 144103 (2009).
- [29] S. KOPELKE, K. GOKHBERG, V. AVERBUKH, A. TARANTELLI, and L. S. CEDERBAUM, *J. Chem. Phys.* **134**, 094107 (2011).
- [30] A. EINSTEIN, *Annalen der Physik* **322**, 891 (1905).
- [31] W. NOLTING, *Grundkurs Theoretische Physik 4*, Springer-Verlag, 5 edition, 2003.
- [32] A. EINSTEIN, *Über die spezielle und die allgemeine Relativitätstheorie*, Springer-Verlag, 23 edition, 2001.
- [33] C. B. KELLOGG, *An Introduction to Relativistic Electronic Structure Theory in Quantum Chemistry*, 1997.
- [34] P. A. M. DIRAC, *Proc. Roy. Soc. London A* **117**, 610 (1928).
- [35] C. D. ANDERSON, *Phys. Rev.* **43**, 491 (1933).
- [36] K. G. DYALL and K. FÆGRI JR., *Relativistic Quantum Chemistry*, Oxford University Press, Inc., 2007.
- [37] M. PERNPOINTNER, *J. Phys. B* **38**, 1955 (2005).
- [38] A. SZABO and N. S. OSTLUND, *Modern Quantum Chemistry*, Dover Publications Inc., 1996.
- [39] L. VISSCHER and E. VAN LENTHE, *Chem. Phys. Lett.* **306**, 357 (1999).
- [40] M. REIHER and A. WOLF, *Relativistic Quantum Chemistry*, Wiley-VCH Verlag GmbH, 2009.
- [41] T. SAUE, *ChemPhysChem* **12**, 3077 (2011).
- [42] W. NOLTING, *Grundkurs Theoretische Physik 5/2*, Springer-Verlag, 6 edition, 2006.
- [43] M. GELL-MANN and M. L. GOLDBERGER, *Phys. Rev.* **91**, 398 (1953).
- [44] J. R. TAYLOR, *Scattering Theory: The Quantum Theory of Nonrelativistic Collisions*, Robert E. Krieger Publishing Company, Inc., 1987.
- [45] S. KLAIMAN and I. GILARY, On Resonance: A First Glance into the Behaviour of Unstable States, in *Adv. Quant. Chem.*, volume 63, chapter 1, pp. 1–31, Elsevier, 2012.

-
- [46] H. FESHBACH, *Ann. Phys.* **5**, 357 (1958).
- [47] H. FESHBACH, *Ann. Phys.* **19**, 287 (1962).
- [48] H. FESHBACH, *Theoretical Nuclear Physics: Nuclear Reactions*, John Wiley & Sons, 1992.
- [49] U. FANO, *Phys. Rev.* **124**, 1866 (1961).
- [50] C. COHEN-TANNOUDJI, B. DIU, and F. LALOË, *Quantenmechanik*, volume Band 2, Walter de Gruyter GmbH & Co. KG, 3. auflage edition, 2008.
- [51] T. ÅBERG and G. HOWAT, *Handbuch der Physik Vol. 31*, chapter Theory of the Auger Effect, p. 469, Springer, Berlin, 1982.
- [52] V. AVERBUKH, P. KOLORENČ, K. GOKHBERG, and L. S. CEDERBAUM, *Quantum Chemical Approach to Interatomic Decay Rates in Clusters*, volume 20, p. 155, Springer Netherlands, 2009.
- [53] G. E. BROWN and D. G. RAVENHALL, *PRSLA* **208**, 552 (1951).
- [54] J. SUCHER, *Phys. Rev. A* **22**, 348 (1980).
- [55] G. PESTKA, M. BYLICKI, and J. KARWOWSKI, *J. Phys. B* **39**, 2979 (2006).
- [56] M. BYLICKI, G. PESTKA, and J. KARWOWSKI, *Phys. Rev. A* **77**, 044501 (2008).
- [57] I. P. GRANT and H. M. QUINEY, *AAMP* **23**, 37 (1988).
- [58] G. WENTZEL, *Z. Physik* **43**, 521 (1927).
- [59] H. ÅGREN, A. CESAR, and C.-M. LIEGENER, *Adv. Quantum Chem.* **23**, 4 (1992).
- [60] R. AHLRICH, *Theor. Chim. Acta* **41**, 7 (1976).
- [61] K. GOKHBERG, S. KOPELKE, N. V. KRZHEVOI, P. KOLORENČ, and L. S. CEDERBAUM, *Phys. Rev. A* **81**, 013417 (2010).
- [62] A. R. EDMONDS, *Angular Momentum in Quantum Mechanics*, Princeton University Press, 1974.
- [63] I. I. SOBEL'MAN, *Introduction to the Theory of Atomic Spectra*, Pergamon Press Ltd., 1972.
- [64] O. BJÖRNEHOLM, G. ÖHRWALL, and M. TCHAPLYGUINE, *Nucl. Instr. Meth. Phys. Res. A* **601**, 161 (2009).

- [65] M. FÖRSTEL, M. MUCKE, T. ARION, T. LISCHKE, S. BARTH, V. ULRICH, G. ÖHRWALL, O. BJÖRNEHOLM, U. HERGENHAHN, and A. BRADSHAW, *Phys. Rev. B* **82**, 125450 (2010).
- [66] T. P. MARTIN, *Phys. Rep.* **273**, 199 (1996).
- [67] B. HARTKE, *Angew. Chem. Int. Ed.* **41**, 1468 (2002).
- [68] K. J. B. and R. D. ETTERS, *J. Chem. Phys.* **66**, 3233 (1977).
- [69] E. T. VERKHOVTSEVA, I. A. GOSPODAREV, A. V. GRISHAEV, S. I. KOVALENKO, D. D. SOLNYSHKIN, E. S. SYRKIN, and S. B. FEODOS'EV, *Low Temperature Physics* **29**, 386 (2003).
- [70] R. E. BENFIELD, *J. Chem. Soc. Faraday Trans.* **88**, 1107 (1992).
- [71] M. FÖRSTEL, *Investigation of non-local autoionization processes in rare gas clusters*, PhD thesis, TU Berlin, 2012.
- [72] A. LINDBLAD, T. RANDEK, G. ÖHRWALL, O. BJÖRNEHOLM, M. MUCKE, V. ULRICH, T. LISCHKE, and U. HERGENHAHN, *Phys. Rev. B* **83**, 125414 (2011).
- [73] A. BONDI, *J. Phys. Chem.* **68**, 441 (1964).
- [74] O. ECHT, K. SATTLER, and E. RECKNAGEL, *Phys. Rev. Lett.* **47**, 1121 (1981).
- [75] A. L. MACKAY, *Acta Cryst.* **15**, 916 (1962).
- [76] E. PAHL, F. CALVO, KOČI, and P. SCHWERDTFEGGER, *Angew. Chem. Int. Ed.* **47**, 8207 (2008).
- [77] J. MOORE, C. DAVIS, M. COPLAN, and S. GREER, *Building scientific apparatus: a practical guide to design and construction*, Cambridge University Press, 2009.
- [78] J. M. SOLER, N. GARCIA, O. ECHT, K. SATTLER, and E. RECKNAGEL, *Phys. Rev. Lett.* **49**, 1857 (1982).
- [79] R. KARNBACH, M. JOPPIEN, J. STAPELFELDT, and J. WÖRMER, *Rev. Sci. Instrum.* **64**, 2838 (1993).
- [80] O. F. HAGENA and W. OBERT, *The Journal of Chemical Physics* **56**, 1793 (1972).
- [81] O. F. HAGENA, *Surf. Sci.* **106**, 101 (1981).
- [82] O. F. HAGENA, *Z. Phys. D* **4**, 291 (1987).
- [83] A. KNOP, B. WASSERMANN, and E. RUEHL, *Phys. Rev. Lett.* **80**, 2302 (1998).

- [84] T. HATSUI, H. SETOYAMA, N. KOSUGI, B. WASSERMANN, I. L. BRADENAUNU, and E. RUEHL, *J. Chem. Phys.* **123**, 211101 (2005).
- [85] M. FÖRSTEL, private communication.
- [86] E. FASSHAUER, M. FÖRSTEL, S. PALLMANN, M. PERNPOINTNER, and U. HERGENHAHN, *New Journal of Physics* (2014), in preparation.
- [87] W. P. REINHARDT, *Computer Physics Communications* **17**, 1 (1979).
- [88] P. W. LANGHOFF, C. T. CORCORAN, F. SIMS, J. S. WEINHOLD, and R. M. GLOVER, *Phys. Rev. A* **14**, 1042 (1976).
- [89] C. T. CORCORAN and P. W. LANGHOFF, *J. Math. Phys.* **18**, 651 (1977).
- [90] Gauss-Quadratur, <http://de.wikipedia.org/wiki/Gauss-Quadratur>.
- [91] F. MÜLLER-PLATHE and G. H. F. DIERCKSEN, Molecular photoionisation cross sections by moment theory. An introduction, in *Electronic Structure of Atoms, Molecules and Solids*, Kluwer Academic Publishers, 1990.
- [92] C. BLUMSTEIN and J. C. WHEELER, *Phys. Rev. B* **8**, 1764 (1973).
- [93] F. MÜLLER-PLATHE and G. H. F. DIERCKSEN, *Phys. Rev. A* **40**, 696 (1989).
- [94] F. MERTINS and J. SCHIRMER, *Phys. Rev. A* **53**, 2140 (1996).
- [95] J. SCHIRMER, A. B. TROFIMOV, and G. STELTER, *J. Chem. Phys.* **109**, 4734 (1998).
- [96] J. SCHIRMER, *Phys. Rev. A* **43**, 4647 (1991).
- [97] A. B. TROFIMOV and J. SCHIRMER, *J. Chem. Phys.* **123**, 144115 (2005).
- [98] I. CACELLI, V. CARAVETTA, and R. MOCCIA, *Mol. Phys.* **59**, 385 (1986).
- [99] K. KAUFMANN, W. BAUMEISTER, and M. JUNGEN, *J. Phys. B* **22**, 2223 (1989).
- [100] J. TULKKI, T. ÅBERG, A. MÄNTYKENTTÄ, and H. AKSELA, *Phys. Rev. A* **46**, 1357 (1992).
- [101] S. FRITZSCHE, *Comp. Phys. Comm.* **183**, 1525 (2012).
- [102] L. J. SAETHRE, T. D. THOMAS, and L. UNGIER, *J. Elec. Spec. Rel. Phen.* **33**, 381 (1984).
- [103] A. E. KRAMIDA, Y. RALCHENKO, J. READER, and N. A. T. (2013), NIST Atomic Spectra Database (version 5.1), 2014, Online.

- [104] P. KOLORENČ and V. AVERBUKH, *J. Chem. Phys.* **135**, 134314 (2011).
- [105] H. P. KELLY, *Phys. Rev. A* **11**, 556 (1975).
- [106] V. G. YARZHEMSKY and A. SGAMELLOTTI, *J. Elec. Spec. Rel. Phen.* **125**, 13 (2002).
- [107] A. ALBIEZ, M. THOMA, W. WEBER, and W. MEHLHORN, *Z. Phys. D* **16**, 97 (1990).
- [108] L. AVALDI, G. DAWBER, R. CAMILLONI, G. C. KING, M. ROPER, M. R. F. SIGGEL, G. STEFANI, M. ZITNIK, A. LISINI, and P. DECLEVA, *Phys. Rev. A* **51**, 5025 (1995).
- [109] K. SIEGBAHN, *ESCA Applied to Free Molecules*, North-Holland Pub. Co., 1969.
- [110] K. G. DYALL, *Theor. Chem. Acc.* **115**, 441 (2006).
- [111] M. PERNPOINTNER and A. B. TROFIMOV, *J. Chem. Phys.* **120**, 4098 (2004).
- [112] M. PERNPOINTNER, *J. Phys. B* **43**, 205102 (2010).
- [113] T. X. CARROLL, J. D. BOZEK, E. KUKK, V. MYRSETH, L. J. SÆTHRE, T. D. THOMAS, and K. WIESNER, *J. Elec. Spec. Rel. Phen.* **125**, 127 (2002).
- [114] A. AUSMEES, A. HAHLIN, S. L. SORENSEN, S. SUNDIN, I. HJELTE, O. BJÖRNEHOLM, and S. S., *J. Phys. B* **32**, 197 (1999).
- [115] H. AKSELA, A. AUSMEES, O.-P. SAIRANEN, S. J. OSBORNE, A. NAVES DE BRITO, A. KIVIMÄKI, J. JAUHAINEN, S. S., and S. AKSELA, *Phys. Rev. Lett.* **73**, 2031 (1994).
- [116] A. MÄNTYKENTTÄ, *Phys. Rev.* **47**, 3961 (1993).
- [117] S. FRITZSCHE, A. N. GRUM-GRZHIMAILO, E. V. GRYZLOVA, and N. M. KABACHNIK, *J. Phys. B* **44**, 175602 (2011).
- [118] G. C. KING, M. TRONC, F. H. READ, and R. C. BRADFORD, *J. Phys. B* **10**, 2479 (1977).
- [119] M. PERNPOINTNER, J. P. ZOBEL, and N. V. KRYZHEVOI, *Phys. Rev. A* **85**, 012205 (2012).
- [120] S. HEINÄSMÄKI, H. AKSELA, J. NIKKINEN, E. KUKK, A. KIVIMÄKI, S. AKSELA, and S. FRITZSCHE, *J. Elec. Spec. Rel. Phen.* **137–140**, 281 (2004).

- [121] J. FREUDENBERG, Berechnung der abstandsabhängigen Spin-Bahn-Kopplungskonstanten in den Edelgasdimeren Ar₂, Kr₂ und ArKr mittels relativistischer Propagatormethoden, Technical report, University of Heidelberg, 2011.
- [122] M. O. KRAUSE, T. A. CARLSON, and P. R. WOODRUFF, *Phys. Rev. A* **24**, 1374 (1981).
- [123] P. KOLORENČ, private communication.
- [124] V. STUMPF, private communication.
- [125] W. JANS, B. MÖBUS, M. KÜHNE, G. ULM, A. WERNER, and K.-H. SCHATNER, *Phys. Rev. A* **55**, 1890 (1997).
- [126] E. FASSHAUER, N. V. KRZHEVOI, and M. PERNPOINTNER, *J. Chem. Phys.* **133**, 014303 (2010).
- [127] J. B. WEST and J. MORTON, *Atomic Data and Nuclear Data Tables* **22**, 103 (1987).
- [128] M. LUNDWALL, W. POKAPANICH, H. BERGERSEN, A. LINDBLAD, T. RANDEK, G. ÖHRWALL, M. TCHAPLYGUINE, S. BARTH, U. HERGENHAHN, S. SVENSSON, and O. BJÖRNEHOLM, *J. Chem. Phys.* **126**, 214706 (2007).
- [129] S. BARTH, *Untersuchung des Interatomaren Coulomb-Zerfalls in schwach gebundenen Systemen*, PhD thesis, TU Berlin, 2007.
- [130] S. P. MARBURGER, *Experimentelle Untersuchungen zum Interatomaren Coulomb Zerfall an Neon Clustern: Nachweis eines ultraschnellen nichtlokalen Zerfallskanals*, PhD thesis, TU Berlin, 2004.
- [131] E. FASSHAUER and M. PERNPOINTNER, in preparation.
- [132] V. AVERBUKH and L. S. CEDERBAUM, *J. Chem. Phys.* **125**, 094107 (2006).
- [133] N. VAVAL and L. S. CEDERBAUM, *J. Chem. Phys.* **126**, 164110 (2007).
- [134] K. SCHNORR, A. SENFTLEBEN, M. KURKA, A. RUDENKO, L. FOUCAR, G. SCHMID, A. BROSKA, T. PFEIFER, K. MEYER, D. ANIELSKI, R. BOLL, D. ROLLES, M. KÜBEL, M. F. KLING, Y. H. JIANG, S. MONDAL, T. TACHIBANA, K. UEDA, T. MARCHENKO, M. SIMON, G. BRENNER, R. TREUSCH, S. SCHEIT, V. AVERBUKH, J. ULLRICH, C. D. SCHRÖTER, and R. MOSHAMMER, *Phys. Rev. Lett.* **111**, 093402 (2013).

- [135] S. SCHEIT, V. AVERBUKH, H.-D. MEYER, J. ZOBELLEY, and L. S. CEDERBAUM, *J. Chem. Phys.* **124**, 154305 (2006).
- [136] J. P. K. DOYE and D. J. WALES, *J. Chem. Soc., Faraday Trans.* **93**, 4233 (1997).
- [137] S. SCHEIT, L. S. CEDERBAUM, and H.-D. MEYER, *J. Chem. Phys.* **118**, 2092 (2003).
- [138] S. LAUER, H. LIEBEL, F. VOLLWEILER, H. SCHMORANZER, B. M. LAGUTIN, P. V. DEMEKHIN, I. D. PETROV, and V. L. SOUKHORUKOV, *J. Phys. B: At. Mol. Opt. Phys.* **32**, 2015 (1999).
- [139] K. CODLING, J. WEST, A. PARR, J. DEHMER, and R. STOCKBAUER, *J. Phys. B* **13**, L693 (1980).
- [140] B. F. J. LUYKEN, F. J. DE HEER, and R. C. BAAS, *Physica* **61**, 200 (1972).
- [141] R. FEIFEL, M. TCHAPLYGUINE, G. ÖHRWALL, M. SALONEN, M. LUNDWALL, R. R. T. MARINHO, M. GISSELBRECHT, S. L. SORENSEN, A. NAVES DE BRITO, L. KARLSSON, N. MÅRTENSSON, S. SVENSSON, and O. BJÖRNEHOLM, *Eur. Phys. J. D* **30**, 343 (2004).
- [142] G. V. MARR and J. B. WEST, *At. Data Nucl. Data Tables* **18**, 497 (1976).
- [143] J. THYSSEN, T. FLEIG, and H. J. A. JENSEN, *J. Chem. Phys.* **129**, 034109 (2008).
- [144] T. FLEIG, J. OLSEN, and L. VISSCHER, *J. Chem. Phys.* **119**, 2963 (2003).
- [145] S. R. KNECHT, *Parallel Relativistic Multiconfiguration Methods: New Powerful Tools for Heavy-Element Electronic-Structure Studies*, PhD thesis, University of Duesseldorf, 2009.
- [146] M. PERNPOINTNER, *J. Chem. Phys.* **121**, 8782 (2004).
- [147] Ikosaeder, <http://de.wikipedia.org/wiki/Ikosaeder>, 2014.
- [148] <http://docs.python.org/2/library/random.html>.
- [149] M. MATSUMOTO and T. NISHIMURA, *ACM Trans. Mod. Comp. Sim.* **8**, 3 (1998).

Publications

Publications Included in this Thesis

E. Fasshauer, M. Pernpointner and K. Gokhberg, *Interatomic decay of inner-valence ionized states in ArXe clusters: Relativistic approach*, J. Chem. Phys. **138**, 014305 (2013).

E. Fasshauer, M. Förstel, S. Pallmann, M. Pernpointner and Uwe Hergenhahn, *Utilizing ICD for structure analysis of clusters. A case study on coexpanded NeAr clusters*, New Journal of Physics, to be submitted.

Further Publications

E. Fasshauer, N. V. Kryzhevoi and M. Pernpointner, *Possible electronic decay channels in the ionization spectra of small clusters composed of Ar and Xe: A four-component relativistic treatment*, J. Chem. Phys. **133**, 014303 (2010).

M. Pernpointner, J. P. Zobel, E. Fasshauer and A. N. Sil, *Spin-orbit effects, electronic decay and breakdown phenomena in the photoelectron spectra of iodomethane*, Chem. Phys. **407**, 39 (2012).

Acknowledgements

First and foremost, I would like to thank my supervisor Markus Pernpointner, for his support through the years of my PhD and for giving me the freedom to follow my own visions.

Furthermore I would like to thank Andreas Dreuw, who spontaneously agreed to step in as second referee of my thesis.

I am grateful for the financial support from the Graduiertenkolleg 850, DAAD and Prof. Dr. Lorenz Cederbaum, who enabled funding in the last year.

I would like to thank

- the members of the Theoretical Chemistry group for wonderful and inspiring working conditions and social recreations, especially the classical quartett and the climbing group
- the Dirac family for their encouragement, the hearty working atmosphere and companionship at conferences around the world
- the system administrators of the TC group: Axel Lode, Evgeniy Gromov, Frank Otto, Markus Schröder and Victor Vysotskiy for their commitment and patience with my requests for new programs or newer compiler versions
- my research internship student Sebastian Pallmann for his work on the NeAr clusters as well as questioning the foundations of my ansatzes and thereby challenging me to find proper answers
- the students of my tutorials asking a lot of questions, which gave me the opportunity to look at generally accepted concepts from a variety of different perspectives
- Přemysl Kolorenč for explaining the concepts of FanoADC and Stieltjes as well as their non-relativistic implementations to me
- Vitali Averbukh for allowing me to use his Stieltjes code
- Radovan Bast for his continuous understanding and help with git, cmake and automatic testing as well as always finding new tools which make coding more elegant and efficient

- Caroline Krauter, Ghazal Jabbari, Jochen Schirmer, Kirill Gokhberg, Marko Förstel, J. Patrick Zobel, Přemysl Kolorenč, Sören Kopelke, Vasili Stumpf and Uwe Hergenbahn for fruitful discussions
- Marko Förstel and Uwe Hergenbahn for performing the experiments for my systems of interest and providing me with experimental input data
- the Theoretical Physics group of the Charles University of Prague for their hospitality during my visits
- my office mates Axel Lode, Caroline Krauter, Julian Grond and Markus Schröder, who made everyday work special
- Annika Bande, Arina Rybina, Axel Lode, Caroline Krauter, Jochen Schirmer, Kirill Gokhberg, Lorenz Cederbaum, Marko Förstel, Markus Hammermann, Markus Schröder, J. Patrick Zobel, Přemysl Kolorenč, Radovan Bast, Sabine Kopec, Solveig Scholl, Stefan Knecht and Vasili Stumpf for their helpful comments on the manuscript
- the Heidelberger Motettenchor for many nice rehearsals and concerts, as well as their sympathies and encouragements especially in the period of thesis writing
- Solveig Scholl for ripping me out of my mental roundabouts and joining me to the swimming bath
- the Geocachers for nice hikes and riddle solvings

Finally, I would like to thank my family and friends for their understanding, their support, their patience and love.

**Eidesstattliche Versicherung gemäß § 8 der Promotionsordnung
der Naturwissenschaftlich-Mathematischen Gesamtfakultät
der Universität Heidelberg**

1. Bei der eingereichten Dissertation zu dem Thema

Investigation of Relativistic Effects in Electronic Decay Processes

in Small and Large Noble Gas Clusters by Ab Initio and New Simulation Methods

handelt es sich um meine eigenständig erbrachte Leistung.

2. Ich habe nur die angegebenen Quellen und Hilfsmittel benutzt und mich keiner unzulässigen Hilfe Dritter bedient. Insbesondere habe ich wörtlich oder sinngemäß aus anderen Werken übernommene Inhalte als solche kenntlich gemacht.

3. Die Arbeit oder Teile davon habe ich ~~wie folgt~~/bislang nicht¹⁾ an einer Hochschule des In- oder Auslands als Bestandteil einer Prüfungs- oder Qualifikationsleistung vorgelegt.

Titel der Arbeit: _____

Hochschule und Jahr: _____

Art der Prüfungs- oder Qualifikationsleistung: _____

4. Die Richtigkeit der vorstehenden Erklärungen bestätige ich.

5. Die Bedeutung der eidesstattlichen Versicherung und die strafrechtlichen Folgen einer unrichtigen oder unvollständigen eidesstattlichen Versicherung sind mir bekannt.

Ich versichere an Eides statt, dass ich nach bestem Wissen die reine Wahrheit erkläre und nichts verschwiegen habe.

Ort und Datum

Unterschrift

¹⁾ Nicht Zutreffendes streichen. Bei Bejahung sind anzugeben: der Titel der andernorts vorgelegten Arbeit, die Hochschule, das Jahr der Vorlage und die Art der Prüfungs- oder Qualifikationsleistung.